Recreating the top quark: Commissioning and monitoring of the ATLAS Inner Detector and search for New Physics with heavy particles.

Arshak Tonoyan

Dissertation for the degree of Philosophiae Doctor (PhD)

Department of Physics and Technology
University of Bergen

October 2011

Acknowledgements

While working on this thesis I have benefited from advice and support of numerous people from all over the world. I will not try to list all of them but would like to mention the ones having the biggest impact on the preparation of this work.

The first person I would like to thank is my supervisor Anna Lipniacka, who has guided me from the first day till the last hour of my PhD term. The advices I got from Anna concerning both theoretical and experimental physics as well as administrative and private matters have made significant impact on the quality of my life as a PhD student at the University of Bergen. I will never forget the hiking with Anna. Very warm gratitude goes to my co-supervisor Heidi Sandaker. Heidi introduced me to the world of detectors and was constantly helping me in all the aspects of scientific work. I am also very grateful to my another co-supervisor, Bjarne Stugu, for his practical help for all matters regarding my work. Special appreciation is addressed to Per Osland for teaching me the basics of theoretical Particle Physics and for the useful discussions on many subjects of theoretical physics.

It is hard to overestimate the input from my colleagues Alex Kastanas and Thomas Burgess whom I am gratefully acknowledging for helping me to develop the code for Inner Detector Global Monitoring and for correcting my silly mistakes in programming. I also thank my other colleagues Therese Sjursen, Øystein Djuvsland, Maren Ugland, and Trygve Buanes both for interesting and useful discussions and for helping me to get adapted for the life in Norway.

I would also like to extend my deepest gratitude to my former colleagues and advisers from the Joint Institute for Nuclear Research in Dubna, together with whom one of the papers presented in this thesis is written. Nikolai Rusakovich and Vadim Bednyakov have put the basement of my knowledge in experimental Particle Physics and helped me to get quickly involved in the top quark related analyses at the ATLAS experiment. Evgeny Khramov deserves a special appreciation not only for his great help in programming, data analysis and simulations and significant contributions both in the $t\bar{t}$ resonance and top quark charge analyses but also for the great times we have spent together in Moscow, Dubna and at CERN.

A very special thanks goes to my Armenian friends Bakur, Hovhannes, Arsen, Artem and Hayk for the fun we have had at CERN (and not only) and for the countless chats on all subjects from politics to art, from sports to programming, from business to physics, which helped me to broaden my outlook on many subjects. It would not have been possible to finish the paper about the top quark charge in time without practical help and advices from Hovhannes.

Last, but not least, I acknowledge and thank my family. I feel my parents support even at a distance of thousands of kilometers. I would like to thank my wife Goar for being so patient and for understanding and constantly supporting me throughout these

years. The quality of my life increased significantly when my little Susanna was born last year. Even though she could not help me practically, the supply of energy which I got every day from her was crucial in completing this thesis. I have already discovered my Susy.

Abstract

The ATLAS (A Toroidal Lhc ApparatuS) experiment is one of the two general purpose experiments at the Large Hadron Collider (LHC) at CERN, the European Organization for Nuclear Research. The LHC is a proton-proton and ion-ion collider built in a 27 km long circular tunnel 100 meter below the surface of the Earth. The maximum energy at which LHC is capable to collide protons is 14 TeV in the center of mass frame, but currently it is being operated at half of its maximum energy, i.e. at 7 TeV. The first collisions at the LHC took place in November 2009. Before that the LHC detectors, including ATLAS (which was already built and installed in 2007) were commissioned using muons produced from the interaction of cosmic rays with the Earth atmosphere.

The Inner Detector is one of components of ATLAS detector, which is responsible for tracking of charged particles. It consists of three independent but complementary sub-detectors, which are built using different types of charged particle detecting concepts.

This thesis is based on four papers. The first paper documents the first measurement of the top quark charge at the LHC. The analysis is done on the data collected by ATLAS in the first half of year 2011. The charge is measured with two different techniques and the results from both show that the top quark charge is in agreement with the Standard Model (SM) prediction.

The second paper is actually a book, written by collaborative efforts of almost all members of the ATLAS collaboration, describing the status of all the analyses before the launch of the LHC. I have contributed in two chapters of this book with performing simulation based analyses of the top quark charge measurement and estimating the possibility to observe supersymmetric signals with help of tau leptons.

The third paper concerns the search for physics beyond the Standard Model. Several extensions of the Standard Model predict the existence of extra gauge bosons heavy enough to decay to top-antitop pairs. The studies based on the simulation of the production of such particles with different masses are performed in order to evaluate the potential of the ATLAS detector to discover them if they exist.

The last paper summarizes the results of the commissioning of the reconstruction software for the ATLAS detector with cosmic muons and with the data from the first proton-proton collisions at the LHC. As a part of ATLAS reconstruction software, the Inner Detector Global Monitoring tool was also commissioned.

List of papers

1. **The ATLAS Collaboration, *Measurement of the top quark charge in pp collisions at $\sqrt{s}$ = 7 TeV in the ATLAS experiment*, ATLAS-CONF-2011-141, Sep. 2011.**

   The measurement of the top quark charge carried out in the lepton+jets final state in the ATLAS experiment is presented in this paper. The results were obtained using the proton-proton collision data at $\sqrt{s}$ = 7 TeV corresponding to an integrated luminosity of about 0.70 fb^{-1}. Production of the exotic quark with charge $-4/3$e is excluded at more than five standard deviations. The study is done by two methods: "jet charge" and "semileptonic B decays". I have performed the analysis with the last method.

2. **The ATLAS Collaboration, *Expected performance of the ATLAS experiment: detector, trigger and physics, chapters "Top Quark Properties", and "Measurements from Supersymmetric Events"*, CERN-OPEN-2008-020, CERN, Geneva, 2009.**

   This is a book summarizing all active analyses of the ATLAS collaboration before the LHC startup. I contributed in the two attached chapters. I estimated the possibility to measure the top quark charge with the ATLAS detector using semileptonic decays of B hadrons. The results of this work in summarized in the section 3 of chapter "Top quark properties". The other contribution I have in this book is in the chapter "Measurements from Supersymmetric Events". I have studied the possibility to determine the endpoint of di-tau distribution in mSUGRA stau co-annihilation region, called SU1 in the book. The results of the study is summarized in sub-section 5.1.

3. **E. Khramov, A. Tonoyan, V. Bednyakov and N. Rusakovich, *On the Possibility of the Search for Top–Antitop Resonances at the LHC*, Physics of Particles and Nuclei Letters, Volume 5, Number 6, 515-519, Jan. 2008**

   Another top quark related study is documented in this paper. Prospects for observation of a narrow $t\bar{t}$-resonance at the LHC are studied. Five distinct masses of the resonance are considered: 0.7, 1.0, 1.5, 2.0 and 3.0 TeV. The minimal production cross-sections needed for the observation of the Z^0-like $t\bar{t}$ resonance at the LHC are estimated for the data corresponding to 1-300 fb^{-1} of integrated luminosity. I have contributed in the simulations of the Z' boson with different masses as well as in the development of the analysis code.

4. **A. Tonoyan, M.J. Costa and J.T. Boyd on behalf of the ATLAS Collaboration, *Commissioning of the ATLAS reconstruction software with first data*, J. Phys.:**

Conf. Ser. 219 032059, 2010.

This paper is based on the poster presented by me at CHEP2009 conference. It summarizes the effort on commissioning of the ATLAS reconstruction software with cosmic muons and with first beams at the LHC. I was responsible for the commissioning of the Inner Detector Global Monitoring tool, which is a part of the ATLAS reconstruction software.

As a member of the ATLAS collaboration I am co-author of more than 80 papers.

Contents

List of Figures

Chapter 1

Introduction

The modern theory of elementary particles is the Standard Model (SM), which is based on the group of gauge symmetries SU(3)×SU(2)×U(1). So far, it successfully describes almost all the physics processes involving electroweak and strong interactions. The elementary particles in SM are divided into two groups: *fermions* and *bosons*. Bosons are responsible for mediating the interaction and they have integer spin. Fermions have spin equal to 1/2 and are the particles which feel the force. We distinguish two types of fermions: leptons and quarks, reflecting their involvement in the electroweak and strong interactions. Leptons feel only electroweak interaction, while quarks can participate also in strong interaction. The property which makes particles (quarks) to feel strong interaction is called *color*. Thus quarks are color-charged, while leptons are colorless. Fermions are grouped in three generation. Fermions from the first generation, electron (e), electron neutrino (ν_e), up quark (u) and down quark (d) constitute the ordinary matter. Members of the second generation are heavier with respect to the ones from the first generation. They are muon (μ), muon neutrino (ν_μ), charm (c) and strange (s) quarks. The third generation fermions are the heaviest ones and are named tau (τ), tau neutrino (ν_τ), top (t) and bottom (b) quarks. Two fundamental properties of fermions, mass and charge are listed in table 1.1. From the same table we can see that there exist 12 types of fermions. All fermions have antiparticles, which have the same properties except of the sign of the charge, which is opposite.

Bosons, the carriers of fundamental interactions, described by the SM are of three types. The massless photon (γ) is the only carrier of the electromagnetic force. Eight gluons (g), which carry the strong interaction are also massless. The weak interaction is mediated by three massive bosons, Z, W^+ and W^-. The mass of Z boson is measured to be 91.1876 ± 0.0021 GeV [5], while the mass of W bosons is 80.399 ± 0.023 [5]. To explain the massiveness of W and Z bosons a new particle, called Higgs boson is introduced into the Standard Model [6]. This particle has not yet been observed experimentally. The discovery of Higgs boson is one of the main goals of the LHC experiments (see section 4.2).

Although the predictions from the Standard Model are in a very good agreement with the experimental results it can not be considered to be a fundamental theory. There are two main reasons for this. The first is that the SM has 19 free parameters. These parameters are not predicted by the SM and need to be measured experimentally. The second reason is that it still does not include the theory of the gravity. In addition to these the SM has several internal problems. A good overview of these problems is

	Quarks			Leptons		
Generation	Symbol	Charge	Mass [MeV/c^2]	Symbol	Charge	Mass [MeV/c^2]
1	u	+2/3	1.7÷3.1	ν_e	0	$<2\times10^{-6}$
1	d	-1/3	4.1÷5.7	e^-	-1	0.51
2	c	+2/3	$1.29^{+0.05}_{-0.11}\times10^3$	ν_μ	0	<0.19
2	s	-1/3	100^{+30}_{-20}	μ^-	-1	105.7
3	t	+2/3	$(173.2\pm0.9)\times10^3$ [7]	ν_τ	0	<0.18
3	b	-1/3	$4.19^{+0.18}_{-0.06}\times10^3$	τ^-	-1	1777

Table 1.1: Three generations of quarks and leptons, their charges and masses.

given in Ref. [8]. Two of them relevant to the work presented in this thesis are listed below:

- **The hierarchy problem:** The Higgs boson couples to all particles which have non-zero mass. This means that the mass of the Higgs particle depends on masses of all massive particles, when calculating it with higher order radiative corrections (loop corrections). The scale of these corrections depends on the renormalization cutoff scale Λ, which is the scale where new physics appears. Assuming that there is no new physics up to the Planck scale (10^{19} GeV), the loop corrections to Higgs mass become much larger than the predicted Higgs mass from the electroweak measurements ($\sim$100 GeV). In order to bring Higgs mass down to the electromagnetic scale careful fine-tuning need to be done, which is an unnatural procedure.

- **Dark matter problem:** The first evidence of dark matter was observed by astrophysicist Fritz Zwicky in 1933 by estimating the cluster's total mass based on the orbital velocities of galaxies in it and comparing it to it's mass estimated from the total brightness of the cluster [9], [10]. Since then several other astronomical and cosmological measurements indicate the presence of dark matter. The amount (mass) of dark matter in the Universe is estimated to be five times more than the amount of ordinary matter. The SM does not provide any dark matter candidate.

Chapter 2

Top quark physics

The top quark (t quark) is the heaviest elementary particle. It was discovered in 1995 by the CDF and DØ collaborations at proton-antiproton collider Tevatron (Fermilab, USA) [11], [12]. Since its discovery the properties of the top quark such as production cross-section, decay channels, mass, helicity, charge are being extensively studied by the scientists working at Tevatron experiments. From the day 1 of the LHC run, the CMS and the ATLAS collaborations started to search for top quark at the LHC and by the end of 2009 they confirmed its existence [13], [14].

The decay width of the top quark predicted in the Standard Model at next-to-leading order is [15]:

$$\Gamma_t = \frac{G_F m_t^3}{8\pi\sqrt{2}}\left(1-\frac{M_W^2}{m_t^2}\right)^2\left(1+2\frac{M_W^2}{m_t^2}\right)\left[1-\frac{2\alpha_s}{3\pi}\left(\frac{2\pi^2}{3}-\frac{5}{2}\right)\right], \tag{2.1}$$

where G_F is Fermi coupling constant, m_t is the top quark mass, M_W is the mass of W boson and α_s is the strong coupling constant. With top mass ~ 172 GeV, Γ_t is equal to 1.3 GeV. The lifetime (τ_t) of the top quark is proportional to $1/\Gamma_t$ and is on the order of 0.5×10^{-24} s [5]. With this short lifetime, the top quark is expected to decay before top-flavoured hadrons or $t\bar{t}$-quarkonium bound states can form [16]. This property makes the top quark unique from the point of view of its detection techniques. Unlike the other quarks, which hadronize and are registered as jets of hadrons, the top quark can be detected via its decay products. It decays to W boson and to one of the down-type quarks (quark having charge $-1/3$). Its decay width is expected to be dominated by the channel $t \to W+b$. The other decay channels, $t \to W+s$ and $t \to W+d$ are expected to be suppressed relative to $t \to W+b$ by the square of the Cabibbo–Kobayashi–Maskawa (CKM) matrix elements $|V_{ts}|$ and $|V_{td}|$. The values of these elements and also the $|V_{tb}|$ element of the CKM matrix are estimated to be [5]:

$$|V_{td}| = 0.00347^{+0.00016}_{-0.00012}, \tag{2.2}$$

$$|V_{ts}| = 0.00347^{+0.0011}_{-0.0007}, \tag{2.3}$$

$$|V_{tb}| = 0.999152^{+0.000030}_{-0.000045}. \tag{2.4}$$

Thus, since the decay ratio of $t \to W+b$ is defined as:

$$R_{t\to W+b} = \frac{Br(t\to W+b)}{Br(t\to W+q)} = \frac{|V_{tb}|^2}{|V_{td}|^2+|V_{ts}|^2+|V_{tb}|^2}, \tag{2.5}$$

in almost 100% of cases the top quark decays to W boson and b quark.

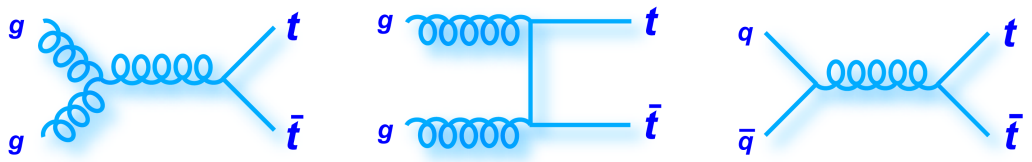

(a) (b) (c)

Figure 2.1: Feynman diagrams of $t\bar{t}$ production mechanisms at the lowest order at the LHC. In 90% of cases top-antitop pairs are produced via gluon fusion (a) and (b), while in 10% of cases the annihilation of a quark and an antiquark (c) is responsible for the $t\bar{t}$ production.

2.1 Production of top quarks

The top quark was the last quark to be discovered. The reason for this is its large mass. Before the launch of the LHC, Tevatron was the only collider able to produce top quarks. At the LHC, the main production scheme of top quarks is via gluon fusion, when two gluons interact strongly and produce a pair of top-antitop quarks ($t\bar{t}$). The $t\bar{t}$ production via quark-antiquark annihilation is less frequent, since at the LHC the particles in both beams are protons, and the only source of an antiquark in protons is sea quarks. In the Tevatron, where one of the beams consisted of antiprotons, the production was mostly via $q\bar{q}$ annihilation due to the presence of valence antiquarks in antiprotons. Figures 2.1a and 2.1b show the Feynman diagrams of gluon fusion at the lowest order, while the $q\bar{q}$ annihilation is described by the diagram in figure 2.1c.

The top quark can also be produced via weak interaction. In this case a single top or antitop quark is produced (not a pair of $t\bar{t}$). The Feynman diagrams for the weak production of single top at the lowest order are illustrated in figure 2.2. The processes described by the diagrams in the upper row of figure 2.2 are called *t-channel*. The figure 2.2d shows the single top production via *Wt channel*, while the diagram in figure 2.2e illustrates the *s-channel*.

2.2 Signatures of top-antitop pairs

Two of the analyses described in this thesis use $t\bar{t}$ production as a signal process. As discussed earlier in this chapter, the top quark decays to W boson and a b quark with almost 100% probability. Thus, decay products of a $t\bar{t}$ pair will consist of one positively charged and one negatively charged W bosons, one b quark and one $\bar{b}$ quark. The b and $\bar{b}$ quarks further hadronize producing hadronic jets, while W bosons decay either to a quark and an antiquark of different flavour or to a charged lepton and its corresponding neutrino. The Feynman diagrams illustrating all possible decay channels of a $t\bar{t}$ pair are shown in figure 2.3. Depending on the decay channel of W bosons we define three types of $t\bar{t}$ final states:

- **Dileptonic channel**, when both W bosons decay leptonically. In this case the final state consists of two jets coming from b and $\bar{b}$ quarks, two charged leptons and two neutrinos. The neutrinos can not be directly detected by ATLAS detector. But they can be detected indirectly via measuring the *missing transverse*

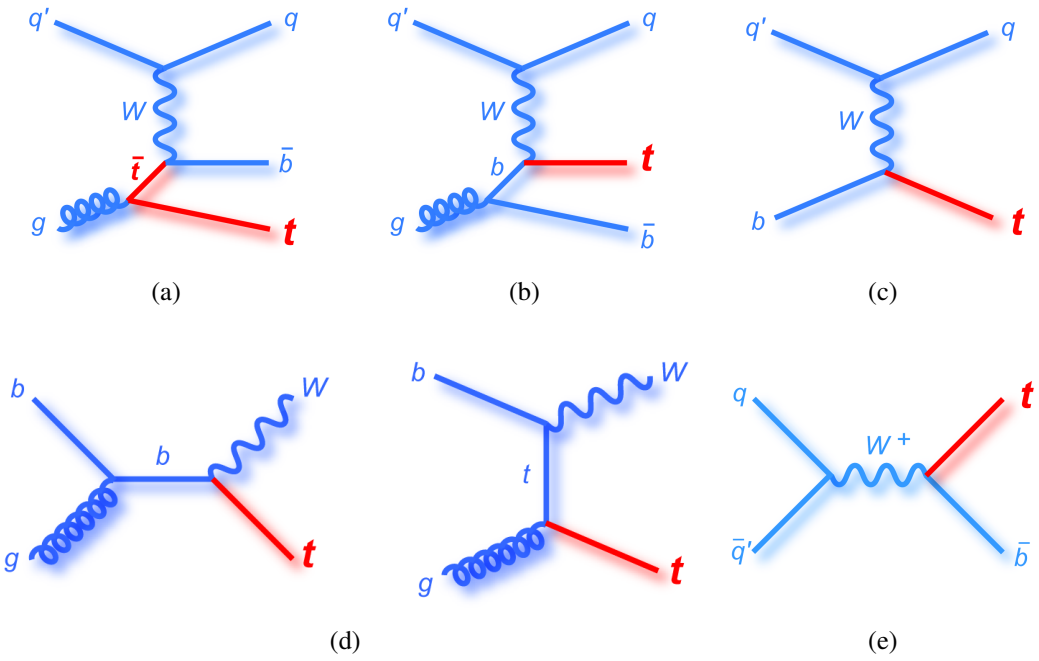

Figure 2.2: Feynman diagrams of single top $t\bar{t}$ production mechanisms at the lowest order at LHC via t-channel (a), (b) and (c), via Wt channel (d) and via s-channel (e). At hadron colliders the main contribution into single top production is coming from the t-channel.

energy, E_T^{miss}. E_T^{miss} is calculated by making use of the fact that the collisions take place along the z axis and thus the sum of transverse (to the z axis) momentum of collision products need to be 0. If by summing the momenta of all detected particles and detector noise we do not get 0 (or close to 0) we conclude that there was produced a particle (or several of them) which escaped the detector without interacting with it. The only known particles of such kind are neutrinos.

- **Lepton+jets channel**, when one of the W bosons decays leptonically, while another decays to quarks. Since these quarks also evolve into jets of hadrons, the final state in this channel includes one charged lepton, one neutrino and four jets. Two of the jets are initiated by b ($\bar{b}$) quarks. These jets can be identified by using *b-tagging* algorithms. These algorithms are based on the fact that tracks coming from decays of B mesons form a secondary vertex (displaced with respect to the collision vertex) and have relatively big impact parameter [17], [18]. This is the consequence of B meson's relatively long lifetime (1.5×10^{-12} s).

- **All-hadronic channel**, when both W bosons decay hadronically. This results in 6 jets in the final state.

Table 2.1 shows the measured values of W boson branching fractions [5]. which are used to calculate the share of each of the $t\bar{t}$ decay channels. The table 2.2 contains the results of these calculations. As can be seen from the table, the contribution of lepton+jets and all-hadronic channels is similar ($\sim 45\%$), while only in about 10% of cases the $t\bar{t}$ pair decays via dileptonic channel.

The channels containing taus are considered separately, due to the specificities of tau lepton reconstruction and identification at ATLAS [19]. Therefore, when talking

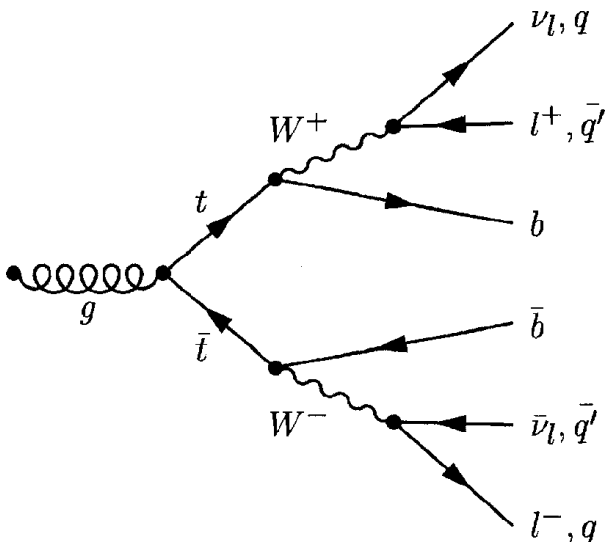

Figure 2.3: Possible decay channels of a $t\bar{t}$ pair. $\ell^{+(-)}$ refers to positively (negatively) charged lepton: electron, muon or tau.

Decay mode	Measured branching fraction, %
$W^+ \to e^+\nu_e$	10.75 ± 0.13
$W^+ \to \mu^+\nu_\mu$	10.57 ± 0.15
$W^+ \to \tau^+\nu_\tau$	11.25 ± 0.20
$W^+ \to u\bar{d}, c\bar{s}$	67.60 ± 0.27

Table 2.1: Measured branching fractions of W^+ boson [5]. Identical values are measured for the W^- boson.

about lepton+jets channel in ATLAS, we mean e+jets and μ+jets. Similarly, dilepton signature includes only ee, $e\mu$ and $\mu\mu$ channels. The pie chart in figure 2.4 shows the theoretical fractions of each of the $t\bar{t}$ decay channels.

The event display of one of the first e-μ $t\bar{t}$ dilepton candidate events with two b-tagged jets observed at ATLAS is shown in figure 2.5. The electron is shown by the green track and calorimeter cluster in the 3D view, and the muon by the long red track intersecting the muon chambers. The two b-tagged jets are shown by the purple cones, whose sizes are proportional to the jet energies.

$t\bar{t}$ pair decay channel	Fraction
$t\bar{t} \to b\bar{b}W^+W^- \to b\bar{b}(\ell^+\nu)(q\bar{q}')$	43.8 %
$t\bar{t} \to b\bar{b}W^+W^- \to b\bar{b}(q\bar{q}')(q''\bar{q}''')$	45.7 %
$t\bar{t} \to b\bar{b}W^+W^- \to b\bar{b}(\ell^+\nu)(\ell^-\bar{\nu})$	10.5 %

Table 2.2: The fractions of $t\bar{t}$ pair decay final states.

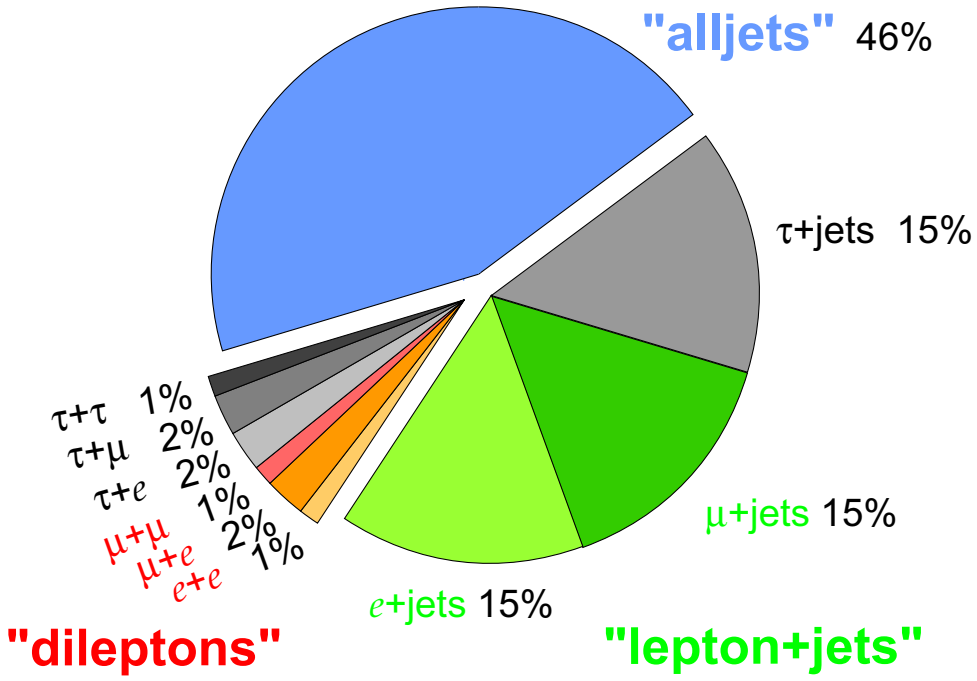

Figure 2.4: The fractions of $t\bar{t}$ decay channels.

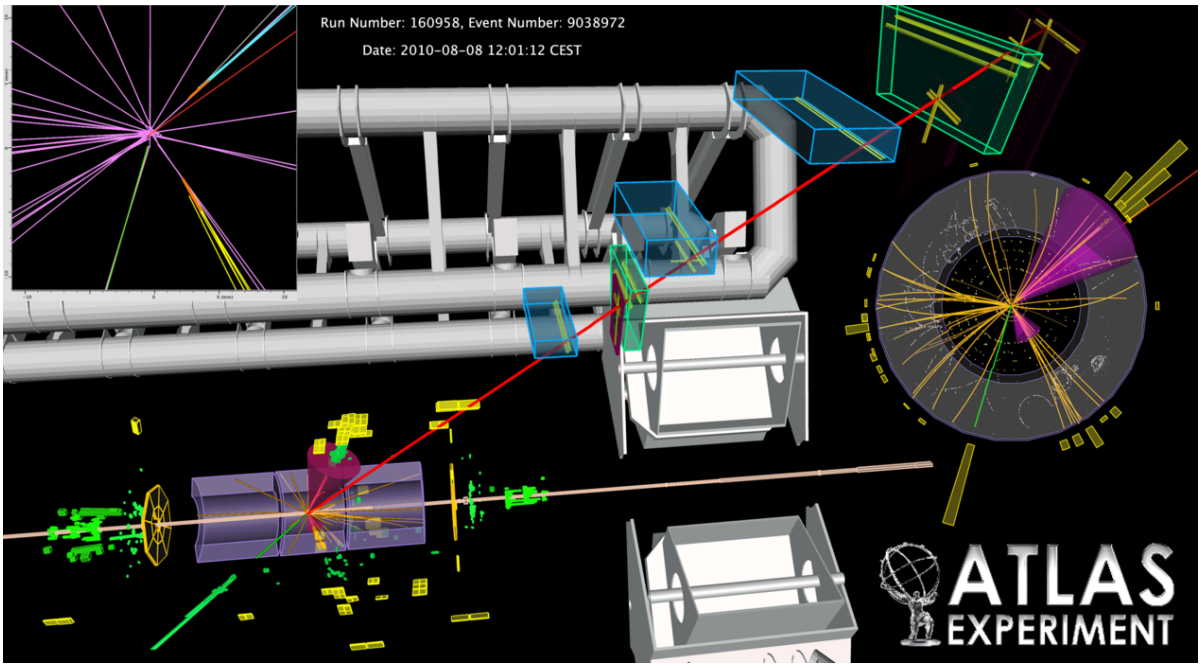

Figure 2.5: One of the first e-μ dilepton candidate events observed in ATLAS. The long red line shows the muon trajectory, while the short green line electron's trajectory. The green cluster at the end of the line shows the energy deposition by the electron in the EM calorimeter.

Chapter 3

Beyond the Standard Model physics

Though the Standard Model was tested in many experiments and has shown good agreement with their results, it is not considered to be a fundamental theory and has several unsolved problems [8]. Many extensions of Standard Model predict the existence of New Physics at the TeV scale of energies [20], at which the LHC operates.

3.1 Supersymmetry

One of the most favored extensions of the Standard Model is Supersymmetry (SUSY) [21]. It implies that all known elementary particles have super-partners in form of heavy particles with spin shifted by 1/2 with respect to the spin of their partners (ordinary particles). This means that super-partners of fermions are bosons and vise versa.

The main problem which is solved by introducing a SUSY theory is the so called *hierarchy problem* in the Standard Model, when the mass of the Higgs boson acquires quadratically divergent loop corrections. The solution comes in the form of a contribution of SUSY particles in the loop corrections, which has exactly the same size as the one from the ordinary particles, but with opposite sign. Thus the loop corrections from Standard Model particles are canceled out by their super-partners.

Another feature of SUSY is that it makes possible the existence of Grand Unified Theories (GUTs) [22], [23], which require the electromagnetic, weak and strong coupling constants to become equal at large (10^{16} GeV) scale as seen in figure 3.1. Thus all these forces can be described by one SU(5) or larger group. If the masses of SUSY particles range from $\sim$ 100 GeV up to $\sim$ 1 TeV, the run of coupling constants can be changed at this scale such that the lines intersect at one point (GUT point).

One of the main advantages of SUSY models is that many of them propose the *Lightest Supersymmetric Particle (LSP)* as a candidate for dark matter. This is the consequence of conserving the symmetry called *R-parity*, which is needed to be done to make protons stable when introducing SUSY. The *R-parity* is defined as:

$$P_R = (-1)^{2S+3B+L}, \tag{3.1}$$

where S is the spin of the particle, B is the baryon number and L is the lepton number. This definition results that all the Standard Model particles have $R = +1$, while for SUSY particles $R = -1$. In order to conserve *R-parity* the SUSY particles should be born in pairs and their decay products should contain at least one SUSY particle, which

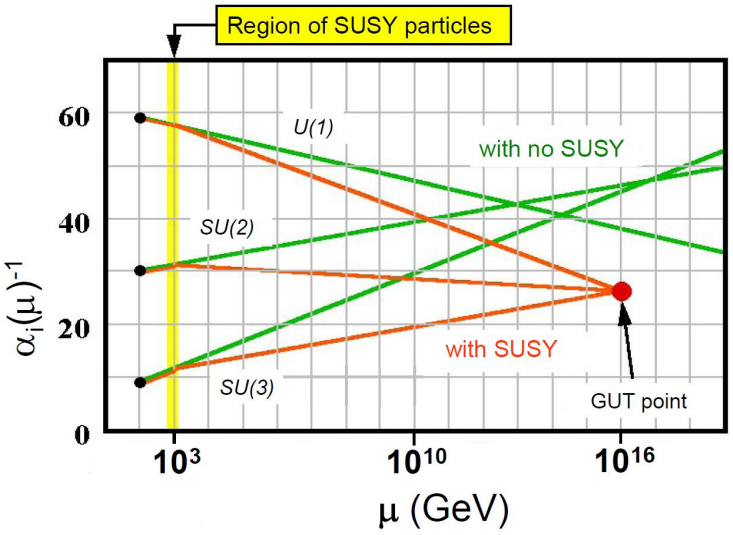

Figure 3.1: The running of all three Standard Model coupling constants without SUSY (green lines) and with SUSY (orange lines) if SUSY particles masses are $\sim$ 1 TeV [1].

implies that the *LSP* is stable. If it is also neutral and massive it becomes an ideal candidate for dark matter. Thus SUSY models can solve also one of the astrophysics problems.

The most studied SUSY model is the one with minimum number of superpartners, called Minimal Supersymmetric Standard Model (MSSM) [21]. It introduces 105 extra free parameters. The number of free parameters can be reduced by making extra assumptions. One of the widely investigated model (among MSSMs) is when SUSY breaking is gravity-mediated, whcih can be constrained by assuming the unification of forces at GUT scale. After this assumption only five free parameters remain [24], [21]. This constrained model is named minimal supergravity (mSUGRA). The mSUGRA parameters are m_0 - the scalar masses, $m_{1/2}$ - the gaugino masses, A_0 - soft breaking trilinear coupling constant, $tan\beta$ - the ratio of the vacuum expectation values of the neutral components of Higgs doublet and the sign of μ - the sign of the Higgsino mass parameter.

3.2 Heavy neutral bosons

There exist many theories of beyond the Standard Model physics that predict the existence of extra heavy neutral bosons, commonly referred to as Z'. Here we name some of the models, where the Z' can decay to top-antitop pairs. One of such models is the topcolor assisted technicolour model [25]. The technicolour models assume the existence of a new gauge interaction which generate the masses of W and Z bosons without a need to introduce the Higgs boson. In this way technicolor models solve also the hierarchy problem.

Another solution of hierarchy problem is proposed by the theories assuming the existence of extra dimensions. In these theories heavy neutral spin-2 particles are introduced, which are the excited states of massless *graviton*, the carrier of gravitational

force. The two common theories of extra dimensions are the ADD (Arkani-Hamed, Dimopoulos, Dvali) model [26], [27] and the RS (Randall, Sundrum) model [28], [29]. In the ADD model our four-dimensional world is on a brane. The extra dimensions are in form of torus with a radius r. The only force which can propagate to the higher dimensions is gravity. Thus gravity is stronger than we see on our brane. This allows to lower the Planck scale down to 1 TeV by introducing just two extra dimensions with r of the order of 0.1 mm. The more extra dimensions we require the smaller radius we need to bring the Planck scale to electroweak scale. In the RS model the Universe is a five-dimensional space with wrapped geometry. There are two branes: the "Planck" brane and the "TeV" brane. Our world with a weak gravitational force is situated on the "TeV" brane, while on the "Planck" brane the gravity is stronger.

Chapter 4

The ATLAS experiment: detector and physics

The ATLAS (A Toroidal Lhc ApparatuS) experiment is one of two general purpose experiments at the Large Hadron Collider at CERN, the European Organization for Nuclear Research. The chapter describes the detector and the physics program of the ATLAS experiment. It contains also a brief overview of the Large Hadron Collider.

4.1 The Large Hadron Collider

The Large Hadron Collider (LHC) [30] is a hadron collider designed to collide beams of protons with total energy up to 14 TeV at the center of mass frame of protons ($\sqrt{s}$ = 14 TeV). Is is also capable to collide heavy ions (*Pb-Pb*) at $\sqrt{s}$ = 2.76 TeV. The LHC is situated in a circular 27 km long tunnel buried around 50 to 175 m underground on the border of France and Switzerland. Currently, the LHC is operating at half of its maximal energy, $\sqrt{s}$ = 7 TeV. The magnets used in the LHC to steer the beams of colliding particles are made of superconducting materials (*Nb-Ti*), requiring extremely low temperatures to stay superconductors. They are cooled down to 1.9 K by a complex cryogenic system [31] using liquid helium as coolant.

The construction of the LHC started in 2001. In September 2008 the first beams were circulated in the accelerator rings. However, no collision took place till next year due to faulty electrical connections between the magnets resulting in mechanical damage and the release of helium from the cryogenic system of magnets. 53 damaged magnets were repaired and replaced. As a result of this incident, which took place 9 days after the first beam circulation, the first collisions which were initially expected to take place at the end of September 2008 were delayed and took place only at the end of November 2009. The first collisions were at injection energy, $\sqrt{s}$ = 900 GeV. The first $\sqrt{s}$ = 7 TeV collision happened in March 2010. After that the intensity of the beams was gradually increased. By September 2011 the beams contained 1.6×10^{14} protons each and were colliding with a luminosity of $\mathcal{L} = 3 \times 10^{33}$ cm^{-2}s^{-1}. The luminosity is defined such that the number of events of a particular process is given by $N = \mathcal{L} \cdot \sigma$, where σ is the cross-section of the this process. The collision rate was 20 MHz as of September 2011, but LHC is designed to be able to collide beams at up to 40 MHz frequency. The collisions take place at four points along LHC. At each of the points one of the major LHC experiments (ALICE, ATLAS, CMS and LHCb) is installed as illustrated in Figure 4.1.

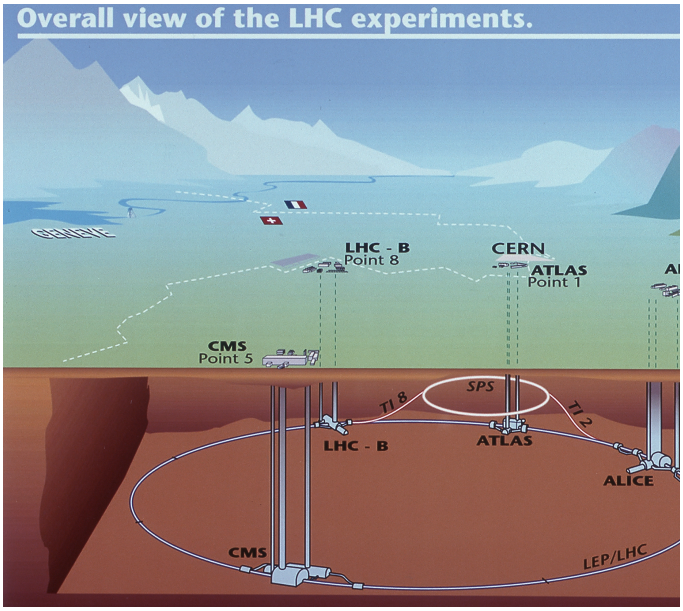

Figure 4.1: The locations of the four main LHC experiments.

4.2 Physics program

The ATLAS experiment was designed to explore the not-yet-explored frontiers of the High Energy particle physics [32]. Its design allows to both study the characteristics of already known particles and search for new particles predicted by both Standard Model (SM) and beyond SM theories. The tasks can be divided into the following groups:

- **Search for the Higgs boson**. The discovery of the Higgs boson is one of primary goals of the ATLAS experiment. The Higgs boson is the main missing piece of the SM. It is needed to describe the mechanism by which the particles obtain their masses. The experiments on the two predecessors of the LHC, the Large Electron Positron Collider (LEP) and Tevatron have performed the extensive hunt for the Higgs boson, but have not observe it. The ATLAS is able to either confirm or refute the existence of the Higgs boson in the whole range of its mass allowed by the theory. All methods of the Higgs boson search are based on the detection of its decay products. The ATLAS detector is designed to perform high precision measurements of the properties of Higgs decay products, such as electrons, muons, tau leptons, photons, quarks. The expected significance for the discovery with data corresponding to 10 fb^{-1} of integrated (by time) luminosity for different decay channels at the mass range [115; 600] is shown in figure 4.2 [2]. It can be noted that in the whole range the signal from the Higgs boson is expected to be observed by at least two standard deviation significance. The preliminary results of analyses using real data corresponding from 1.0 to 2.3 fb^{-1} of integrated luminosity are summarized in figure 4.3 [3]. The plot shows that, ATLAS can already exclude with 95% confidence the existence of Higgs boson in the mass ranges where the solid line dips below the horizontal dashed line at 1. These ranges are $(146; 232)\bigcup(256; 282)\bigcup(296; 466)$. But the Higgs particle can be hiding in the range most favoured by electroweak measurements, which indicate that it should be lighter than 148 GeV at 90% C.L [5].

- **Precision measurements of the Standard Model parameters**. Along with the Higgs searches ATLAS is designed to perform measurements of a number of SM parameters. ATLAS can measure many of these parameters with better precision than the previous experiments. The main fields where ATLAS is capable to perform precise measurements include top quark physics, W/Z boson physics and B physics.

- **Search for New Physics**. The searches for new particles predicted by the Beyond Standard Model theories (some of which are described in chapter 3) is also one of the main goals of the ATLAS experiment. The majority of the new particles in these theories decay into the known elementary particles which then can be detected. Depending on the model, the decay products can be leptons, photons, quarks, neutrinos or any combination of them. ATLAS is performing the searches for new particles by detecting their decay products.

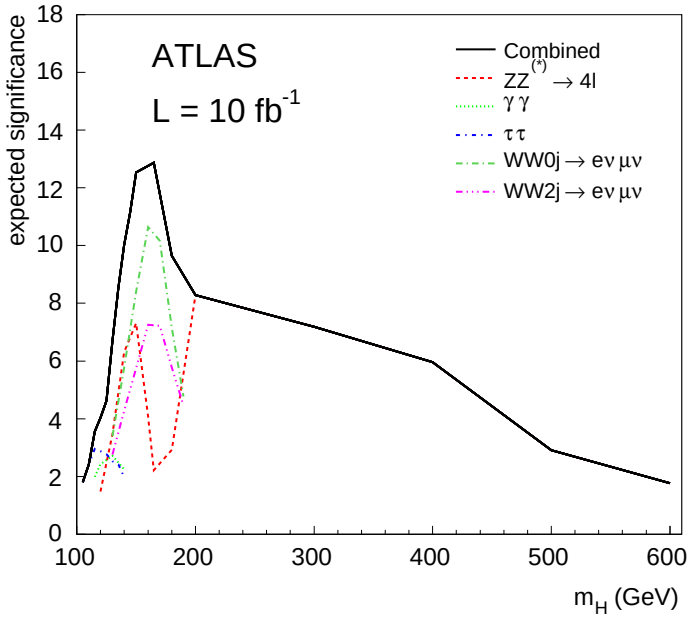

Figure 4.2: The Higgs boson discovery significance for the various decay channels and the combination with an integrated luminosity of 10 fb^{-1} for masses up to 600 GeV [2].

To perform all above mentioned tasks the ATLAS detector has to have the following components:

- High performance electromagnetic calorimeters for electron and photon identification and precise measurements of their kinematics;

- Full-coverage hadronic calorimeter with high granularity for the precise measurements of jets energy and missing transverse energy;

- Muon system capable to carry out high-precision muon momentum measurements;

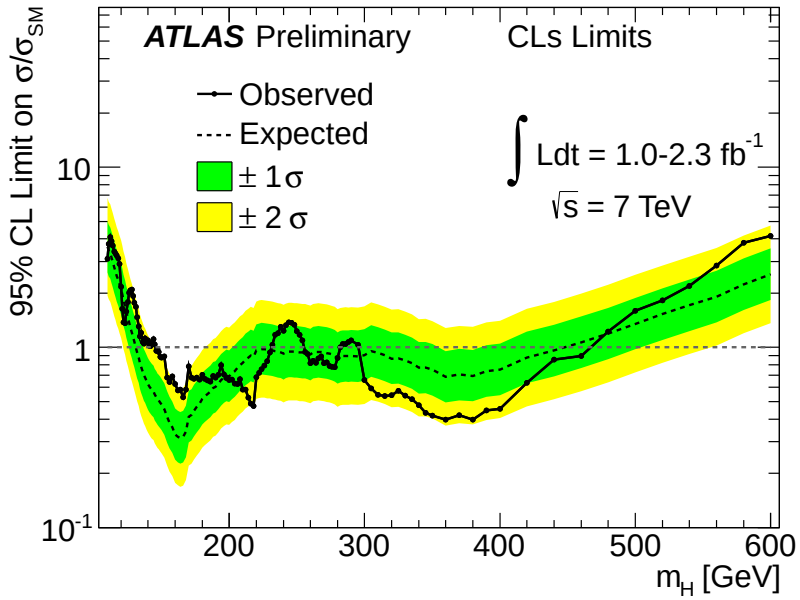

Figure 4.3: The expected and observed sensitivity of the search for the Higgs boson that arises from combining the results of searches in all decay modes studied to date. The black undulating dashed line shows ATLAS' predicted sensitivity to the Higgs boson in the mass range 115-600 GeV, based on simulations. The green and yellow bands correspond to the uncertainty in these predictions. The solid black line shows ATLAS' limit on Higgs production based on data collected up to date. ATLAS excludes with 95% confidence the existence of the Higgs boson in the mass ranges when the solid line dips below the horizontal dashed line at 1 [3].

- Efficient tracking for momentum and charge sign measurements of charged particles, reconstruction of primary (collision) and secondary (heavy flaviour and tau lepton decays) vertices;
- Fast triggering and data acquisition systems;
- The tracker and the muon system should be in a strong magnetic field in order to be able to measure track curvatures of high-momentum (up to several TeV) particles.

4.3 Overview of the ATLAS detector

The ATLAS is a multipurpose detector designed to perform searches of new physics as well as to measure the properties of already known particles and processes. The ATLAS is the largest detector among all LHC detectors. It has cylindrical shape with 25 m in diameter and 44 m in length. It consists of three main detector systems: The Inner Detector, Calorimeters and Muon System. Each of these detectors in their turn are made of several sub-detectors. Most of the ATLAS sub-detectors are divided into three parts: barrel, which is the central part of the particular sub-detector and two end-caps situated on each side of the barrel part. This division is conditioned by the orientation of detecting modules with respect to the beam (z) axis. The modules in barrel part are

oriented parallel to the beam axis, while in the end-caps the modules are placed in x-y plane. This is done to efficiently detect both particles flying at large angles with respect to the beam axis and thus crossing the sub-detectors at their central part and the ones having tracks with small θ, and passing mostly through end-caps.

ATLAS has two magnetic systems in addition to the main detector systems: Solenoid Magnet, surrounding the Inner Detector and inducing a 2 T magnetic field and three Toroid Magnets which are constructed such that the magnetic field they produce has average strength of 0.5 T and covers the area where the chambers of Muon System are situated. The cut-away view of the ATLAS detector demonstrating its size and location of its sub-detectors is illustrated in Figure 4.4. The detailed description of the ATLAS detector can be found in Ref. [33]. The features of the ATLAS detector needed to understand the work presented in this thesis are summarized in this section.

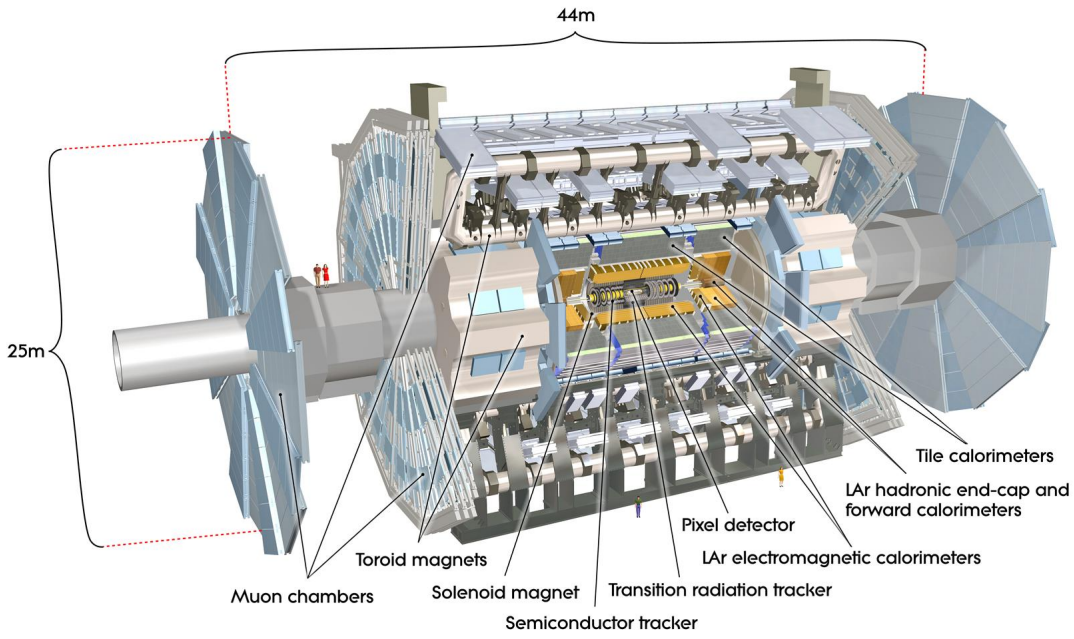

Figure 4.4: The schematic view of the ATLAS detector illustrating its size and components.

4.3.1 ATLAS coordinate system

ATLAS uses two coordinate systems: spherical and Cartesian. The ATLAS coordinate system if defined as follows:

- The origin is at the nominal interaction point.
- z-axis is along beam pipe. y points up and x points towards the center of the accelerator.
- In spherical coordinates, instead of polar angle, θ, pseudo-rapidity is used, which is defined as:

$$\eta = -ln\left(tan\frac{\theta}{2}\right). \tag{4.1}$$

4.4 The Inner Detector

Hundreds of charged particles can be produced as a result of each beam crossing creating large track density in the volume close to the interaction point. The Inner Detector (ID) is the innermost sub-detector and is responsible for detecting the tracks of charged particles. The main tasks of the ID are to measure the momentum of charged particles with high precision and to reconstruct both primary and secondary vertices with high accuracy. In order to be able to perform these tasks the ID consists of three independent but complementary sub-detectors each with high granularity of detecting elements. The cut-away view of the ID is illustrated in Figure 4.5. At inner radii, where the track density is high, high-accuracy pattern recognition requirements are met by using layers of silicon pixels (Pixel detector) and stereo pairs of silicon micro-strip layers (Semi-Conductor Tracker). At larger radii, the Transition Radiation Tracker (TRT) comprises several layers of gaseous straw tube elements interleaved with transition radiation material. With an average of 36 hits per track, it provides continuous tracking to enhance the pattern recognition and improve the momentum resolution. In addition to contributions to pattern recognition and track reconstruction TRT can provide particle identification by doing electron/pion separation over the large range of energies.

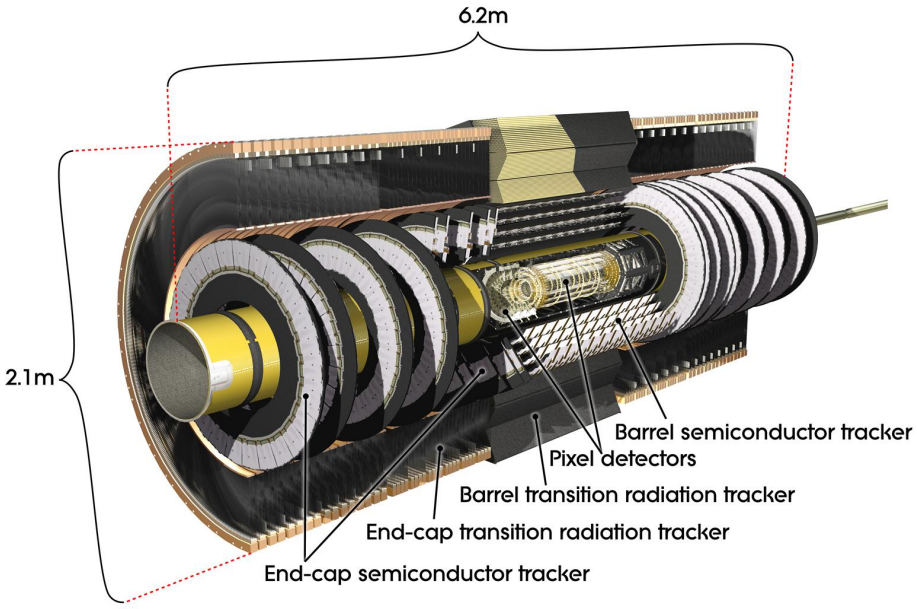

Figure 4.5: Cut-away view of the ATLAS Inner Detector.

The ID design resolutions can be parametrized with the following formula [33]:

$$\sigma(p_T) = \sigma(\infty)(1 \oplus p_T^s/p_T), \tag{4.2}$$

where $\sigma(\infty)$ is the asymptotic resolution expected at infinite momentum (intrinsic detector resolution) and p_T^s is the transverse momentum, for which the intrinsic detector resolution becomes equal to the one from the multiple-scattering. The expression (4.2) is an approximation, which works well both at high transverse momentum values, when the resolution is dominated by the intrinsic detector resolution and at low transverse momentum values, when the resolution is dominated by multiple scattering.

Track parameter	$0.25 < \|\eta\| < 0.50$		$1.50 < \|\eta\| < 1.75$	
	$\sigma(\infty)$	p_T^s (GeV)	$\sigma(\infty)$	p_T^s (GeV)
Inverse transverse momentum ($1/p_T$)	0.34 TeV^{-1}	44	0.41 TeV^{-1}	80
Azimuthal angle (ϕ)	70 μrad	39	92 μrad	49
Polar angle ($\cot\theta$)	0.7×10^{-3}	5.0	1.2×10^{-3}	10
Transverse impact parameter (d_0)	10 μm	14	12 μm	20
Longitudinal impact parameter ($z_0\times \sin\theta$)	91 μm	2.3	71 μm	3.7

Table 4.1: Expected resolution of track parameters at infinite momentum ($\sigma(\infty)$) and the transverse momentum, p_T^s, at which the multiple-scattering contribution equals that of the detector resolution [33].

The parameters $\sigma(\infty)$ and p_T^s for two pseudo-rapidity regions, one in barrel and one in end-cap, are found in table 4.1.

The tracking performance expectations from simulations are checked both with cosmic muons [34] and $\sqrt{s} = 900$ MeV and 7 TeV proton-proton collision data and are confirmed to be in good agreement with data [35], [36],[37].

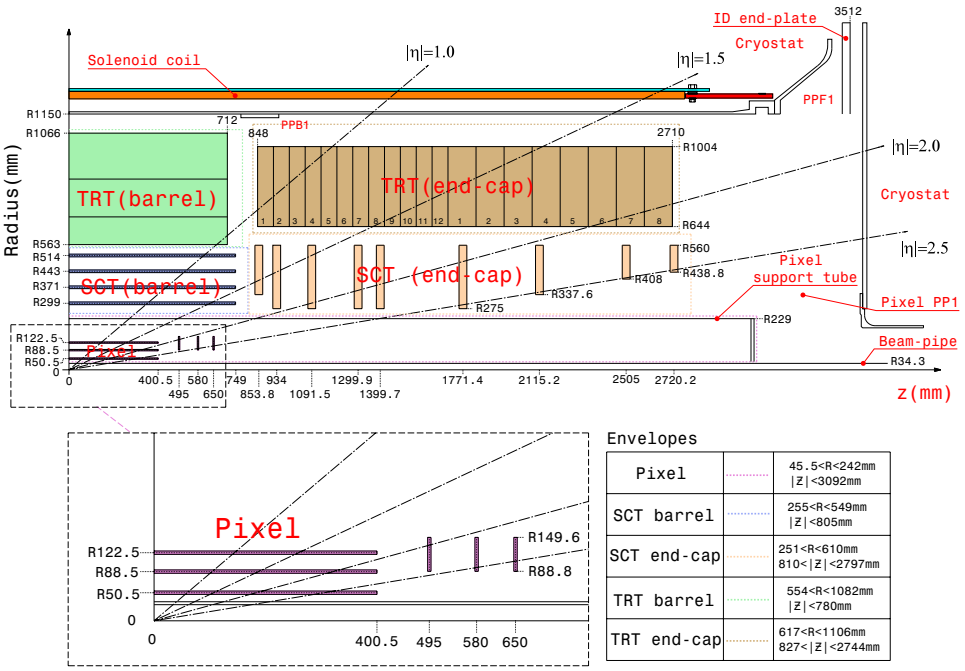

Figure 4.6: Plan view of a quarter-section of the ATLAS Inner Detector showing each of the major detector elements with its active dimensions and envelopes.

4.4.1 The Pixel detector

The Pixel detector is the closest one to the beam axis. It consists of three concentric layers of silicon pixel sensors in the central (barrel) part and three disks of sensors in each of the end-caps. The disks and layers are placed such that any particle coming from the interaction point and having a trajectory with $|\eta| < 2.5$ crosses three layers of Pixel detector (see Figure 4.6). The sensors are 250 μm thick detectors, made of

oxygenated n-type wafers with readout pixels on the n^+-implanted side of the detector. Overall 80 million sensors with size 50×400 (600) μm^2 are assembled on 1744 identical modules. Each sensor is read out by a separate electronic channel.

4.4.2 The SemiConductor Tracker

The Pixel detector is surrounded by one barrel with four layers of silicon micro-strip sensors called SemiConductor Tracker (SCT). In each of the end-caps the SCT is made in a form of nine disks placed such that silicon micro-strips are perpendicular to the beam axis. Together with three pixel disks at the end-cap part of the Pixel detector they make it possible to detect particles flying at low angles (downq to $|\eta| < 2.5$) with respect to the beam axis as shown in Figure 4.6. The SCT is made of 4088 two-sided modules. One module is composed of four silicon detectors. Each pair of these are bonded together to form 12 cm long readout strips. The pairs are glued on each side of the module at an angle of 40 μrad. The p^+-doped strips are implemented into the n-doped silicon wafer at 80 μm separation forming $p-n$ configuration. There are 768 active strips per sensor, plus two strips at bias potential to define the sensor edge. Thus SCT has approximately 6.3 million readout channels. The intrinsic resolution per module is 17 μm in r-ϕ plane and 580 μm in z direction.

4.4.3 The Transition Radiation Tracker

The third and outermost sub-detector of the ID is the Transition Radiation Tracker (TRT) consisting of 73 planes of 4 mm diameter straw tubes in the barrel part and 160 planes in each of the end-caps, thus providing large number of hits (in average 36) per track. The tubes are filled with gas mixture in following proportions: 70% Xe, 27% CO_2 and 3% O_2 [38]. In the barrel region, where the straws are parallel to the beam axis there are 52 544 straws with length of 144 cm. Each end of the straw is read out by a separate channel. In the end-caps region, the 37 cm long straws are arranged radially in wheels making them perpendicular to the beam axis. These straws are read out only from one end. The total number of straws in both end-caps is 245 760. End-caps and barrel together provide approximately 351 000 read-out channels [38]. The TRT covers the pseudo-rapidity range of $|\eta| < 2$ (Figure 4.6). Its intrinsic resolution in r-ϕ plane is 0.13 mm per straw. TRT does not provide measurement of the z coordinate.

4.5 Calorimeters

All calorimeters in ATLAS, except of the Forward Calorimeter, are sampling calorimeters made by alternating of layers of active medium and absorbers. They provide good containment for electromagnetic and hadronic showers, and also limit hadron punch-through into the muon system. The total thickness of the calorimeters at $\eta = 0$ is 11λ (interaction length). This has shown to be sufficient to reduce the punch-through into the muon system to an acceptable level. All calorimeters together cover the $|\eta| < 4.9$ range. The components of the ATLAS calorimeter system are illustrated in figure 4.7.

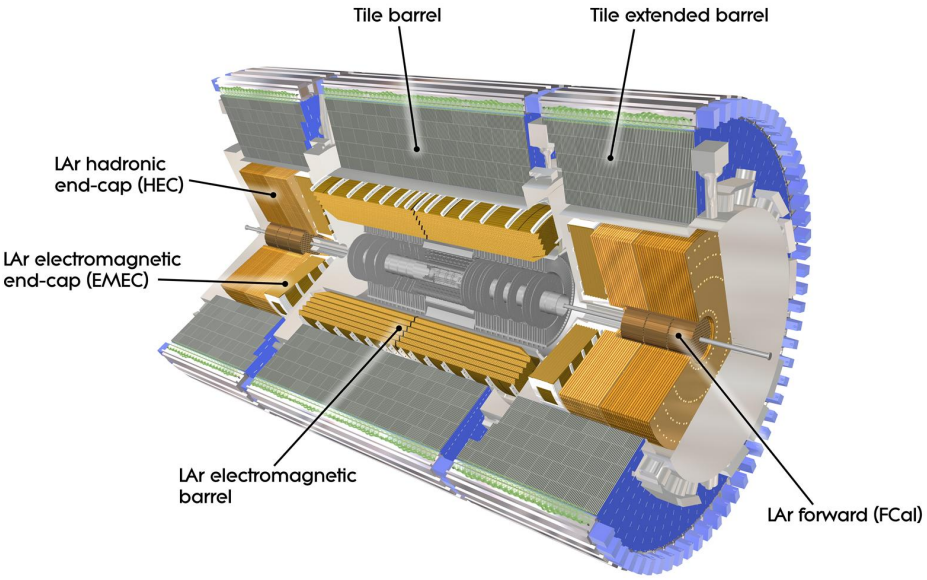

Figure 4.7: Cut-away view of ATLAS calorimeters.

4.5.1 The Electromagnetic calorimeter

The Electromagnetic (EM) Calorimeter is surrounding the Inner Detector and is a liquid argon (LAr) detector with accordion-shaped electrodes and lead absorber plates over its full coverage. The electrodes are made of three layers of copper interlayed with kapton. The two outer layers are under high voltage, while the middle one is used for read out of the signal. The gaps between absorbers and electrodes are filled with liquid argon, which is the active material of the detector. The accordion geometry provides complete ϕ symmetry without azimuthal cracks.

When an electron or a photon passes through the calorimeter, it initiates an electromagnetic shower when interacting with the lead absorbers. The components of the shower, then ionize the LAr, and the current produced by the drift of the ionization products towards electrodes is read out as signal. The EM calorimeter is divided into barrel part ($|\eta| < 1.475$) and two end-caps ($1.375 < |\eta| < 3.2$). The barrel part has a cylindrical shape with inner diameter of 2.8 m and outer diameter of 4 m. The length of the cylinder is 6.4 m. The end-caps have a wheel-shape. They are 0.63 m thick and with inner diameter of 0.66 m and external diameter of 4.2 m. In the precision measurement region which is defined as $|\eta| < 2.5$ the EM consists of three layers in depth. The rest of the EM is segmented into two layers. The granularity of samplings are η and layer dependent and are from 0.025×0.25 to 0.1×0.1 in the η-ϕ plane. In the region ($|\eta| < 1.8$) the EM calorimeter is complemented by presamplers consisting of a LAr layer of thickness of 1.1 cm (0.5 cm) in the barrel (end-cap) region in order to pick up the showers which started before the particle reached the EM calorimeter.

4.5.2 The Hadronic Tile calorimeter

The Hadronic Tile Calorimeter (TileCal) is placed behind the EM calorimeter and covers the range $|\eta| < 1.7$. It has a cylindrical shape with internal and external radii of 2.28

m and 4.25 m respectively. The total length is 11 m. It is made of 14 mm thick layers of iron absorbers interlayed with 3 mm thick scintillating tiles. When interacting with iron, a hadron produces a hadronic shower. The signal from the components of the shower is then collected by the scintillators. The total thickness of the TileCal is 2 m, which corresponds to 8 λ (interaction length). It is segmented in three layers in depth. The granularity of samplings in the first two layers are 0.1×0.1, while the last layer has coarser samplings with 0.2×0.1 size in the η-ϕ plane.

4.5.3 The Hadronic End-cap calorimeter

The Hadronic End-cap calorimeter (HEC) consists of two wheel-shaped parts, each placed at one of the two ends of the EM calorimeter. Its covers $1.5 < |\eta| < 3.2$ range. The HEC uses the same detecting technology as the EM calorimeter, but with flat absorbers made of copper. The first 24 plates of absorbers (counted from the side closer to the EM calorimeter) have 25 mm thickness, while the remaining 16 are two times thicker. The size of the readout cells is $\Delta\eta \times \Delta\phi = 0.1\times0.1$ in the region $|\eta| < 2.5$ and 0.2×0.2 for larger values of η.

4.5.4 The Forward calorimeter

The purpose of the Forward Calorimeter (FCAL) is to measure both electromagnetic and hadronic showers at high eta region. Its coverage is $3.1 < |\eta| < 4.9$. The FCAL has LAr as a sensitive medium, but uses different detecting technology. It consists of three modules in each end-cap. The first module is intended to register the electromagnetic shower, while the second and third module is designed to catch the hadronic shower. All modules are made of copper plates placed next to each other. The plates of the first module have 12260 holes in them, in which the electrodes are placed. An electrode consist of a copper-made rod placed into a copper-made tube. The gap between the rod and the tube is filled with LAr. The second and third modules have 10200 and 8224 electrodes respectively. The electrods in these modules consist of tungsten rods placed into copper tubes.

4.6 The Muon spectrometer

The outermost sub-detector of the ATLAS is the Muon spectrometer (figure 4.8). It triggers muons and provides precision measurements of the their track parameters. The Muon spectrometer is situated in a magnetic field with average strength of 0.5 T, generated by air-core toroidal magnets. The magnets are configured such that the field they produce is orthogonal to the trajectories of the muons coming from the interaction point. The muon system uses four different types of detecting technologies: Monitored Drift Tubes (MDT), Resistive Plate Chambers (RPC), Thin Gap Chambers (TGC) and Cathode-Strip Chambers (CSC). The MDTs and the CSCs are used to measure the track curvature with high precision, while the RPCs and TGCs are primarily aimed for triggering purposes.

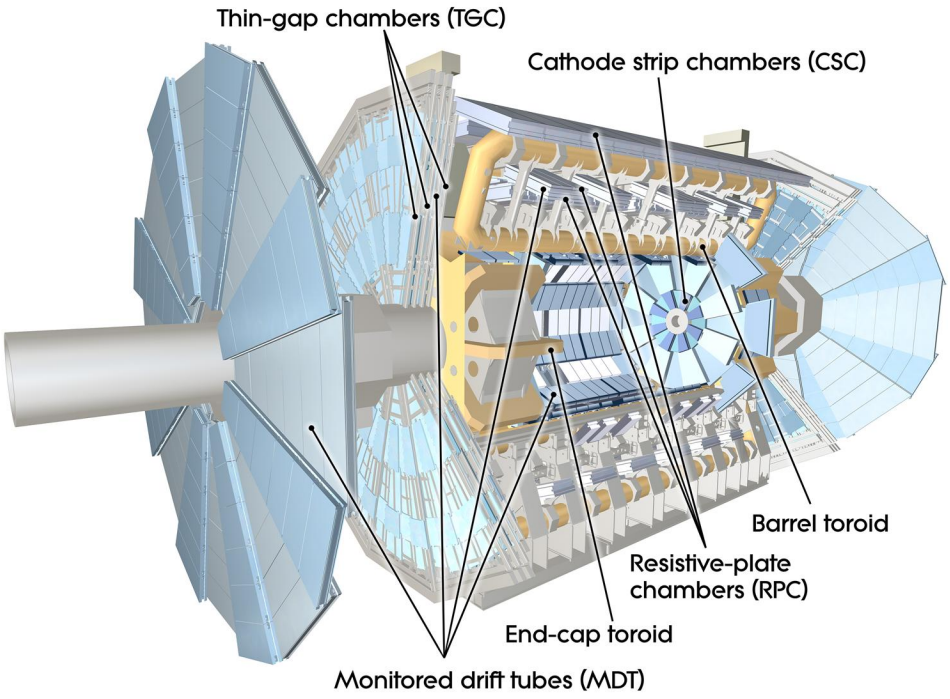

Figure 4.8: Cut-away view of ATLAS Muon spectrometer.

4.6.1 Monitored Drift Tubes

The MDT is the main technology for the precision measurements of muon track parameters at ATLAS. The muon passing through the ATLAS detector in the range of $|\eta| < 2.7$ can cross three to eight layers of MDTs. The MDTs are drift tubes filled with Ar/CO_2 (93%/7%) gas mixture under 3 bar pressure. The tubes are aluminum made with 30 mm in diameter and are concentric around a tungsten-rhenium 50 μm thick wire. Muons crossing an MDT ionize the gas and the electrons are collected by the wire which is at 3080 V potential with respect to the tube walls.

4.6.2 Cathode-Strip Chambers

The particle flux at the first layer in the region $|\eta| > 2.0$ is above the threshold at which MDT can provide efficient counting. Therefore the first layer of muon system in the range $2.0 < |\eta| < 2.7$ consists of cathode-strip chambers, which are multiwire proportional chambers. The strips of the cathodes on one side is parallel to the wire while on the other side it is perpendicular. The position of the muon trajectory intersection is defined by interpolation between the charges induced on neighbouring strips. The wires are 30 μm thick. The operation voltage is 1900 V.

4.6.3 Resistive Plate Chambers

The RPCs have a threefold purpose. They provide bunch-crossing identification (BCID), discriminate based on the muon transverse momentum and provide a complementary measurement of the muon coordinate which can be used for pattern recognition and muon track reconstruction. RPCs cover only the barrel region $|\eta| < 1.05$. They are

gaseous parallel electrode-plate detectors. The electric field between the plates is 4.9 kV/mm. The signal is read out through capacitive coupling to metallic strips mounted on the plates.

4.6.4 Thin Gap Chambers

The TGCs were selected to perform triggering in end-cap region $1.05 < |\eta| < 2.4$. They, like RPCs, can also provide the measurement of the ϕ coordinate to complement the measurements of the MDTs in the bending direction. The TGCs are multi-wire proportional chambers with small space between wires and the cathode and large space between the wires.

4.7 Magnets

In order to measure the momentum of charged particle a complex system of superconducting magnets is employed by ATLAS. It consists of two parts. The first part is a 5.8 m long solenoid surrounding the Inner Detector with diameter of 2.5 m. It generates a 2 T axial field at the center and 2.6 T at the windings. The field of this magnet is used to measure the momentum of charged particles in the Inner Detector. The second part consists of three air-core toroid magnets, each made of eight coils. Each of these coils is placed in a separate cryostat. The goal of toroid magnets is to bend trajectories of muons in Muon Spectrometer. In the range $|\eta| < 1.4$, the bending is provided by the large barrel toroid. The two smaller end-cap toroids cover the range of $1.6 < |\eta| < 2.7$, while in the range of $1.4 < |\eta| < 1.6$, the field is generated both by the barrel and end-cap magnets. The outer size of the magnet system is 22 m in diameter and 26 m in length. The operational temperature of all magnets is 4.5 K.

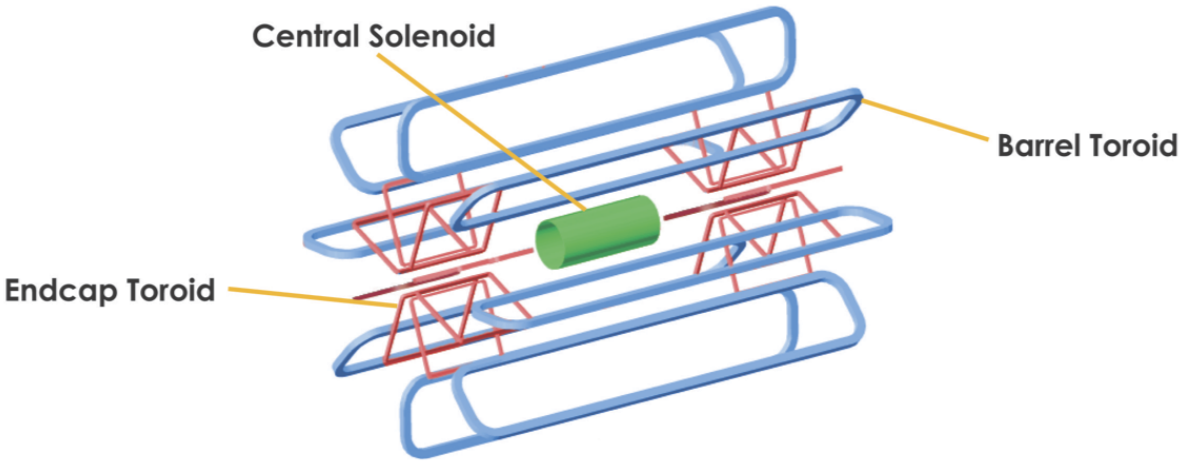

Figure 4.9: The geometry of ATLAS magnet system.

4.8 Trigger

As mentioned in section 4.1, the design frequency of collisions at the LHC is 40 MHz. It is not possible to record events at this high frequency from all $\sim 10^8$ read-out channels of the ATLAS detector. Therefore a trigger system is needed to reduce the 40 MHz input rate to an output rate of about 200 Hz for recording and offline processing. This limit is conditioned by the average data rate of $\sim$ 300 MB/s, determined by the computing resources for data storage and processing. The ATLAS trigger chain has three levels. The level 1 (L1) trigger uses data from the the calorimeters and muon system to decide weather event looks interesting or not. The output rate of L1 can be up to 75 kHz. L1 is a hardware based trigger. The level 2 (L2) as well as level 3 (Event Filter, EF) are software based triggers. They can use the data from all sub-detectors, but L2 reconstructs the data only from the Regions of Interests (RoI) determined by the L1 trigger. At the input of the Event Filter the data rate is already reduced to 3 kHz. In its turn the EF reconstruct the full event and based on the predefined signatures selects events to be recorded. The signatures depend on the goal of a particular run and are based on combinations of reconstructed physics objects, i.e. electrons, muons, jets, taus, photons or transverse missing energy. There are also signatures when the trigger is fired if cosmic muon passes through the detector or if inelastic collisions take place. The schematic view of ATLAS trigger system can be seen in figure 4.10.

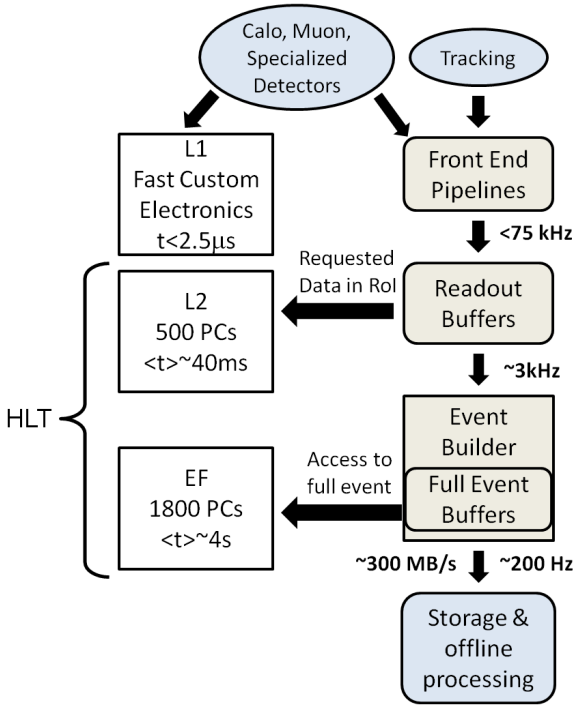

Figure 4.10: The schematic view of ATLAS trigger chain.

4.9 Data and simulation processing skim

When a trigger is fired the signals from the whole detector is read out. These signals come from a single event: either bunch crossing or passage of cosmic muon through

the detector. They are digitized and saved in a format called Raw Data Objects (RDO). Then, the reconstruction procedure is performed which converts the digitized signals from the detector into objects and stores the events in ESD (Event Summary Data) format. The ESD has an object-oriented representation. Physics analysis can already be performed using ESD files, but the event size in these files is big since the event contains the information from all the channels of the detector. Therefore ESD is not suitable for physics analysis. A reduced event representation, derived from ESD and called Analysis Object Data (AOD) is more suited for analysis. It contains physics objects and other elements of analysis interest. To even more reduce the size of an event, the Derived Physics Data (DPD) is introduced. It is an ntuple-style representation of event data and can be directly used by the analysis tool ROOT [39], widely used in High Energy experiments. Events in DPD files contain objects intended to be used by a particular type of analysis. RDO, ESD and AOD files are produced centrally, while DPDs are produced either by working groups or by individual users.

The simulation of physics processes at the ATLAS detector are performed in several steps. The first step is the event generation, which is the simulation of production and decay of particles. This is done by using one of C++ or Fortran based event generators. Pythia [40] and Herwig [41] are among the most widely used event generators in Particle Physics. The next step is the simulation of interaction of generated particles with the ATLAS detector. This is done by using GEANT4 simulation toolkit [42] intended to simulate the physics processes of particles interaction with matter. The third step is so called digitization, which is the simulation ot detector response. After this step the simulated data has the same format as the real data coming from the detector, i.e. RDO format. Thus the reconstruction and further steps on simulated data are done in the same way and with help of the same software as for real data.

All the procedures described above are carried out within the ATLAS software framework, Athena [43].

Chapter 5

The Inner Detector Global Monitoring

The Inner Detector Global Monitoring (ID Global Monitoring) is a tool which is responsible for monitoring how the ATLAS Inner Detector (ID) works as a tracker. Combined ID tracks, made of hits from all three sub-detectors are used as the primary tool. In addition to combined tracks, track segments made by hits from a single sub-detector are used. Besides tracks, the occupancy of the ID, ID hit timing information and bunch crossing and level 1 trigger identifiers (BCID and L1ID respectively) are used to monitor the stability and the synchronization of ID sub-detectors. The aim is to determine both the status of the detectors and the impact which the sub-detector issues have on the tracking performance of the ID. The ID Global Monitoring was launched in 2005, when the ID, being still on the surface, took its first cosmic muons data. Since then it has been continuously developed and commissioned first with cosmic muons and later with $\sqrt{s} = 900$ GeV and $\sqrt{s} = 7$ TeV proton-proton collisions. The ID Global Monitoring is part of the ATLAS Data Quality Monitoring (DQM). It produces and analyzes over 250 histograms both in online mode, when a quick feedback is required and in offline mode, when more detailed analysis is provided. The results shown here are based on the cosmic muons runs taken from September 2008 till March 2009 and proton-proton collision runs taken from October 2009 till March 2010. An event with a cosmic muon passing through the Inner Detector is shown in figure 5.1.

5.1 Software Design and Tools

From the software point of view the ID Global Monitoring is one of the packages of ATLAS reconstruction software. It is a C++ based package and consists of several different tools. When each tool is called it produces a set of ROOT [39] histograms based on the data. The core functionality for this is provided by the `ManagedMonitoringToolBase` Athena package from which ID Global Monitoring inherits. A basic set of functions is implemented in this package to store histograms in the Athena Histogramming service, to save and to retrieve the monitoring related information.

Figure 5.2 shows the structure of the ID Global Monitoring package and its class inheritance. In the center is the `InDetGlobalMotherMonTool`, the base class of all tools, providing some basic functionality for the monitoring. This is an extension of the functions provided by `ManagedMonitoringToolBase` that is common to all monitoring tools. For tools requiring trigger awareness the class `InDetGlobalMotherTrigMonTool`

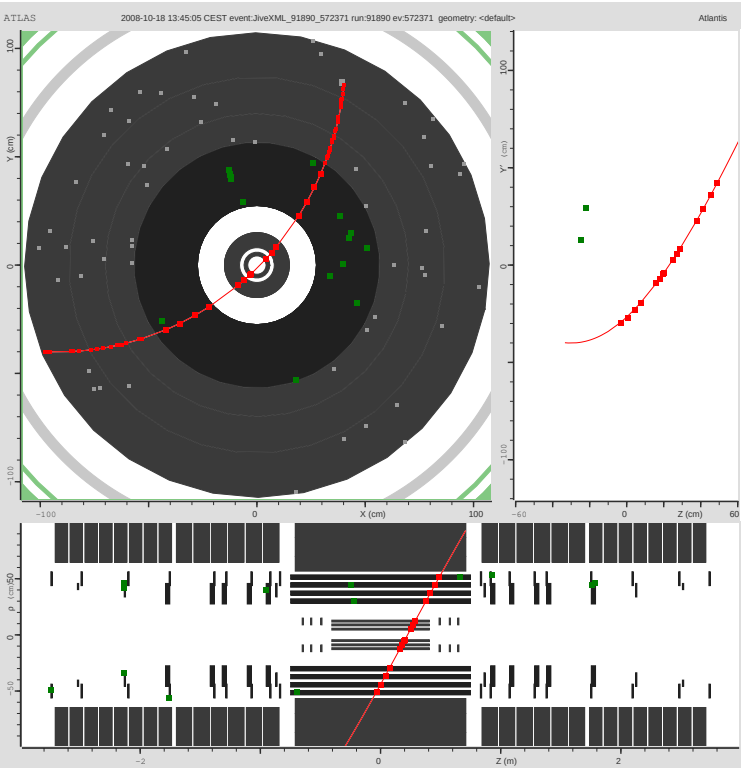

Figure 5.1: An event display showing the x-y (top left), z-ρ (bottom) and z-y (top right) projections of the track of a cosmic muon passing through the Inner Detector. The track is shown by a red line. The hits associated to the track are shown by red squares.

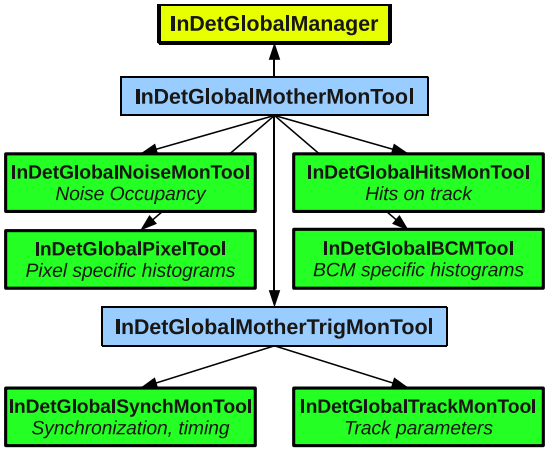

Figure 5.2: The class structure of ID Global monitor. The blue boxes are the base classes of all the tools. The boxes in green are tools called by the monitor to produce the Data Quality histograms. The manager is in yellow.

extends to cover these too. All tools inherit from one of these classes. In addition these, one monitoring manager, the `InDetGlobalManager`, is set up to control the execution of each tool and to set common options. In order to save CPU overhead the manager also retrieves the data collections used by the monitoring tools.

The ID Global monitoring runs as a part of the ATLAS reconstruction chain. This means that after reconstruction is finished the monitoring runs on the data produced by reconstruction. The package relies on both tracking information and information on raw hits in the detector. It runs both at the data taking stage (onine) and at the bulk data reconstruction stage (offline). The code is the same for these two modes, but the infrastructure to run it differs. During online running the checks are primarily intended to spot problems as they arise and give quick feedback to detector operation team. The online plots are checked by the General Online Data Quality (DQ) shifter and can assist the online DQ shifters of the ID sub-detectors. In online running mode the events are sampled after the level 1 trigger and only a fraction of all recorded events are passed through the monitoring tools. The main limiting factor for the sampling rate is the number of monitoring applications running in parallel, which is limited by CPU capacity. When the monitoring is enabled in the offline reconstruction stage the full run is checked and the output is made for each trigger stream, making it possible to have the checks on exactly the data that will be used for physics analyses.

5.2 Monitored Objects and Quantities

5.2.1 Tracks

Tracks are very sensitive to problems which may occur during the operation and reconstruction of the data from the ID. They are the final reconstructed ID objects and thus they carry information about the ID as a single tracker. Looking at the distribution of track parameters, number of hits and track quality variables it is possible to get indications about misalignment, inefficient or noisy modules, wrong magnetic field

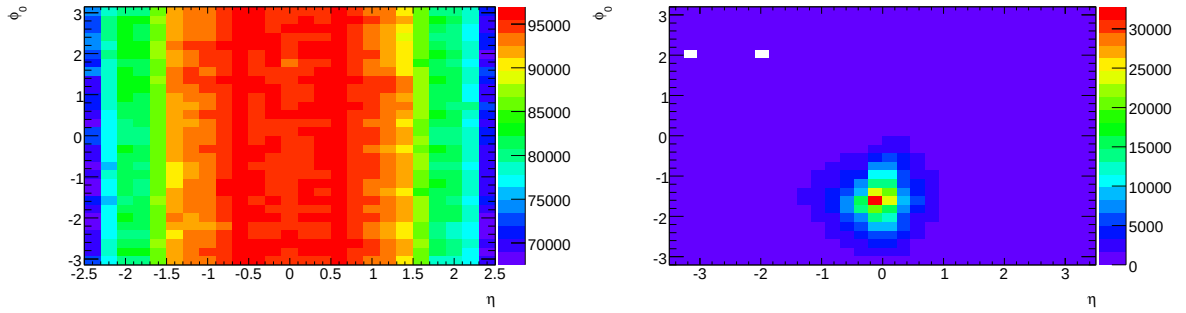

(a) (b)

Figure 5.3: Examples of 2D histograms showing distributions of ϕ_0 versus η of tracks in proton-proton collision run number 155112 (a) and in cosmic muon run 121513 (b). They show how the distribution looks like when the ID sub-detectors and tracking algorithm are performing as expected.

map or problems in track reconstruction algorithms. Tracks are the main tool of the ID Global monitoring. All available ID track collections are used by the ID Global monitoring. The following parameters of combined tracks made of both from TRT and Silicon (Pixel + SCT) hits are monitored: azimuthal angle ϕ_0, pseudo-rapidity η, longitudinal and transverse impact parameters z_0 and d_0 and charge over momentum q/p. Besides the track parameters, the track multiplicities (number of tracks per event) and the χ^2/Ndf of track fit are also monitored. Each of the monitored quantities are stored in one-dimensional (1D) histograms. The track parameters as well as track multiplicities and rates are monitored not only per run, but also for smaller time periods called Luminosity Blocks (LBs). One LB contains roughly 2 minutes of data taking, but this can vary due to run conditions and other operational issues. This kind of plots help to check if the monitored quantities are stable during the run.

In addition to 1D histograms, several 2D histograms are filled with the different combinations of track parameters, like ϕ_0 vs η or d_0 vs ϕ_0. Figure 5.3a shows the ϕ_0 vs η distribution in case of a collision run. The distribution is expected to be homogeneous in ϕ_0 and symmetric in η with respect to $\eta = 0$. Holes and asymmetries in this distribution may indicate regions where the tracking is not as efficient as expected. The distribution of the same parameters for cosmic muon runs are completely different as seen on figure 5.3b. As most of the tracks in this plot are tracks from the cosmic muons, and the muons are coming straightly from the open shaft above ATLAS, they have ϕ_0 equal to $\pi/2$ and η close to 0. Both plots illustrate runs where the ID and tracking reconstruction algorithms worked as expected.

5.2.2 Hits on tracks

To further check the properties of tracks, the hits associated with a track are considered. This is done by monitoring the number of hits on track in every sub-detector (Pixel, SCT and TRT). An example histogram for this check is shown in figure 5.4. As can be seen from the figure, most tracks have 11 Silicon hits (8 SCT + 3 Pixel), and 30-35 TRT hits. Another important goal is to find areas with malfunctioning detector parts or inefficient tracking. This is done by both looking at average number of hits on tracks

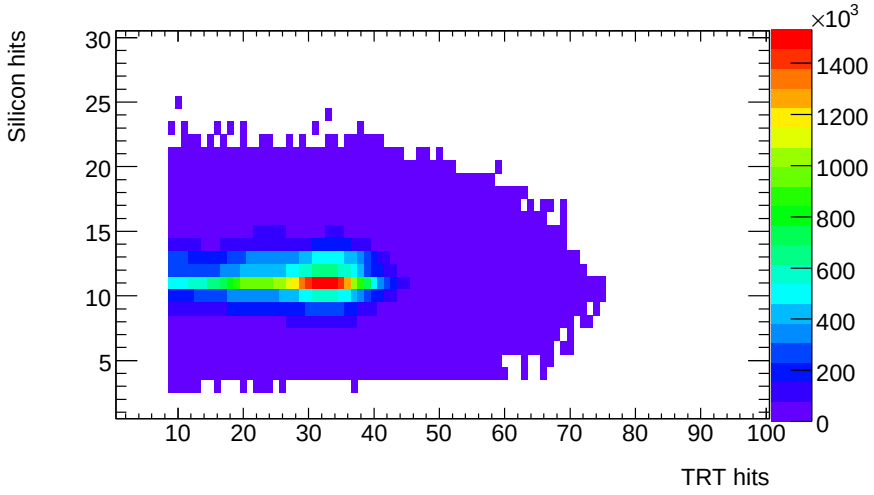

Figure 5.4: Number of Silicon hits on track versus number of TRT hits on track, showing the expected distribution of hits when the tracking is efficient.

by ϕ_0 or η of tracks as well as with help of 2D histograms showing one of coordinates of the hits versus other. Figure 5.5 illustrates the number of hits versus spatial X and Y coordinates in runs 155112 (5.5a) and 141561 (5.5b). Run 155112 has the typical distribution of the hits when the full ID is operational and tracking performs well. In run 141561 only TRT was operational and the TRT tracking algorithm had a problem in the code which made it unable to reconstruct tracks crossing the x-axis at its negative side. As can be seen from the figure, the number of hits at the negative side of the x-axis is smaller than in other regions of the detector.

5.2.3 Noise occupancy

One of the main parameters monitored by individual sub-detector monitoring systems is the noise of the detecting units (pixels, strips, straws). For correct track reconstruction it is important to ensure that the noise is as low as possible and that noisy detecting elements are known and taken into account. Unlike the individual sub-detector monitoring systems, the ID Global monitoring does not monitor the noise of a single detecting element, but it monitors the noise occupancy of the particular whole sub-detector. Noise occupancy is defined as number of hits not associated with tracks divided to the number of all detecting channels. This definition was initially chosen for cosmic data taking mode. As these hits are not necessarily introduced by noisy detector elements but can also originate from particles whose tracks were not reconstructed, this definition does not always represent the noise originating from electronics. This is especially true for collision data taking mode when the particle multiplicity is high. Thus the Noise occupancy tool monitors a quantity which has contributions both from the electronic noise and from the tracking algorithm inefficiency. The Noise occupancy tool is made to mostly serve for online purpose, when a shifter can follow the stability of the noise occupancy during the run looking at the noise occupancy plotted for last sampled 2000 events.

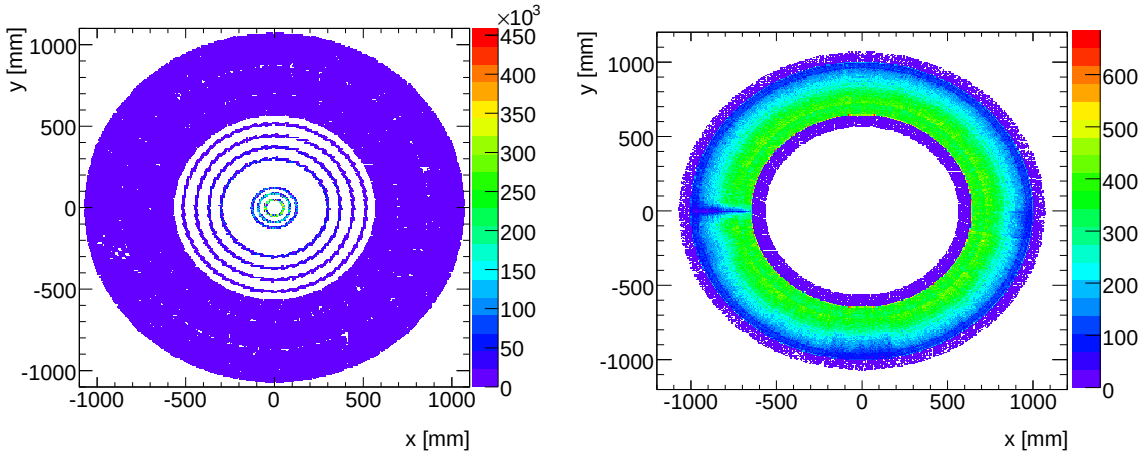

(a) (b)

Figure 5.5: Hit map of the ID barrel hits on track in x-y plane of runs 155112 (a) and 141561 (b). In the run 155112 all the ID sub-detectors were operational and the tracking algorithms performed well. All 3 layers of Pixel detector and all 4 layers of SCT are seen and the hits are equally distributed in them. Only TRT was operational in the run 141561 and the TRT tracking algorithm had a problem in the code, which made it inefficient in the reconstruction of the tracks crossing the x-axis at its negative side.

5.2.4 Synchronization

One of the main goals of the ID Global Monitoring is to ensure that the ID is synchronized with the LHC clock and ATLAS Level 1 trigger and that the sub-detectors of the ID are working synchronized against each other. The quantities used for this purpose are bunch crossing identifier (BCID) and level 1 trigger identifiers (L1ID). Both these identifiers are cyclic. They go from 0 to 3563 and correspond to each possible crossings of bunches at the LHC. All read-out drivers (ROD) use these identifiers to ensure that the signals collected from the detecting moduls belong to the same event. It is expected that the hit occupancy is significantly higher for the BCIDs corresponding the paired colliding bunches than for the ones corresponding to empty bunches. Figure 5.6a shows the average number of hits in Pixel detector as function of BCID. In this run the bunches having BCID 1, 201 and 401 are paired (there are 2 bunches with the same BCID circulating in the LHC in opposite directions) and colliding. Thus the average number of Pixel hits for events corresponding these BCIDs are more than 650. In addition to paired bunches, there are 6 unpaired bunches in this run, which do not collide with other bunches, but they circulate through ATLAS and interact with collimators. While these bunches do not collide, the number of Pixel hits for these BCIDs is still high enough (200-300) to be distinguished from the noise, which in average gives 4-5 Pixel hits per event. Figure 5.6b shows that significant amount of ID tracks are reconstructed only in the case of colliding bunches. This is expected despite the high occupancy of Pixel detector, since the particles produced from the interaction of unpaired beams with collimators move almost horizontally and do not pass through the other ID sub-detectors (SCT and TRT) and thus do not satisfy the tracking algorithm requirements.

The BCID and L1ID taken from the RODs of the ID sub-detectors are checked

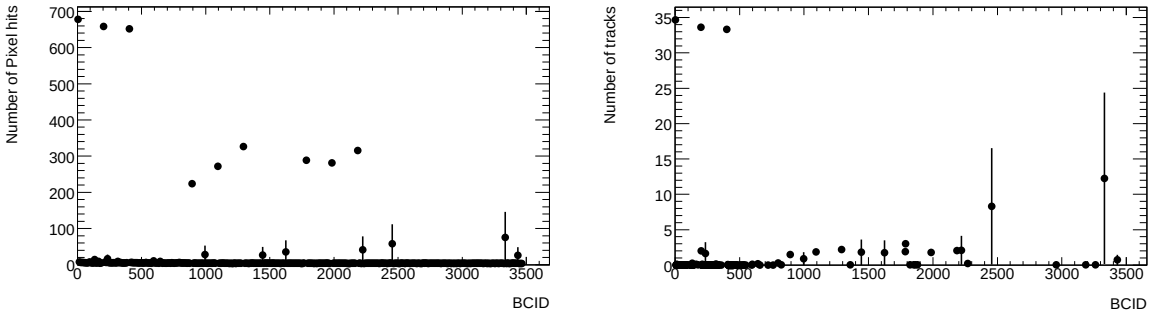

(a) (b)

Figure 5.6: a) Example plot showing the average number of Pixel hits as a function of BCID. The three points with high number of hits (600-700) correspond to the colliding bunches. The six points where number of hits is 200-300 correspond to non-colliding bunches. They are clearly distinguishable from the colliding ones. b) Example plot showing the average number of the ID tracks as a function of BCID. Colliding bunches produce in average 33-35 tracks, while number of tracks corresponding to BCIDs of unpaired or empty bunches usually does not exceed 5. The ones which exceed are single events (see the size of the error) when a cosmic muon passed through the detector.

against each other to verify if all RODs are correctly timed. If a timing mismatched is observed it is logged in a histogram as in the case of the run 155122 (figure 5.7a), when during 35 events some of TRT RODs were having different BCIDs than their neighbor RODs. To trace exactly which RODs were mismatched, one can use the histogram shown in figure 5.7b. It shows that the RODs number 31-33 and 35 are mismatched with their neighbors.

5.3 Data Quality Checks

Plots produced by the monitoring packages are checked automatically via the Data Quality Monitoring Framework (DQMF) [44]. This framework performs automated

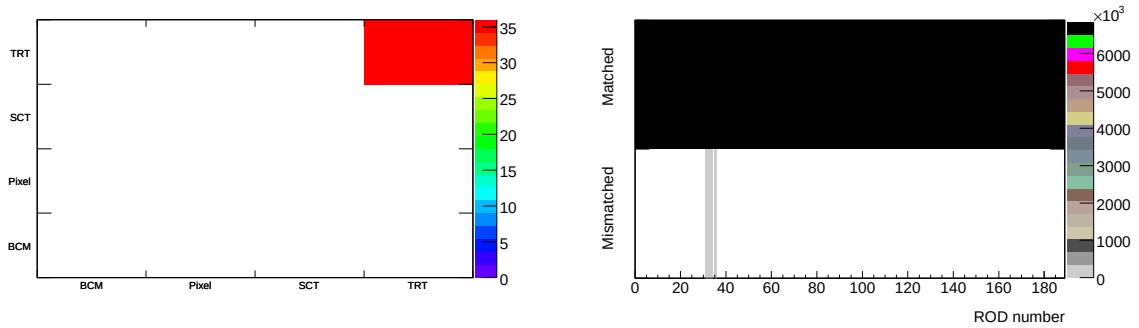

(a) (b)

Figure 5.7: a) An example plot of a warning histogram showing that during 35 events the BCID of some of TRT RODs were mismatched with their neighbor RODs BCIDs. b) An example plot of a clarifying histogram, helping to trace the RODs which were mismatched.

checks on the histograms whenever possible. This check is done in addition to the check performed by a human shifter to provide an initial assessment. The checks can be as simple as to check if the histogram is not empty and as complex as to check if the shape of the distribution is as expected. The results of these checks are combined into DQ flags, provided and stored for each monitoring system. The flags can have five different values: good (green), flawed (yellow), bad (red), undefined (gray) and off (black). The online checks need to be confirmed by the offline event reconstruction, on the one hand to verify the online decision and on the other hand to clarify undefined flags. The final DQ decisions are stored into a database for further analysis. The ID Global monitoring sets one DQ flag which is stored in the database under *IDGL* name. The flag can be set automatically after the online and offline DQ checks and by the offline shifter who can override the automatic decision after more detailed checks of the histograms.

5.4 Summary

When I took the responsibility of the ID Global Monitoring package it had very limited functionalities and was suited to work only in the regime of cosmic muon detection. I improved its code, added several new functionalities and added the possibility to work in the proton-proton collision regime. The long cosmic runs in 2008 and 2009 as well as collision runs at the end of 2009 and in the beginning of 2010 were used to commission the performance of the ID Global Monitoring tool. As a result of the commissioning campaign many histograms were improved and several new histograms were added to the tool, making it more useful for the shifters. The status of the tool described in this thesis is as of the beginning of 2010, when I finished my duties as a developer of the ID Global Monitoring tool. Since then the tool has evolved and some of the descriptions above are not valid anymore.

Chapter 6

Search for New Physics with heavy particles

There are several unsolved mass problems in the present particle physics. The fact that W and Z bosons are heavy while photon is massless is presently explained by Higgs mechanism [6], but the Higgs particle was not observed yet [3] [45]. Precise electroweak measurements point to the Higgs boson being lighter than 148 GeV at 95% C.L [46]. Such a light Higgs boson means that the Standard Model breaks down well before the GUT scale.

Another unsolved problem is large difference between masses of elementary fermions. The top quark, the heaviest elementary particle has the mass close to the electroweak scale. Its influence on the mass of the Higgs boson leads to a conjecture that there exist a scalar version of the top, which partially cancels this influence. In SUSY, one of the theories where such scalar tops exist, the partners of top, bottom and tau can be light due to the mass splitting introduced by the masses of third family fermions. If SUSY exists final states of decay of supersymmetric particles might contain excess of tau leptons, top and bottom quarks compared to what is expected in the SM. Thus production and properties of third family (generation) particles might reveal properties of beyond the SM physics.

The top quark is one of the most powerful tools used both for constraining the Higgs boson mass and for search for New Physics. In the SM, all quarks and leptons couplings to the Higgs boson (Yukawa couplings) are small compared to the top quark coupling. This introduces large difference between the top quark mass and other fermions masses. This also makes the top quark to be the main contributor into the loop corrections of the Higgs mass creating the hierarchy problem mentioned in section 3.1. Thus the value of the top quark mass and its error put constraints on the Higgs boson mass as seen in figure 6.1. Therefore it is important to measure the top quark mass as precisely as possible.

An example of the search for New Physics with top quarks is the search for even heavier particles decaying to the pair of $t\bar{t}$ quarks. For this purpose the cross-section of the $t\bar{t}$ production needs to be estimated and measured accurately. Any excess in the estimated $t\bar{t}$ system invariant mass spectrum can indicate the presence of $t\bar{t}$ resonances predicted by several beyond the Standard Model theories (see section 3.2). The measurement of the electric charge of the top quark can directly indicate the New Physics [47] if the measured value differs from the one, predicted by the SM. The difference between the expected and measured values of the top quark spin polarization and correlations in $t\bar{t}$ events can be a sign of New Physics. In some beyond the Standard

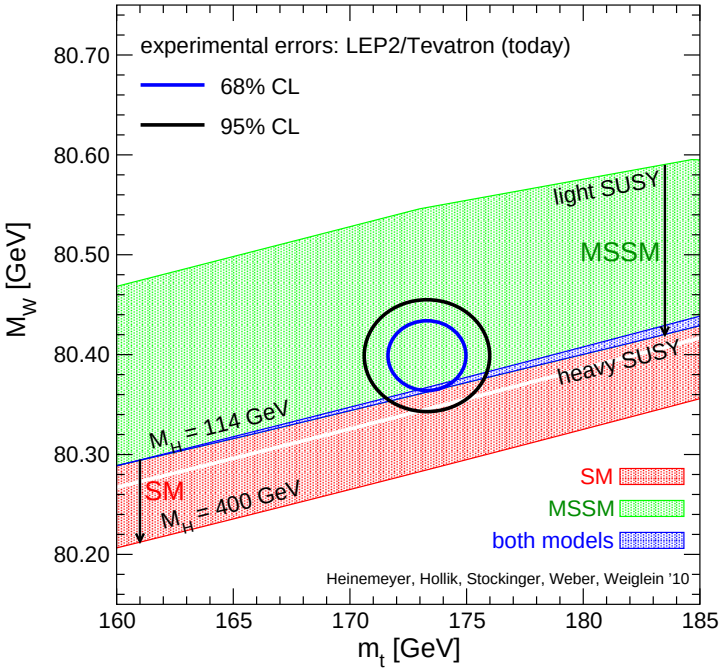

Figure 6.1: Top quark and W boson mass constraints to the Higgs boson mass and SUSY parameters. The allowed region in the MSSM, corresponding to the light-shaded (green) and dark-shaded (blue) bands, results from varying the SUSY parameters independently of each other in a random parameter scan. The allowed region in the SM, corresponding to the medium-shaded (red) and dark-shaded (blue) bands, results from varying the mass of the SM Higgs boson from M_H = 114 GeV to M_H = 400 GeV. (Plot is taken/updated from [4]).

Model theories, the value of the $|V_{tb}|$ element of the Cabibbo–Kobayashi–Maskawa matrix described in chapter 2 can be different than the SM prediction [48], [49]. Some other extensions of the Standard Model predict the Flaviour Changing Neutral Currents (FCNC) at the tree level [50], [51] while the Standard Model allows only small contribution of the FCNC at the loop level [52], [53]. Thus the search for decays of the top quark to another up-type quark and a neutral boson can be used to test the Standard Model and to search for physics beyond it. All above mentioned studies are possible to conduct thanks to the large mass of the top quark and its short life-time making it the only quark which decays before hadronizing.

The heaviest lepton, τ lepton, is also a commonly used tool in the searches for New Physics, especially for SUSY. SUSY models in general violate the $e/\mu/\tau$ universality. In some regions of SUSY parameters (large $tan\beta$) the signatures involving τ leptons become dominant making τ leptons attractive both for search for SUSY particles and for measurements of their properties (mainly masses).

As stated above the measurement of the properties of the top are important in the sense of the search for New Physics. The sensitivity of the ATLAS experiment to the measurement of the top quark properties is evaluated in the paper "Expected performance of the ATLAS experiment: detector, trigger and physics" using Monte Carlo simulations. The top quark charge is one of these properties. The aim of the measurement of the top quark charge is to check if it has the value predicted by the SM (+2/3e) or the particle discovered at Tevatron is not a top quark but an exotic quark with charge −4/3e as claimed in Ref. [47]. The measurement of the top quark charge is

carried out by reconstructing the charges of its decay products in the lepton+jets channel of $t\bar{t}$ events. The charge of the W boson is relatively easy to reconstruct since the charged lepton (electron of muon) to which it decays has the same charge as the W boson. The measurement of the charge of the b quark is harder. It is measured by two methods: track charge weighting and semi-leptonic decays of B hadrons. The former one is based on finding a correlation between the b quark charge and the charges of the tracks belonging to the jet it forms (b-jet). In the later method the charge of the b quark is determined via semi-leptonic decays of B hadrons, where the sign of the lepton (decay product of B hadron) can indicate the sing of the b quark charge. Another challenge of the top quark charge measurement is the correct pairing of the lepton and the b quark to ensure that they are decay products of the same (anti-)top quark. This is done using the fact that if they are products of the same (anti-)top quark then their invariant mass can not exceed the top mass (see figure 1 of paper 2), while if they are not correlated then their invariant mass can be both less or more than the top quark mass. The results of the simulations using both methods show that ATLAS is able to distinguish between the SM and exotic scenarios with 0.1-1 fb^{-1} data.

The top quark charge has been measured with proton-proton collision data as soon as enough data (0.7 fb^{-1}) was collected by the ATLAS experiment. The results of this measurement is documented in the paper "Measurement of the top quark charge in pp collisions at $\sqrt{s} = 7$ TeV in the ATLAS experiment". The measurement is done with the techniques described above except that more advanced way of pairing of the lepton and b-jet is used for "semi-leptonic decays of B hadrons" method. The pairing is done using Kinematic Likelihood Fitter to increase the efficiency of the method. The hypothesis that the top quark is instead an exotic quark with charge $-4/3$e is excluded at more than five standard deviations in this paper.

Another simulation based study involving top quarks is documented in paper "On the Possibility of the Search for Top–Antitop Resonances at the LHC". The paper is dedicated to the estimation of the possibility to find generic heavy particles (Z') decaying to $t\bar{t}$ pair at the LHC for $\sqrt{s} = 14$ TeV. The analysis makes use the lepton+jets signature of $t\bar{t}$ events. Five different masses of the resonance are considered: 0.7, 1.0, 1.5, 2.0 and 3.0 TeV. Two types of event selection (loose and tight), three methods of top quark reconstruction (reconstructed mass closest to the generated, highest transverse momentum of top quarks and smallest ΔR between jets) and two ways of Z' reconstruction (with and without cut on the transverse momentum of top quarks) are examined. Tight event selection together with the requirement of the reconstructed top quark mass to be closest to the generated one was selected as the base method. The cut on the transverse momentum of top quarks has shown to improve the resolution and accuracy of the Z' mass measurements. In addition, the case when reconstruction of the final state is done without making use of b-tagging information is also briefly studied. The minimal cross-sections of Z' production needed to discover it are estimated for data corresponding to 1-300 fb^{-1} of integrated luminosity. The analysis is phenomenological and does not consider systematic errors and other backgrounds than direct production of $t\bar{t}$ events.

Among other studies carried out by the ATLAS collaboration using Monte Carlo simulations, the ones dedicated to the measurement of SUSY parameters (mostly particles masses) are documented in paper "Expected performance of the ATLAS experiment: detector, trigger and physics". By measuring the endpoint of the invariant mass

distribution of two charged leptons, final products of SUSY particles decays, it is possible to obtain a relation between masses of lightest neutralino, $\tilde{\chi_1}^0$, next-to-lightest neutralino, $\tilde{\chi}_2^0$, and slepton, $\tilde{\ell}$ with help of the following equation:

$$m_{\ell\ell}^{edge} = m_{\tilde{\chi}_2^0}\sqrt{1-\left(\frac{m_{\tilde{\ell}}}{m_{\tilde{\chi}_2^0}}\right)^2}\sqrt{1-\left(\frac{m_{\tilde{\chi}_1^0}}{m_{\tilde{\ell}}}\right)^2}. \tag{6.1}$$

The endpoint measurement for the cases when leptons are electrons or muons is relatively easy since the invariant mass distribution in these cases has sharp edge which is not the case for tau leptons. Due to the presence of neutrinos from the tau decays, the $m_{\tau\tau}$ distribution (where $m_{\tau\tau}$ indicates the visible decay products of tau pairs) falls off smoothly below the maximum value given by equation 6.1. Despite this, it is still possible to find the endpoint by fitting $m_{\tau\tau}$ distribution with function:

$$f(x) = \frac{p_0}{x}\cdot exp\left(-\frac{1}{2p_2^2}(ln(x)-p_1)^2\right), \tag{6.2}$$

finding the inflection point, m_{IP}, and relating it to the endpoint, m_{EP}, with help of a linear calibration function:

$$m_{IP} = (0.47\pm0.02)m_{EP} + (15\pm2)GeV, \tag{6.3}$$

obtained from Monte Carlo-based calibration procedure. Only hadronic decaying tau leptons could be unambigously identified in the ATLAS setector with help of tau identification algorithms. Two such algorithms are part of the ATLAS reconstruction software. One of them seeds tau candidates from tracks in Inner Detector and searches for energy deposition in the calorimeter while the other first selects a cluster in the calorimeter and then looks if there are tracks behind this cluster. At the time of this study the track-seeded had higher efficiency for low-p_T taus while the calorimeter-seeded was more efficient in high p_T region. The endpoint is determined for two SUSY points: "Coannihilation" and "Bulk". The estimations show that for "Bulk" point the endpoint can be measured already with 1 fb^{-1} of integrated luminosity. Since the cross-section of the "Coannihilation" point is considerably lower more data (up to 18 fb^{-1}) is needed to perform a good fit and estimate the endpoint in this case.

Chapter 7

Concluding remarks and further work

Three different methods of the search for New Physics are presented in the dissertation. One of the searches is performed by measuring the top quark charge from the data of the ATLAS experiment and comparing the results with the hypothesis of the existence of an exotic quark with electric charge of $-4/3e$. As a result of this measurement the hypothesis assuming that the particle with mass $\sim$ 172 GeV observed at the LHC is an exotic quark was ruled out by more than 5 standard deviations. Another analysis involving top quarks estimates the possibility of the LHC experiments to detect extra gauge bosons via their decays to top-antitop pair. This can be done by searching for an excess of events in the top-antitop invariant mass spectrum predicted by the Standard Model. The third analysis is again based on the simulations and checks the possibility of the ATLAS detector to reconstruct the end-point of di-tau invariant mass distribution in the stau co-annihilation region of mSUGRA model. Although the specific models on which the study was performed are already excluded with the ATLAS data, SUSY with taus is still a viable model in the slightly higher mass range. If SUSY with taus is discovered, the techniques to measure $m_{\tau\tau}$ endpoint presented in this thesis can be applied. Several of my colleagues form the University of Bergen are currently analyzing the ATLAS data trying to find an indication of SUSY with tau leptons.

To perform the above mentioned and any other analysis on the ATLAS detector, one first needs to ensure that the detector is working as expected. For this purpose a software intended to monitor the ATLAS Inner Detector was developed and commissioned with cosmic muons and with first data from proton-proton collisions at the LHC. The software is currently running both in online data taking and offline bulk reconstruction modes and its results are used by shifters to monitor the ATLAS Inner Detector.

Searches of heavy $t\bar{t}$ resonances have been performed by the ATLAS collaboration and up to date no evidence of New Physics is observed [54]. The search is performed continuously, and with more data higher masses of particular types of resonances can be excluded and lower limits on the production of generic resonances can be set.

SUSY search is one of the tasks in which many of ATLAS collaboration members are involved. No signal is observed and models with parameters in certain ranges are excluded [55] [56] [57]. The search for SUSY is also a continuous process. The more data ATLAS collects the higher masses of SUSY particles can be possibly discovered. If SUSY is the solution to the hierarchy problem the masses of SUSY particles are kinematically accesible at the LHC. Thus SUSY will be either discovered or excluded by the LHC experiments.

Bibliography

[1] Ugo Amaldi, Wim de Boer, and Hermann Furstenau. Comparison of grand unified theories with electroweak and strong coupling constants measured at LEP. *Phys.Lett.*, B260:447–455, 1991. (document), 3.1

[2] The ATLAS Collaboration, G. Aad et al. Expected Performance of the ATLAS Experiment Detector, Trigger and Physics. *CERN-OPEN-2008-020*, 2008. (document), 4.2, 4.2

[3] The ATLAS Collaboration, G. Aad et al. Update of the Combination of Higgs Boson Searches in pp Collisions at sqrt(s) = 7 TeV with the ATLAS Experiment at the LHC. *ATLAS-CONF-2011-135*, Sep 2011. (document), 4.2, 4.3, 6

[4] Sven Heinemeyer, Wolfgang Hollik, Dominik Stöckinger, Arne M. Weber, and Georg Weiglein. Precise prediction for M_W in the MSSM. *Journal of High Energy Physics*, 2006(08):052, 2006. (document), 6.1

[5] Particle Data Group, K Nakamura et al. Review of Particle Physics. *Journal of Physics G: Nuclear and Particle Physics*, 37(7A):075021 and 2011 partial update for the 2012 edition., 2010. 1, 2, 2.2, 2.1, 4.2

[6] Peter W. Higgs. Broken Symmetries and the Masses of Gauge Bosons. *Phys. Rev. Lett.*, 13:508–509, Oct 1964. 1, 6

[7] Tevatron Electroweak Working Group, CDF and D0 Collaborations. Combination of CDF and D0 results on the mass of the top quark using up to 5.8 fb^{-1} of data. *FERMILAB-TM-2504-E*, Jul 2011. 1

[8] V. Christianto and F. Smarandache. Thirty Unsolved Problems in the Physics of Elementary Particles. *Progress in Physics*, 4:112–114, 2007. 1, 3

[9] F. Zwicky. Die Rotverschiebung von extragalaktischen Nebeln. *Helvetica Physica Acta*, 6:110–127, 1933. 1

[10] F. Zwicky. On the Masses of Nebulae and of Clusters of Nebulae. *Astrophysical Journal*, 86:217, oct 1937. 1

[11] CDF Collaboration, F. Abe et al. Observation of Top Quark Production in $\bar{p}p$ Collisions with the Collider Detector at Fermilab. *Phys. Rev. Lett.*, 74:2626–2631, Apr 1995. 2

[12] D0 Collaboration, S. Abachi et al. Observation of the Top Quark. *Phys. Rev. Lett.*, 74:2632–2637, Apr 1995. 2

[13] The ATLAS Collaboration, G. Aad et al. Measurement of the top quark-pair production cross section with ATLAS in pp collisions at $\sqrt{s} = 7$ TeV. *Eur. Phys. J. C*, 71:1577, 2011. 2

[14] The CMS Collaboration, V. Khachatryan et al. First measurement of the cross section for top-quark pair production in proton–proton collisions at. *Physics Letters B*, 695(5):424 – 443, 2011. 2

[15] M. Jeżabek and J.H. Kühn. QCD corrections to semileptonic decays of heavy quarks. *Nuclear Physics B*, 314(1):1 – 6, 1989. 2

[16] I. Bigi, Y. Dokshitzer, V. Khoze, J. Kühn, and P. Zerwas. Production and decay properties of ultra-heavy quarks. *Physics Letters B*, 181(1-2):157 – 163, 1986. 2

[17] The ATLAS Collaboration, G. Aad et al. Performance of the ATLAS Secondary Vertex b-tagging Algorithm in 7 TeV Collision Data. *ATLAS-CONF-2010-042*, Jul 2010. 2.2

[18] The ATLAS Collaboration, G. Aad et al. Performance of Impact Parameter-Based b-tagging Algorithms with the ATLAS Detector using Proton-Proton Collisions at *sqrts* = 7 TeV. *ATLAS-CONF-2010-091*, Oct 2010. 2.2

[19] The ATLAS Collaboration, G. Aad et al. Reconstruction, Energy Calibration, and Identification of Hadronically Decaying Tau Leptons. *ATLAS-CONF-2011-077*, May 2011. 2.2

[20] Joseph D Lykken. Beyond the Standard Model. *CERN Yellow Report*, pages 101–109, May 2010. 3

[21] Stephen P. Martin. A Supersymmetry Primer. *arXiv:hep-ph/9709356v6*. 3.1, 3.1

[22] Howard Georgi and S. L. Glashow. Unity of All Elementary-Particle Forces. *Phys. Rev. Lett.*, 32:438–441, Feb 1974. 3.1

[23] H. Georgi, H. R. Quinn, and S. Weinberg. Hierarchy of Interactions in Unified Gauge Theories. *Phys. Rev. Lett.*, 33:451–454, Aug 1974. 3.1

[24] H.P. and Nilles. Supersymmetry, supergravity and particle physics. *Physics Reports*, 110(1-2):1 – 162, 1984. 3.1

[25] Christopher T. and Hill. Topcolor assisted technicolor. *Physics Letters B*, 345(4):483 – 489, 1995. 3.2

[26] Nima Arkani–Hamed, Savas Dimopoulos, and Gia Dvali. The hierarchy problem and new dimensions at a millimeter. *Physics Letters B*, 429(3-4):263 – 272, 1998. 3.2

[27] Nima Arkani-Hamed, Savas Dimopoulos, and Gia Dvali. Phenomenology, astrophysics, and cosmology of theories with submillimeter dimensions and TeV scale quantum gravity. *Phys. Rev. D*, 59:086004, Mar 1999. 3.2

[28] Lisa Randall and Raman Sundrum. Large Mass Hierarchy from a Small Extra Dimension. *Phys. Rev. Lett.*, 83:3370–3373, Oct 1999. 3.2

[29] Lisa Randall and Raman Sundrum. An Alternative to Compactification. *Phys. Rev. Lett.*, 83:4690–4693, Dec 1999. 3.2

[30] Oliver Sim Brüning, Paul Collier, P Lebrun, Stephen Myers, Ranko Ostojic, John Poole, and Paul Proudlock. *LHC Design Report*. CERN, Geneva, 2004. 4.1

[31] P Lebrun. Large Cryogenic Helium Refrigeration System for the LHC. *LHC-Project-Report-629*, Feb 2003. 4.1

[32] The ATLAS Collaboration, G. Aad et al. *ATLAS detector and physics performance: Technical Design Report*. Technical Design Report ATLAS. CERN, Geneva, 1999. 4.2

[33] The ATLAS Collaboration, G. Aad et al. The ATLAS Experiment at the CERN Large Hadron Collider. *Journal of Instrumentation*, 3(08):S08003, 2008. 4.3, 4.4, 4.1

[34] The ATLAS Collaboration, G. Aad et al. The ATLAS Inner Detector commissioning and calibration. *Eur. Phys. J. C*, 70:787–821, Jun 2010. 4.4

[35] The ATLAS Collaboration, G. Aad et al. Estimating Track Momentum Resolution in Minimum Bias Events using Simulation and Ks in sqrt(s) = 900 GeV collision data. *ATLAS-CONF-2010-009*, Jun 2010. 4.4

[36] The ATLAS Collaboration, G. Aad et al. Tracking Results and Comparison to Monte Carlo simulation at sqrt(s) = 900 GeV. *ATLAS-CONF-2010-011*, Jul 2010. 4.4

[37] Performance of the ATLAS Silicon Pattern Recognition Algorithm in Data and Simulation at sqrt(s) = 7 TeV. *ATLAS-CONF-2010-072*, Jul 2010. 4.4

[38] The ATLAS Collaboration, G. Aad et al. The ATLAS Transition Radiation Tracker (TRT) proportional drift tube: design and performance. *Journal of Instrumentation*, 3(02):P02013, 2008. 4.4.3

[39] Rene Brun and Fons Rademakers. ROOT - An object oriented data analysis framework. *Nucl. Inst. and Meth. in Phys. Res*, 389(1-2):81–86, 1997. 4.9, 5.1

[40] T. Sjostrand and S. Mrenna and P.Z. Skands. PYTHIA 6.4 Physics and Manual. *JHEP*, 05:026, 2006. 4.9

[41] G. Corcella et al. HERWIG 6: An Event generator for hadron emission reactions with interfering gluons (including supersymmetric processes). *JHEP*, 0101:010, 2001. 4.9

[42] S. Agostinelli et al. GEANT4 - A Simulation Toolkit. *Nucl. Instr. and Meth.*, A506:250, 2003. 4.9

[43] The ATLAS Collaboration, G. Aad et al. *Atlas Computing: technical design report*. CERN, Geneva, 2005. 4.9

[44] S Kolos, A Corso-Radu, H Hadavand, M Hauschild, and R Kehoe. A software framework for Data Quality Monitoring in ATLAS. *J. Phys.: Conf. Ser.*, 119:022033, 2008. 5.3

[45] CMS Collaboration. Combination of Higgs Searches. *CMS-PAS-HIG-11-022*, 2011. 6

[46] Jens Erler. Mass of the Higgs boson in the standard electroweak model. *Phys. Rev. D*, 81:051301, Mar 2010. 6

[47] Darwin Chang, We-Fu Chang, and Ernest Ma. Alternative interpretation of the Fermilab Tevatron top events. *Phys. Rev. D*, 59:091503, Apr 1999. 6

[48] J.A. Aguilar-Saavedra. Hierarchy plus anarchy in quark masses and mixings. *Phys.Rev.*, D67:073026, 2003. 6

[49] Francisco del Aguila and Jose Santiago. Signals from extra dimensions decoupled from the compactification scale. *Journal of High Energy Physics*, 2002(03):010, 2002. 6

[50] G. M. de Divitiis, R. Petronzio, and L. Silvestrini. Flavour changing top decays in supersymmetric extensions of the standard model. *Nuclear Physics B*, 504:45, 1997. 6

[51] David Atwood, Laura Reina, and Amarjit Soni. Probing flavor changing top-charm-scalar interactions in $e\hat{+}e\hat{-}$ collisions. *Phys. Rev. D*, 53:1199, 1996. 6

[52] B. Grzadkowski, J.F. Gunion, and P. Krawczyk. Neutral current flavor changing decays for the Z boson and the top quark in two-Higgs doublet models. *Physics Letters B*, 268(1):106 – 111, 1991. 6

[53] G. Eilam, J. L. Hewett, and A. Soni. Rare decays of the top quark in the standard and two-Higgs-doublet models. *Phys. Rev. D*, 44:1473–1484, Sep 1991. 6

[54] The ATLAS Collaboration, G. Aad et al. A Search for ttbar Resonances in the Dilepton Channel in 1.04 fb^{-1} of pp Collisions at sqrt(s) = 7 TeV. *ATLAS-CONF-2011-123*, Aug 2011. 7

[55] The ATLAS Collaboration, G. Aad et al. Searches for supersymmetry with the ATLAS detector using final states with two leptons and missing transverse momentum in *sqrts* = 7 TeV proton-proton collisions. *arXiv:1110.6189v1 [hep-ex]*, 2011. 7

[56] The ATLAS Collaboration, G. Aad et al. Search for supersymmetry in final states with jets, missing transverse momentum and one isolated lepton in $\sqrt{s} = 7$ TeV pp collisions using 1 fb-1 of ATLAS data. *arXiv:1109.6606v1 [hep-ex]*, September 2011. 7

[57] CMS Collaboration. Search for Supersymmetry at the LHC in Events with Jets and Missing Transverse Energy. *arXiv:1109.2352v1 [hep-ex]*, September 2011. 7

Paper 1: Measurement of the top quark charge in pp collisions at $\sqrt{s}$ = 7 TeV in the ATLAS experiment

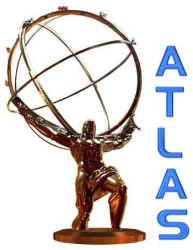

ATLAS NOTE

ATLAS-CONF-2011-141

September 26, 2011

Measurement of the top quark charge in pp collisions at $\sqrt{s} = 7$ TeV in the ATLAS experiment

ATLAS Collaboration

Abstract

A measurement of the top quark charge using the lepton+jets final state resulting from $t\bar{t}$ pair production is presented, using data from the ATLAS detector. The results were obtained using proton-proton collision data at $\sqrt{s} = 7$ TeV corresponding to an integrated luminosity of 0.70 fb^{-1}. The hypothesis that the top quark is instead an exotic quark with charge -4/3e is excluded at more than five standard deviations.

1 Introduction

Discovered in 1995 by the CDF and D0 experiments, the top quark is the heaviest known elementary particle [1]. Its properties might offer a hint of physics beyond the Standard Model. It is thus of interest to measure them as precisely as possible. In this note, a measurement of the top quark charge at the Large Hadron Collider with 0.70 fb^{-1} of proton-proton collision data at $\sqrt{s} = 7$ TeV is presented.

The top quark charge measurement is based on reconstructing the charges of the top quark decay products. The dominant decay channel of the top quark, $t \to W^+ b (\bar{t} \to W^- \bar{b})$, has a W boson and a b-quark in the final state. To measure the top quark charge one needs to determine the charge of both the W boson and *b*-quark. While the charge of the W boson can be determined through its leptonic decay, the *b*-quark charge is not directly measurable, as the *b*-quark hadronisation process results in a jet of hadronic particles (*b*-jet). It is possible however to establish a correlation between the charge of the *b*-quark and a weighted sum of the electric charges of the particles belonging to the *b*-jet (track charge weighting technique). Semileptonic B-hadron decays ($b \to c, u + W^-, W^- \to \ell^- + \bar{\nu}_\ell$) can also be used. In this case the sign of the lepton arising from the semileptonic decay defines the sign of the *b*-quark charge (soft lepton technique). In the soft lepton approach, the presence of B-oscillations and semileptonic decays of *c* quarks dilutes the correlation between the apparent charge of the *b*-jet and the charge of the initial *b*-quark. B-oscillations also affect the track charge weighting technique.

Both methods of determining the *b*-jet charge are presented in this note. Final states from $t\bar{t}$ production in which one of the W bosons decays to an electron or a muon, and the other to a quark-antiquark pair (resulting in a pair of jets, jj, $t\bar{t} \to \ell^\pm \nu jj b\bar{b}$) are used.

The possibility that an exotic quark with charge of $-4e/3$ is produced instead of a Standard Model top quark was excluded by the D0 Collaboration at the 92% C.L. [2] and recently by the CDF experiment at the 95% C.L. [2] with methods similar to the ones presented in this note.

2 Detector and Data Sample

The ATLAS detector [3] at the LHC covers nearly the entire solid angle around the collision point. It consists of an inner tracking detector (ID) comprising a silicon pixel detector, a silicon microstrip detector and a transition radiation tracker. The ID is surrounded by a thin superconducting solenoid providing a 2 T magnetic field, and by liquid-argon electromagnetic sampling calorimeters with high granularity. An iron-scintillator tile calorimeter provides hadronic energy measurements in the central rapidity region ($|\eta| < 1.7$)[1]. The end-cap and forward regions are instrumented with liquid-argon calorimeters for both electromagnetic and hadronic energy measurements out to $|\eta| < 4.9$. The calorimeter system is surrounded by a muon spectrometer incorporating three air-core superconducting toroid magnet assemblies.

A three-level trigger system is used to select the high-p_T events for this analysis. The level-1 trigger is implemented in hardware and uses a subset of the detector information to reduce the trigger rate to a design value up to 75 kHz. This is followed by two software-based trigger levels that together reduce the event rate to about 200-400 Hz.

The data accumulated during the first three months of 2011, with an integrated luminostity of 0.70 fb^{-1} (with uncertainty of 3.7 % [4]) were used to obtain the results presented here.

[1]The ATLAS coordinate system is right-handed with pseudorapidity, η, defined as $\eta = -\ln[\tan(\theta/2)]$, where the polar angle θ is measured with respect to the LHC beamline. The azimuthal angle, ϕ, is measured with respect to the *x*-axis, which points towards the centre of the LHC ring. The *z*-axis is parallel to the counterclockwise beam viewed from above. Transverse momentum and energy are defined as $p_T = p \sin\theta$ and $E_T = E \sin\theta$, respectively.

3 Monte Carlo samples

Simulated top pair events were generated using a next-to-leading-order (NLO) Monte Carlo (MC) generator MC@NLO [5] with the NLO parton density (PDF) set CTEQ6.6 [6]. Parton showering and the underlying event were modeled using HERWIG [7] and JIMMY [8]. This sample was normalised to a cross-section of 164.6 pb, obtained with the latest theoretical computation which approximated the next-to-next-to leading order prediction [9]. Single top events were also generated using MC@NLO while the production of W/Z bosons in association with jets was simulated using the ALPGEN generator [10] interfaced to HERWIG and JIMMY. Production of the W/Z boson in association with heavy flavours was simulated separately. Diboson events (WW, WZ, ZZ) were produced using HERWIG.

All Monte Carlo simulation samples were generated with multiple pp interactions (pile-up). These simulated events were re-weighted so that the distribution of the number of interactions per crossing in simulation matched that observed in the data. The samples were then processed through the GEANT4 [11] simulation and reconstruction software of the ATLAS detector [12]. More details can be found in [13].

Both data and simulation were used to estimate backgrounds stemming from QCD processes and the production of a W boson in association with jets, as described in the next section. The POWHEG [14] generator interfaced with HERWIG and PYTHIA [15] was used as an alternative to MC@NLO for the study of systematic effects in the simulation of the $t\bar{t}$ signal process.

4 Event selection

Candidate $t\bar{t} \longrightarrow W^{\pm}bW^{\mp}\bar{b}$ events in which one of the W bosons decays leptonically and the other hadronically were selected following the criteria used previously in [13]. These events are characterised by the presence of an isolated high-p_T lepton. In addition, the presence of a neutrino results in missing transverse energy (E_T^{miss}), and jets are present, both from b-quarks and light quarks from the W boson decay.

The $t\bar{t}$ candidates in the electron or muon plus jets final states were first selected with the electron or muon trigger with a transverse energy (E_T) threshold of 20 GeV for electrons and 18 GeV for muons. There had to be exactly one isolated lepton (electron or muon) with E_T exceeding 25 GeV (electron) or 20 GeV (muon) in the event and this lepton had to be matched to the object firing the lepton trigger. Jets were reconstructed in candidate events using the standard ATLAS implementation of the "anti-k_t" algorithm [16] with jet separation parameter $R = 0.4$. At least four jets with transverse momentum $p_T > 25$ GeV and within the pseudorapidity range $|\eta| < 2.5$ were required. The value of E_T^{miss} had to exceed 35 GeV for the events with electrons, and 20 GeV for the events with muons. To ensure a good event quality, a primary vertex containing at least five charged particles was required, and events containing jets in poorly instrumented regions with transverse momentum exceeding 20 GeV were removed. The transverse mass of the leptonically decaying W boson in the event was reconstructed as: $m_T(W) = \sqrt{2p_T^l p_T^\nu (1 - cos(\phi^l - \phi^\nu))}$, where the measured E_T^{miss} provided information on the transverse momentum and ϕ angle of the neutrino. For the events with electrons this mass had to exceed 25 GeV, while the sum of this mass and E_T^{miss} had to exceed 60 GeV for the events with muons. Finally, at least one jet was required to be b-tagged by a well-reconstructed secondary vertex with a weight exceeding 5.85, as described in [17]. This common selection was followed by requirements specific for each of the two methods used to reconstruct the charge of b-quarks. For the track charge weighting method, the presence of a second b-tagged jet was required. Each of the two b-tagged jets had to contain at least two well-reconstructed charged particles with transverse momentum above 1 GeV within the pseudorapidity region $|\eta| < 2.5$. For the soft lepton method, a muon with transverse momentum greater

than 4 GeV had to be found within a cone of radius $\Delta R = \sqrt{\Delta\eta^2 + \Delta\phi^2} < 0.4$ from a jet axis.

Table 1 shows the numbers of events selected in the data and simulated Standard Model processes with the common requirements described above. Results requiring in addition either a second tagged *b*-jet or a soft muon are shown as well. The comparison between data and the simulation of the transverse momentum of the isolated lepton in events passing the common selection are shown in Figure 1. Backgrounds stemming from single top production, diboson production and Z+jets production were simulated to obtain the Standard Model prediction for the numbers of selected events, as shown in Table 1. Data, as well as simulations, were used to estimate the number of events from QCD processes and from W+jets production.

Channel	μ + jets			e + jets		
Selection	Preselection	2 *b*-tags	soft muon	Preselection	2 *b*-tags	soft muon
$t\bar{t}$	3219	1127	895	2242	749	628
Single top	163	35	39	125	25	28
W+jets (DD)	491	39	79	315	25	49
Z+jets	41	4	13	34	3	6
Diboson	8	1	2	5	1	1
QCD (DD)	227	17	41	54	4	9
Total	4200 ± 700	1220 ± 190	1070 ± 190	2800 ± 400	810 ± 130	720 ± 120
Observed	4315	1227	1033	3001	859	844

Table 1: The numbers of events following the standard selection of semileptonic $t\bar{t}$ events as in [13]. The numbers after requiring in addition either a second *b*-jet or a soft muon with $p_T > 4$ GeV are shown as well. The quoted uncertainties reflect the statistical and the dominant systematic effects described later. The background contributions that have been estimated using data-driven methods are marked with (DD).

The number of W+jets events expected in the data was estimated assuming that the theoretical prediction for the ratio of the number of produced W^+ bosons to the number of produced W^- bosons (r_{MC}) is more reliable than the absolute prediction of the W+jets cross-section themselves. The difference of the numbers of data events with a positive and negative lepton ($DL^+ - DL^-$) passing the nominal selection in Table 1 was corrected for non-W+jet events using the simulation prediction and then used together with r_{MC} to infer the total number of W+jets events in the data sample. The number of $W^{\pm}$+jets events was obtained by multiplying $(DL^+ - DL^-)$ by the factor $(r_{MC}+1)/(r_{MC}-1)$ which was obtained from simulation.

Events from QCD multijet processes could enter the data sample if they contain a lepton (for example from *b*-quark decays) or a hadron passing the lepton selection criteria. Both categories are labeled "fake leptons" in the following description of the method used to estimate the number of such events. The so called Matrix Method is based on selecting two categories of events, using loose and tight lepton selection requirements. The numbers of events containing one loose or tight lepton can be written as:

$$N^{loose} = N^{loose}_{real} + N^{loose}_{fake} \quad \text{and} \quad N^{tight} = \varepsilon_{real} N^{loose}_{real} + \varepsilon_{fake} N^{loose}_{fake} \tag{1}$$

where N^{loose}_{real} and N^{loose}_{fake} are the number of events containing real and fake leptons that passed the loose lepton requirements, while ε_{real} and ε_{fake} are the efficiencies for real and fake loose leptons to pass the tight leptons criteria. These efficiencies are defined as:

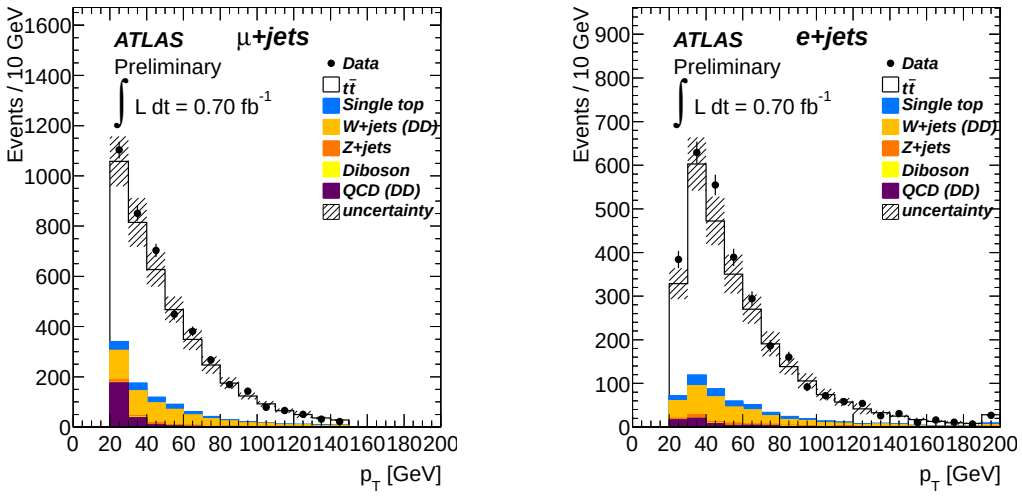

Figure 1: Comparison between the data and the simulation for the transverse momentum of the isolated lepton in muon + jets (left) and electron + jets (right) events. The error bands indicate statistical and systematic uncertainties on the predicted number of selected events.

$$\varepsilon_{real} = \frac{N_{real}^{tight}}{N_{real}^{loose}} \quad \text{and} \quad \varepsilon_{fake} = \frac{N_{fake}^{tight}}{N_{fake}^{loose}} \tag{2}$$

Equations 1 and 2 lead to the number of events with fake leptons passing the tight lepton requirement and thus the standard $t\bar{t}$ selection:

$$N_{fake}^{tight} = \frac{\varepsilon_{fake}}{\varepsilon_{real} - \varepsilon_{fake}}(\varepsilon_{real} N^{loose} - N^{tight}) \tag{3}$$

The efficiency ε_{real} was measured using data control samples of Z bosons decaying to two leptons, while ε_{fake} was measured with data in the control regions defined separately for the electron and muon channels. In these control regions the contribution of fake leptons is expected to be dominant. They were selected either requiring low transverse mass (less than 20 GeV for events with muons) or low missing tranverse energy (between 5 and 20 GeV, for events with electrons). The contribution of real isolated leptons in the control regions was subtracted using predictions from simulation.

5 Methods of top quark charge determination

The charge of the Standard Model top (or exotic) quark was determined by studying the charges of its decay products. The Standard Model top quark is expected to decay via

$$t^{(2/3)} \to b^{(-1/3)} + W^{(+1)}, W^{+} \to \ell^{+} + \nu_{\ell} \tag{4}$$

while a quark with exotic charge ($\tilde{t}$) will decay as

$$\tilde{t}^{(-4/3)} \to b^{(-1/3)} + W^{(-1)}, W^{-} \to \ell^{-} + \bar{\nu}_{\ell} \tag{5}$$

In the Standard Model the lepton ℓ^+ is accompanied by a b-quark ($Q = -1/3e$). In the decay of the quark with charge $Q = -4/3e$, the ℓ^- is accompanied by a b-quark.

In order to determine the charge of the heavy decaying quark, the charge of the W boson was first determined via its leptonic decay. The charge of the b-jet was then determined through the charges of the particles inside the b-jet or through the charge of a soft muon from a semileptonic b-decay. The pairing of the lepton and b-jet from the same heavy quark was decided upon using two different pairing techniques for the two methods of determining the b-quark charge. The soft muon method requires a pairing technique with a higher efficiency, due to the the small b-quark semileptonic branching ratio. These techniques are described in Sections 5.1 and 5.2.

5.1 Weighting procedure for the b-jet charge and the lepton – b-jet pairing algorithm

To determine the b-jet charge a weighting technique [18, 19] was employed in which the b-jet charge is defined as a weighted sum of the b-jet track charges:

$$Q_{bjet} = \frac{\sum_i q_i |\vec{j} \cdot \vec{p}_i|^\kappa}{\sum_i |\vec{j} \cdot \vec{p}_i|^\kappa}, \tag{6}$$

where $q_i(p_i)$ is the charge (momentum) of the i^{th} track, $\vec{j}$ is the b-jet axis direction and $\kappa = 0.5$ is a parameter optimized for the best separation of b- and $\bar{b}$-jets. The charge weighting procedure was also optimized for the minimal track p_T, the maximal number of tracks used, and the size of the cone inside of which tracks are included. The decision to use at most the ten highest p_T charged particle tracks with $p_T > 1$ GeV pointing to a b-jet within a cone of $\Delta R < 0.25$ follows from the optimization. It was verified that the optimization is not very sensitive to multiple events in one beam crossing ("pile-up").

To distinguish between the Standard Model and exotic model scenarios the combined charge, Q_{comb}, was used. It is defined as:

$$Q_{comb} = Q_{bjet} \cdot Q_\ell, \tag{7}$$

where Q_{bjet} and Q_ℓ are respectively the b-jet charge as measured in Eq. 6 and the lepton charge, where the b-jet and lepton ℓ were assumed to come from the same top quark. The lepton and b-jet pairing was performed using the invariant mass distribution of the lepton and the b-tagged jet, $m(\ell, b_{jet})$. If the assignment is correct, $m(\ell, b_{jet})$ cannot exceed the top quark mass. Figure 2 shows the invariant mass distribution for correct and incorrect assignments for the signal simulation after the standard selection.

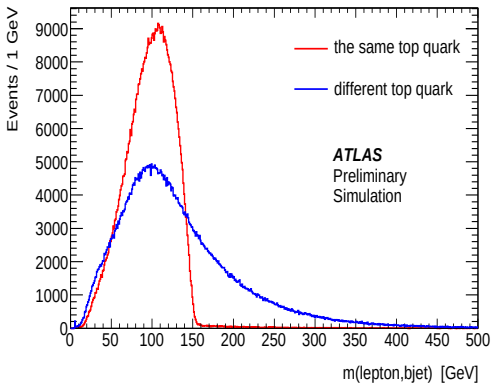

Figure 2: Lepton – b-jet invariant mass spectra for the lepton and b-jet from the same top quark (red line) and for those originating in different top quarks (blue line).

As the result of the matching procedure, only the events with the b-jets ($bjet_a, bjet_b$) satisfying

$$m(\ell, bjet_a) < m_{cr} \quad \text{and} \quad m(\ell, bjet_b) > m_{cr} \tag{8}$$

were accepted, and $bjet_a$ was matched with the lepton. The optimal value for the pairing mass cut was found to be $m_{cr} = 155$ GeV. This value was chosen to maximize the product of efficiency and purity ($\varepsilon \times P$) in the $t\bar{t}$ environment in the presence of QCD background using the simulated $t\bar{t}$ and QCD events. The purity is defined as the fraction of events with the correct pairing assignment.

The efficiency and purity of the invariant mass criterion for the signal $t\bar{t}$ sample with two b-tagged jets are ε= 28 % and P = 87 %, respectively. The efficiency of the invariant mass criterion together with the requirement of two b-tagged jets when measured on the sample of events passing the standard semileptonic $t\bar{t}$ selection described in Section 4 is ε_{tot} = 9.3 %.

5.2 Semileptonic decays of B-hadrons and the lepton – b-jet pairing with the KLFitter

The semileptonic decay branching ratio of B-hadrons to muons is $BR(b \to \mu + \nu + X) \approx 11\%$. The muon from such a decay will be identified as a non-isolated muon inside the corresponding b-jet, and its charge has the same sign as the charge of the b quark that produced the jet. However not all non-isolated muons in b-jets are products of B-hadron direct decays. They may also originate from sequential decays of B-hadrons, when a B-hadron decays to a D-hadron (containing a charm quark), which in turn decays semileptonically. The branching ratio of this decay chain is $BR(b \to c \to \mu + \nu + X) \approx 10\%$. These muons usually have the opposite charge to the initial b quark charge and thus they contaminate the selected signal sample. Leptons having opposite charge to the initial b quark may also come from neutral B-meson oscillations, when a B^0-meson transforms to a $\bar{B}^0$ and vice versa.

Figure 3 illustrates the variable $Q^{test}_{comb} = Q_{soft\mu} \times sign(-Q_{bquark})$ for different sources of the soft muon. If the signs of the charges of the soft muon and the b quark are the same, i.e. the charge of the soft muon correctly represents the charge of the b quark, then the variable defined above is equal to -1, otherwise it is +1. The soft muons coming from the decays of D-hadrons mostly have the wrong sign. To reduce the number of these muons, a cut on the p_{T} of the soft muon with respect to the jet axis (p_T^{rel}) of 800 MeV was employed, as described later. The distributions of p_T^{rel} for soft muons coming from the decays of B, D and light hadrons are shown in the right hand side of Figure 3.

As described in Section 4 the presence of at least one soft muon was required in each $t\bar{t}$ event candidate in order to tag the b-quark charge. A likelihood based method [13] (Kinematic Likelihood Fitter, KLFitter) to was used to determine the correct event topology, specifically the correct pairing of a jet (b-tagged or not) with the isolated lepton stemming from the semileptonic W decay. The KLFitter used the four highest transverse momentum jets in the event, the isolated lepton and the missing transverse energy to construct the likelihood for each jet to originate either from the decay of the W boson or directly from one of the top quarks. In addition the KLFitter corrected the energies and directions of the final state particles with a non-Gaussian parametrization of the energy resolution using transfer functions. The jet that had the highest likelihood to originate from the leptonically decaying top quark was selected. It was later required that there was at least one soft muon in the selected jet. This muon had to have p_T^{rel} greater than 800 MeV. This requirement preferentially removed muons produced by charm decay and light quarks. If two or more muons passed this cut, the one with the highest p_T^{rel} was selected. The cut value of 800 MeV was chosen to maximize the product of efficiency and purity ($\varepsilon \times P$) in the $t\bar{t}$ environment using the $t\bar{t}$ simulated events. The efficiency (ε), defined as the ratio of the number of muons coming from the direct decay of a B-hadron after applying the p_T^{rel} cut to the number of muons from direct B-hadron decays in the entire p_T^{rel} range, is 85 %. The purity (P), defined as the ratio of the number of muons coming from the direct decay of a B-hadron to the number of muons coming from all sources (B, D and light hadrons),

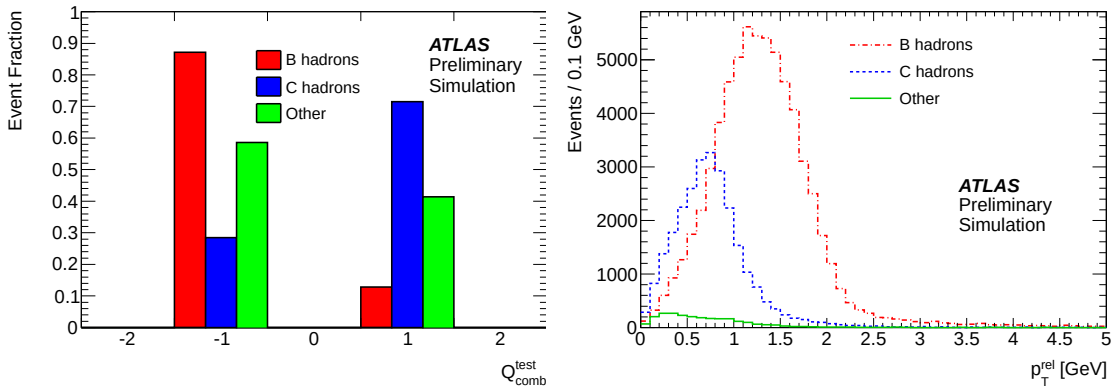

Figure 3: Left: the distribution of Q^{test}_{comb} (as introduced earlier). The distributions for each hadron flavour are normalised to 1. Right: the p_{T} of the soft muon with respect to the b-jet direction, p_T^{rel}, for b-jets with $p_T > 20$ GeV, for soft muons originating from B-hadrons, D-hadrons (containing a c quark) and light hadrons (other), in simulated $t\bar{t}$ events. Soft muons were required to have transverse momentum in excess of 4 GeV.

is 70 %. The p_{T} and p_T^{rel} of the soft muons before the selection on p_T^{rel} are shown in Figures 4 and 5 respectively.

The KLFitter assigned the selected jet to the correct lepton in 68 % of events. The total selection efficiency relative to the standard semileptonic $t\bar{t}$ selection described in Section 4 was ε_{tot} = 4 %. This number reflects the product of the semileptonic B-hadron branching fraction, the efficiency of selecting the soft muon and the efficiency of the cut on p_T^{rel}.

6 Results

For the track charge weighting method, the combined b-jet charge, Q_{comb} was defined as the product of the b-jet charge and the lepton charge for the b-jet associated with the leptonically decaying W (see Eq. 7). Figure 6 shows the Q_{comb} distribution for the data and the Standard Model simulation. Figure 7 shows the results for the soft muon method where the charge Q^{soft}_{comb} was defined as the product of the soft muon charge and the charge of the lepton from the W decay. Good agreement with the Standard Model prediction is observed in both cases.

The values of $< Q^{soft}_{comb} >$ (soft muon method) and $< Q_{comb} >$ (track charge weighting method) are shown in Table 2. The data are consistent with the Standard Model prediction.

6.1 Systematic uncertainties

Several systematic checks were performed to validate the b-quark charge measurement methods.

A calibration of the b-jet track charge weighting technique was performed using a sample of $b\bar{b}$ dijet events, where both jets were tagged with a secondary vertex tag [17]. In both data and simulation the charge of one of the b-jets was tagged with the soft muon method, and the charge of the other was determined with the track charge weighting technique. Agreement between the data and the simulations was studied for a range of selections on p_T^{rel} of the soft muon and as a function of the b-jet transverse momentum. In the region of b-jet transverse momenta similar to that from $t\bar{t}$ decays the mean reconstructed b-jet charge for the data and the simulation agree within a statistical uncertainty of 25%, which is taken

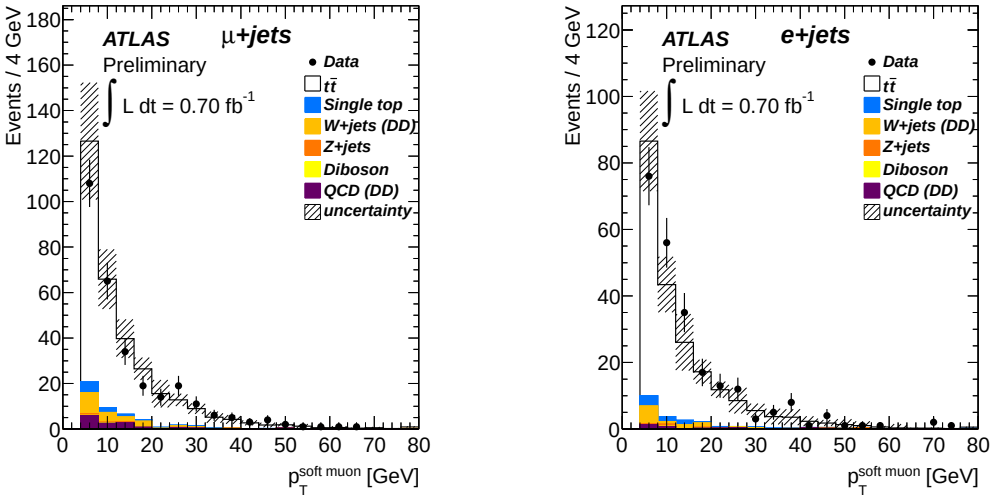

Figure 4: The comparison between data and simulation of the transverse momentum of soft muons in muon + jets (left) and electron + jets (right) events. The error bands indicate statistical and systematic uncertainties on the predicted number of selected events.

here as a systematic uncertainty. It is then taken into account in Section 7 as a variable scale factor (SF) when estimating the compatibility of the result with the Standard Model and exotic quark hypotheses. The p_T distribution of soft muons and the product of the charge of the soft muon and that of the b-jet belonging to the opposite hemisphere obtained with the track charge weighting method was compared for $b\bar{b}$ dijet events in the data and the simulation. Good agreement was observed. A similar check was performed for events where a soft muon was found in each of the b-jets. The data was compared with the simulation for the average product of the charges of the soft muons as a function of the b-jet p_T. Good agreement was observed within the statistical errors.

It should be noted that the performance of the jet charge measured here is not comparable to that which would be needed for B-physics (*e.g.* B-oscillations measurement), due to the different jet p_T spectrum and jet multiplicity in the events.

It was also verified, using the sample of events in Table 1, that the distribution of the absolute value of the reconstructed b-jet charge does not depend on the charge of the isolated lepton; thus the method works equally well for b-quarks and $\bar{b}$-quarks, and there is no correlation between the lepton charge and the absolute value of the reconstructed b-jet charge. It was verified that the reconstructed b-jet charge does not depend on the transverse momentum of the b-jet.

Systematic uncertainties resulting from the limited accuracy of the simulation's determination of the missing transverse energy, the energies of jets, electrons, and muons as well as the isolated lepton selection efficiency were estimated as in [13]. Uncertainties connected with leptons typically have a very small effect. Uncertainties connected with the measurement of jets, the amount of initial and final state radiation and the simulation description of the fragmentation process, have a more significant effect that differs in the two methods of b-jet charge determination, partly due to the different b-jet-lepton pairing methods used.

The following sources of systematic uncertainties were considered and are summarized in Table 3.

- **Description of the Standard Model processes:** The systematic uncertainty connected with limited accuracy of the simulation description of the Standard Model $t\bar{t}$ production process was esti-

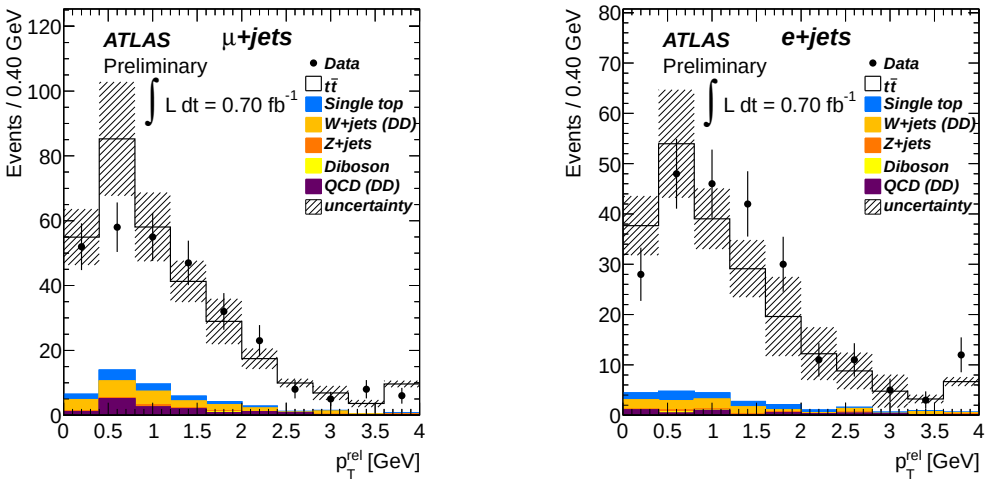

Figure 5: The p_T^{rel} of soft muons in the muon + jets channel (left) and the electron + jets channel (right). The last bin of the histogram includes the overflow. The error bands indicate statistical and systematic uncertainties on the predicted number of selected events.

mated by comparing the results obtained with MC@NLO and POWHEG+HERWIG samples.

- **Fragmentation modeling:** Simulated data generated with fragmentation modeling of PYTHIA and HERWIG were compared and the difference was taken as the uncertainty due to the choice of showering model.

- **Top Quark Mass:** The uncertainty in the result due to the uncertainty in the top quark mass was estimated using simulated $t\bar{t}$ data samples with the top quark mass in the range of 165 to 180 GeV varying in steps of 2.5 GeV. For the soft muon method, the top mass was a fixed parameter when using the KLFitter. The dependence of the mean value of Q_{comb}^{soft} on the top quark mass was fitted with a parabola. The systematic uncertainty due to the top quark mass was taken as the largest difference between the fit function values for top masses in the range 172.5 ± 0.9 GeV and the top mass equal to 172.5 GeV. The same approach was used for the track charge weighting method, but a straight line fit was used in this case.

- **ISR/FSR:** Initial and final state radiation are the dominant source of systematic uncertainty. The uncertainty was calculated using simulated signal samples where the amount of ISR and FSR was varied up and down within the range allowed by present data on multijet production, in a range comparable to those used in Perugia Soft/Hard tune variations in [20]. The maximum deviation from the nominal value was considered to be the systematic uncertainty due to ISR/FSR. The large sensitivity to ISR/FSR for the soft muon method is due to the additional jets that can give false lepton–*b*-jet pairing in the KLFitter. With more data in the future, this systematic uncertainty can be reduced by a cut on the likelihood of the fit.

- **Amount of background from QCD processes:** A data-driven QCD multijet background estimation was employed as described in Section 4. Conservatively a 100 % uncertainty on the size of the QCD background was taken to calculate the uncertainty on $< Q_{comb} >$ and $< Q_{comb}^{soft} >$. This choice was justified by comparing several methods of the QCD background estimation.

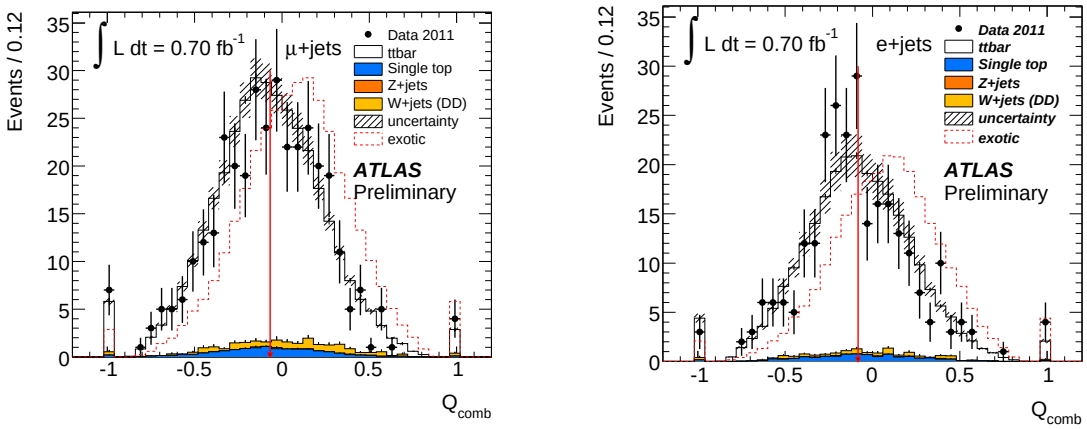

Figure 6: Comparison of the combined b-jet charge Q_{comb} in the muon (left) and the electron (right) final states in the data with the Standard Model expectations for signal and background events. The mean Q_{comb} expected for the SM top quark is marked with an arrow. The top quark with $Q = -4/3e$ would result in the distribution marked with the red dashed line, thus with a positive mean.

- **Single top production cross-section:** The cross section of single top production was varied within its theoretical uncertainty and the largest difference from the nominal value is quoted as a systematic uncertainty.

- **Cross-sections for the W+jets and Z+jets processes:** The number of W+jets events was estimated with use of the data as described in Section 4. The uncertainty on the r_{MC} factor was estimated to be 5%. The resulting uncertainty for W plus 4-jet processes was found to be 48%. The same uncertainty was assumed for Z plus 4-jets processes. Thus the cross-sections for W and Z plus 4-jets processes were varied up and down by 48%. The maximum difference from the result with the nominal cross-section was taken to be the systematic uncertainty. Independently the scaling factors correcting the fraction of heavy flavor contributions in simulated W+jets samples were estimated from collision data. The relative uncertainties on such factors were taken to be 47% for W $b\bar{b}$+jets and W $c\bar{c}$+jets contributions, and 32% for W c+jets contributions.

- **Multiple interactions per beam-crossing (pile-up):** The dependence of reconstructed $< Q_{comb} >$ and $< Q_{comb}^{soft} >$ on the number of interactions within the beam-crossing was studied. No significant dependence was found within the statistical errors.

7 Statistical methods to exclude the top quark with an exotic charge

Given the good agreement between the results presented in the previous section and the Standard Model, the top quark with an exotic charge of $-4/3e$ can be excluded. To quantify this exclusion a standard likelihood approach [21] was adopted. Two hypotheses: the Standard Model (null hypothesis) where the top quark has charge $2/3e$, and the exotic quark hypothesis, with a charge of $-4/3e$, were compared. In the following, the statistical significance for excluding the exotic charge is presented separately for the two methods of determining the b-jet charge. The test statistic used to distinguish between different hypotheses, was either the sample mean combined charge, $< Q_{comb} >$, for the weighting method or corresponding quantity, $< Q_{comb}^{soft} >$, for the semileptonic method. The expected spread of these variables

channel	$< Q_{comb} >$		
	Data	SM (MC)	SM $t\bar{t}$
e + jets	-0.088 $\pm$ 0.020 (stat) $\pm$ 0.012 (syst)	-0.084 $\pm$ 0.020	-0.086 $\pm$ 0.021
μ +jets	-0.078 $\pm$ 0.018 (stat) $\pm$ 0.010 (syst)	-0.081 $\pm$ 0.018	-0.086 $\pm$ 0.019
e/μ + jets	-0.082 $\pm$ 0.013 (stat) $\pm$ 0.011 (syst)	-0.082 $\pm$ 0.013	-0.086 $\pm$ 0.014
channel	$< Q_{comb}^{soft} >$		
	Data	SM (MC)	SM $t\bar{t}$
e + jets	-0.36 $\pm$ 0.07 (stat) $\pm$ 0.04 (syst)	-0.237 $\pm$ 0.016	-0.266 $\pm$ 0.010
μ + jets	-0.26 $\pm$ 0.07 (stat) $\pm$ 0.06 (syst)	-0.232 $\pm$ 0.015	-0.240 $\pm$ 0.009
e/μ + jets	-0.31 $\pm$ 0.05 (stat) $\pm$ 0.04 (syst)	-0.234 $\pm$ 0.011	-0.251 $\pm$ 0.007

Table 2: Comparison of the data and Standard Model simulation (MC) for the product of b-jet and isolated lepton charges, $< Q_{comb} >$, and for the average value of the product of the soft muon and isolated lepton charges, $< Q_{comb}^{soft} >$. The column marked SM $t\bar{t}$ indicates the result obtained when using only the Standard Model $t\bar{t}$ events selected in the simulated data (no background). For a top quark with the exotic charge $Q = -4/3e$, a result equal to the absolute value of SM $t\bar{t}$ result but with a positive sign is expected (neglecting the effect of background). The errors on the simulation prediction are statistical only. A more complete comparison with the predictions of the exotic top quark model can be found in Table 4.

Source	$< Q_{comb} >$ (%)		$< Q_{comb}^{soft} >$ (%)	
	e + jets	μ + jets	e + jets	μ + jets
ISR/FSR	13.8	11.0	15	24
Other $t\bar{t}$ modeling uncertainties	2.1	1.6	7	10
W+jets uncertainties	1.2	1.9	1.8	5.5
QCD uncertainties	0.4	1.6	4.0	1.0
Other SM background modeling uncertainties	2.0	1.0	< 1	1.6
Jet/$E_{\mathrm{T}}^{\mathrm{miss}}$ systematics	7.2	7.6	5	7.5
Lepton systematics	2.9	4.1	2	1.5
b-tagging systematics	1.1	< 1	1	< 1
Total uncertainty (%)	16.2	14.4	18	27

Table 3: Systematic uncertainties for $< Q_{comb} >$ and $< Q_{comb}^{soft} >$ in percent. The total uncertainty was calculated by adding the individual ones in quadrature. The estimation of some of the systematic uncertainties suffers from a small number of simulated events. The statistical error is in these cases conservatively included in the systematic effect estimation.

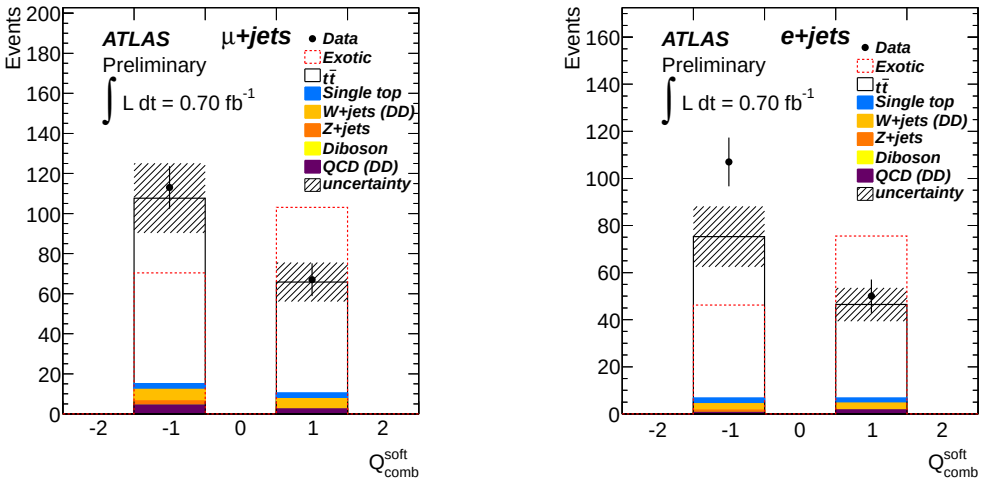

Figure 7: Distribution of the combined charge Q_{comb}^{soft} in muon + jets (left-hand side) and electron + jets (right-hand side) events in the data and Standard Model simulation. (DD) denotes the background contribution estimated with data-driven methods. Prediction for the exotic top quark with $Q = -4/3e$ is shown in red dashed line.

due to systematic effects and the limited amount of data was estimated in a large number of pseudoexperiments, as described below.

Track charge weighting method:
The test statistic for this method was the mean value of combined b-jet charge (Eq. 7):
$< Q_{comb} > \; = \; < Q_{bjet} \cdot Q_{\ell} >$. The observed average value of this charge can be expressed as

$$< Q_{comb} > = (1 - r_b - r_t) \cdot Q_s + r_b \cdot Q_b + r_t \cdot Q_t, \tag{9}$$

where Q_s, Q_b and Q_t are the expected mean combined charges for signal, background and single top quark processes, respectively, and r_b (r_t) is the fraction of the background (single top quark production) in the candidate events.

It was assumed that the quantities Q_s, Q_b, Q_t, r_b and r_t were uncorrelated Gaussian random variables, with their mean values and statistical uncertainties estimated from the simulations of the Standard Model top quark and exotic quark scenarios for the existing integrated luminosity, L = (0.70 $\pm$ 0.02) fb^{-1}. In addition, the mean combined charge, resulting from Eq. 9, was assigned an additional spread using a Gaussian distribution with the systematic error (see Table 3) used as a standard deviation.

In order to take into account possible differences between the data and the simulation for the average b-jet charge, the value of $< Q_{comb} >$ resulting from the procedure above was multiplied by a scale factor, S_F, which was defined as the ratio of the results obtained from data and simulation control samples. This scale factor was taken to be a random distributed Gaussian variable with a mean value $S_F \; = \; 1$ and a spread σ = 0.25. This scale factor resulted in assigning an additional Gaussian spread to $< Q_{comb} >$. The spread is determined from the statistics of the b-jet charge calibration with $b\bar{b}$ dijet events described in section 6.1.

Pseudo-experiments in which Q_s, Q_b, Q_t, r_b, r_t as well as the $< Q_{comb} >$ systematic error and S_F were sampled from Gaussian distributions were performed for the Standard Model and the exotic scenario. The simulation results with and without the scale factor are compared with the data in Table 4

below.

Soft muon method:
A similar procedure to that above was applied. The test statistic for the soft muon method was the average of the product of the charges of the soft muon and the lepton from the W decay, Q^{soft}_{comb}. The mean value of the Q^{soft}_{comb} distribution is expected to be negative for the Standard Model scenario, as shown in Table 2, but positive for the exotic scenario.

The distribution of Q^{soft}_{comb} expected for the exotic case was constructed by flipping the +1 and -1 bin contents of the corresponding simulated distribution for Standard Model $t\bar{t}$. Then pseudo-experiments were performed with Poisson variations in the numbers of events with Q^{soft}_{comb} = -1 and +1. The same procedure was repeated for the single top background process, assuming that the singly produced top quark has the exotic charge as well. The Q^{soft}_{comb} distribution for the other background processes were the same for the two hypotheses, with a Poisson variation of the bin content for each pseudo-experiment. In each pseudo-experiment the average $< Q^{soft}_{comb} >$ value was calculated. The results from one million pseudo-experiments were fitted with a Gaussian and used to calculate the statistical uncertainty for the average Q^{soft}_{comb} for the Standard Model and the exotic scenarios. The results are summarized in Table 4.

Model	$< Q_{comb} >$		
	e + jets	μ + jets	combined
SM	-0.084 $\pm$ 0.020 (stat)	-0.081 $\pm$ 0.018 (stat)	-0.082 $\pm$ 0.013 (stat)
Exotic	+0.085 $\pm$ 0.019 (stat)	+0.088 $\pm$ 0.018 (stat)	+0.083 $\pm$ 0.013 (stat)
Model	$< Q_{comb} >$ with SF		
	e + jets	μ + jets	combined
SM	-0.084 $\pm$ 0.028 (stat)	-0.081 $\pm$ 0.023 (stat)	-0.082 $\pm$ 0.020 (stat)
Exotic	+0.085 $\pm$ 0.028 (stat)	+0.088 $\pm$ 0.023 (stat)	+0.083 $\pm$ 0.020 (stat)
Measured	-0.088 $\pm$ 0.022	-0.078 $\pm$ 0.020	-0.082 $\pm$ 0.015
Model	$< Q^{soft}_{comb} >$		
	e + jets	μ + jets	combined
SM	-0.237 $\pm$ 0.016 (stat)	-0.232 $\pm$ 0.015 (stat)	-0.234 $\pm$ 0.011 (stat)
Exotic	+0.241 $\pm$ 0.016 (stat)	+0.180 $\pm$ 0.015 (stat)	+0.209 $\pm$ 0.011 (stat)
Measured	-0.36 $\pm$ 0.09	-0.26 $\pm$ 0.10	-0.31 $\pm$ 0.07

Table 4: The measured and the expected average values of Q_{comb} with two scale factor (SF) hypotheses and for Q^{soft}_{comb}. The expected values are for the Standard Model top and the exotic quark scenarios. The errors on the measured values include both the statistical and the systematic uncertainties.

The distributions of the average $< Q_{comb} >$ (track charge weighting method) and $< Q^{soft}_{comb} >$ (soft muon method) from pseudo-experiments for Standard Model and exotic quark hypotheses are shown in Figure 8. The arrows point to the $< Q_{comb} >$ and $< Q^{soft}_{comb} >$ observed in the data. The measured values in both methods are consistent with the expectations from the Standard Model.

The measured $< Q_{comb} >$ and $< Q^{soft}_{comb} >$ are each more than 4.5 σ away from the values expected from the exotic quark hypothesis when the two lepton flavors are treated separately. If electron and muon channels are combined, the exotic quark scenario is excluded at a confidence level greater than 5 σ with either of the b-quark charge measurement methods.

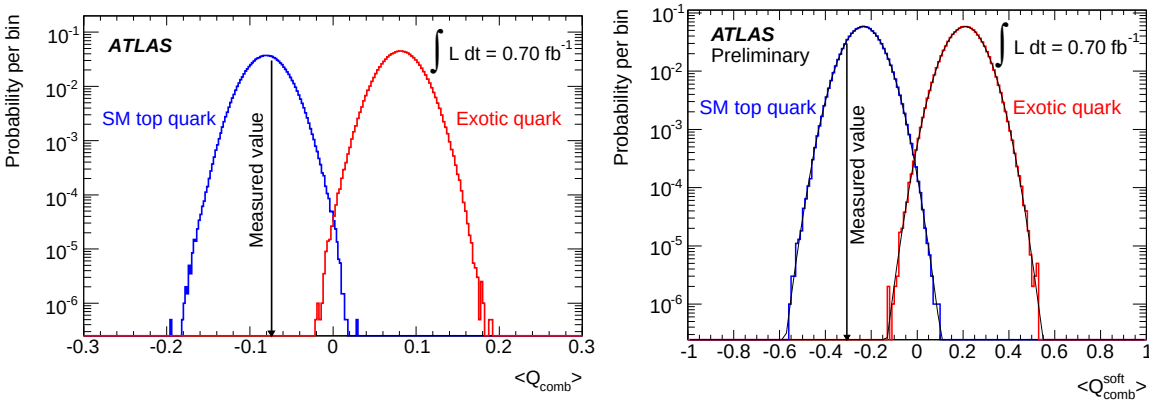

Figure 8: The expected distributions of $< Q_{comb} >$ and $< Q_{comb}^{soft} >$ obtained from the large number of pseudo-experiments combining the electron+jets and the muon +jets channels in the Standard Model (blue) and the exotic (red) scenarios. The measured values from the data are marked with arrows. The $< Q_{comb} >$ distribution includes the scale factor (SF) with a spread of 25% resulting from the calibration of the track charge weighting method.

8 Conclusion

The top quark charge was measured in the isolated-lepton+jets final states using 0.70 fb^{-1} of data accumulated in the ATLAS experiment at a center of mass energy of 7 TeV . The results were compared with expectations for the Standard Model top quark and for a “top-like” quark with an exotic charge of $-4/3e$. The exotic scenario is excluded at more than 5 σ.

References

[1] CDF Collaboration, F. Abe et al. (1995). *"Observation of Top Quark Production in pp Collisions with the Collider Detector at Fermilab"*, Physical Review Letters **74** (14): 2626;
D0 Collaboration, Abachi et al. (1995). *"Search for High Mass Top Quark Production in pp Collisions at $\sqrt{s}$ = 1.8 TeV"*, Physical Review Letters **74** (13): 2422.

[2] D0 Collaboration, V.M. Abazov et al., *Experimental Discrimination between Charge 2e/3 Top Quark and Charge 4e/3 Exotic Quark Production Scenarios*, Physical Review Letters **98**, (2007) 041801;
CDF Collaboration, T. Aaltonen et al., *Exclusion of an Exotic Top Quark with -4/3 Electric Charge Using Soft Lepton Tagging*, Physical Review Letters **105** (2010) 101801.

[3] ATLAS Collaboration, *The ATLAS Experiment at the CERN Large Hadron Collider*, JINST **3** (2008) S08003.

[4] ATLAS Collaboration, *Luminosity Determination in pp Collisions at sqrt(s) = 7 TeV using the ATLAS Detector in 2011*, ATLAS-CONF-2011-116 (2011).

[5] S. Frixione and B.R. Webber, *Matching NLO QCD computations and parton shower simulations*, JHEP **0206** (2002) 029, hep-ph/0204244.

[6] J. Pumplin et al., *New generation of parton distributions with uncertainties from global QCD analysis*, JHEP **07** (2002) 12.

[7] G. Corcella et al., *HERWIG 6: An Event generator for hadron emission reactions with interfering gluons (including supersymmetric processes)*, JHEP **0101** (2001) 010, hep-ph/0011363.

[8] J. M. Butterworth, J. R. Forshaw, and M. H. Seymour, *Multiparton interactions in photoproduction at HERA*, Z. Phys. **C72** (1996) 637646.

[9] M. Aliev, H. Lacker, U. Langenfeld, S. Moch, P. Uwer, et al., *HATHOR: HAdronic Top and Heavy quarks crOss section calculatoR*, Comput. Phys. Commun. **182** (2011) 10341046.

[10] M.L. Mangano et al., *ALPGEN, a generator for hard multiparton processes in hadronic collisions*, JHEP **0307** (2003) 001, hep-ex/0206293.

[11] S. Agostinelli et al., *Geant4 A Simulation Toolkit*, Nucl. Instrum. Meth. **A506** (2003) 250.

[12] ATLAS Collaboration, *The ATLAS Simulation Infrastructure*, Eur. Phys. J. **C70** (2010) 823-874. arXiv:1005.4568 [physics.ins-det].

[13] ATLAS Collaboration, *Measurement of the charge asymmetry in top quark pair production in pp collisions at sqrt(s)=7 TeV using the ATLAS detector*, ATLAS-CONF-2011-106 (2011).

[14] S. Frixione, P. Nason and C. Oleari, *Matching NLO QCD computations with Parton Shower simulations: the POWHEG method*, JHEP **0711** (2007) 070, arXiv:0709.2092.

[15] T. Sjostrand and S. Mrenna and P.Z. Skands, *PYTHIA 6.4 Physics and Manual*, JHEP **05** (2006) 026, hep-ph/0603175.

[16] M. Cacciari and G. P. Salam, *Dispelling the N3 myth for the kt jet-finder*, Physics Letters B **641** (2006) no. 1, 57 – 61.

[17] ATLAS Collaboration, *Performance of the ATLAS secondary vertex b-tagging algorithm in 7 TeV collision data*, ATLAS-CONF-2010-041 (2010).

[18] R.D.Field and R.P.Feynman, *A Parameterization of the properties of Quark Jets*, Nucl. Phys. **B136** (1978) 1–76.

[19] R. Barate et al., *Determination of A(b)(FB) using jet charge measurements in Z decays*, Phys. Lett. **B426** (1998) 217–230.

[20] P. Z. Skands, *Tuning Monte Carlo Generators: The Perugia Tunes*, Phys. Rev. **D82** (2010) 074018, arXiv:1005.3457 [hep-ph].

[21] W.A. Rolke, A.M. Lopez, J. Conrad, *Limits and Confidence Intervals in Presence of Nuisance Parameters*, Nucl. Instr. Meth. **A551** (2005) 493.

Paper 2: Expected performance of the ATLAS experiment: detector, trigger and physics

Top Quark Properties

Abstract
The ATLAS potential for the study of top quark properties and physics beyond the Standard Model in the top sector, is reviewed in this paper. Measurements of the top quark charge, the spin and spin correlations, the Standard Model decay ($t \to bW$), rare top quark decays associated to flavour changing neutral currents ($t \to qX, X = \gamma, Z, g$) and $t\bar{t}$ resonances are discussed. The expected sensitivity of the ATLAS experiment is estimated for an integrated luminosity of 1 fb^{-1} at the LHC. For the Standard Model measurements the expected precision is presented. For the tests of physics beyond the Standard Model , the 5σ discovery potential (in the presence of a signal) and the 95% confidence level limit (in the absence of a signal) are given.

1 Introduction

Several properties of the top quark have already been explored by the Tevatron experiments, such as the mass, charge and lifetime, the rare decays through flavour changing neutral currents (FCNC) and the production cross-sections. The structure of the Wtb vertex and the main top quark decay mode ($t \to bW$) within the Standard Model were also investigated together with the measurements of the W-boson helicity fractions. Many of these studies were performed by reconstructing $t\bar{t}$ pairs in the semileptonic, dileptonic and fully hadronic decay modes. Given the current Tevatron luminosity, most of these studies are limited by the statistics acquired.

The electric charge of the top quark is one of its fundamental properties and will be probed with high statistics at the LHC. The measurement of the top quark charge can be performed either by identifying the charge of its decay products in the main decay channel $t \to bW$ or by studying radiative top quark processes. At the Tevatron the D0 [1] and CDF [2] collaborations have already initiated the study of the top quark charge and, with the available statistics, they showed that the data gives preference to the Standard Model top quark hypothesis (with a charge of $+2/3$) over the scenario with an exotic quark (XM) of charge $-4/3$ and mass ≈ 170 GeV, fully consistent with the present precision electroweak data [3,4]. The D0 and CDF exclude the exotic quark hypothesis with 92 and 87 % confidence, respectively.

As the top quark decays before it can form hadronic bound states, a consequence of its high mass, the spin information of the top quark is propagated to its decay products. This unique behaviour among quarks allows direct top quark spin studies, as spin properties are not washed out by hadronization. Through the measurement of the angular distributions of the decay products the information of the top quark spin can be reconstructed. Top quark spin polarization and correlations in $t\bar{t}$ events produced at the LHC are precisely predicted by the Standard Model and are sensitive to the fundamental interactions involved in the top quark production and decay. By testing only the top quark decay, the W-boson polarization measurement complements top quark spin studies, helping to disentangle the origin of new physics, if observed. The W-boson polarization states can be measured through the longitudinal (F_0), left-handed (F_L) and right-handed (F_R) helicity fractions. At the present, the most stringent limits on the W-boson helicity fractions were obtained at the Run-II of the Tevatron [5–13]. Analysing 1.9 fb^{-1} of data, the CDF experiment measured [5] $F_0 = 0.62 \pm 0.11$ with F_R fixed to zero and $F_R = -0.04 \pm 0.05$ with F_0 fixed to the Standard Model expectation for $m_t = 175$ GeV. For 2.7 fb^{-1}, the D0 experiment measured [10] $F_0 = 0.490 \pm 0.106(\text{stat}) \pm 0.085(\text{syst})$ with F_R fixed to zero, and $F_R = 0.110 \pm 0.059(\text{stat}) \pm 0.052(\text{syst})$ with F_0 fixed to the Standard Model value.

Within the Standard Model, the Wtb coupling is purely left-handed (at the tree level), and its size is given by the Cabibbo-Kobayashi-Maskawa (CKM) matrix element V_{tb}. In Standard Model extensions,

Table 1: The values of the branching ratios of the FCNC top quark decays, predicted by the SM, the quark-singlet model (QS), the two-higgs doublet model (2HDM), the minimal supersymmetric model (MSSM) and SUSY with R-parity violation are shown [30–36].

Process	SM	QS	2HDM	MSSM	$R\!\!\!/$ SUSY
$t \to uZ$	8×10^{-17}	1.1×10^{-4}	–	2×10^{-6}	3×10^{-5}
$t \to u\gamma$	3.7×10^{-16}	7.5×10^{-9}	–	2×10^{-6}	1×10^{-6}
$t \to ug$	3.7×10^{-14}	1.5×10^{-7}	–	8×10^{-5}	2×10^{-4}
$t \to cZ$	1×10^{-14}	1.1×10^{-4}	$\sim 10^{-7}$	2×10^{-6}	3×10^{-5}
$t \to c\gamma$	4.6×10^{-14}	7.5×10^{-9}	$\sim 10^{-6}$	2×10^{-6}	1×10^{-6}
$t \to cg$	4.6×10^{-12}	1.5×10^{-7}	$\sim 10^{-4}$	8×10^{-5}	2×10^{-4}

departures from the Standard Model expectation $V_{tb} \simeq 0.999$ [1] are possible [14, 15], as well as new radiative contributions to the Wtb vertex [16, 17]. These deviations might be observed in top quark production and decay processes at LHC. The most general Wtb vertex for on mass shell W-boson, top quark and b quark, containing terms up to dimension five can be written as

$$\mathscr{L} = -\frac{g}{\sqrt{2}}\bar{b}\,\gamma^{\mu}\,(V_L P_L + V_R P_R)\,t\,W_{\mu}^{-} - \frac{g}{\sqrt{2}}\bar{b}\,\frac{i\sigma^{\mu\nu}q_{\nu}}{M_W}\,(g_L P_L + g_R P_R)\,t\,W_{\mu}^{-} + \text{h.c.}\,, \qquad (1)$$

with $q = p_t - p_b$ the W-boson momentum and $P_{R(L)}$ the chirality projectors. Additional $\sigma^{\mu\nu}k_{\nu}$ and k^{μ} terms, where $k = p_t + p_b$, can be absorbed into this Lagrangian using Gordon identities. If the W-boson is on its mass shell or it couples to massless fermions $q^{\mu}\varepsilon_{\mu} = 0$, and terms proportional to q^{μ} can be dropped from the effective vertex. The new constants V_R, g_L and g_R [18, 19], are vector like (V_R) and tensor like (g_L and g_R) anomalous couplings, can be related to f_1^R, f_2^L and f_2^R in Ref. [20] (and references therein) as $f_1^R = V_R$, $f_2^L = -g_L$ and $f_2^R = -g_R$. If we assume CP is conserved, these couplings can be taken to be real. Within the Standard Model $V_L \equiv V_{tb} \simeq 0.999$ and the other couplings (V_R, g_L, g_R) vanish at the tree level, while nonzero values are generated at higher orders [21, 22]. Indirect limits on the Wtb vertex anomalous couplings can be inferred from radiative B-meson decays and $B\bar{B}$ mixing [23]. Taking into account the current world average [23], $BR(\bar{B} \to X_s\gamma) = (3.55 \pm 0.24^{+0.09}_{-0.10} \pm 0.03) \times 10^{-4}$, varying one parameter at a time, the 95% C.L. bounds on V_R, g_L and g_R are in the range $[-0.0007, 0.0025]$, $[-0.0015, 0.0004]$ and $[-0.15, 0.57]$, respectively [22, 24].

Flavour Changing Neutral Currents are strongly suppressed in the Standard Model due to the Glashow-Iliopoulos-Maiani (GIM) mechanism [25]. Although absent at tree level, small FCNC contributions are expected at one-loop level, determined by the CKM mixing matrix [26–29]. For the top quark within the framework of the Standard Model, these contributions limit the FCNC decay branching ratios to the gauge bosons, $BR(t \to qX, X = Z, \gamma, g)$, to below 10^{-12}. There are however extensions of the SM, like supersymmetry (SUSY) [30], multi-Higgs doublet models [31] and models with exotic (vector-like) quarks [32–34], which predict the presence of FCNC contributions already at tree level and significantly enhance the FCNC decay branching ratios compared to the Standard Model predictions [35, 36]. The branching ratio for the different models are shown in Table 1. FCNC processes associated with the production and decay of top quarks have been studied at colliders and the observed upper limits on the branching ratios at 95% C.L., from the direct searches, are shown in Table 2.

Since the top quark mass is much larger than the other quarks, the top quark may play a privileged role in the electroweak symmetry breaking (EWSB) mechanism. Any new physics connected to the EWSB could be preferentially coupled to the top quark sector. This would lead to deviations from the

[1] Three generations of quarks and unitarity of the CKM matrix are assumed.

Table 2: Experimental observed upper limits on the branching ratios at 95%C.L. for the FCNC top quark decays.

	LEP	HERA	Tevatron
$BR(t \to qZ)$	7.8% [37–41]	49% [42]	3.7% [43]
$BR(t \to q\gamma)$	2.4% [37–41]	0.75% [42]	3.2% [44]
$BR(t \to qg)$	17% [45]	13% [42,46,47]	$0.1-1$ % (estimated from [46,48])

expected Standard Model $t\bar{t}$ production rate and could distort the top quark kinematics. New resonances and gauge bosons strongly coupled to the top quark are expected in a large variety of models, in particular those with strong EWSB [49–51]. The $t\bar{t}$ final states are also interesting for leptophobic Z' bosons which can appear in Grand Unification Models [52]. These new particles could reveal themselves in the $t\bar{t}$ invariant mass distribution. At the Tevatron experimental upper limits were set at 95 %C.L. for the $\sigma(p\bar{p} \to Z') \times BR(Z' \to t\bar{t})$ with Z' masses between 450 GeV and 900 GeV. A topcolor leptophobic Z' is ruled out below 720 GeV and the cross section of any narrow Z' decaying to a $t\bar{t}$ is less than 0.64 pb at 95%C.L., for Z' masses above 700 GeV [53].

In this note the ATLAS potential for the study of the top quark properties and tests of physics beyond the Standard Model in the top quark sector are reviewed for an expected luminosity of 1 fb^{-1} at the LHC. The note is organized as follows: the basic event selection and the trigger used are reminded in Section 2. In Sections 3, 4, 5 and 6 the studies of the top quark charge, the W-boson and top quark polarisation studies and the Wtb anomalous couplings, the top quark FCNC decays and the production of $t\bar{t}$ resonances are discussed respectively. The summary and conclusions are presented in Section 7. The top quark mass, one of the most important top quark properties, is not investigated here as a separate note is devoted to this issue [54].

2 Basic event selection

As most of the studies performed in this paper are related to either the semileptonic ($t\bar{t} \to WWb\bar{b} \to l\nu j_1 j_2 b\bar{b}$ with $l = e, \mu$) or the dileptonic ($t\bar{t} \to WWb\bar{b} \to l\nu l'\nu' b\bar{b}$ with $l, l' = e, \mu$) decays of $t\bar{t}$ events, basic criteria for the event selection were defined for each one of these final state topologies. Changes to the criteria are to be expected depending on the type of top quark property under study. For the background studies several sources were considered, $t\bar{t}$, W+jets, $Wb\bar{b}$+jets, $Wc\bar{c}$+jets, Z+jets, WW, ZZ, WZ and single top events (see the introduction of the Top Chapter for a full list of backgrounds). The backgrounds are also described in more detail separatly for each section of the note. All signal and background events were required to pass the single lepton trigger requirements for electrons and muons. The triggers considered were L1_EM18I (L1_MU20,L1_MU40) for electrons (muons) at L1, e22i (mu20) for electrons (muons) at L2 and e22i (mu20) for electrons (muons) at the Event Filter (EF) [55].

Different selection criteria are applied for the top quark FCNC analyses, as the final state topology is different from those considered above. These criteria are explained in Section 5.

Semileptonic topology

In the semileptonic topology, signal events have a final state with one isolated lepton (electron or muon), at least four jets (two of them from the hadronization of b quarks and labelled b-jets) and large transverse missing energy from the undetected neutrino. More information on the signal can be found in the introduction of the Top Chapter. The basic selection criteria were defined by requiring that the events should have:

Table 3: Cumulative efficiencies of the standard top quark selection criteria for the semileptonic and dileptonic type of events with electrons and muons for the pseudorapidity range $|\eta| \leq 2$.

criterion	$\varepsilon(\%)$	criterion	$\varepsilon(\%)$
Semileptonic events	100	Dileptonic events	100
1 isol.lept. (p_T >25/20 GeV)	58.9	2 isol.lept. (p_T >25/20 GeV)	35.5
$\geq$ 4 jets (p_T >30 GeV)	34.2	$\geq$ 2 jets (p_T >30 GeV)	31.8
$\geq$ 2 b-tagged	10.5	= 2 b-tagged	8.3
missing $E_T > 20$ GeV	8.5	missing $E_T > 30$ GeV	6.5

- exactly one isolated electron (muon) with $|\eta| < 2.5$ and $p_T > 25$ GeV ($p_T > 20$ GeV);
- at least 4 jets with $|\eta| < 2.5$ and $p_T > 30$ GeV;
- at least 2 jets tagged as b-jets;
- missing transverse energy above 20 GeV.

Dileptonic topology

In the dileptonic topology, signal events have a final state with two isolated leptons (electrons and/or muons), at least two jets (tagged as b-jets) and large transverse missing energy from the two undetected neutrinos. The basic selection criteria were defined by requiring that the events should have:

- exactly two isolated electrons (muons) with $|\eta| < 2.5$ and $p_T > 25$ GeV ($p_T > 20$ GeV);
- at least 2 jets with $|\eta| < 2.5$ and $p_T > 30$ GeV;
- 2 jets tagged as b-jets;
- missing transverse energy above 30 GeV.

Selection efficiency

The efficiency of the basic selection criteria was examined using $\approx$ 450 000 events from the $t\bar{t} \to bWbW \to bqqb\ell\nu, b\ell\nu b\ell\nu$ signal sample. The results are presented in Table 3.

The effect of the trigger efficiency is investigated separately for the individual analysis.

3 Top quark charge reconstruction

There are several techniques to determine the electric charge of the top quark at hadron collider experiments [56–58]. The top quark charge measurement presented here is based on the reconstruction of the charges of the top quark decay products. As the dominant decay channel of the top quark is $t \to W^+b(\bar{t} \to W^-\bar{b})$, the top quark charge determination requires the measurement of both the W boson and the b quark charges. While the charge of the W boson can be determined through its leptonic decay, the b quark charge is not directly measurable due to quark confinement in hadrons. In this note two possible ways to determine the b quark charge were investigated:

- The charge weighting technique: this approach is based on finding a correlation between the b quark charge and the charges of the tracks belonging to the b-jet [59, 60].
- The semileptonic b-decay approach: in this case the b quark charge is determined using the semileptonic b-decays ($b \to c, u + W^-, W^- \to \ell^- + \bar{\nu}_\ell$), where the sign of the soft lepton indicates the sign of the b quark charge.

Two major issues have to be addressed. The first one is to find the selection criteria to perform the correct pairing of the lepton and the b-jet originated in the same top quark decay. In the Standard Model a b-jet, coming from a b quark, should be associated with a positive lepton (ℓ^+), while in the exotic case it should be associated with a negative one (ℓ^-). The second issue is the assignment of a charge to the b-jet selected by the pairing criterion. While the former issue is common for both the approaches, the latter one is tackled in different ways.

3.1 Event generation and selection

The standard $t\bar{t} \longrightarrow W^+bW^-\bar{b}$ samples were used as signal events in both the semileptonic and the dileptonic channels (only electrons and muons are taken as signal). For the background studies, the W+jets sample was used. The $t\bar{t}$ all jets channels as well as the semileptonic and dileptonic channels of τ leptons were analysed as they can contribute to background (all jets channel) and to signal (events with the leptonic decays of τ leptons). In the present analysis the common selection criteria were used, as defined in Section 2. In addition, for each approach, specific criteria were applied to the events.

3.2 The lepton and b-jet pairing algorithm

The lepton and b-jet pairing was done using the invariant mass distribution of the lepton and the b-tagged jet, $m(l, b_{jet})$. If the assignment is correct, $m(l, b_{jet})$ is limited by the top quark mass, otherwise there is no such restriction, as can been seen in Figure 1, where the signal sample with the standard cuts applied was analysed. To find the connection between the b-quarks and reconstructed b-jets and the parton level leptons and reconstructed leptons, the MC truth was used: the matching was treated as successful if the cone difference, ΔR between b-quark and b-jet was less than 0.4 (in the lepton case $\Delta R < 0.2$). For double b-tagged events, only the b-jets that satisfy

$$m(l, b_{jet}^{(1,2)}) < m_{cr} \quad \text{and} \quad m(l, b_{jet}^{(2,1)}) > m_{cr} \tag{2}$$

were accepted. In the di-lepton case both leptons should fulfill the condition (2). The optimal value for the pairing mass cut, $m_{cr} = 155$ GeV, is a trade-off between the efficiency (ε) and purity (P) of the pairing method. The factor $\varepsilon(2P-1)^2$ was maximised to find the optimum working point. As this criterion requires events with two b-tagged jets and one combination for the lepton and b-jet invariant mass must be below m_{cr} and the other one above m_{cr}, the efficiency of the method is small. On the other hand, this criterion gives a high purity sample as is shown in Section 3.5.1. In the analysis two variants of b-tagged events treatment were considered. In the first one exactly two b-jets were required while in the second one two and more b-jets were allowed (the two with the highest p_T treated as true b-jets). Slightly better results were obtained for the former variant and the results presented here correspond to this case. To suppress the background some additional cuts were tried: W boson mass (M_W) window, top quark mass (m_{top}) window, etc. By using the combined W boson and top quark mass window the background can be reduced by factor more than 10 at the expense of a factor 2 loss in signal. The M_W window requires that at least one pair of non b-tagged jets should have an invariant mass within 10 GeV of the W boson mass. The m_{top} window requires that the reconstructed W boson can be combined with a b-jet (not previously paired with a high-p_T lepton) to give an invariant mass within 40 GeV of the top

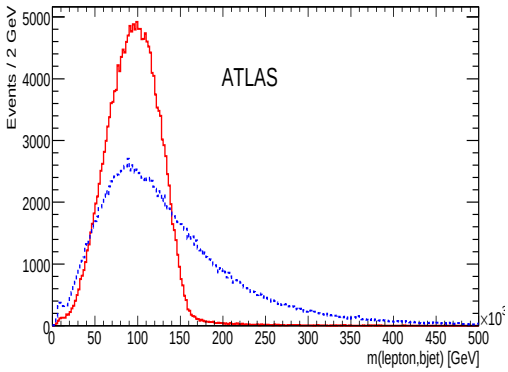

Figure 1: Lepton - b-jet invariant mass spectra for the lepton and b-jet pairs from the same top quark (full line) and from different top quarks (dashed line).

quark mass. This extra mass cut was applied by default in the whole top quark charge analysis using the weighting approach.

3.3 The jet track charge weighting approach

The determination of the average b-jet charge was done using a weighting technique in which the b-jet charge is evaluated as the weighted sum of the b-jet track charges:

$$Q_{\text{bjet}} = \frac{\sum_i q_i |\vec{j}_i \cdot \vec{p}_i|^\kappa}{\sum_i |\vec{j}_i \cdot \vec{p}_i|^\kappa} \tag{3}$$

where $q_i(p_i)$ is the charge (momentum) of the i^{th} track inside the jet and $\vec{j}$ is the b-jet axis unit vector. The κ parameter was optimised for the best separation between b- and $\bar{\text{b}}$-jets and the optimum value was found to be $\kappa = 0.5$. In addition, for the charge weighting technique, it was further required, using only tracks with $p_{\text{T}} > 1.5$ GeV, that at least two tracks must be found within a cone with $\Delta R < 0.4$ with respect to the jet axis. For b-jets with more than seven such tracks, only the seven with the highest p_{T} are used. The parameters of the weighting procedure are the result of a maximisation of the difference between the mean values of the b- and $\bar{\text{b}}$-jet charge distributions - these mean values were found for a set of the parameters values (κ and track p_{T}) and compared. For the procedure optimisation the signal $\text{t}\bar{\text{t}}$-sample was used.

3.4 Semileptonic b-decay approach

In this approach the pairing procedure described in Section 3.2 is also used. But in this case the b quark charge is determined through its semileptonic decay. The sign of the b-jet charge is determined by the lepton charge within the b-jet,

$$\text{b} \to \text{c},\text{u} + \ell^- + \bar{\nu}\,, \qquad \bar{\text{b}} \to \bar{\text{c}},\bar{\text{u}} + \ell^+ + \nu.$$

The lepton from the b-decay will be identified as a non-isolated lepton inside the corresponding b-jet, and its charge (Q_{nonIs}) defines the b quark charge. The non-isolated lepton is searched for among the tracks pointing to the treated b-jet and originating in the corresponding secondary vertex. Several processes can lead to an incorrect b quark charge assignment with this approach. Semileptonic decays of D mesons produced in the B decay chain, and the B^0-$\bar{\text{B}}^0$ mixing are examples of such processes. To

suppress the contribution from D mesons, the non-isolated lepton transverse momentum with respect to the b-jet axis, $p_{\mathrm{T}}^{\mathrm{rel}}$, can be used. The fact that the lepton $p_{\mathrm{T}}^{\mathrm{rel}}$ from b-decays is, on average, higher than from D meson decays can be used to diminish this contamination. The $p_{\mathrm{T}}^{\mathrm{rel}}$ cut was optimised using a sample of ≈ 555000 signal $\mathrm{t\bar{t}}$ events and the value of 1 GeV has been found as the optimum cut. An additional source of wrong b quark charge assignments is mistagging, i.e. light jets incorrectly tagged as b-jets.

The main drawback of this approach is that, from all the selected lepton plus b-jet pairs, only those with a b-jet containing a non-isolated lepton can be used in the analysis. In addition to that, due to difficulties in selecting a pure sample of electrons from within jets, only muons were taken as the non-isolated leptons.

3.5 Results

In both approaches, the Standard Model scenario of top quark production and decay is assumed. The corresponding results are discussed in the following sections.

3.5.1 Weighting technique approach results

As a first step, the efficiency and purity of the lepton b-jet pairing was investigated. Using the events which passed the selection criteria, the obtained pairing efficiency is $\varepsilon = 30.5\%$ and the pairing purity is $P = 85.6\%$. The purity of pairing is defined as $P = N_{\mathrm{good}}/N_{\mathrm{all}}$, where N_{good} (N_{all}) is the number of correctly paired lepton – b-jet pairs (all treated pairs) and the Monte Carlo truth is used to find N_{good}.

The b-jet charge spectra reconstructed using the Monte Carlo truth and invariant mass pairing procedure for the signal $\mathrm{t\bar{t}}$ events are presented in Figure 2, left and right respectively. From Figure 2, the shift of the b-jet charges associated with ℓ^+, $Q_{\mathrm{bjet}}^{(+)}$, and ℓ^-, $Q_{\mathrm{bjet}}^{(-)}$, (or with b and $\bar{\mathrm{b}}$ quark in the Monte Carlo case) is clearly seen. The obtained b-jet charge purity, defined as the percentage of b-jets with the correct charge ($Q_{\mathrm{bjet}}^{(+)} < 0$ and $Q_{\mathrm{bjet}}^{(-)} > 0$), is $P \approx 62\%$. In addition to that, the Q_{comb} b-jet charge spectrum, defined as $Q(\ell) \times Q_{\mathrm{bjet}}^{(\ell)}$, has been reconstructed. The influence of trigger was also investigated, namely the lepton level 1 and level 2 triggers as well as the event filter (EF). The results with and without trigger are summarised in Table 4. No significant impact of the trigger is observed. A small asymmetry in favour of the positive b-jet charge, as was revealed by the analysis, is due to the dominance of positive charge in the initial state (two colliding protons).

Note that the peaks at ± 1 in Fig. 2 correspond to the cases when all the tracks pointing to a b-jet have the same charge sign - in this case the weighting procedure (2) gives $Q_{\mathrm{bjet}} = \pm 1$.

Table 4: The mean b-jet charge associated with positive (Q_+) and negative (Q_-) lepton and combined b-jet charge (Q_{comb}) without (no) and with (yes) EF trigger; two b-tags required.

trigger	Q_+	Q_-	$\mid Q_{\mathrm{comb}} \mid$	Nevent	efficiency
no	-0.092 $\pm$ 0.006	0.103 $\pm$ 0.006	0.097 $\pm$ 0.004	7129	100.0
yes	-0.095 $\pm$ 0.006	0.106 $\pm$ 0.006	0.101 $\pm$ 0.004	6130	86.0

The main background processes for the top quark charge measurement in the semileptonic mode are: $W+$ jets production (the most important background in this mode), QCD multi-jets, di-boson and single top quark production. The single top production is not a genuine background as it gives the same sign of the b-jet charge asymmetry as the signal. For the selection criteria that were used, the ratio of the accepted semileptonic $\mathrm{t\bar{t}}$ events to the accepted single lepton ones is more than 15:1. In the dileptonic

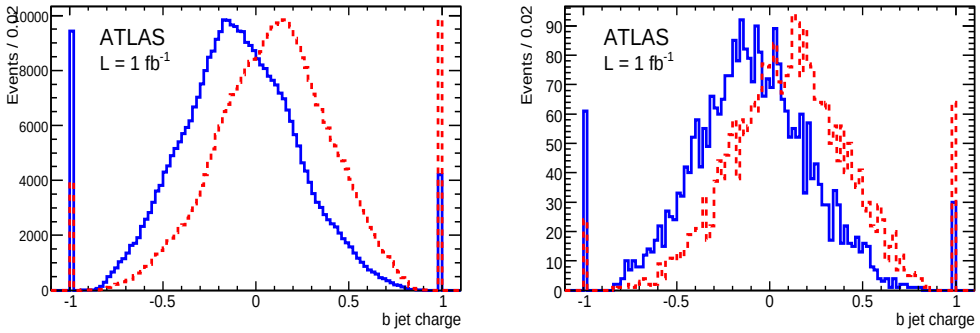

Figure 2: The b-jet charge associated with positive (full line) and negative (dashed line) lepton using the Monte Carlo truth (left) and invariant mass criteria (right) for the ℓb-pairing.

mode, the background is composed of Drell-Yan pairs (the most significant background), multi-jet QCD processes and di-boson production [2].

The background studies for this analysis require large Monte Carlo samples (in addition to the standard cuts the invariant mass criterion is highly restrictive) not available at present. The ideal way to determine the basic background parameters, the S:B ratio and background charge asymmetry, is to use the W+jets (dominant background) samples. However, after applying the selection criteria to the available W+jets samples, only a few events remained (20 lepton b-jet pairs). It is clear that due to poor statistics the samples are not suitable for a valuable background analysis. Nonetheless, combining the b-jet charge spectra, obtained for the individual W+jets channels (W+n$\times$jets and W$b\bar{b}$, W$c\bar{c}$ + n $\times$jets) scaled according to their cross sections to 1 fb, a S:B ratio of $\approx 38 \pm 8$ was obtained. To fix the S:B ratio we need to include other backgrounds and take a regard for the poor statistics. Taking into account only the standard cuts with a loose M_{W} window ($\pm$30 GeV) a value of 7:1 was obtained for the S:B ratio which is compatible with that of the CDF background studies [2]. As a result, a nominal S:B ratio of 30:1 has been assumed, with 7:1 as a very conservative lower limit for studying systematic uncertainties related to the background.

The poor statistics of the available W+jets samples does not enable the background b-jet charge asymmetry to be determined precisely, the obtained value being $\approx -0.02 \pm 0.05$. On the other hand, as it was shown by CDF [2], no marked background asymmetry is expected. For this reason, as a background, we use the signal events but without the pairing of leptons and b-jets. As a consequence the obtained b-jet charge spectrum is not correlated with the high p_{T} lepton charge and should not have any charge asymmetry. Assuming the nominal S:B ratio, the spectrum is normalized to 1/30 of the signal statistics. The analysis showed that this background exhibits practically no asymmetry. For the systematics studies, a background corresponding to S:B=7:1 was also considered.

To find a realistic b-jet charge distribution, the signal and background distributions are combined. In Figure 3 (left) the expected b-jet charge (Q_{comb}) distribution combining the signal with the background (full line) and the background itself (dashed line) are shown. From the reconstructed b-jet charge spectra using the two treated backgrounds, the expected mean b-jet charge (assuming the Standard Model) is:

$$Q_{\mathrm{comb}} = -0.094 \pm 0.0042 \ (\mathrm{stat}).$$

The Q_{comb} value is obtained as the mean value of the signal plus background (S+B) distribution combining signal with the background.

In conclusion, $\approx$ 6000 ℓb combinations could be selected for the top quark b-jet charge analysis, using the 1 fb^{-1} sample. The expected combined b-jet charge purity, $N(Q_{\mathrm{bjet}} < 0)/N_{\mathrm{all}}$, is $\approx 0.62 \pm 0.01$ for the Standard Model case.

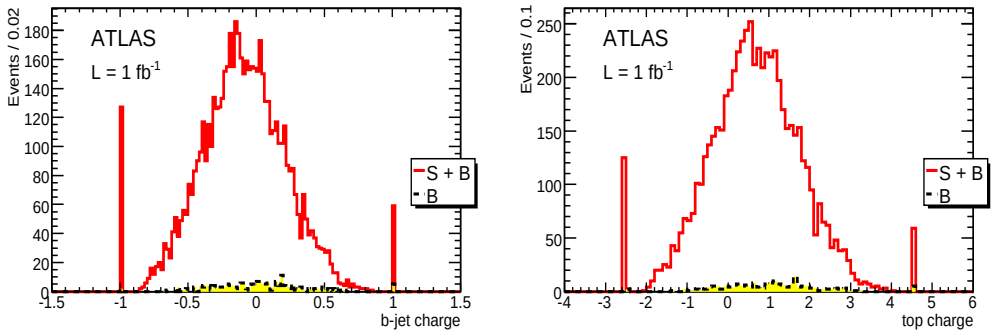

Figure 3: Left: the full S+B b-jet charge (Q_{comb}) distribution (full line) and the background itself (dashed line); right: the reconstructed top quark charge ($Q_{\mathrm{t}}^{\mathrm{comb}}$) (full line) and its background (dashed line).

Taking into account the statistical uncertainty of the obtained mean b-jet charge (Q_{comb}) it can be stated that the obtained value will differ from 0 by more than 20σ. Using a simple statistical treatment it is easy to show that for a reliable determination of Q_{comb} ($\geq 5\sigma$) a sample of ≈ 0.1 fb^{-1} should be sufficient. In addition to that the analysis has revealed that the reconstructed b-jet charge is more influenced by the size of the S:B ratio than by the background asymmetry: going from the pure signal b-jet charge spectrum to that of the 7:1 mixture of signal and background, the mean b-jet charge decreased by 14%, while a replacement of the symmetric background by the asymmetric one with an asymmetry 1/4 of the signal one, leads to only 3% change of the charge at the 7:1 S:B ratio.

The direct reconstruction of the top quark charge can be done relying on the obtained value of Q_{comb} (see above). Using the Standard Model value of the b quark charge ($Q_{\mathrm{b}} = -1/3$) and the mean reconstructed value of the b-jet charge (Q_{comb}), the b-jet charge calibration coefficient $C_{\mathrm{b}} = Q_{\mathrm{b}}/Q_{\mathrm{comb}}$ is 3.54 ± 0.16 and the top quark charge then reads:

$$Q_{\mathrm{t}} = Q(\ell^{+}) + Q_{\mathrm{bjet}}^{(+)} \times C_{\mathrm{b}}\,, \qquad Q_{\bar{\mathrm{t}}} = Q(\ell^{-}) + Q_{\mathrm{bjet}}^{(-)} \times C_{\mathrm{b}} \tag{4}$$

where $Q(\ell^{\pm}) = \pm 1$ is the lepton charge and $Q_{\mathrm{bjet}}^{(\pm)}$ is as above.

The reconstructed top quark charge is shown in Figure 3 (right) for the sample of 1 fb^{-1}. The absolute value of top quark charge obtained by combining Q_{t} and $Q_{\bar{\mathrm{t}}}$ for the above mentioned sample is $Q_{\mathrm{t}}^{\mathrm{comb}} = 0.67 \pm 0.06\,(\mathrm{stat}) \pm 0.08\,(\mathrm{syst})$. The statistical error assumes that the relative error of C_{b} is the same as that of Q_{comb}. The systematic error of $Q_{\mathrm{t}}^{\mathrm{comb}}$ can be studied comprehensively only by using experimental data [2]. In this case the main source of the systematic error is the weighting procedure that influences the coefficient C_{b}, that should be determined independently on the investigated b-jet charge, as well as the mean b-jet charge. In our case only the systematics stemming from determination of the mean b-jet charge were taken into account.

3.5.2 Semileptonic b-decay approach results

The charge of the non-isolated lepton found within the b-jet provides discrimination between the Standard Model and the exotic hypotheses on a statistical basis. Figure 4 shows the number of b-jets, which have been paired with positive (left) and negative (right) high p_{T} lepton and which contain inside a non-isolated lepton, as a function of the charge (Q_{nonIs}) of the contained non-isolated lepton. The mean values

[2] The reconstructed b-jet charge or coefficient C_{b} for an experimental sample, e.g. dijet $\mathrm{b\bar{b}}$ data, should be compared with the corresponding Monte Carlo one to look for a possible difference in the b-jet track topology between Monte Carlo and real data.

of the non-isolated lepton charge obtained from these figures are:

$$\bar{Q}^{(+)}_{\text{nonIs}} = \frac{N(\ell^+) - N(\ell^-)}{N(\ell^+) + N(\ell^-)} = -0.32 \pm 0.05, \quad \bar{Q}^{(-)}_{\text{nonIs}} = \frac{N(\ell^+) - N(\ell^-)}{N(\ell^+) + N(\ell^-)} = 0.30 \pm 0.05,$$

where $\bar{Q}^{(+)}_{\text{nonIs}}$ ($\bar{Q}^{(-)}_{\text{nonIs}}$) is the mean charge of the non-isolated leptons in the b-jets paired with the positive (negative) high p_{T} lepton. $N(\ell^-)$ ($N(\ell^+)$) is the number of b-jets with a negative (positive) charged lepton. The quantity $Q(\ell) \times Q^{(\ell)}_{\text{nonIs}}$, where $Q(\ell)$ is the charge of the lepton paired with the b-jet containing a non-isolated lepton, can be used to combine both histograms. The obtained mean combined charge in the Standard Model is $\bar{Q}^{(\text{comb})}_{\text{nonIs}} = -0.31 \pm 0.04$, showing a potential to distinguish between the Standard model and exotic hypothesis even with 1 fb^{-1} of data, as in the case of the exotic scenario the opposite value of $\bar{Q}^{(\text{comb})}_{\text{nonIs}}$ is expected.

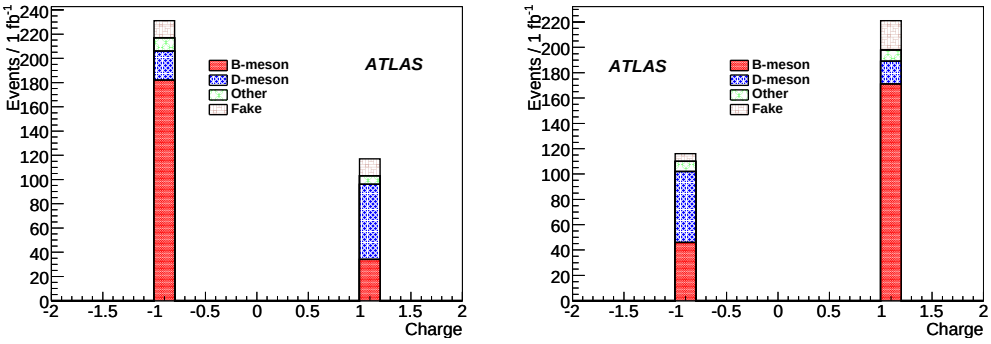

Figure 4: Number of b-jets, containing a non-isolated lepton inside, associated with positive (left) and negative (right) high p_{T} lepton vs the charge of the non-isolated lepton. The contribution of different sources of leptons are marked by different shading styles.

3.6 Systematic uncertainties

The systematic studies have been done following the prescription described in Section 6 of Chapter 1. The resulting systematic errors are summarised in Table 5. The systematic uncertainty caused by the top quark mass was estimated from the absolute difference between the Q_{comb} reconstructed at the nominal value (175 GeV) and m_{t}=160 and 190 GeV and rescaling to an effective 2 GeV uncertainty. The systematic uncertainty connected with the signal to background ratio was found assuming that this ratio is known with 30% uncertainty. The background asymmetry systematics was estimated assuming that the background charge spectrum asymmetry is at a level of 10% of the signal one.

The systematic uncertainties due to Monte Carlo modeling of $\text{t}\bar{\text{t}}$ signal were studied by comparing samples with different fragmentation parameters: an AcerMC/Pythia sample and the standard signal MC@NLO/Herwig one, giving values of 18 $\pm$ 13% and 16 $\pm$ 13% for the weighting and semileptonic approaches, respectively. The large uncertainties are due to a limited Monte Carlo statistics, so these values cannot be considered as a reliable estimate of the corresponding systematic uncertainties and are therefore not included in Table 5.

Pileup background affects the weighting technique procedure, as tracks from additional minimum-bias interactions get included in the jet charges. The associated systematic uncertainty was evaluated by comparing the standard sample to a dedicated $\text{t}\bar{\text{t}}$ sample including pileup, leading to a shift of 20$\pm$18%. Since the Monte Carlo statistical error is large, and it is expected that any pileup effect can be minimised

(at least at moderate LHC luminosities) by applying track impact parameter cuts to eliminate tracks from pileup vertices, this value is also not included Table 5.

Table 5: The systematic uncertainties (%) of the mean reconstructed charge, Q_{comb}, the weighting technique and b-decay approaches.

Source	Weighting (%)	b-decay (%)
jet scale	0.7	0.3
b-jet scale	1.9	6
Δm_{t}	1.3	7
PDF	0.6	–
ISR	2.8	15
FSR	7.8	8
Pile-up	–	1.8
Background asymmetry	1	–
S/B ratio	9	–
total	12.5	19.3

4 Polarization studies in $\mathrm{t\bar{t}}$ semileptonic events

The measurements of the W-boson and top quark polarizations in $\mathrm{t\bar{t}}$ events provide a powerful test of the top quark production and decay mechanisms and are a sensitive probe of new physics. W-boson or top quark spin information can be inferred from the angular distributions of the daughter particles in the W-boson or top quark rest frame, respectively. The W-boson can be produced with right, left or longitudinal polarizations, with corresponding partial widths Γ_{R}, Γ_{L}, Γ_0 that depend on new anomalous couplings [61] (V_{R}, V_{L}, g_{L} and g_{R}) which can appear at the Wtb vertex (see Eq. 1).

4.1 W-boson polarization and $\mathrm{t\bar{t}}$ spin correlation measurements

The probability for the three helicity states of W-boson produced in top quark decay, F_0 (longitudinal), F_{L} (left-handed) and F_{R} (right-handed), can be extracted from the Ψ angular distribution [61] :

$$\frac{1}{N}\frac{dN}{d\cos\Psi} = \frac{3}{2}\left[F_0\left(\frac{\sin\Psi}{\sqrt{2}}\right)^2 + F_{\mathrm{L}}\left(\frac{1-\cos\Psi}{2}\right)^2 + F_{\mathrm{R}}\left(\frac{1+\cos\Psi}{2}\right)^2\right], \tag{5}$$

where Ψ is the angle between the W-boson direction in the top quark rest frame and the charged lepton direction in the W-boson rest frame obtained by a boost along the W-boson flying direction in the top quark rest frame. The correlation between the parameter couples (F_0,F_{L}), (F_0,F_{R}) and (F_{L},F_{R}) are -0.9, -0.8 and 0.4, respectively.

Although, in the Standard Model, top quarks are produced unpolarised in $\mathrm{t\bar{t}}$ events, their spins are correlated [62]. The production asymmetry A in these events, measures the spin correlation and is defined as

$$A = \frac{\sigma(t_\uparrow\bar{t}_\uparrow) + \sigma(t_\downarrow\bar{t}_\downarrow) - \sigma(t_\uparrow\bar{t}_\downarrow) - \sigma(t_\downarrow\bar{t}_\uparrow)}{\sigma(t_\uparrow\bar{t}_\uparrow) + \sigma(t_\downarrow\bar{t}_\downarrow) + \sigma(t_\uparrow\bar{t}_\downarrow) + \sigma(t_\downarrow\bar{t}_\uparrow)}, \tag{6}$$

where $\sigma(t_{\uparrow/\downarrow}\bar{t}_{\uparrow/\downarrow})$ denotes the production cross-section of a top quark pair with spins up or down with respect to a selected quantisation axis. It can be extracted from the θ_1 and θ_2 angular distributions [62]:

$$\frac{1}{N}\frac{d^2N}{d\cos\theta_1 d\cos\theta_2} = \frac{1}{4}(1 - A|\alpha_1\alpha_2|\cos\theta_1\cos\theta_2), \tag{7}$$

where θ_1 (θ_2) is the angle between the t ($\bar{t}$) direction, measured in the $t\bar{t}$ rest frame, and the direction of the t ($\bar{t}$) decay product in the t ($\bar{t}$) rest frame obtained by a boost along t ($\bar{t}$) direction in the $t\bar{t}$ rest frame, α_i is the spin analysing power of the top quark decay product i, which ranges between -1 and 1 and measures the degree to which its direction is correlated with the spin of the parent top quark. The parameter A_D defined in [20], used to measure the production asymmetry in another basis, is extracted from the Φ angular distribution [62] :

$$\frac{1}{N}\frac{dN}{d\cos\Phi} = \frac{1}{2}(1 - A_D|\alpha_1\alpha_2|\cos\Phi), \tag{8}$$

where Φ is the angle between the direction of flight of the two spin analysers, defined in the t and $\bar{t}$ rest frames respectively.

Table 6: Standard Model values of W-boson polarization parameters(F_0, F_L, F_R) at the next-to-leading order and $t\bar{t}$ spin correlation parameters (A, A_D) at leading order for a top quark mass of 175 GeV. For A and A_D the asterisk superscript means that $m_{t\bar{t}} < 550$ GeV is applied.

F_0	F_L	F_R	A*	A_D*
0.695	0.304	0.001	0.422	-0.290

The Standard Model predictions for the W-boson polarization (F_0, F_L, F_R), at next-to-leading order, and $t\bar{t}$ spin correlation (A, A_D), at leading order, are given in Table 6. The ATLAS sensitivity to these observables has been evaluated with an ATLFAST simulation [20] and a full simulation of a perfect detector [63]. A precision of 1% to 5% should be achievable with 10 fb^{-1} of data, dominated by systematic uncertainties (in particular from the b-jet energy scale). This measurement requires a complete reconstruction of the $t\bar{t}$ system and a reliable Monte Carlo description to correct the distortion induced by trigger, cuts and reconstruction. In this section the robustness of the analysis with a realistic detector simulation including triggering is assessed. Only the semileptonic topology of the $t\bar{t}$ events ($t\bar{t} \to WWb\bar{b} \to \ell\nu j_1 j_2 b\bar{b}$ with $\ell = e, \mu$) is used as signal (an analysis using $t\bar{t}$ dilepton events as signal can improve the results of this study, especially for the $t\bar{t}$ spin correlation measurements). In this case the most powerful spin analysers of the top quark are the charged lepton ($\alpha_1 = 1$) and the least energetic non b-jet in the top quark rest frame ($\alpha_{jet} = 0.51$) [64], which are chosen afterwards for the spin correlation measurement.

4.1.1 Event simulation and selection

The largest statistics Monte Carlo sample was generated with MC@NLO which does not implement $t\bar{t}$ spin corelations, so it can only be used to study W-boson polarisation. Spin correlations were studied using the smaller AcerMC sample. In both cases, non-semileptonic $t\bar{t}$, semileptonic $t\bar{t}$ which decay to τ, W-boson+jets and single top quark events were considered as background. Semileptonic signal events are characterised by one (and only one) isolated lepton, at least 4 jets, of which at least 2 jets are tagged as b-jets, and missing transverse energy. Following the common criteria for the semileptonic selection, all kinematic cuts are summarised in Table 7 together with the corresponding signal efficiencies.

After kinematic cuts are applied, the event is fully reconstructed, as described below. The angles Ψ, θ_1, θ_2 and Φ are computed and the polarization parameters are extracted.

Table 7: Selection cuts used and corresponding efficiencies for semileptonic $t\bar{t}$ MC@NLO events and $t\bar{t}$ AcerMC events.

Variables	Cuts	Efficiency (%)	
		MC@NLO	AcerMC
Lepton	exactly 1 identified	57.8	58.7
Jets	at least 4 selected jets	59.3	62.1
b-tagging	at least 2 are tagged as b	32.0	31.0
Missing energy	$p_T^{miss} > 20$ GeV	92.0	92.2
Cumulative efficiency		9.4	9.8

4.1.2 W-boson and top quark reconstruction

The energies of all jets are calibrated according to the comparison with the energies of corresponding parton level quarks before selection and reconstruction. Then, in the event reconstruction, the light jet pair with invariant mass m_{jj} closest to the known W-boson mass, m_W, is selected to reconstruct the W-boson which decays hadronically. This W-boson is then combined with one of the b-jets to reconstruct the top quark. As there are several possible combinations, the one which gives the mass closest to the top quark mass m_t is assumed to be the correct one. The b-jet which is closest to the lepton in ΔR among the remaining b-jets, is reserved for reconstructing the other top quark whose daughter W-boson decays leptonically. To reconstruct the W-boson which decays leptonically, the neutrino p_T is taken as the missing transverse energy. Its longitudinal component p_z is determined by constraining $m_{l\nu}$ to m_W [63]. When two solutions for p_z are found, the one giving $m_{\ell\nu b}$ closer to m_t is kept.

Quality cuts $|m_{jjb} - m_t| < 35$ GeV, $|m_{\ell\nu b} - m_t| < 35$ GeV and $|m_{jj} - m_W| < 20$ GeV are applied to reject badly reconstructed events. At this stage, 2.8% of the signal events are kept for MC@NLO events and 2.7% for AcerMC events, corresponding to 7000 signal events for 1 fb^{-1} of data (Table 8). After this event selection, the main background comes from the $t\bar{t} \to \tau + X$ events, where the tau decays to electron or muon. The number of events from W-boson+jets and single top quark channels is less than 3% of the selected number of signal events, so we neglect them in the following sections. Due to this cancellation of the background, the S/B ratio can be affected as much as 20%, which is taken as a systematic uncertainty (see Table 10).

After event reconstruction, the angle Ψ (W-boson polarization) as well as the angles θ_1, θ_2 and Φ ($t\bar{t}$ spin correlations) are computed using the prescription descibed at the beginning of Section 4. The measured distributions of $\cos\Psi$, $\cos\theta_1 \times \cos\theta_2$ and $\cos\Phi$ are distorted, compared with their distributions at parton level. The detector resolution results in much smaller smearing effect on the final particles than that coming from particle radiation, quark fragmentation-hadronization and final event reconstruction. That is to say, the latter effects dominate the resolution of the reconstructed objects from top quark decay [65]. A correction function, taken from the ATLFAST simulation, is used to recover the distributions at parton level. With ATLFAST data, the correction function is obtained from the ratio between the two normalized distributions of the $\cos\Psi$ (i.e. after reconstruction of the signal and main background events and at parton level of the pure signal). To correct for the distortion, a weight derived from this function is applied on all the reconstructed $\cos\Psi$ of full simulation, on an event by event basis, allowing to recover, as much as possible, the shape of the distribution of the $\cos\Psi$ of the pure signal at parton level. A detailed description of the method can be found in [20].

Table 8: The number of signal (MC@NLO) and the most important background events before (left) and after (right) selection for 1 fb^{-1}. $*$: in the single top quark decay W$\rightarrow$ e/$\mu/\tau+\nu$ mode

	Events for 1 fb^{-1}($\times 10^3$)	Selected events full simulation
Signal ($t\bar{t}$ semileptonic)	250	7000
$t\bar{t} \rightarrow \tau + X$	130	710
$W(\rightarrow l\nu)$+ jets	800	[10,55]
Single t (Wt channel)	25*	90
Single t (t channel)	80*	55

4.1.3 Impact of the trigger on the analysis

Semileptonic $t\bar{t}$ events are characterised by a single isolated lepton, which can be used to trigger the events with high efficiency. Applying the trigger selection to events passing the standard selection cuts, 15% of well reconstructed events are lost. The measurement results with and without trigger applied on the data, while keeping all other aspects of the measurement unchanged, were compared. The effect of the trigger on the measurements of the W-boson polarization is almost zero But the effect on the $t\bar{t}$ spin correlations is not negligible, and is taken as a systematic error, shown in Table 10.

4.1.4 Measurement of the W-boson polarization

Figure 5 shows the correction function (left) and the reconstructed cosΨ distribution (right) after applying the correction function. This distribution is fitted to Eq. (5) varying F_0, F_L and F_R, but constrained by $F_0 + F_L + F_R = 1$. The fit is restricted to the region $-0.9 < \cos\Psi < 0.8$, which is the most extended region where the correction is varying slowly. The results are shown in Table 9.

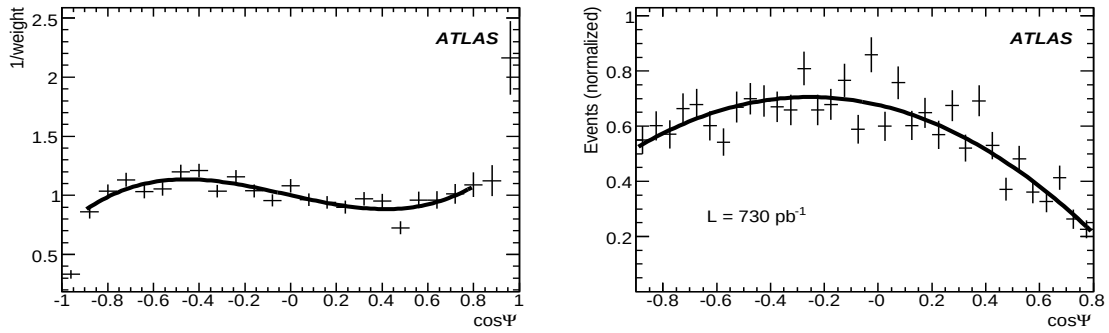

Figure 5: Left: Correction function taken from ATLFAST simulation fitted with a third order polynomial function. Right: Normalised reconstructed and corrected distribution of cosΨ, the full line corresponds to the fit to Eq. (5). The sample has an integrated luminosity of 730 pb^{-1}.

Two complementary methods to extract the W-boson helicity fractions, using the observed angular distribution between the charged lepton direction in the W-boson rest frame and the W-boson direction in the top quark rest frame, are currently under development at ATLAS inspired on Tevatron methods [5,66].

4.1.5 Measurement of $t\bar{t}$ spin correlation

At parton level, before any phase space cut, the two estimators $C = -9 \times \cos\theta_1 \cos\theta_2$ and $D = -3 \times \cos\Phi$ are unbiased [20]. Figure 6 shows the reconstructed distributions of $-9 \times \cos\theta_1 \cos\theta_2/0.51$ and $-3 \times \cos\Phi/0.51$ after correction. It should be stressed that, in the evaluation of the $t\bar{t}$ spin correlation parameters, the theoretical value for the spin analyzing power for signal events (0.51) was assumed for both cases. The means of the distributions are unbiased estimators of A and A_D, provided corrections for

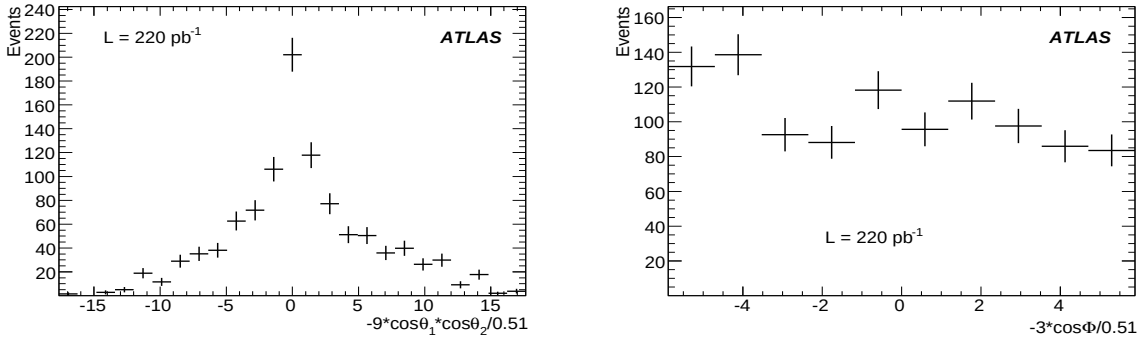

Figure 6: Left: Reconstructed and corrected distribution of $-9 \times \cos\theta_1 \cos\theta_2/0.51$. Right: Reconstructed and corrected distribution of $-3 \times \cos\Phi/0.51$. The integrated luminosity of the sample is 220 pb^{-1} in each case.

physics effects and detector effects are fully carried out.

Due to the fact that the ATLFAST was used to extract the correction function, an additional systematic uncertainty of 0.25 was derived for the A spin correlation parameter. This uncertainty reflects the different parametrizations of the Monte Carlo simulations. Preliminary studies suggest that this shift can be removed by using high statistics full simulation samples to derive the correction functions and for this reason this uncertainty was not included in Table 10.

Table 9: W-boson polarization and top quark spin correlation parameters extracted after triggering. The indicated errors are statistical and systematic, respectively.

W-boson polarization	F_L	F_0	F_R
	0.29 $\pm$0.02 $\pm$0.03	0.70 $\pm$0.04 $\pm$0.02	0.01 $\pm$0.02 $\pm$0.02
$t\bar{t}$ spin correlation	A	A_D	
	0.67 $\pm$0.17$\pm$0.18 $\pm$0.25	-0.40 $\pm$0.11 $\pm$0.09	

4.1.6 Systematic uncertainties

The systematic uncertainties were estimated with ATLFAST simulation for the factorisation scale, structure function, ISR, FSR, b-fragmentation, top quark mass, hadronization scheme and pile-up effects, and with full simulation for the b-tagging efficiency, b-jet energy scale, light jet energy scale and signal to background ratio (S/B scale) as listed in Table 10, for the measurement of the W-boson helicity fractions and top quark pair spin correlations respectively.

With data, $t\bar{t}$ events can be reconstructed without requiring b-jet tagging on the side of top quark whose daughter W-boson decays leptonically. This can provide a pure sample of b-jets which can be

Table 10: Systematics for W-boson polarization and top quark spin correlation measurement.

Source of uncertainty	F_L	F_0	F_R	A	A_D
Factorisation	0.000	0.001	0.001	0.029	0.006
Structure function	0.003	0.003	0.004	0.033	0.012
ISR	0.001	0.002	0.001	0.002	0.001
FSR	0.009	0.007	0.002	0.023	0.016
b-fragmentation	0.001	0.002	0.001	0.031	0.018
Hadronization scheme	0.010	0.016	0.006	0.006	0.008
Pile-up (2.3 events)	0.005	0.002	0.006	0.001	0.005
Input top quark mass (2 GeV)	0.015	0.011	0.004	0.028	0.013
b-tagging efficiency (5%)	0.007	0.002	0.005	0.027	0.07
b-jet energy scale (5%)	0.02	0.002	0.02	0.07	0.015
light-jet energy scale (5%)	-	-	-	0.11	0.017
S/B scale (20%)	0.004	0.002	0.001	0.000	0.004
Trigger	-	-	-	0.10	0.03
TOTAL	0.03	0.02	0.02	0.18	0.09

used to check the uncertainty on the b-tagging efficiency [67]. The b-jet energy miscalibration can also be obtained from other control samples, such as Z+b-jet events [68].

4.2 Anomalous couplings at the Wtb vertex

The W-boson polarisation is sensitive to new anomalous couplings (V_L, V_R, g_L and g_R) associated with the Wtb vertex. Although the W-boson helicity fractions (F_0, F_L and F_R) depend on these couplings, the helicity ratios $\rho_{R,L} \equiv \Gamma_{R,L}/\Gamma_0 = F_{R,L}/F_0$, were found to be more sensitive to V_L, V_R, g_L and g_R. The ρ_R and ρ_L observables are independent quantities and take the LO values $\rho_R = 5.1 \times 10^{-4}$, $\rho_L = 0.423$ in the Standard Model. General expressions for $\rho_{R,L}$ in terms of the new anomalous couplings can be found in Ref. [19]. As for the helicity fractions, the measurement of helicity ratios sets bounds on V_R, g_L and g_R. A third and simpler method to extract information about the Wtb vertex is through angular asymmetries involving the angle of the charged lepton in the W-boson rest frame and the W-boson direction in the top quark rest frame (introduced in the previous section). For any fixed z in the interval $[-1,+1]$, one can define asymmetries as the difference between the number of events above and below z, normalised to the total number of events. The most obvious choice is $z = 0$, giving the forward-backward asymmetry A_{FB} [18, 69]. The forward-backward asymmetry is related to the W-boson helicity fractions by $A_{FB} = \frac{3}{4}[F_R - F_L]$. Other convenient choices are $z = \mp(2^{2/3} - 1)$. Defining $\beta = 2^{1/3} - 1$, we have $A_+ = 3\beta[F_0 + (1+\beta)F_R]$ and $A_- = -3\beta[F_0 + (1+\beta)F_L]$. Thus, A_+ (A_-) only depend on F_0 and F_R (F_L). The LO Standard Model values of these asymmetries are $A_{FB} = -0.223$, $A_+ = 0.548$, $A_- = -0.840$. They are sensitive to anomalous Wtb interactions, and their measurement allows to probe this vertex without the need of a fit to the distribution of the angle between the charged lepton direction in the W-boson rest frame and the W-boson direction in the top quark rest frame. In the present analysis the ATLAS sensitivity to the ρ_L, ρ_R, A_{FB}, A_+ and A_- observables is studied.

4.2.1 Event selection

In this section an alternative two-level likelihood analysis is explored for the semileptonic channel, i.e. $t\bar{t} \to W^+bW^-\bar{b}$ where one of the W-bosons decays hadronicaly and the other one decays in the leptonic

channel $W \to \ell\nu_\ell$ (with $\ell = e, \mu$). Any other process constitutes a background to this signal. In particular, it should be noticed that the fully hadronic, dileptonic and semileptonic (with one of the W-bosons decaying into $\tau\nu$) $t\bar{t}$ channels are considered backgrounds to the present analysis. Additionally, the following Standard Model processes were considered as background: single top production, W+jets, $Wb\bar{b}$+jets, $Wc\bar{c}$+jets, $Z \to e^+e^-$, $Z \to \mu^+\mu^-$, $Z \to \tau^+\tau^-$, WW, ZZ and WZ. The likelihood analysis is based on the construction of a discriminant variable which uses distributions of some kinematical properties of the events. In the first analysis level (called the pre-selection), the common selection criteria for the semileptonic topology, with the exception of the b-tagging requirement on jets, was applied to the event. The full event reconstruction was performed using a χ^2, defined by

$$\chi^2 = \frac{(m_{\ell\nu j_a} - m_t)^2}{\sigma_t^2} + \frac{(m_{j_b j_c j_d} - m_t)^2}{\sigma_t^2} + \frac{(m_{\ell\nu} - m_W)^2}{\sigma_W^2} + \frac{(m_{j_c j_d} - m_W)^2}{\sigma_W^2}\,, \tag{9}$$

where $m_t = 175$ GeV, $m_W = 80.4$ GeV, $\sigma_t = 14$ GeV and $\sigma_W = 10$ GeV are the expected top quark and W-boson mass resolutions[3], ℓ represents the selected electron or muon, $m_{\ell\nu}$ is the invariant mass of the electron (muon) and the neutrino, and $j_{a,b,c,d}$ corresponds to all the possible combinations among the four jets with highest p_T (with $m_{\ell\nu j_a}$, $m_{j_b j_c j_d}$ and $m_{j_c j_d}$ being the corresponding invariant masses). The neutrino was reconstructed using the missing transverse energy and allowing the p_z^ν to vary in the range $[-500, +500]$ GeV. The solution corresponding to the minimum χ^2 was chosen. The jets used to reconstruct the hadronic W-boson will be labelled "non-b" jets and the remaining two are labelled "b-jets". It should be stressed that no b-tagging information was used so far. The pre-selection was completed by requiring $\chi^2 < 16$. In the second level (the final selection), signal and background-like probabilities were constructed for each event ($\mathscr{P}_i^{\text{signal}}$ and $\mathscr{P}_i^{\text{back.}}$, respectively) using probability density functions (p.d.f.) built from relevant physical variables: the cosine of the angle between the leptonic top quark and the leptonic "b-jet", the transverse momentum of the hadronic W, the hadronic and leptonic top quark masses, the transverse momentum of the two "b-jets", the transverse momentum of the lepton and the $\sqrt{\chi^2}$ distribution. It should be stressed that the objective is to test the sensitivity for new physics exclusion, under the hypothesis that the Standard Model holds, and the simulation was done assuming no anomalous couplings. Signal ($\mathscr{L}_S = \Pi_{i=1}^n \mathscr{P}_i^{signal}$) and background ($\mathscr{L}_B = \Pi_{i=1}^n \mathscr{P}_i^{back.}$) likelihoods (with $n = 8$, the number of p.d.f.) are used to define a discriminant variable $L_R = \log_{10}(\mathscr{L}_S/\mathscr{L}_B)$. The distribution of this variable is shown in Figure 7(a). The final event selection is done by applying the cut $L_R > 0.1$ on the discriminant variable. The number of signal and background events (normalised to $L = 1$ fb^{-1}) after the pre-selection and final selection are shown in Table 11. After the final selection (including the trigger), the dominant backgrounds are W+jets and semileptonic $t\bar{t}$ with taus in the final state (corresponding to 49%, and 29% of the total background, respectively, as shown in Table 12).

The effect of the single lepton trigger on the event selection was studied. The results are summarised in Table 11. In what follows, only events passing the trigger are considered.

Once b-tagging is well understood, additional information can be used. In this case only jets with a positive b-tagging weight were considered as "b-jet" candidates for the χ^2 minimisation method. In addition, the b-tagging weights of these jets were considered as p.d.f.s for the discriminant variable evaluation. In this case, the number of selected signal and background events for $L = 1$ fb^{-1} is expected to be $(6.6 \pm 0.1) \times 10^3$ and $(0.9 \pm 0.1) \times 10^3$, respectively. The $t\bar{t}$ background is expected to be dominant (72% of the total background, mainly due to the semileptonic channel with taus in the final state) and the W+jets and single top processes correspond to 15% and 13% of the total background, respectively. The discriminant variables corresponding to the analysis with and without b-tagging are shown in Figure 7.

[3]These resolutions are taken from the top quark mass measurement analyses [70]. It should be noticed that σ_t and σ_W can be interpreted as weights for each term of the χ^2 definition. By changing their values by a factor ~ 2, the obtained observables (ρ_L, ρ_R,A_+ and A_-) are the same within the statistical error.

Table 11: Number of signal $t\bar{t} \to \ell\nu b\bar{b}q\bar{q}'$ and background events (and corresponding statistical error), normalised to $L = 1$ fb^{-1}, after the pre-selection and final selection for the analysis without b-tagging. The effect of the trigger on the event selection is also shown.

		$e+\mu$ sample	e sample	μ sample
Total background	presel.	$(15.8 \pm 0.4) \times 10^3$	$(7.2 \pm 0.3) \times 10^3$	$(8.6 \pm 0.3) \times 10^3$
	final sel.	$(5.2 \pm 0.2) \times 10^3$	$(2.5 \pm 0.2) \times 10^3$	$(2.8 \pm 0.2) \times 10^3$
	trigger	$(4.0 \pm 0.2) \times 10^3$	$(1.8 \pm 0.2) \times 10^3$	$(2.1 \pm 0.2) \times 10^3$
Signal	presel.	$(27.4 \pm 0.2) \times 10^3$	$(12.0 \pm 0.1) \times 10^3$	$(15.5 \pm 0.1) \times 10^3$
	final sel.	$(15.2 \pm 0.1) \times 10^3$	$(6.5 \pm 0.1) \times 10^3$	$(8.8 \pm 0.1) \times 10^3$
	trigger	$(12.6 \pm 0.1) \times 10^3$	$(5.8 \pm 0.1) \times 10^3$	$(6.9 \pm 0.1) \times 10^3$

Table 12: Background composition and corresponding statistical error, normalised to $L = 1$ fb^{-1}, after the final selection, including the effect of the trigger, for the analysis without b-tagging.

	$e+\mu$ sample	e sample	μ sample
W+jets, Wb$\bar{\text{b}}$+jets, Wc$\bar{\text{c}}$+jets	$(19.6 \pm 1.9) \times 10^2$	$(8.8 \pm 1.4) \times 10^2$	$(10.3 \pm 1.4) \times 10^2$
Z+jets	$(1.6 \pm 0.4) \times 10^2$	$(1.2 \pm 0.4) \times 10^2$	$(0.5 \pm 0.3) \times 10^2$
WZ, ZZ, WW	$(0.4 \pm 0.2) \times 10^2$	$(0.3 \pm 0.1) \times 10^2$	$(0.2 \pm 0.1) \times 10^2$
$t\bar{t}$ (except signal)	$(13.1 \pm 0.6) \times 10^2$	$(5.4 \pm 0.3) \times 10^2$	$(7.9 \pm 0.4) \times 10^2$
single top	$(5.3 \pm 0.3) \times 10^2$	$(2.5 \pm 0.2) \times 10^2$	$(2.7 \pm 0.2) \times 10^2$

4.2.2 Measurement of the angular distribution and asymmetries

The experimentally observed angular distribution, which includes the $t\bar{t}$ signal as well as the Standard Model background, is affected by detector resolution, $t\bar{t}$ reconstruction and selection criteria [71]. In order to recover the Standard Model distribution, it is necessary to subtract the background and correct for the effects of the detector, event selection and reconstruction. For this purpose, two different sets of signal and background event samples were used: one "experimental" set, which simulates a possible experimental result, and one "reference" set, which is used to parametrise the effects mentioned, and correct the previous sample. The procedure is as follows. After subtracting reference background samples, the full "experimental" distribution is multiplied by a correction function f_c in order to recover the Standard Model one. This correction function is determined by assuming that the charged lepton distribution corresponds to the Standard Model. In case that a deviation from Standard Model predictions (corresponding to anomalous couplings) is found, the correction function must be modified accordingly, and the expected distribution recalculated in an iterative process. These issues have been analysed in detail in Ref. [20], where it was shown that this process quickly converges. The correction function is calculated, for each bin of the angular distribution, by dividing the number of generated events by the number of selected events, using the reference sample. In order to avoid non-physical fluctuations due to the limited amount of Monte Carlo statistics, a smoothing procedure was applied to the obtained correction function. The value of f_c is in the range [0.2,1.4]. Other methods of correcting the angular distribution are under investigation.

The procedure of correcting for detector and reconstruction effects in the asymmetries is similar to that used with the full angular distribution, but using only two or three bins. This has the advantage that the asymmetry measurements are less sensitive to the extreme values of the angular distributions,

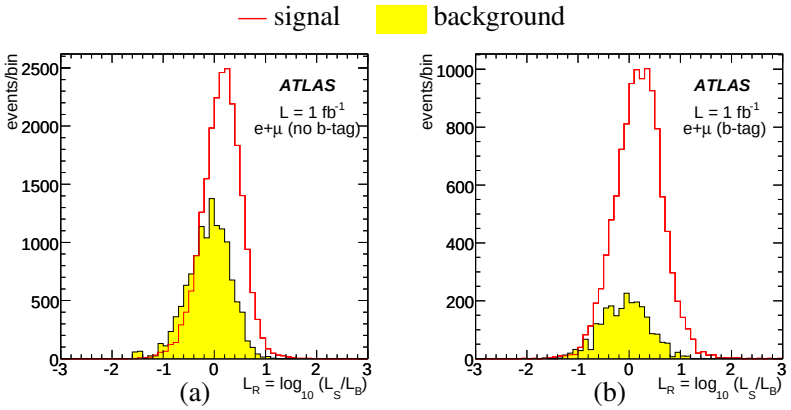

Figure 7: Discriminant variables for the Standard Model background (shaded region) and the $t\bar{t}$ signal (full line), normalised to $L = 1$ fb^{-1} corresponding to the (a) analysis without b-tagging and (b) analysis using the b-tagging weights of the "b-jets" selected by the χ^2 minimisation method.

where correction functions deviate from unity. Moreover, it should be noticed that the extreme bins of the angular distribution have a very significant impact on the measurement of the ρ_{L} and ρ_{R} helicity ratios. The values obtained from a fit to the corrected distribution, as well as the angular asymmetries $A_{\mathrm{FB}}, A_{\pm}$, are collected in Table 13, with their statistical uncertainties. Although the statistical errors of the observables obtained for the analyses without and with b-tagging are similar, the use of this tool allows to improve the signal to background ratio, leading to smaller systematic uncertainties, as discussed below.

Table 13: Expected values and corresponding statistical errors for the helicity ratios and angular asymmetries. The results for an integrated luminosity of 1 fb^{-1} (analyses with and without b-tagging) are shown.

	ρ_{L}	ρ_{R}	A_{FB}	A_{+}	A_{-}
Analysis without b-tagging					
$e+\mu$	0.402 ± 0.050	-0.008 ± 0.008	-0.220 ± 0.025	0.560 ± 0.024	-0.845 ± 0.012
Analysis with b-tagging					
$e+\mu$	0.453 ± 0.048	-0.004 ± 0.007	-0.229 ± 0.026	0.542 ± 0.028	-0.830 ± 0.014

4.2.3 Systematic uncertainties

The study of the systematic uncertainties considered possible errors from different sources: jet energy scale, luminosity, top quark mass, background level, ISR and FSR, Monte Carlo generator and pile-up. The jet calibration used in the present analyses is described in Ref. [70]. As for the reference analyses, full simulation Monte Carlo samples were used for the study of all the systematic sources of uncertainty. Only the simulated sample used as the "experimental" set (which fakes the data) was changed for each systematic source of uncertainty. The correction function and the Monte Carlo sample used to perform the background subtraction were kept unchanged. The impact on the measurements is summarised in Tables 14 and 15. As the background subtraction is based on Monte Carlo simulation, the background estimation required a luminosity value and therefore the corresponding systematic uncertainty was considered. Once the cross-sections for known backgrounds are measured with data, a data-driven normali-

sation will be possible and the luminosity systematic error should be reduced. Moreover, with data it will be possible to compare the discriminant variable distributions for selected events obtained from data and Monte Carlo. This comparison will allow the correction of systematic uncertainties caused by inaccurate description of data by the Monte Carlo simulation.

Table 14: Sources of systematic uncertainties in the determination of the helicity ratios and angular asymmetries (analysis without b-tagging).

Source	ρ_L	ρ_R	A_{FB}	A_+	A_-
Jet energy scale	0.02	0.003	0.004	0.006	0.002
Luminosity	0.02	0.002	0.006	0.005	0.001
Top quark mass	0.02	0.002	0.009	0.006	0.004
Background	0.01	0.002	0.005	0.003	0.002
ISR+FSR	0.13	0.009	0.044	0.046	0.011
MC generator	0.18	0.013	0.039	0.042	0.001
Pile-up	0.14	0.004	0.053	0.039	0.017
Total	0.27	0.017	0.080	0.074	0.021

Table 15: Sources of systematic uncertainties in the determination of the helicity ratios and angular asymmetries (analysis with b-tagging).

Source	ρ_L	ρ_R	A_{FB}	A_+	A_-
Jet energy scale	0.04	0.001	0.010	0.004	0.002
Luminosity	0.01	0.000	0.006	0.005	0.001
Top quark mass	0.03	0.003	0.013	0.008	0.006
Background	0.01	0.000	0.003	0.002	0.004
ISR+FSR	0.05	0.006	0.024	0.028	0.015
MC generator	0.01	0.008	0.009	0.011	0.000
Pile-up	0.15	0.006	0.012	0.041	0.022
Total	0.16	0.012	0.033	0.052	0.027

4.2.4 Constraints on the anomalous couplings

Using the parametric dependence of the observables on V_R, g_L and g_R (and considering the correlations between them, which are shown in Table 16), constraints can be set on the anomalous couplings. The helicity ratios $\rho_{R,L}$ and the asymmetries $A_\pm$ were used as input for the program `TopFit` [19]. The expected 68% CL allowed regions on the Wtb anomalous couplings for $L = 1$ fb^{-1} (analyses with and without b-tagging) are shown in Figure 8. In addition to the allowed regions of Figure 8, additional solutions can be found at $g_R \sim 0.8$. Such solutions are due to a large cancellation between $\mathcal{O}(g_R)$ and $\mathcal{O}({g_R}^2)$ terms and can be excluded by the measurement at the LHC of the single top cross-section [72].

Table 16: Correlation matrix for the $A_{\pm}$, $\rho_{R,L}$ observables.

	A_+	A_-	ρ_L	ρ_R
A_+	1	0.16	-0.73	-0.14
A_-	0.16	1	-0.10	0.55
ρ_L	-0.73	-0.10	1	0.42
ρ_R	-0.14	0.55	0.42	1

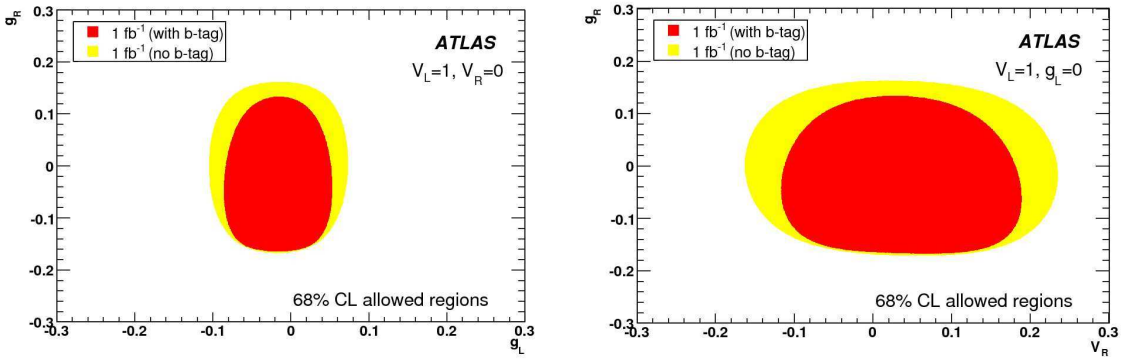

Figure 8: Expected 68% CL allowed regions on the Wtb anomalous couplings for luminosities of 1 fb^{-1} (with and without b-tagging), obtained from the $\rho_{R,L}$ and $A_{\pm}$ observables using `TopFit`.

5 Rare Top Quark Decays and FCNC

This section discusses the study of rare top quark decays via FCNC ($t \to qX, X = \gamma, Z, g$) using $t\bar{t}$ events produced at the LHC. These decays are strongly suppressed in the Standard Model at tree level due to the GIM mechanism. In the effective Lagrangian approach [73, 74] the new top quark decay rates to the gauge bosons can be expressed in terms of the κ^g_{tq}, κ^γ_{tq}, $(|v^Z_{tq}|^2 + |a^Z_{tq}|^2)$ and κ^Z_{tq} anomalous couplings to the g, γ and Z bosons respectively, and Λ, the energy scale associated with the new physics.

5.1 Event samples

The signal event samples used in this analysis correspond to $t\bar{t} \to b\ell\nu qX$, where $X = \gamma, Z \to \ell\ell, g$ and $\ell = e, \mu$. The following common Standard Model samples were considered as background: fully hadronic, fully leptonic and semi-leptonic $t\bar{t}$, all from MC@NLO; Wt, *s*- and *t*- channels of single top production, all from AcerMC; W+jets, $Wb\bar{b}$+jets and $Wc\bar{c}$+jets, all from ALPGEN; $Z \to e^+e^-$, $Z \to \mu^+\mu^-$ and $Z \to \tau^+\tau^-$, all from PYTHIA; WW, ZZ and WZ, all from HERWIG.

5.2 Event selection

The $t\bar{t}$ final states corresponding to the different FCNC top quark decay modes lead to different topologies according to the number of jets, leptons and photons. There is however a common characteristic of all channels under study, *i.e.* in all of them one of the top quarks is assumed to decay through the dominant Standard Model decay mode $t \to bW$ and the other is forced to decay via one of the FCNC modes $t \to qZ$, $t \to q\gamma$ or $t \to qg$. The QCD backgrounds at hadron colliders make the search for the signal via the fully hadronic channels (when the W and the Z bosons decay to quarks) difficult. For this reason only the

Table 17: Selection cuts applied to the FCNC analyses. For the $t \to qg$ channel, E_{vis}, p_{T_g} and m_{qg} represent the total visible energy, the transverse momentum of the jet associated with the gluon and the reconstructed mass of the top quark with FCNC decay, respectively (see text for details).

Channel	$t\bar{t} \to bWq\gamma$	$t\bar{t} \to bWqg$	$t\bar{t} \to bWqZ$
Pre-selection	$= 1\ell$ ($p_T > 25$ GeV)	$= 1\ell$ ($p_T > 25$ GeV)	$= 3\ell$ ($p_T > 25, 15, 15$ GeV)
	$\geq 2j$ ($p_T > 20$ GeV)	$= 3j$ ($p_T > 40, 20, 20$ GeV)	$\geq 2j$ ($p_T > 30, 20$ GeV)
	$= 1\gamma$ ($p_T > 25$ GeV)	$= 0\gamma$ ($p_T > 15$ GeV)	$= 0\gamma$ ($p_T > 15$ GeV)
	$\not{p}_T > 20$ GeV	$\not{p}_T > 20$ GeV	$\not{p}_T > 20$ GeV
Final selection	$p_{T\gamma} > 75$ GeV	$E_{vis} > 300$ GeV $p_{T_g} > 75$ GeV $m_{qg} > 125$ GeV $m_{qg} < 200$ GeV	2 ℓ same flavour, oppos. charge
Trigger	e22i, mu20 or g55	e22i or mu20	e22i or mu20

Table 18: The trigger efficiency, in percentage, for the background and signal events after all the other cuts of the FCNC analyses.

	$t \to q\gamma$		$t \to qZ$		$t \to qg$	
	Sig.	Back.	Sig.	Back.	Sig.	Back.
Trigger	99.6	99.5	99.2	95.0	83.2	82.2

leptonic decays of both W and Z to e and μ were taken into account. Only isolated muons, electrons and photons separated by $\Delta R > 0.4$ from other reconstructed objects, were considered. Specific pre-selection and selection cuts were applied for each FCNC channel, as outlined in Table 17. For the $t \to q\gamma$ channel, exactly one reconstructed lepton and one reconstructed photon where required in the events. Additionally, at least two jets were required. For the $t \to qg$ channel, the events had to have exactly one reconstructed lepton, three jets and no reconstructed photon. Finally, for the $t \to qZ$ channel, only the events with at least two jets, exactly three reconstructed leptons and no reconstructed photons were accepted. Therefore, the selection criteria for these channels are orthogonal. The expected number of background events and signal efficiencies after the final selection are shown in Table 19. The effect of the trigger on the background and signal events, after all the other cuts, is shown in Table 18. It should be noticed that the events of the $t \to q\gamma$ ($t \to qZ$) channel can be triggered by the lepton or the photon (one of the three leptons), which results on higher trigger efficiencies, when compared with the $t \to qg$ channel with just one lepton. For the $t \to q\gamma$ channel, the dominant backgrounds are $t\bar{t}$, Z+jets and W+jets events, which correspond to 38%, 30% and 29% of the total background. The total background for the $t \to qZ$ channel is mainly composed of $t\bar{t}$ and Z+jets events (59% and 28% of the total background, respectively), while for the $t \to qg$ it is mainly composed of W+jets and $t\bar{t}$ events (which correspond, respectively, to 64% and 25% of the total background).

For all the channels, the top quark with Standard Model semileptonic decay ($t \to b\ell\nu$) cannot be directly reconstructed due to the presence of an undetected neutrino in the final state. The neutrino four-momentum was estimated with a method similar to the one used in Section 4.2, by finding the p_Z^ν value and the jet combination (and the lepton combination in the case of the qZ topology) which minimizes the following expression:

$$\chi^2 = \frac{\left(m_t^{FCNC} - m_t\right)^2}{\sigma_t^2} + \frac{\left(m_{\ell_a \nu j} - m_t\right)^2}{\sigma_t^2} + \frac{\left(m_{\ell_a \nu} - m_W\right)^2}{\sigma_W^2} + \frac{\left(m_{\ell_b \ell_c} - m_Z\right)^2}{\sigma_Z^2}, \quad (10)$$

Table 19: The expected number of background events and signal efficiencies after the final selection level (the trigger is included) of the analyses for each FCNC channel. The corresponding statistical errors are also shown. The expected background numbers are normalised to $L = 1$ fb^{-1}.

	e	μ	ℓ
$t\bar{t} \to bWq\gamma$:			
Total	$(4.4 \pm 0.6) \times 10^2$	$(2.2 \pm 0.6) \times 10^2$	$(6.5 \pm 0.7) \times 10^2$
Signal %	3.6 ± 0.2	4.1 ± 0.2	7.6 ± 0.2
$t\bar{t} \to bWqZ$:			
Total	$(0.3 \pm 0.6) \times 10^2$	$(0.1 \pm 0.6) \times 10^2$	$(1.3 \pm 0.6) \times 10^2$
Signal %	1.4 ± 0.1	2.5 ± 0.1	7.6 ± 0.2
$t\bar{t} \to bWqg$:			
Total	$(11.0 \pm 0.3) \times 10^3$	$(8.3 \pm 0.2) \times 10^3$	$(19.3 \pm 0.4) \times 10^3$
Signal %	1.3 ± 0.1	1.5 ± 0.1	2.9 ± 0.1

where m_t^{FCNC}, $m_{\ell_a \nu j}$, $m_{\ell_a \nu}$ and $m_{\ell_b \ell_c}$ are, for each jet and lepton combination, the reconstructed mass of the top quark decaying via FCNC, the top quark decaying through the Standard Model, the W-boson from the top quark with Standard Model decay and the Z boson from the top quark FCNC decay, respectively. The last term of Eq. 10 was only used in the $t \to qZ$ channel. The following values are used for the constraints: $m_t = 175$ GeV, $m_W = 80.42$ GeV, $m_Z = 91.19$ GeV, $\sigma_t = 14$ GeV, $\sigma_W = 10$ GeV and $\sigma_Z = 3$ GeV[4]. No b-tag information was used to reconstruct the event kinematics. The jet chosen to reconstruct the top quark with Standard Model decay is labeled as b quark. For the $t \to q\gamma$ and the $t \to qZ$ channels, the other jet, which was used to reconstruct the top quark with FCNC decay, is denoted by q quark. For the $t \to qg$ channel, it is assumed that the jet created by the gluon is the most energetic from the two which reconstruct the top quark with FCNC decay and the other is created by the light quark.

Following the selection cuts, a likelihood-based type of analysis was applied, as described in section 4.2. Due to the small statistics of the available full simulation samples, ATLFAST samples were used to obtain the probability density functions (p.d.f.s). The p.d.f.s of the $t \to q\gamma$ channel were built based on the following variables: the mass of the top quark with FCNC decay (m_t^{FCNC}); the reconstructed mass of the photon and the b quark ($m_{b\gamma}$) and the transverse momentum of the leading photon (p_T^{γ}). For the $t \to qZ$ channel, the p.d.f.s were based on the following physical distributions: the mass of the top quark with FCNC decay (m_t^{FCNC}); the minimum invariant mass of the three possible combinations of two leptons ($m_{\ell\ell}^{min}$); the reconstructed mass of the Z and the b quark (m_{bZ}); the reconstructed mass of the two quarks (m_{qb}); the transverse momentum of the third lepton ($p_T^{\ell_3}$) and the transverse momentum of the light quark (p_T^q). The following variables were used to build the p.d.f.s of the $t \to qg$ channel: the mass of the top quark with FCNC decay (m_t^{FCNC}); the mass of the top quark with Standard Model decay ($m_{\ell_a \nu j}$); the reconstructed mass of the light and the b quark (m_{qb}); the transverse momentum of the b quark (p_T^b); the transverse momentum of the light quark (p_T^q) and the angle between the lepton and the gluon ($\alpha_{\ell g}$). The distributions of the discriminant variables are presented in Figure 9. It can be seen that ATLFAST describes the fully simulated distributions fairly well, when there are sufficient statistics to tell.

[4]These resolutions are taken from the top quark mass measurement analyses [70]. The effect of changing their values was considered as one of the systematic source of uncertainties. Its impact on the observables is below the statistical error.

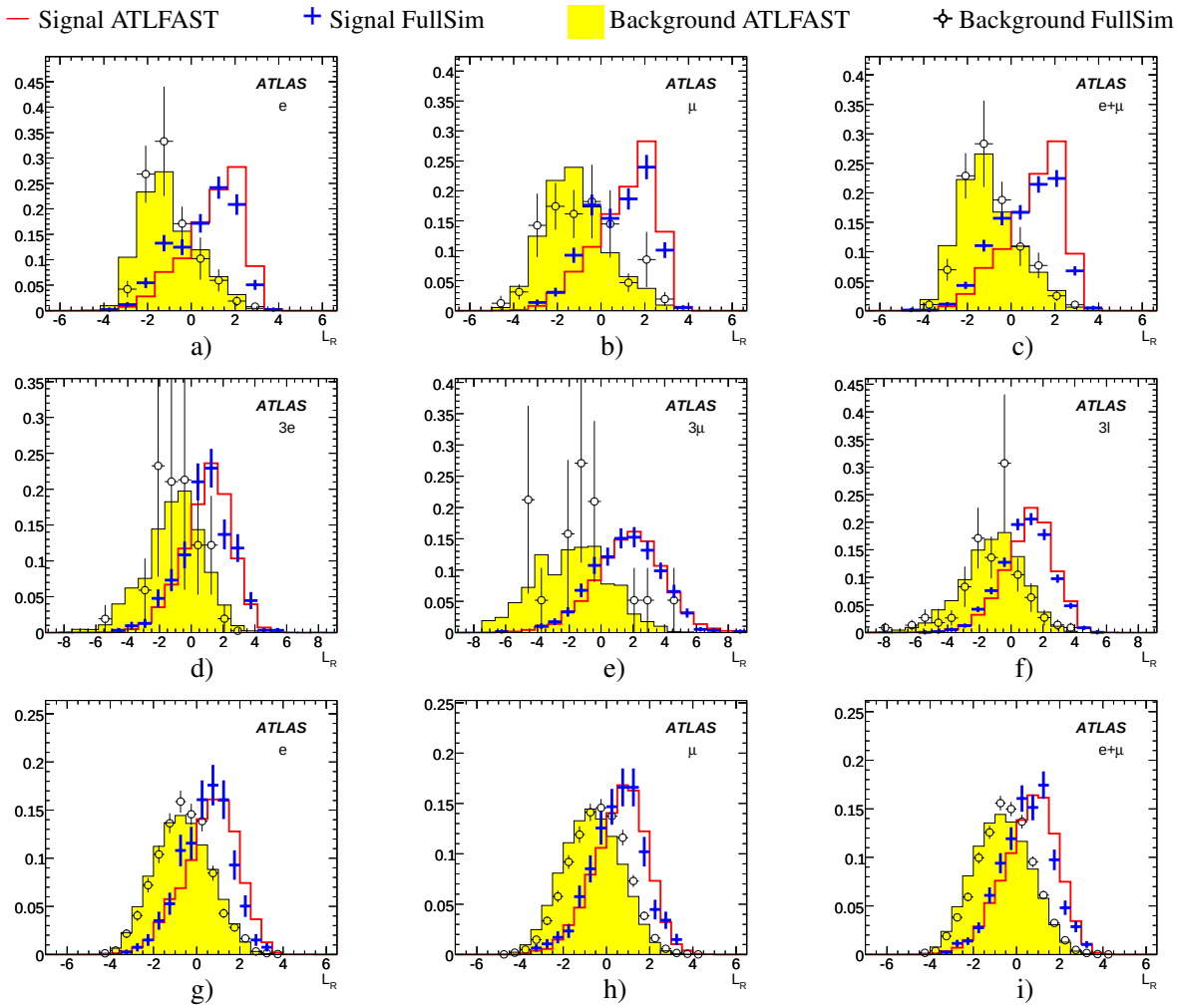

Figure 9: Distributions of the normalised discriminant variables for the expected background and signal after the final selection level of the $t \to q\gamma$ channel when the isolated lepton is identified as (a) an electron, (b) a muon and (c) electron or muon; of the $t \to qZ$ channel when the 3 isolated leptons are identified as (d) electrons, (e) muons and (f) electrons or muons and of the $t \to qg$ channel, when the isolated lepton is identified as (g) an electron, (h) a muon and (i) electron or muon.

Table 20: The expected 95% confidence level limits on the FCNC top quark decay branching ratio, in the absence of signal, are shown for a luminosity of $L = 1$ fb^{-1}. The central values are represented together with the 1σ bands, which include the contribution from the statistical and systematic uncertainties.

	-1σ	Expected	$+1\sigma$
$t\bar{t} \to$ bWqγ:			
e	4.3×10^{-4}	1.1×10^{-3}	1.9×10^{-3}
μ	4.5×10^{-4}	8.3×10^{-4}	1.3×10^{-3}
ℓ	3.8×10^{-4}	6.8×10^{-4}	1.0×10^{-3}
$t\bar{t} \to$ bWqZ:			
3e	5.5×10^{-3}	9.4×10^{-3}	1.4×10^{-2}
3μ	2.4×10^{-3}	4.2×10^{-3}	6.4×10^{-3}
3ℓ	1.9×10^{-3}	2.8×10^{-3}	4.2×10^{-3}
$t\bar{t} \to$ bWqg:			
e	1.3×10^{-2}	2.1×10^{-2}	3.0×10^{-2}
μ	1.0×10^{-2}	1.7×10^{-2}	2.4×10^{-2}
ℓ	7.2×10^{-3}	1.2×10^{-2}	1.8×10^{-2}

5.3 Results and systematic uncertainties

In the absence of a FCNC top quark decay signal, expected limits at 95% CL were derived using the modified frequentist likelihood method [75] and the discriminant variables obtained with the full simulation samples. No cuts on the discriminant variables were used. Using the Standard Model $t\bar{t}$ production cross-section these limits were converted into limits on the branching ratios. The central values of these limits are shown in Table 20. The branching ratio sensitivity for each FCNC channel, assuming a signal discovery with a 5σ significance, is on average 3.0 times larger than the central values presented in Table 20.

Several sources of systematic uncertainties were studied following the common criteria used for this note and the results are shown in Table 21. The jet energy scale (the jet calibration used in the present analyses is described in Ref. [70]), the luminosity, the influence of the cross-section values, ISR/FSR, Monte Carlo generator and pile-up effects were studied. For the top quark mass, the full simulation samples were analysed using the values of 170 and 180 GeV (i.e. p.d.f.s, Eq. 10 and limit computation). The systematic error was taken from a linear fit of the values found, for a top quark mass error of ± 2 GeV. To study the effect of the mass resolutions in Eq. 10, and since no cut is applied to the χ^2 distribution, the ratio σ_t/σ_W was changed by a factor 2. The total systematic uncertainties, computed as the quadratic sum of these individual contributions, are also shown in Table 21. The analysis stability was also cross-checked by varying the kinematic cuts by about 10%, and the maximum relative change on the expected 95% CL limits was 3%, 9% and 5% for the $t \to q\gamma$, $t \to qZ$ and $t \to qg$ channels, respectively. Table 20 shows the obtained central values for the BR limits. The $\pm 1\sigma$ contributions from statistical and systematic uncertainties (added in quadrature) are also shown. The contribution from the luminosity and the absolute value of background level may be reduced with data, by normalising to measured processes.

Figure 10 shows the ATLAS 95% CL expected sensitivity for the first fb^{-1} in the absence of signal, for the $t \to q\gamma$ and $t \to qZ$ channels taking into account the contributions from both the statistical and systematic uncertainties.

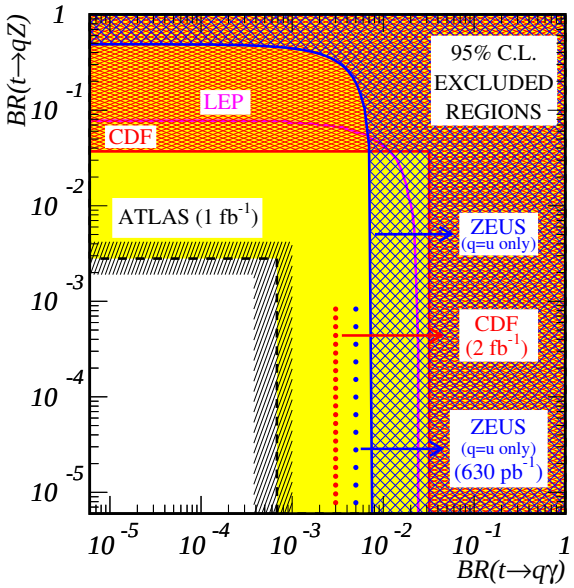

Figure 10: The present 95% CL observed limits on the $BR(t \to q\gamma)$ vs. $BR(t \to qZ)$ plane are shown as full lines for the LEP, ZEUS and CDF collaborations. The expected sensitivity at ZEUS, CDF and ATLAS (together with the statistic plus systematic 1σ band) is also represented by the dotted and dashed lines.

Table 21: Maximum changes (with respect to the central values of Table 20) of the expected 95% CL limits for each FCNC top quark decay branching ratio for different systematic error sources.

	$t \to q\gamma$			$t \to qZ$			$t \to qg$		
Source	e	μ	ℓ	3e	3μ	3ℓ	e	μ	ℓ
Jet energy calibration	1%	2%	2%	3%	2%	5%	4%	4%	4%
Luminosity	9%	8%	10%	3%	2%	6%	10%	8%	10%
Top quark mass	7%	7%	6%	6%	4%	12%	7%	5%	5%
Backgrounds σ	6%	10%	7%	4%	7%	12%	17%	16%	15%
ISR/FSR	21%	18%	17%	6%	29%	7%	3%	7%	9%
Pile-up	37%	21%	22%	30%	14%	0%	8%	10%	13%
Generator	34%	18%	4%	4%	14%	14%	5%	0%	4%
χ^2	5%	0%	4%	2%	5%	7%	3%	7%	9%
Total	56%	36%	32%	32%	36%	25%	24%	24%	27%

6 $t\bar{t}$ resonances

New resonances or gauge bosons strongly coupled to the top quark could manifest themselves in the $t\bar{t}$ invariant mass distribution. Due to the large variety of models and their parameters, studies have been done in a model-independent way searching for a "generic" narrow resonance decaying into $t\bar{t}$ (semileptonic channel) [51,76]. The ATLAS discovery potential is assessed using the latest available simulations and detector description, performing the $t\bar{t}$ event reconstruction along the same lines as done for the high precision measurement of the top quark mass in the semileptonic decay channel [54]. Alternative methods are currently under investigation to study the production of high mass resonances ($m > 2$ TeV), where the decay products of the top quark are close together, so requiring a modified selection.

6.1 Event generation and selection

In this study, $t\bar{t}$ resonances were produced with PYTHIA. The $Z' \rightarrow t\bar{t}$ channel without interference in the Z' production has been chosen [77]. Only the semileptonic decay (electrons and muons) of $t\bar{t}$ pairs is considered. Five samples of Z' resonances with mass 700 GeV (the lower limit from CDF and D$\emptyset$ measurements [78,79]), 1000 GeV, 1500 GeV, 2000 GeV and finally 3000 GeV have been produced.

The common $t\bar{t}$ semileptonic selection criteria were used to accept signal events. Once these criteria are applied, the main source of physical background to be considered in the search for $t\bar{t}$ resonances comes from Standard Model $t\bar{t}$ events. The other sources of background, dominated by W+jets events, are negligible [54].

6.2 Data characteristics

6.2.1 $t\bar{t}$ reconstruction

Several ways to reconstruct the W-bosons and the top quarks have been investigated [54]. The simplest of them is used here. This method selects, among all jets from light quarks (u,d,c and s), the two jets which are closest in ΔR to build the hadronic W-boson. The hadronic top quark is reconstructed combining the nearest b-jet to the hadronic W-boson. For the leptonic side, the constraint on the W-boson mass is used to compute the longitudinal momentum of the neutrino, identifying the missing transverse energy as the neutrino transverse momentum. Among the 2 p_{z^ν} solutions, the one providing the leptonic top quark mass closest to the mean value of the hadronic top quark mass is chosen. To reduce both the physical background and the combinatorial background (which dominates), cuts are applied on the hadronic W-boson mass spectrum, and on both top quark mass spectra. The resulting $t\bar{t}$ mass distribution, given in Figure 11, is used as a starting point for the discovery potential determination.

This method does not need a well understood jet energy scale and it is also one of the most efficient. More sophisticated methods to select the top quarks, such as a kinematic fits of the $t\bar{t}$-pairs (used by the D$\emptyset$ experiment [79]), or a matrix-element motivated method (used by CDF [78]), are not described here. The method used could be considered as a baseline for the $t\bar{t}$ resonance search.

6.2.2 Event yield

The reconstruction efficiency of Standard Model $t\bar{t}$ pairs corresponding to the reconstruction scheme and cuts described above is shown in Figure 13. The fact that the produced particles are closer together when the generated $t\bar{t}$ mass is higher explains the drop of efficiency observed as a function of the $t\bar{t}$ mass. Part of the efficiency can be recovered if another jet finding algorithm, better at resolving nearby jets (such as a cone jet algorithm with smaller cone radius), is used.

Figure 14 gives the reconstruction efficiency of Z' resonances as a function of their mass. This reconstruction efficiency is of the same order as for the Standard Model $t\bar{t}$ pairs. Nevertheless, some

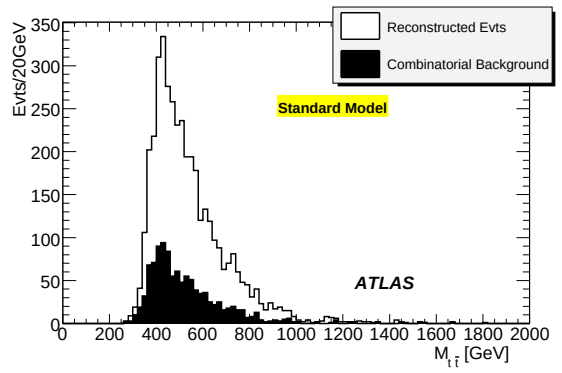

Figure 11: Standard Model $t\bar{t}$ mass spectrum. The black area represents the combinatorial background where at least one of the selected jets or leptons does not match the corresponding parton.

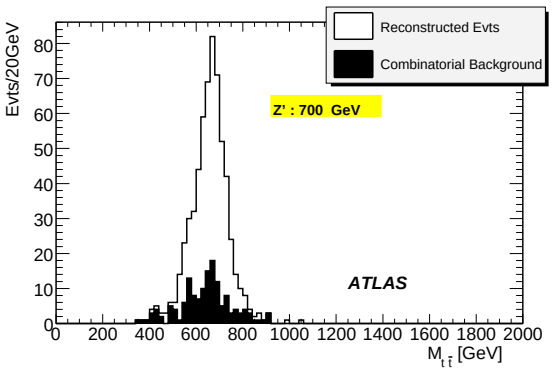

Figure 12: A 700 GeV Z' reconstructed mass spectrum. The black area represents the combinatorial background where at least one of the selected jets or leptons does not match the correspondent parton.

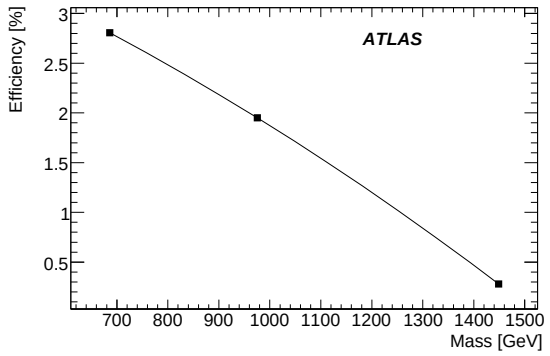

Figure 13: Reconstruction efficiency of Standard Model $t\bar{t}$ pairs as a function of the $t\bar{t}$ mass.

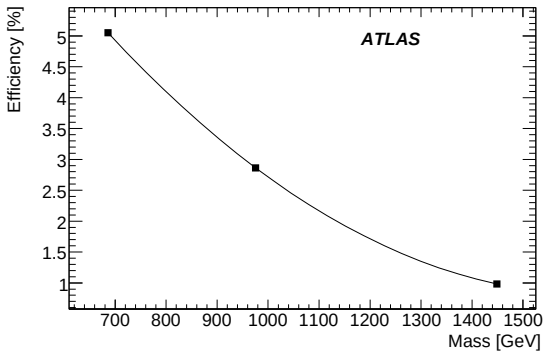

Figure 14: Reconstruction efficiency of $Z' \rightarrow t\bar{t}$ resonances as a function of the Z' mass.

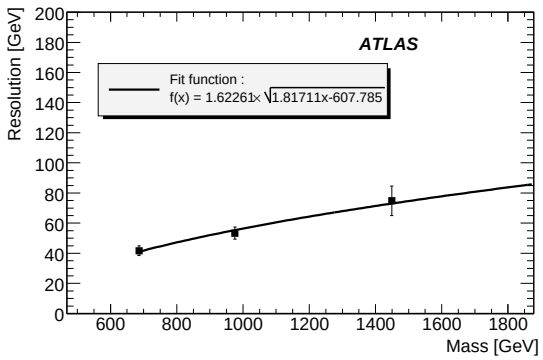

Figure 15: Z' mass resolution as a function of the Z' mass.

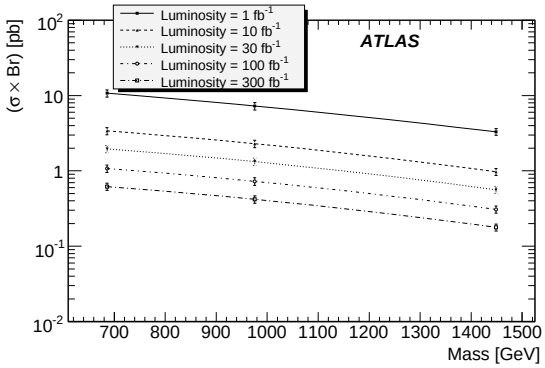

Figure 16: 5σ discovery potential of a generic narrow $t\bar{t}$ resonance as a function of the integrated luminosity.

small differences arise due to the different production mechanism and spin. Thus, the final result is not completely model-independent. The purity (fraction of well reconstructed events among all selected events) in each Z' sample is of the order of 80-85%.

6.3 Discovery potential

6.3.1 Method and results

The method used to extract the 5σ discovery sensitivity consists of counting the number of Standard Model $t\bar{t}$ events in a sliding mass window over the invariant mass spectrum. The 5σ sensitivity means that an effect is seen over the expected background with a deviation at least 5 times the background fluctuation in the mass window. The width of the window is twice the detector resolution for a given resonance mass. Then, the lowest cross section times branching ratio $\sigma \times Br(Z' \to t\bar{t})$ is computed for the discovery of a resonance at a given mass.

The produced resonances are expected to have a width smaller than the resolution, leading to a gaussian shape for the reconstructed invariant mass. The discovery potential is thus estimated here only for narrow $t\bar{t}$ resonances.

This method, explained in detail in [76], requires as input the Z' mass resolution (Figure 15), the reconstruction efficiency of both Standard Model $t\bar{t}$ events and resonance events, and the purity of the final samples.

The resulting sensitivity is shown on Figure 16. For example, a 700 GeV Z' resonance produced with a $\sigma \times Br(Z' \to t\bar{t})$ of 11 pb should be discovered with a 5σ significance after 1 fb^{-1} of data taking. The $t\bar{t}$ mass spectrum associated with such a case is shown in Figure 17.

6.3.2 Measurement uncertainties

Uncertainties on the sensitivity arise from:

- the reconstruction efficiency for the Z' signal and $t\bar{t}$ background. The main contribution arises from the expected error on the b-tag efficiency, which is set to $\pm 5\%$.
- the background contribution (Standard Model $t\bar{t}$). The main contribution comes from the $t\bar{t}$ cross section uncertainty $^{+6.2}_{-4.7}$ %.

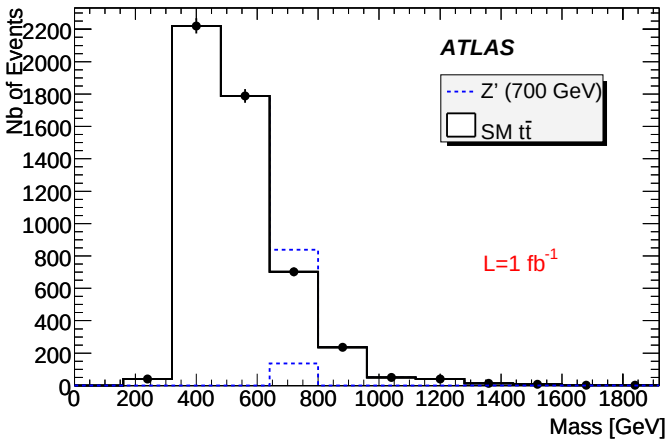

Figure 17: Expected $t\bar{t}$ invariant mass spectrum for the discovery threshold of a 700 GeV Z' resonance $\sigma \times Br(Z' \to t\bar{t}) = 11.07$ pb with 1 fb^{-1} of data.

Table 22: Sources of uncertainties considered on the 5σ discovery potential computation.

Source of uncertainty	Error (%)	Effect on the discovery potential (%)
Reconstruction efficiency	16.6	8.3
Background contribution	$^{+6.2}_{-4.7}$	3.1
$t\bar{t}$ mass resolution	$\pm 1\sigma_{\text{resolution}}$	2 to 11
Luminosity	5	2.5
Jet energy scale	5	-

- the $t\bar{t}$ mass resolution (Figure 15). The effect on the discovery potential increases with the resonance mass.
- the uncertainty on the integrated luminosity.

The 5σ discovery potential is given as a function of the $t\bar{t}$ resonance mass. The position of the resonance mass peak depends on the accuracy of the jet energy scale. This will be constrained by the W-boson and top quark events themselves.

All these quantities have been varied within expected errors. The impact on the sensitivity is reported in Table 22.

7 Summary and conclusions

The ATLAS sensitivity to the measurement of several top quark properties was reviewed in this paper for an expected luminosity of 1 fb^{-1} at the LHC. The precision of several measurements was estimated, using the full simulation of the ATLAS detector. For the tests of physics beyond the Standard Model associated with the production of top quarks, the 95% CL limit (in the absence of a signal) was presented. In Table 23 a summary of the expected sensitivity on these observables is shown, for a luminosity of 1 fb^{-1}. Several sources of systematic errors were considered using an approach common to all studies appearing in this note.

Table 23: Expected ATLAS sensitivity for the top quark properties, for a luminosity of 1 fb^{-1}. For the Standard Model measurements the sensitivity is given as the total error divided by the expected Standard Model value, for the searches the absolute value is presented.

Observables	Expected Precision
Top quark charge (2/3 versus -4/3)	$\geq 5\sigma$
Spin Correlations:	
A	50%
A_D	34%
W-boson Polarisation:	
F_0	5%
F_L	12%
F_R	0.03
Angular Asymmetries:	
A_{FB}	19%
A_+	11%
A_-	4%
Anomalous Couplings:	
V_R	0.15
g_L	0.07
g_R	0.15
Top quark FCNC decays (95% C.L.):	
$Br(t \to q\gamma)$	10^{-3}
$Br(t \to qZ)$	10^{-3}
$Br(t \to qg)$	10^{-2}
$t\bar{t}$ Resonances (discovery):	
$\sigma \times Br$ ($m_{t\bar{t}}$=700GeV)	$\geq$ 11 pb

The sensitivity of the ATLAS experiment to the top quark charge measurement was evaluated. The analysis shows that using the weighting technique, already with 0.1 fb^{-1} it is possible to distinguish with a 5σ significance, between the b-jet charges associated with leptons of opposite charges, which allows to distinguish the Standard Model from an exotic scenario. For the semileptonic b-decay method the required luminosity is $\simeq 1$ fb^{-1}. The top quark charge itself was reconstructed relying on a Monte Carlo calibration of the b-jet charge. Although the reconstruction of the numeric value of the top quark charge using the weighting technique seems possible with $\simeq 1$ fb^{-1}, it will be necessary to check the performance of the method with real data e.g. di-jet $b\bar{b}$ events, once available. A more realistic treatment of the background processes will be required for a full understanding of the top quark charge issues.

A study of the W-boson polarisation fractions (F_0, F_L and F_R) and $t\bar{t}$ spin correlation parameters (A and A_D) has been performed in the semileptonic $t\bar{t}$ channel. Reconstructed angular distributions were used to set the ATLAS sensitivity to the measurement of the W-boson polarisations and top quark spin correlation parameters.

The W-boson polarisation ratios (ρ_R and ρ_L) and the angular asymmetries (A_+ and A_-) dependence on the anomalous couplings (V_R, g_L and g_R) was used to find the sensitivity to the Wtb anomalous couplings (for the analyses with and without b-tag).

Top quark rare decays through FCNC processes ($t \to qZ, q\gamma, qg$) were studied in this note using $t\bar{t}$ events produced at the LHC. Expected limits on the branching ratios were set at 95% CL in the absence

of signal.

The discovery potential of the ATLAS experiment for narrow $t\bar{t}$ resonances decaying in the semileptonic channel, was studied as a function of the resonance mass.

References

[1] V. M. Abazov et al., Phys. Rev. Lett. **98** (2007) 041801.

[2] A. Abulencia et al., *First CDF Measurement ot the TopQuark Charge using the Top Decay Products*, 2007, CDF Note 8783.

[3] D. Chang, W.F. Chang, E. Ma, Phys. Rev. D **59** (1999) 091503.

[4] D. Chang, W.F. Chang, E. Ma, Phys. Rev. D **61** (2000) 037301.

[5] CDF Collaboration, *Measurement of W-Boson Helicity Fractions in Top-Quark Decays Using* $\cos\theta^*$, 2008, Conf. Note 9431.

[6] Abulencia, A. *et al.*, Phys. Rev. Lett. **98** (2007) 072001.

[7] CDF Collaboration, *Measurement of W Boson Helicity Fractions in Top Quark Decay to Lepton+Jets Events using a Matrix Element Analysis Technique with 1.9* fb^{-1} *of Data*, 2007, Conf. Note 9144.

[8] CDF Collaboration, *Measurement of W Helicity in Fully Reconstructed Top Anti-Top Events using 1.9* fb^{-1}, 2007, Conf. Note 9114.

[9] Abulencia, A. *et al.*, Phys. Rev. **D73** (2006) 111103(R).

[10] D0 Collaboration, *Model-Independent Measurement of the W-Boson Helicity in Top-Quark Decays at D0*, 2008, D0 Note 5722-CONF.

[11] Abazov, V. M. *et al.*, Phys. Rev. Lett. **100** (2008) 062004.

[12] Abazov, V. M. *et al.*, Phys. Rev. **D75** (2007) 031102(R).

[13] Abazov, V. M. *et al.*, Phys. Rev. **D72** (2005) 011104(R).

[14] J. A. Aguilar-Saavedra, Phys. Rev. D **67** (2003) 035003.

[15] F. del Aguila and J. Santiago, JHEP **0203** (2002) 010.

[16] J. j. Cao, R. J. Oakes, F. Wang and J. M. Yang, Phys. Rev. D **68** (2003) 054019.

[17] X. l. Wang, Q. l. Zhang and Q. p. Qiao, Phys. Rev. D **71** (2005) 014035.

[18] F. del Aguila and J. A. Aguilar-Saavedra, Phys. Rev. D **67** (2003) 014009.

[19] J. A. Aguilar-Saavedra, J. Carvalho, N. Castro, A. Onofre and F. Veloso, Eur. Phys. J. C **50** (2007) 519.

[20] F. Hubaut, E. Monnier, P. Pralavorio, K. Smolek and V. Simak, Eur. Phys. J. C **44S2** (2005) 13.

[21] H. S. Do, S. Groote, J. G. Korner and M. C. Mauser, Phys. Rev. D **67** (2003) 091501.

[22] Grzadkowski, Bohdan and Misiak, Mikolaj, *Anomalous Wtb coupling effects in the weak radiative B- meson decay*, 2008, arXiv:0802.1413 [hep-ph].

[23] Barberio, E. *et al.*, *Averages of b-hadron properties at the end of 2006*, 2007, arXiv:0704.3575 [hep-ex].

[24] F. del Aguila et al., *Collider aspects of flavour physics at high Q*, 2008, arXiv:0801.1800 [hep-ph].

[25] S.L.Glashow, J.Iliopoulos, L.Maiani, Phys. Rev. D **2** (1970) 1285.

[26] B.Grzadkowski, J.F.Gunion, P.Krawczyk, Phys. Lett. B **268** (1991) 106.

[27] G.Eilam, J.L.Hewett, A.Soni, Phys. Rev. D **44** (1991) 1473.

[28] G.Eilam, J.L.Hewett, A.Soni, Phys. Rev. D **59** (1998) 039901.

[29] M. E. Luke, M. J. Savage, Phys. Lett. B **307** (1993) 387.

[30] G. M. de Divitiis, R. Petronzio, L. Silvestrini, Nucl. Phys. B **504** (1997) 45.

[31] D.Atwood, L.Reina, A.Soni, Phys. Rev. D **53** (1996) 1199.

[32] F. del Aguila, J.A.Aguilar-Saavedra, R.Miquel, Phys. Rev. Lett. **82** (1999) 1628.

[33] Aguilar-Saavedra, J. A. and Nobre, B. M., Phys. Lett. **B553** (2003) 251–260.

[34] Aguilar-Saavedra, J. A., Phys. Rev. **D67** (2003) 035003.

[35] del Aguila, F. and Aguilar-Saavedra, J. A., Nucl. Phys. **B576** (2000) 56–84.

[36] Aguilar-Saavedra, J. A., Acta Phys. Polon. **B35** (2004) 2695–2710.

[37] ALEPH, DELPHI, L3, OPAL & the LEP EXOTICA WG, *Search for Single Top Production Via Flavour Changing Neutral Currents: Preliminary Combined Results of the LEP Experiment*, 2001, LEP Exotica WG 2001-01.

[38] Heister, A. *et al.*, Phys. Lett. **B543** (2002) 173–182.

[39] Abdallah, J. *et al.*, Phys. Lett. **B590** (2004) 21–34.

[40] Abbiendi, G. *et al.*, Phys. Lett. **B521** (2001) 181–194.

[41] Achard, P. *et al.*, Phys. Lett. **B549** (2002) 290–300.

[42] Chekanov, S. and others, Phys. Lett. **B559** (2003) 153–170, Note: the branching ratio limits are a private communication.

[43] CDF Collaboration, *Search for the Flavor Changing Neutral Current Decay $t \to Zq$ in $p\bar{p}$ Collisions at $\sqrt{s} = 1.96$ TeV with 1.9 fb^{-1} of CDF-II Data*, 2008, Conf. Note 9202.

[44] F. Abe et al. [CDF Collaboration], Phys. Rev. Lett. **80** (1998) 2525.

[45] M. Beneke *et al.*, *Top quark physics*, 2000, hep-ph/0003033.

[46] Ashimova, A. A. and Slabospitsky, S. R., *The constraint on FCNC coupling of the top quark with a gluon from e p collisions*, 2006, hep-ph/0604119.

[47] Aktas, A. *et al.*, Eur. Phys. J. **C33** (2004) 9–22.

[48] Abazov, V. M. *et al.*, Phys. Rev. Lett. **99** (2007) 191802.

[49] T. Hill and E. H. Simmons, *Strong Dynamics and Electroweak Symmetry Breaking*, 2002, hep-ph/0203079.

[50] M. Beneke et al, *Top Quark Physics, Proceedings of the workshop on Standard Model Physics (and more) at the LHC*, 2000, CERN 2000-004 (2000).

[51] ATLAS Collaboration, *Detector and Physics Performance Technical Design Report*, 1999, CERN/LHCC/99-14(1999).

[52] F. del Aguila and J.A. Aguilar-Saavedra, JHEP **11** (2007) 072.

[53] T. Aaltonen et al.(CDF collaboration), Phys. Rev. D **77** (2008) 051102(R).

[54] ATLAS Collaboration, *Top Quark Mass Measurements*, this volume.

[55] ATLAS Collaboration, *Triggering Top Quark Events*, this volume.

[56] U.Baur,M. Buice, L.H.Orr, Phys. Rev. D **64** (2001) 094019.

[57] G. Altarelli and M. Mangano (Ed.), *Proc. of the workshop on Standard Model Physics (and more) at the LHC*, 2000, CERN 2000-004, May 2000, Geneva.

[58] M.Ciljak, M.Jurcovicova, S. Tokar and U. Baur, Top charge measurement at ATLAS detector, 2003, ATLAS Note PHYS-2003-35.

[59] R.D.Field and R.P.Feynman, Nucl. Phys. **B136** (1978) 1–76.

[60] R. Barate et al., Phys. Lett. **B426** (1998) 217–230.

[61] G.L. Kane, G.A. Ladinsky and C.-P. Yuan, Phys. Rev. D **45** (1992) 124.

[62] W. Bernreuther, Nucl. Phys. B **690** (2004) 81.

[63] F. Hubaut *et al.*, *Polarization studies in* $t\bar{t}$ *semileptonic events with ATLAS full simulation*, 2006, ATL-PHYS-PUB-2006-022.

[64] F. Hubaut, E. Monnier and P. Pralavorio, *ATLAS sensitivity to* $t\bar{t}$ *spin correlation in the semileptonic channel*, 2005, ATL-PHYS-PUB-2005-001.

[65] F. Hubaut et al., *Comparison between full and fast simulations in top physics*, 2006, ATL-PHYS-PUB-2006-017.

[66] CDF collaboration, *Measurement of W Boson Helicity Fractions in Top Quark Decays Using* $\cos\theta^*$, 2008, Conf. Note 9215,.

[67] ATLAS Collaboration, *b-Tagging Calibration with* $t\bar{t}$ *Events*, this volume.

[68] ATLAS Collaboration, *Jets from Light Quarks in* $t\bar{t}$ *Events*, this volume.

[69] B. Lampe, Nucl. Phys. B **454** (1995) 506.

[70] ATLAS Collaboration, *Top Quark Mass Measurements*, this volume.

[71] J. A. Aguilar-Saavedra, J. Carvalho, N. Castro, A. Onofre and F. Veloso, Eur. Phys. J. C **53** (2008) 689.

[72] J.A. Aguilar-Saavedra, *Single top quark production at LHC with anomalous Wtb couplings*, 2008, hep-ph/0803.3810.

[73] C.Caso et al., Eur. Phys. J. C **3** (1998) 1.

[74] W.Hollik, J.I.Illana, S.Rigolin, C.Schappacher, D.Stockinger, Nucl. Phys. B **551** (1999) 3.

[75] A.L. Read, *Modified Frequentist Analysis of Search Results (The CL_S Method)*, 2000, CERN report 2000-005.

[76] E. Cogneras and D. Pallin, *Generic $t\bar{t}$ resonance search with the ATLAS detector*, 2006, ATL-PHYS-PUB-2006-033.

[77] ATLAS Collaboration, *Cross-Sections, Monte Carlo Simulations and Systematic Uncertainties*, this volume.

[78] CDF Collaboration, *Limit on Resonant $t\bar{t}$ Production in $p\bar{p}$ Collisions at $\sqrt{s}$=1.96 TeV*, 2007, CDF Note 8675.

[79] D0 Collaboration, *Search for $t\bar{t}$ Resonance in the Lepton+Jets Final State in $p\bar{p}$ Collisions at* $\sqrt{s} = 1.96$ TeV, 2007, Note 5443-CONF.

Measurements from Supersymmetric Events

Abstract

We review the techniques used to reconstruct the decay of supersymmetric particles and measure their properties with ATLAS at the LHC, concentrating on strategies to be applied to a data set of integrated luminosity of 1 fb^{-1} that can be expected after the first year of operation of the LHC. These techniques are illustrated using several benchmark points chosen in the mSUGRA parameter space, but they are applicable to a broader range of supersymmetric (and other similar) models. The most appropriate methods will be selected and fine-tuned once (and if) signatures consistent with Supersymmetry are established. Supersymmetric cascade decays typically have large transverse missing energy due to the presence of undectected neutralinos, and have characteristic edges and thresholds in the dilepton, dijet and lepton-jet invariant mass distributions. The reconstruction of such edges is the focus of the first part of the paper. The second part of the paper concentrates on the reconstruction of more specific decay channels, involving light stops, staus and Higgs bosons. The final section indicates how sparticle masses and other supersymmetric parameters could be constrained using such measurements.

1 Introduction

Supersymmetry (SUSY) can be discovered by the ATLAS experiment at the LHC during the initial running period if some coloured sparticles have masses of the order hundreds of GeV and hence production cross-sections of the order of a few pb. A strategy to establish SUSY discovery is outlined in another paper in this collection [1], while here we concentrate on parameter measurements that can be performed with the early data. The same particle identification conventions and selection criteria as in [2] are used in this paper.

Once a signature consistent with Supersymmetry has been established, the experimental emphasis will move on to measuring the sparticle mass spectrum and constraining the parameters of the model. In the case of R-parity-conserving models, the decay chain of sparticles cannot be completely reconstructed, as sparticles eventually decay into LSPs that can not be detected. For this reason edge positions, rather than mass peaks, are measured in the invariant mass distribution of sparticle decay products. In R-parity-violating models sparticles can have long lifetimes and can be detected by studying their decay in-flight within the detector. These types of signatures are discussed in [3].

A complete coverage of all allowed SUSY models is impossible, so we limit this study to a subset of the models where SUSY breaking is mediated by gravity (mSUGRA), and to the points in parameter space described in [2], however the measurement techniques and fit methods developed can be adapted for many models. During initial data-taking, the error on such measurements will be limited by statistics, making measurements possible only for models with moderate ($\lesssim 1$ TeV) values of the SUSY mass scale where enough events can be isolated. In this paper we study the cases of a total integrated luminosity of 0.5 fb^{-1} for the "Low Mass" point (SU4) and of 1 fb^{-1} for the "Bulk" point (SU3), with the idea of developing the experimental analyses which might be performed after the first year or so of data taking. Some benchmark points require somewhat larger datasets in order to perform kinematic measurements; as an example we show a measurement of the dilepton mass edges for the "Coannihilation" point (SU1) with a dataset corresponding to 18 fb^{-1}.

In sections 3 and 4 we study the decay chain:

$$\tilde{q}_{\mathrm{L}} \rightarrow \tilde{\chi}_2^0 q(\rightarrow \tilde{\ell}^{\pm}\ell^{\mp}q) \rightarrow \tilde{\chi}_1^0 \ell^+\ell^- q \tag{1}$$

in events containing two opposite-sign isolated electrons or muons, hard jets and missing energy. Kinematic endpoints in the invariant mass spectra of lepton pairs and lepton+jet combinations are fitted and used to derive relations between the masses of sparticles. In the case of first- and second-generation squarks, it will often not be possible to experimentally determine squark flavour, so we define $m_{\tilde{q}_L}$ to be the average of the masses of the $\tilde{u}_L$ and $\tilde{d}_L$ squarks, and $m_{\tilde{q}_R}$, the average mass of $\tilde{u}_R$ and $\tilde{d}_R$.

Events with tau leptons in the final state are studied in Section 5 and di-tau mass edges in the $\tilde{\chi}_2^0$ decay chain reconstructed. This signature is particularly important in the co-annihilation region where the decay into tau stau pairs is favoured.

In Section 6 we analyse events with two hard jets and missing energy in order to to measure the jet "stransverse mass". This variable is sensitive to the mass of the right-handed squark in events where a pair of squarks are produced, each decaying as:

$$\tilde{q}_R \rightarrow q\tilde{\chi}_1^0 \tag{2}$$

A kinematical edge depending on the mass of the light stop is reconstructed in Section 7 by exploiting the decay:

$$\tilde{g} \rightarrow \tilde{t}_1 t \rightarrow \tilde{\chi}_1^{\pm} bt \tag{3}$$

and reconstructing the tb invariant mass.

The reconstruction of the lightest Higgs bosons, produced by the $\tilde{\chi}_2^0$ decay followed by the Higgs decay into a pair of b quarks, is investigated in Section 8. Simulations of the "Higgs" point (SU9) show that if these decays are allowed, then the Standard Model Higgs boson may be initially detected as a SUSY decay product rather than by signatures that involve its production via Standard Model processes.

In Section 9 the parameters measured in sections 3 to 8 are combined to extract information about the SUSY model such as the sparticle mass spectrum and the mSUGRA parameters (under the hypothesis that mSUGRA is realised).

All of these studies use a realistic detector geometry with residual misalignments, and all relevant Standard Model backgrounds are taken into account, as are the trigger efficiencies. The reconstruction of final state objects, the event selection criteria, the strategy used to simulate both signal and background events, and the methods for estimating systematic uncertainties are common across all SUSY analyses and are discussed in the introduction to this chapter [2].

2 Measurement of endpoints

The decay chain in Eq. (1) is particularly suited to measure the mass of SUSY particles, as the presence in the final state of charged leptons, missing energy from the escaping neutralino and hadronic jets ensures a large signal to background ratio. Thus, fit results are not very dependent on the precise measurement of the Standard Model background. Although we discuss the reconstruction of edges and thresholds within the mSUGRA framework, the same methodology can be applied to the large variety of SUSY models where the $\tilde{q}_L$ decay channel in Eq. (1) is open. In the following we indicate with ℓ only electrons and muons (with $\tilde{\ell}$ being their superpartners) while τ leptons are indicated explicitly.

The endpoint in the di-lepton invariant mass distribution is a function of the masses of the particles involved in the decay. If the sleptons are heavier than the $\tilde{\chi}_2^0$ then the decay proceeds through the three body channel $\tilde{\chi}_2^0 \rightarrow \tilde{\chi}_1^0 \ell^+ \ell^-$ as in the SU4 model. In this case, the distribution of the invariant mass of the two leptons has a non-triangular shape described in [4, 5] with an endpoint equal to the difference of the mass of the two neutralinos:

$$m_{\ell\ell}^{\text{edge}} = m_{\tilde{\chi}_2^0} - m_{\tilde{\chi}_1^0} \tag{4}$$

If at least one of the sleptons is lighter than the $\tilde{\chi}_2^0$ then the two-body decay channel $\tilde{\chi}_2^0 \to \tilde{\ell}^{\pm}\ell^{\mp} \to \tilde{\chi}_1^0\ell^+\ell^-$ dominates. The distribution of the invariant mass of the two leptons is triangular with an endpoint at:

$$m_{\ell\ell}^{\text{edge}} = m_{\tilde{\chi}_2^0}\sqrt{1-\left(\frac{m_{\tilde{\ell}}}{m_{\tilde{\chi}_2^0}}\right)^2}\sqrt{1-\left(\frac{m_{\tilde{\chi}_1^0}}{m_{\tilde{\ell}}}\right)^2}\,. \tag{5}$$

For the SU3 point, where the $\tilde{\ell}_{\text{R}}$ and the $\tilde{\tau}_1$ are lighter than the $\tilde{\chi}_2^0$, such an endpoint is expected in the $\ell^+\ell^-$ ($\tau^+\tau^-$) distribution for $m_{\ell\ell}^{\text{edge}} = 100.2$ GeV ($m_{\tau\tau}^{\text{edge}} = 98.3$ GeV). For the SU1 point both $\tilde{\ell}_{\text{R}}$ and $\tilde{\ell}_{\text{L}}$ as well as $\tilde{\tau}_1$ and $\tilde{\tau}_2$ are lighter than $\tilde{\chi}_2^0$, resulting in a double triangular distribution for the dilepton invariant mass with two edges.

Measuring the dilepton endpoint allows us to establish a relationship between the masses of the two lightest neutralinos and any sleptons that are lighter than the $\tilde{\chi}_2^0$. For a determination of the masses of all the particles involved in the decay chain Eq. (1), further mass distributions involving a jet are used: $m_{\ell\ell q}$, $m_{\ell\ell q}^{\text{thr}}$, $m_{\ell q(\text{low})}$ and $m_{\ell q(\text{high})}$. Since it is not possible to identify the quark from the $\tilde{q}_{\text{L}}$ decay, we make the assumption that it generates one of the two highest p_{T} jets in the event, as is normally the case if the $\tilde{q}_{\text{L}}$ is much heavier than the $\tilde{\chi}_2^0$. Hence only the two leading jets are considered. For the $m_{\ell\ell q}$ distribution a maximum value of the distribution is expected so the jet giving the lowest $m_{\ell\ell q}$ value is used. The $m_{\ell\ell q}^{\text{thr}}$ distribution is defined by the additional constraint $m_{\ell\ell} > m_{\ell\ell}^{\text{edge}}/\sqrt{2}$, giving a non-zero threshold value [6, 7]. Since a minimum is sought, the jet giving the highest $m_{\ell\ell q}$ value is used in this distribution. The distributions $m_{\ell q(\text{low})}$ and $m_{\ell q(\text{high})}$ are formed from the lower and higher m_{lq} value of each event using the same jet as for $m_{\ell\ell q}$. Both distributions have well-defined endpoints.

The theoretical values of the kinematic threshold and endpoints listed above can be calculated using the analytical expressions given in [6, 7]. The theoretical positions of the end points for the SU1, SU3 and SU4 models are summarised in Table 1.

Table 1: Value of the end points of the invariant mass distributions for the three benchmark points considered in this section. For SU1 the two endpoints correspond to the two available decay chains of the $\tilde{\chi}_2^0$ involving a right or left slepton.

Mass Distribution	SU1 end point (GeV)	SU3 end point (GeV)	SU4 end point (GeV)
$m_{\ell\ell}^{\text{edge}}$	56.1, 97.9	100.2	53.6
$m_{\tau\tau}^{\text{edge}}$	77.7, 49.8	98.3	53.6
$m_{\ell\ell q}^{\text{edge}}$	611, 611	501	340
$m_{\ell\ell q}^{\text{thr}}$	133, 235	249	168
$m_{lq(\text{low})}^{\text{max}}$	180, 298	325	240
$m_{lq(\text{high})}^{\text{max}}$	604, 581	418	340

Another advantage of the decay chain in 1 is the possibility of estimating both the SUSY combinatorial background and the Standard Model background from the data with high accuracy. The technique, known as *flavour subtraction*, is based on the fact that the signal contains two opposite-sign same-flavour (OSSF) leptons, while the background leptons come from different decay chains, which can be of the same flavour or of different flavour with the same probability. The background thus cancels in the subtraction:

$$N(e^+e^-)/\beta + \beta N(\mu^+\mu^-) - N(e^{\pm}\mu^{\mp}) \tag{6}$$

where $\beta = 0.86$ is an efficiency correction factor equal to the ratio of the electron and muon reconstruction efficiencies. The value of β is taken from [8, 9], and is assumed in the following to be known with an uncertainty of 10%.

3 Dilepton edges

3.1 Event Selection

Events with two or three isolated leptons (electrons or muons) with $p_{\mathrm{T}} > 10$ GeV and $|\eta| < 2.5$ are selected. If two leptons are selected, they are required to have opposite signs. If three leptons are present, the two opposite-sign combinations are considered and treated independently in the rest of the analysis.

In order to select SUSY events and reject the Standard Model background it is necessary to require the presence of energetic jets and missing energy. The variables used to discriminate SUSY from the SM background are the transverse missing energy, the transverse momenta of the four leading jets, the ratio between the transverse missing energy and the effective mass, and the transverse sphericity (S_T). In order to optimise the cuts on these variables, the value of:

$$S \equiv (N_{\mathrm{OSSF}} - N_{\mathrm{OSDF}})/\sqrt{N_{\mathrm{OSSF}} + N_{\mathrm{OSDF}}} \tag{7}$$

is maximized for each SUSY point, where N_{OSSF} and N_{OSDF} are the number of same-flavour and different-flavour lepton pairs respectively.

The S variable can be computed from collider data, since no Monte Carlo information is used. By maximizing the value of S we are maximizing the selection efficiency for signal events while suppressing the Standard Model and the SUSY combinatorial backgrounds.

In order to improve the sensitivity to the signal, only lepton pairs with an invariant mass $m_{\ell\ell} < m_{\ell\ell}^{\mathrm{edge}} + 10$ GeV are considered. Since the true value of the endpoint is *a priori* unknown, this choice implies that the edge has already been observed, and that afterwards the selection cuts are optimised as described here in order to improve the separation between signal and background and the measurement of the endpoint. We are thus focusing here on determining selection cuts that would allow a precise measurement of the endpoint with moderate statistics, rather than on finding the first evidence for an excess of different-flavour lepton pairs or the first evidence for the presence of the edge.

In Table 2 the optimal selection resulting from the scan is shown. For all three points a 2-jet selection is preferred, leaving out cuts on the third and fourth jets, on S_{T} and on the ratio $E_{\mathrm{T}}^{\mathrm{miss}}/M_{\mathrm{eff}}$. For the "Coannihilation" point (SU1) and the "Bulk" point (SU3) the S-value is found to be stable in an interval around the maximum value. For the "Low Mass" point (SU4) the best S-value is found for the loosest cut allowed by the available Monte Carlo samples. Hence even looser cuts may be preferred as far as the value of S is concerned. The cuts on $E_{\mathrm{T}}^{\mathrm{miss}}$ and the p_{T} of leading jet are however required in order to have a high trigger efficiency[1].

The number of signal and background lepton pairs passing the selection cuts is shown in Table 3. All numbers are for 1 fb^{-1}. The main Standard Model background is always $t\bar{t}$ accounting for about 95% of the total background. The remaining background events are from W, Z and WW, WZ, ZZ production. The background due to QCD jets is negligible. The fraction of SUSY events in the selected sample with OSSF leptons is 59% for SU1, 77% for SU3, and 80% for SU4.

Table 2: Results of the event-selection optimisation for the S-variable Eq. (7) for signal (s) and Standard Model background (b) with range limit $m_{\ell\ell} < m_{\ell\ell}^{\text{edge}} + 10$ GeV, for SU1, SU3 and SU4 for 1 fb^{-1}. The best selection is shown.

	p_{T}^{j1}	p_{T}^{j2}	p_{T}^{j3}	p_{T}^{j4}	$E_{\text{T}}^{\text{miss}}$	$E_{\text{T}}^{\text{miss}}/M_{\text{eff}}$	S_{T}	s_{OSSF}	s_{OSDF}	b_{OSSF}	b_{OSDF}	S
SU1	200	150	-	-	120	-	-	120	64	69	53	5.1
SU3	180	100	-	-	120	-	-	615	149	93	92	15.1
SU4	100	50	-	-	100	-	-	3048	1574	411	419	19.9

Table 3: Number of lepton pairs passing the selection cuts optimized for the SUSY sample SU1 (above), SU3 (middle) and SU4 (below), for 1 fb^{-1} of integrated luminosity. The contribution from $t\bar{t}$ production is indicated separately as it constitutes most of the Standard Model background. The remaining background events are from W, Z and WW, WZ, ZZ production. The background due to QCD jets is negligible.

Sample	e^+e^-	$\mu^+\mu^-$	OSSF	OSDF
SUSY SU1	56	88	144	84
Standard Model ($t\bar{t}$)	35 (35)	65 (63)	101 (99)	72 (68)
SUSY SU3	274	371	645	178
Standard Model ($t\bar{t}$)	76 (75)	120 (115)	196 (190)	172 (165)
SUSY SU4	1729	2670	4400	2856
Standard Model ($t\bar{t}$)	392 (377)	688 (657)	1081 (1035)	1104 (1063)

3.2 Reconstruction of the dilepton edge

The distribution of the invariant mass of same-flavour and different-flavour lepton pairs is shown in Fig. 1 for the SUSY benchmark points and backgrounds, after the selection cuts optimized for SU3 (left plot) and SU4 (right plot), and for an integrated luminosity of 1 fb^{-1} and 0.5 fb^{-1} respectively. It can be seen from regions where the signal does not contribute (i.e. for the Standard Model backgrounds and for $m_{\ell\ell} > m_{\ell\ell}^{\text{edge}}$ for SUSY) that the different-flavour distributions are similar to the same-flavour backgrounds.

The invariant mass distribution after flavour subtraction is shown in the left plot of Fig. 2 in the presence of the SU3 signal and for an integrated luminosity of 1 fb^{-1}. The distribution has been fitted with a triangle smeared with a Gaussian. The value obtained for the endpoint is $(99.7 \pm 1.4 \pm 0.3)$ GeV where the first error is due to statistics and the second is the systematic error on the lepton energy scale and on the β parameter [2]. This result is consistent with the true value of 100.2 GeV calculated from Eq. (5).

The right plot of Fig. 2 shows the flavour-subtracted distribution in the presence of the SU4 signal for an integrated luminosity of 0.5 fb^{-1}. The fit was performed using the function from [5] which describes the theoretical distribution for the 3-body decay in the limit of large slepton masses, smeared for the experimental resolution. This function vanishes near the endpoint and is a better description of the true distribution for SU4 than the triangle with a sharp edge. The endpoint from the fit is $(52.7 \pm 2.4 \pm$

[1]For this channel, both the lepton triggers and the trigger based on $E_{\text{T}}^{\text{miss}}$ may be relied upon. The latter are however less efficient, and they would imply different p_{T} thresholds for electrons and muons.

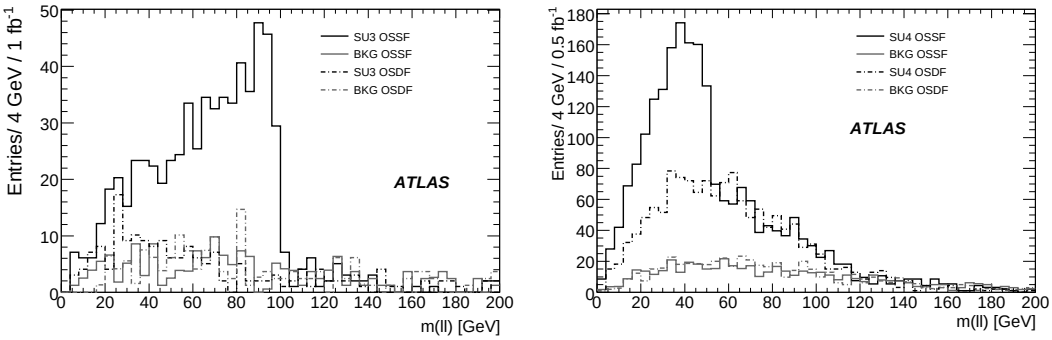

Figure 1: Left: distribution of the invariant mass of same-flavour and different-flavour lepton pairs for the SUSY benchmark points and backgrounds after the cuts optimized from data in presence of the SU3 signal (left), and the SU4 signal (right). The integrated luminosities are 1 fb^{-1} and 0.5 fb^{-1} respectively.

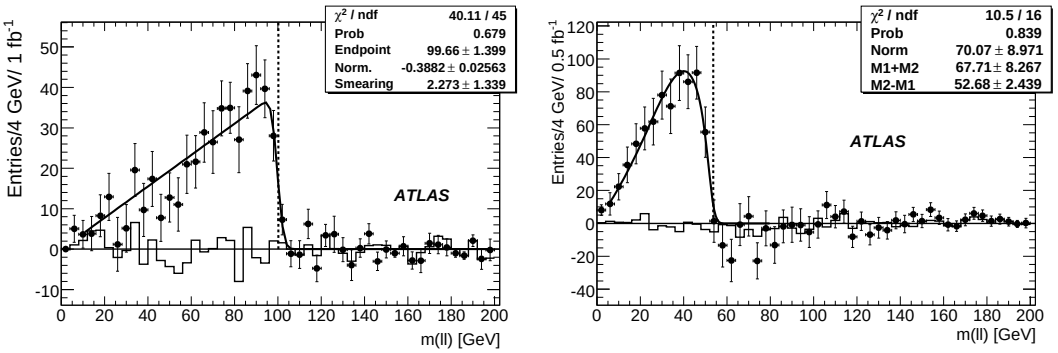

Figure 2: Left: Distribution of invariant mass after flavour subtraction for the SU3 benchmark point with an integrated luminosity of 1 fb^{-1}. Right: the same distribution is shown for the SU4 benchmark point and an integrated luminosity of 0.5 fb^{-1}. The line histogram is the Standard Model contribution, while the points are the sum of Standard Model and SUSY contributions. The fitting function is superimposed and the expected position of the endpoint is indicated by a dashed line.

0.2) GeV, consistent with the theoretical endpoint of 53.6 GeV.

Since the true distribution will not be known for data, the distribution was also fitted with the smeared triangle expected for the 2-body decay chain. This also gives a good χ^2 with an endpoint of $(49.1 \pm 1.5 \pm 0.2)$ GeV. A larger integrated luminosity will be required to use the shape of the distribution to discriminate between the two-body and the three-body decays.

In Fig. 3 the flavour-subtracted distribution of the dilepton mass is shown for the SU1 point at an integrated luminosity of 1 fb^{-1} (left) and 18 fb^{-1} (right) [2]. While there is already a clear excess of SF-OF entries at 1 fb^{-1} , a very convincing edge structure cannot be located. At 18 fb^{-1} the two edges are visible. A fit function consisting of a double triangle convoluted with a Gaussian, the latter

[2]Only 1 fb^{-1} of simulated Standard Model background was available. To scale the Standard Model contribution to higher luminosities a probability density function for the m(ll) distribution was constructed by fitting a Landau function to the 1 fb^{-1} distribution, assuming statistically identical shapes for e^+e^-, $\mu^+\mu^-$ and $e^\pm\mu^\mp$ and normalisation according to a β of 0.86. The systematic uncertainty on the endpoint determination from this procedure was estimated to be a small fraction of the statistical uncertainty.

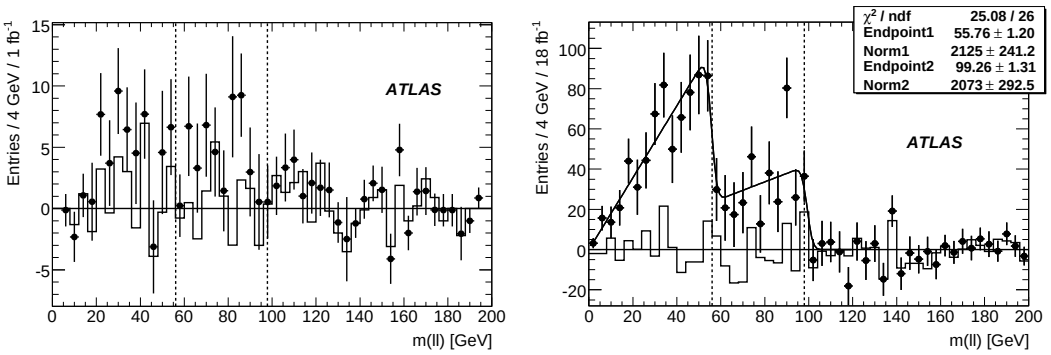

Figure 3: Distribution of invariant mass after flavour subtraction for the SU1 point and for an integrated luminosity of 1 fb^{-1} (left) and 18 fb^{-1} (right). The points with error bars show SUSY plus Standard Model, the solid histogram shows the Standard Model contribution alone. The fitted function is superimposed (right), the vertical lines indicate the theoretical endpoint values.

having a fixed width of 2 GeV, returns endpoint values of $55.8 \pm 1.2 \pm 0.2$ GeV for the lower edge and $99.3 \pm 1.3 \pm 0.3$ GeV for the upper edge, consistent with the true values of 56.1 and 97.9 GeV. As can be seen from Fig. 3 (right) the $m_{\ell\ell}$ distribution also contains a noticeable contribution from the leptonic decay of Z bosons present in SUSY events. Even though the upper edge is located close to the Z mass, adding a Z peak of fixed mass and width to the fit function only affects the endpoints at the 0.2-0.3 GeV level. However the Z peak changes the normalisation of the upper triangle so for considerations of couplings and branching ratios it should be included.

4 Leptons+Jets edges

In events selected for the dilepton analysis in the previous section, jets are added to construct further distributions as described in Sect. 2. Additional selection cuts are applied to refine the distributions:

$$m_{\ell\ell} < m_{\ell\ell}^{\text{edge}} + \Delta_1 \qquad (\text{all distributions}) \tag{8}$$

$$m_{\ell\ell q} < m_{\ell\ell q}^{\text{edge}} + \Delta_2 \qquad (m_{\ell q} \text{ distributions}) \tag{9}$$

Here $m_{\ell\ell}^{\text{edge}}$ and $m_{\ell\ell q}^{\text{edge}}$ refer to experimental values found in this and the previous section. The value Δ_1 is a small number, 10 (3.3) GeV for SU3 (SU4), to account for the fact that the edge stretches slightly beyond the fitted endpoint. One can see from Fig. 1 that this cut should be very effective for SU4, but much less so for SU3. The value Δ_2 serves a similar purpose, but since the determination of $m_{\ell\ell q}^{\text{edge}}$ is less reliable, a looser cut is used, 155 (37) GeV for SU3 (SU4).

The invariant mass distributions $m_{\ell\ell q}$ and $m_{\ell q}$ are shown in Figures 4 and 5 for both the "Bulk" point (SU3) and the "Low Mass" point (SU4) after efficiency-corrected flavour subtraction.

While the Standard Model background causes considerable bin-by-bin fluctuations for integrated luminosities $\lesssim 1$ fb^{-1}, the net contribution of entries beyond the endpoints is mainly due to combinatorics from choosing the wrong jet in a true SUSY event. For the distributions where a clear tail is visible, a straight line is assumed for the background, otherwise it is set to zero. (The statistics box of the plots indicates which background hypothesis is used.) Since the tail is due to SUSY events, it will not be known beforehand and a data-driven approach (not described here) would be required.

The lepton+jet distributions have shapes which depend on the sparticle masses [10]. Depending on the sparticle spectrum, the edge region may contain non-trivial features such as experimentally unde-

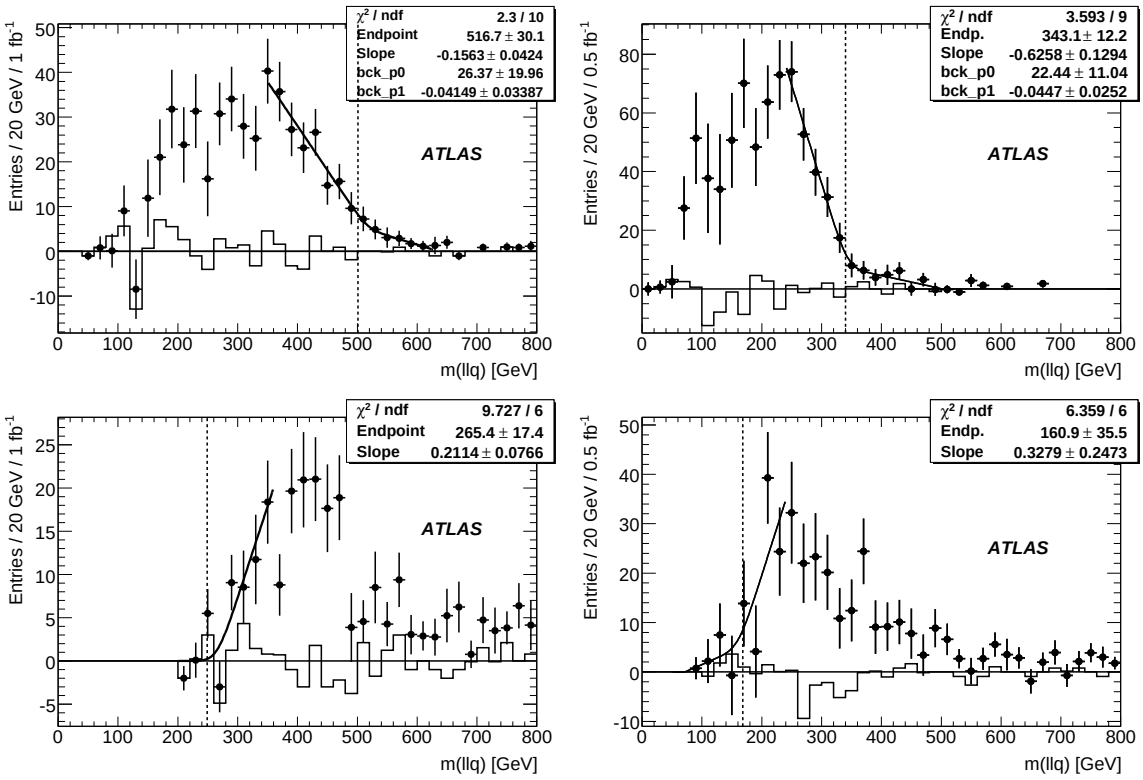

Figure 4: Efficiency-corrected flavour-subtracted distributions of $m_{\ell\ell q}$ (top) and $m^{\rm thr}_{\ell\ell q}$ (bottom) for SU3 (left) for 1 fb^{-1} and SU4 (right) with 0.5 fb^{-1} of integrated luminosity. The points with error bars show SUSY plus Standard Model, the solid histogram shows the Standard Model contribution alone. The fitted function is superimposed, the vertical line indicates the theoretical endpoint value.

tectable 'feet' containing very few events or vertical drops. For all the relevant distributions of two-body scenarios, analytic formulas describing the shape in terms of the sparticle masses are known [11, 12]. With low statistics a straight-line fit is likely to give to give a sufficiently good description in many cases. All the edges and thresholds were fitted with the following formula,

$$f(m) = \frac{1}{\sqrt{2\pi}\sigma}\int \exp\Big(-\frac{(m-m')^2}{2\sigma^2}\Big)\max\{A(m'-m^{\rm EP}),0\}\;{\rm d}m' + \max\{a+bm,0\}\;, \qquad (10)$$

where $m^{\rm EP}$ represents the endpoint (or threshold), A is the slope of the signal distribution, while a and b are the background parameters. The Gaussian smearing gives a smooth transition between the two straight lines and mimics in a simple way the smearing of an edge due to mismeasurement of jet momenta. The smearing parameter σ was fixed to 15 GeV. The fitted endpoint values were found not to be very sensitive to the choice of σ in the range 0–20 GeV. For $m_{\ell\ell q}$ and the $m_{\ell q}$ distributions the integration range is (0, $m^{\rm EP}$). For the $m^{\rm thr}_{\ell\ell q}$ distribution the lower integration limit is $m^{\rm EP}$ while some 100–200 GeV above the upper fit range is a safe upper integration limit. The endpoints resulting from the fits to the distributions in Figures 4 and 5 are summarised in Table 4.

For the "Bulk" point (SU3) the edges are found to be sufficiently well described by a straight line in Eq. (10) for the signal region, however describing the background region by a straight line results in large systematic uncertainties in the endpoint fit. In particular, the $m_{\ell\ell q}$ distribution does not have a clear edge. Even though the $m_{\ell\ell q}$ cut in Eq. (9) removes a considerable amount of background for the $m_{\ell q({\rm low})}$

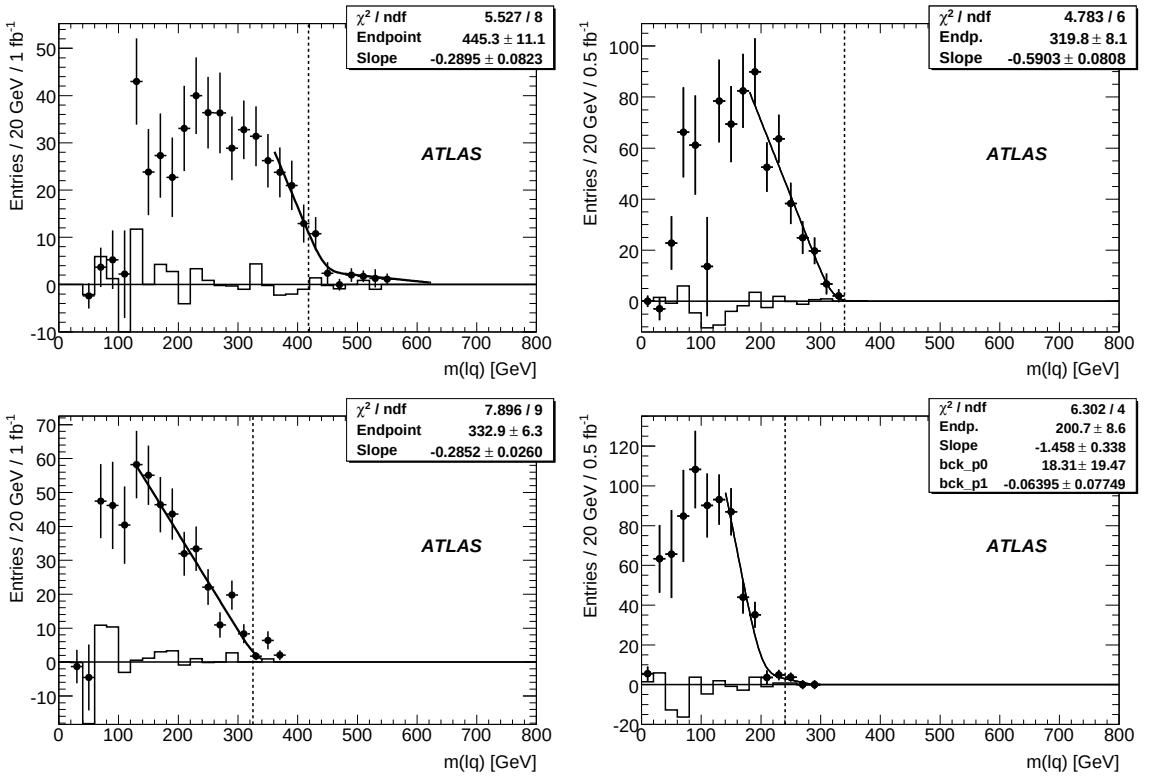

Figure 5: Efficiency-corrected flavour-subtracted distributions of $m_{\ell q(\mathrm{high})}$ (top) and $m_{\ell q(\mathrm{low})}$ (bottom) for SU3 (left) with 1 fb^{-1} and SU4 (right) with 0.5 fb^{-1} of integrated luminosity. The points with error bars show SUSY plus Standard Model, the solid histogram shows the Standard Model contribution alone. The fitted function is superimposed, the vertical line indicates the theoretical endpoint value.

distribution there is still some background left for the $m_{\ell q(\mathrm{high})}$ distribution. A systematic uncertainty is assigned to account for the background estimation for both fits. In case of $m_{\ell q(\mathrm{low})}$ a background-free fit can be made resulting in a few GeV uncertainty. The $m^{\mathrm{thr}}_{\ell\ell q}$ distribution is expected to be concave, so a systematic uncertainty is added in the estimation when fitting the threshold by a straight line fit.

For SU4, the $m_{\ell\ell q}$ and both of the $m_{\ell q}$ distributions have edges which are well described by the fit function Eq. (10). This is confirmed by the dominance of the statistical errors over the systematics ones. The $m^{\mathrm{thr}}_{\ell\ell q}$ fit is more problematic resulting in somewhat larger errors. This could be expected since the contributions from different-family and non-signal same-family peaks in this mass region, whereas they are close to vanishing in the edge regions of the other distributions. Another reason (although probably of less importance at 0.5 fb^{-1}) is that the threshold edge is concave and only moderately well described by a straight line.

While the fit values of $m^{\mathrm{edge}}_{\ell\ell q}$ and $m^{\mathrm{thr}}_{\ell\ell q}$ are compatible with the theoretical values, the fitted $m^{\mathrm{max}}_{lq(\mathrm{high})}$ and $m^{\mathrm{max}}_{lq(\mathrm{low})}$ are off by 2σ and 4σ, respectively. This comes from the fact that in SU4 the decay of $\tilde{\chi}^0_2$ is a three-body decay. In such scenarios the $m_{\ell q}$ distributions, and in particular $m_{\ell q(\mathrm{low})}$ are often so sparsely populated towards the high mass values that the endpoints are not experimentally deducible from the edges. Note, however, that there is no hint from the χ^2 of the $m_{\ell q(\mathrm{low})}$ fit that we are in such a situation. This topic is discussed further in Sect. 9.1 where endpoint relations are inverted to give sparticle masses.

Table 4: Endpoint positions for SU3 and SU4, in GeV. The first error is statistical, the second and third are the systematic and the jet energy scale uncertainty, respectively. The theoretical values are also given for ease of comparison to the left of the fitted values. The integrated luminosity assumed is 1 fb^{-1} for SU3 and 0.5 fb^{-1} for SU4.

Endpoint	SU3 truth	SU3 measured	SU4 truth	SU4 measured
$m_{\ell\ell q}^{\text{edge}}$	501	$517 \pm 30 \pm 10 \pm 13$	340	$343 \pm 12 \pm 3 \pm 9$
$m_{\ell\ell q}^{\text{thr}}$	249	$265 \pm 17 \pm 15 \pm 7$	168	$161 \pm 36 \pm 20 \pm 4$
$m_{lq(\text{low})}^{\text{max}}$	325	$333 \pm 6 \pm 6 \pm 8$	240	$201 \pm 9 \pm 3 \pm 5$
$m_{lq(\text{high})}^{\text{max}}$	418	$445 \pm 11 \pm 11 \pm 11$	340	$320 \pm 8 \pm 3 \pm 8$

5 Tau signatures

5.1 Determination of the di-tau endpoint position

The endpoint of the invariant mass distribution from two taus emerging from a $\tilde{\chi}_2^0$ decay,

$$\tilde{\chi}_2^0 \to \tilde{\tau}_1 \tau \to \tilde{\chi}_1^0 \tau^{\pm} \tau^{\mp} \,, \tag{11}$$

depends on the masses of the $\tilde{\chi}_2^0$, the $\tilde{\chi}_1^0$ and the $\tilde{\tau}_1$, and therefore can contribute to the determination of SUSY parameters.

Taus play an important role in scenarios like mSUGRA where $\tilde{\chi}_2^0$ is mostly wino, and therefore preferentially couples to *L*-type sfermions. The large *L*-*R* mixing in the stau sector significantly enhances the branching ratio for the decay $\tilde{\chi}_2^0 \to \tilde{\tau}_1^{\pm} \tau^{\mp}$ with respect to other leptons. In the scenarios SU1 and SU3 studied here, for example, the branching ratio for the decays into taus is a factor of 10 larger than for decays into electrons or muons. Since in many models (including mSUGRA) the $\tilde{\tau}_1$ is the lightest slepton, for certain values of the SUSY parameters the only allowed two body decay is $\tilde{\chi}_2^0 \to \tilde{\tau}\tau$ as $\tilde{\chi}_2^0 \to \tilde{\chi}_1^0$h, $\tilde{\chi}_2^0 \to \tilde{\chi}_1^0$Z, and $\tilde{\chi}_2^0 \to \tilde{e}e$ or $\tilde{\mu}\mu$ are kinematically forbidden.

Finally, whereas mass information about $\tilde{\chi}_1^0$ and $\tilde{\chi}_2^0$ can often be obtained more precisely from $\tilde{\chi}_2^0$ decays into electrons and muons (if these decays are open), decays into taus are needed to probe the $\tilde{\tau}$ mass parameters.

In contrast to $\tilde{\chi}_2^0$ decays into electrons or muons, the di-tau invariant mass spectrum does not have a sharp endpoint at the maximum kinematic value. Due to the presence of neutrinos from the tau decays, the $m_{\tau\tau}$ distribution (where $m_{\tau\tau}$ indicates the invariant mass of the visible decay products of the tau pair) falls off smoothly below the maximum value given by either Eq. (4) or Eq. (5). Only hadronic tau decays are considered for tau identification: the tracking-seeded reconstruction algorithm [13] is used to reconstruct taus in the "Coannihilation" point (SU1), while the calorimeter-seeded algorithm [13] is used for the "Bulk" point model (SU3). This choice is motivated by the higher efficiency of the former in reconstructing the low p_{T} taus that are present in the SU1 model.

The SU1 point also has a considerably lower cross-section than the SU3 point, so different selection procedures are used to maximize the signal significance. For the SU3 point events are selected with two taus, $E_{\text{T}}^{\text{miss}} > 230$ GeV, and at least four jets with p_{T} greater than 220, 50, 50, 30 GeV respectively. For the SU1 point the cut on $E_{\text{T}}^{\text{miss}}$ is relaxed to 100 GeV and at least two jets with p_{T} greater than 100 and 50 GeV respectively. In addition, an elliptical cut in the space of $E_{\text{T}}^{\text{miss}}$ and the sum $p_{\text{T}}(1) + p_{\text{T}}(2)$ of the two highest p_{T} jets is applied to SU1. The semi-axes of the ellipse are 450 GeV for $E_{\text{T}}^{\text{miss}}$ and 500 GeV for the sum of jet p_{T}. This cut exploits the anticorrelation between $E_{\text{T}}^{\text{miss}}$ and $(p_{\text{T}}(1) + p_{\text{T}}(2))$ which is different for the signal and the Standard Model background.

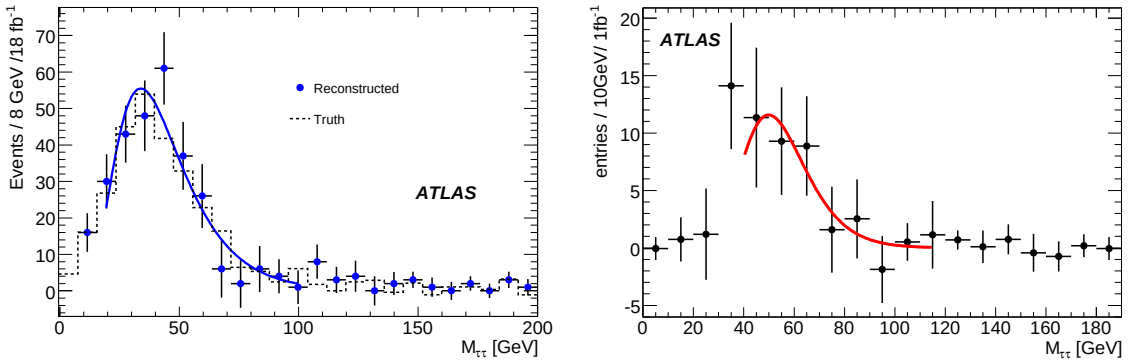

Figure 6: Invariant mass distribution of opposite-sign tau pairs with same-sign tau distribution subtracted, for the SU1 (18 fb^{-1}, left) and SU3 scenarios (1 fb^{-1}, right). The dashed histogram in the left plot shows the distribution at the generator level, while points show the reconstruction-level distribution.

The invariant mass distribution emerging after the above cuts are applied is shown in Figure 6 for the SU1 and SU3 scenarios, where the corresponding distribution of two taus with the same sign of electric charge is subtracted from tau pairs with opposite sign in order to reduce combinatorial background. This is possible because uncorrelated and fake taus should arise about as often with the same charge as with opposite charges. To decrease the SUSY background further, the two taus arising from the same decay chain are required to have a maximum separation $\Delta R < 2$ in the η-ϕ-plane.

The following log normal function with three parameters, inspired by [14], is used to fit the $m_{\tau\tau}$ distribution:

$$f(x) = \frac{p_0}{x} \cdot \exp\left(-\frac{1}{2p_2^2}(\ln(x) - p_1)^2\right) \tag{12}$$

This function does not contain the endpoint position explicitly, but approaches the x-axis asymptotically. The endpoint is then derived from the inflection point m_{IP} of the fit function:

$$m_{IP} = \exp\left(-\frac{1}{2}p_2^2\left(3 - \sqrt{1 + \frac{4}{p_2^2}}\right) + p_1\right) \tag{13}$$

using a Monte Carlo-based calibration procedure.

The inflection point obtained for 14 SU3-like models is plotted against the theoretical endpoint value for each of these models. The SU3-like points are generated using the ATLAS fast simulation program [15] and varying the masses of the $\tilde{\chi}_2^0$, the $\tilde{\tau}_1$ and the $\tilde{\chi}_1^0$ separately, while keeping the other two masses fixed. In Figure 7 the inflection point is plotted as a function of the endpoint m_{EP} and fitted with a straight line, yielding the following calibration function:

$$m_{IP} = (0.47 \pm 0.02) m_{EP} + (15 \pm 2)\ \text{GeV} \tag{14}$$

The covariance between the slope and the axis intercept is -0.034 GeV.

The fit using function Eq. (12) for the SU1 and SU3 models is shown in Fig. 6 giving an inflection point at $m_{IP} = 48 \pm 3$ GeV and $m_{IP} = 62 \pm 8$ GeV respectively, which translates into endpoints at $m_{EP} = (70 \pm 6.5^{\text{stat}} \pm 5^{\text{syst}})$ GeV (SU1) and $(102 \pm 17^{\text{stat}} \pm 5.5^{\text{syst}})$ GeV (SU3) using the calibration relation in Eq. (14). The systematic uncertainty is dominated by the fitting procedure and is evaluated by changing the binning and fit ranges. The effects of 1% and 5% jet energy scale uncertainies have been tested and found to introduce an additional systematic uncertainty on the endpoint measurement well below 3%, so

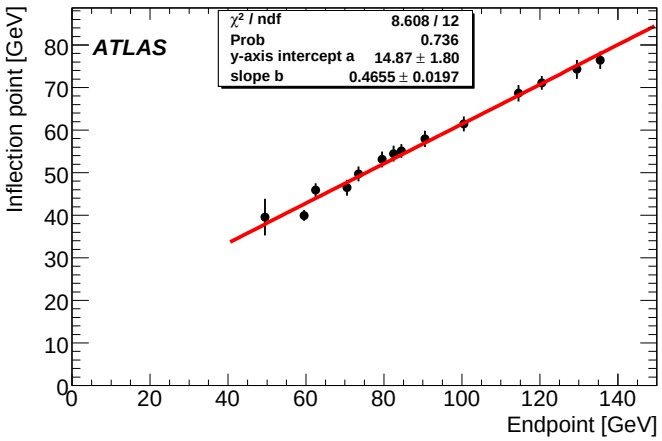

Figure 7: Calibration curve showing the relation between the position of the inflection point (measured and fitted with function Eq. (12) after ATLFAST based detector simulation) and the endpoint (calculated with equation Eq. (5)) of the di-tau mass distribution. The SU3 point is not included.

they are negligible compared to the systematic error introduced by the fitting procedure. The theoretical expectation for the SU1 (SU3) endpoint is 78 GeV (98 GeV). The difference between the theoretical and the extracted endpoint comes from the fitting and fit-calibration procedure rather than from detector effects. As Fig. 6 (left) shows, the generator-level distribution of the visible products is close to the reconstruction-level distribution and after fitting gives an endpoint value of 70 GeV for the SU1 scenario which is the same as for the reconstructed distribution.

5.2 Impact of the tau polarization on the di-tau mass spectrum

The method discussed in the previous section assumes a fixed polarization of the two taus from the $\tilde{\chi}_2^0$ and therefore neglects the effect of the polarization on the invariant mass spectra. However, the polarization of the taus from the decay cascade can vary significantly between different SUSY models. Polarization effects on the di-tau mass distribution are studied by simulating samples of events where the polarization of the two taus from the decay Eq. (11) is allowed to vary. The ATLAS fast simulation program [15] is used to simulate a data sample equivalent to 51 fb^{-1} of data.

Parity violation in weak interactions in conjunction with momentum and angular momentum conservation leads to a correlation between the visible tau energy and the polarization of the tau. In case of the decay $\tau- > \nu_\tau\pi^-$, since the pion is a scalar particle the neutrino spin is forced to be parallel to that of the tau and therefore the fixed neutrino helicity determines the neutrino momentum direction. Thus, to conserve momentum, the direction of the pion momentum is forced to be parallel or antiparallel to that of the tau depending on the tau polarization. This leads to the pion getting a boost parallel or antiparallel to the tau momentum resulting in harder and softer pions. This affects the di-tau mass spectrum, as shown in Fig. 8. The curves in the plot are theoretical predictions from [16]. The invariant masses of taus with left chirality (LL) are on average smaller than for right (RR) taus.

For decays via the vector mesons ρ and a_1, the momentum of the vector meson has the same (opposite) direction as in the case of pions for longitudinal (transverse) polarization of the vector meson.

Adding all hadronic tau decay modes finally yields the invariant mass distributions shown in Figure 8 for the chirality options LL, RR and LR/RL. The position of the trailing edge is clearly shifted for different polarizations whereas the shape difference calculated in [16] is barely visible after detector

simulation.

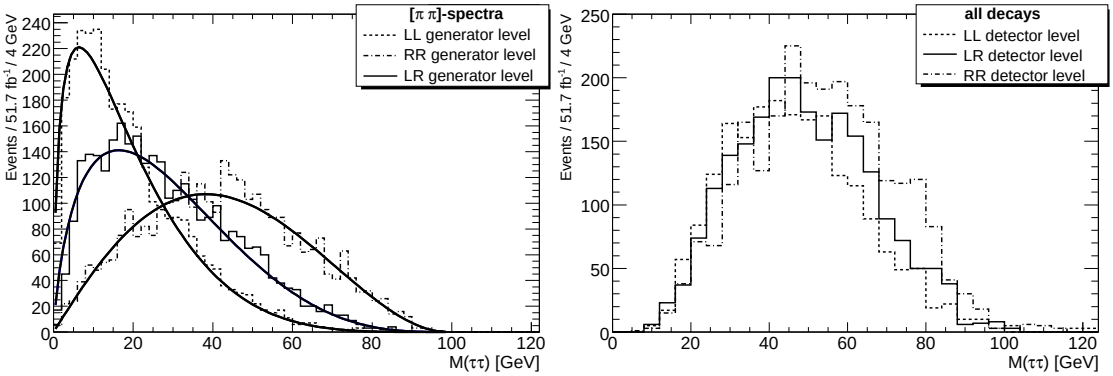

Figure 8: Left: Di-tau invariant mass spectrum for $\tau \to \pi\nu_\tau$ decays as obtained from Monte Carlo truth information together with the expectation from theory. Right: Di-tau invariant mass spectrum for all hadronic decays after an ATLFAST based detector simulation. Both plots show the mass distributions for the chirality states *LL*, *RR* and *LR*/*RL*.

As a consequence, the inflection point of the distribution is shifted due to polarization effects. The maximum difference in the inflection point measurement $\Delta m_{IPA}(RR-LL)$ has been found to be 7 GeV which is comparable to the statistical error on the position of the inflection point presented in the previous section. Without additional information on the tau polarization we might quickly reach a point where it is not possible to improve the di-tau endpoint measurement. In this case the achievable precision for an integrated luminosity of 1 fb^{-1} for the SU3 model is:

$$m_{\tau\tau}^{\max} = 102 \pm 17^{\text{stat}} \pm 5.5^{\text{syst}} \pm 7^{\text{pol}}$$

The uncertainty due to the polarization effects dominates over the other systematic uncertainties and therefore needs special attention. A study of the different polarization dependencies of the decay kinematics for different decay modes of the tau might be helpful. As the emission direction of vector mesons is opposite for longitudinal and transversal states the net effect is determined by the branching ratio into the two states. It turns out that for the a_1 there are as many longitudinal as transverse polarized whereas for the ρ there are more longitudinal vector mesons, leading to different polarization dependencies.

6 $\tilde{q}_{\text{R}}$ pair reconstruction

Events where a pair of $\tilde{q}_{\text{R}}$ particles is produced, and where each decays through the process

$$\tilde{q}_{\text{R}} \to \tilde{\chi}_1^0 q \tag{15}$$

lead to a characteristic signature with two high-p_{T} jets and large $E_{\text{T}}^{\text{miss}}$ from the escaping neutralinos. $\tilde{q}_{\text{R}}$ pair production represents about 10% (5%) of the total SUSY production cross-section for the "Bulk" point SU3 ("Low Mass" SU4). For both points (and more generally in most of mSUGRA parameter space) the $\tilde{q}_{\text{R}}$ decays almost entirely through the process in Eq. (15).

Events with large $E_{\text{T}}^{\text{miss}}$ and a pair of high-p_{T} jets are selected by requiring:

- $E_{\text{T}}^{\text{miss}} > \max(200\text{ GeV},\ 0.25M_{\text{eff}})$ and $M_{\text{eff}} > 500$ GeV
- Two jets with $p_{\text{T}} > \max(200\text{ GeV}, 0.25M_{\text{eff}})$, $|\eta| < 1$ and $\Delta R > 1$

Table 5: The total event yield and the number of Standard Model background events satisfying selection criteria for m_{T2} reconstruction, signal-to-background ratio and signal statistical significance. Only errors from the detector systematic uncertainties are quoted.

	Integrated luminosity (fb^{-1})	Event yield	Standard Model	S/B_{SM}	$S/\sqrt{B_{SM}}$
SU3	1.0	282 ± 20	18	14.7 ± 1.1	62.2 ± 4.7
SU4	0.5	258 ± 65	9	27.7 ± 7.2	83.0 ± 21.7

- No additional jet with $p_{\mathrm{T}} > \min(200\ \mathrm{GeV}, 0.15 M_{\mathrm{eff}})$
- No isolated leptons and no jets tagged as b jets
- Transverse sphericity $S_T > 0.2$

These selection cuts are tuned using the information from the event generation to select $\tilde{q}_{\mathrm{R}}$ pair production.

The systematic uncertainty originating from the jet and $E_{\mathrm{T}}^{\mathrm{miss}}$ energy scale and resolution [2] change the event yield by 7% for the case of SU3 and by 25% for the case of SU4. The systematic effect on the energy scale and resolution of leptons is negligible.

The total event yield and the number of Standard Model background events satisfying the selection criteria for 1 fb^{-1} for SU3 and 0.50 fb^{-1} for SU4 are given in Table 5 together with the signal-to-background ratio and the signal statistical significance.

To reconstruct the $\tilde{q}_{\mathrm{R}}$ mass we use the the m_{T2} variable [2, 17, 18], sometimes referred to as "stranverse" mass. This variable uses the kinematic features of the $\tilde{q}_{\mathrm{R}}$ decays to reconstruct $m_{\tilde{q}_{\mathrm{R}}}$[3] making the assumption that $m_{\tilde{\chi}_1^0}$ is known from the measurements in Section 4. The m_{T2} distributions for the SU3 and SU4 points are shown in Figure 9. As is common for SUSY measurements, the distribution is expected to have an edge at $m_{\tilde{q}_{\mathrm{R}}}$ rather than a peak. A linear fit is applied to the right part of the distribution to determine the edge position at $590 \pm 9(\mathrm{stat})^{+13}_{-6}(\mathrm{sys})$ GeV for SU3 and $421 \pm 17(\mathrm{stat})^{+10}_{-3}(\mathrm{sys})$ GeV for SU4. This can be compared to the expected positions of $m_{\tilde{q}_{\mathrm{R}}} = 611$ GeV for SU3 and $m_{\tilde{q}_{\mathrm{R}}} = 406$ GeV for SU4. The systematic error accounts for the choice of the fit limits as well as the jet energy scale systematic.

7 Light stop signature

In the "Low Mass" benchmark point (SU4), the SUSY masses are all in the range $m_{\tilde{\chi}_1^0} = 60\ \mathrm{GeV} < m < m_{\tilde{t}_2} = 445\ \mathrm{GeV}$. The stop $\tilde{t}_1$ is light ($m_{\tilde{t}_1} = 206$ GeV) and always decays by $\tilde{t}_1 \to \tilde{\chi}_1^{\pm} b$. A detailed analysis of the phenomenology of this point can be found in [19].

At this SU4 benchmark point the light stop is produced in the gluino decay Eq. (3) which has a branching ratio of 42%. Associated gluino production with a $\tilde{q}_{\mathrm{L}}$ or $\tilde{q}_{\mathrm{R}}$ followed by the decay in Eq. (3) occurs in $\sim 18\%$ of all SU4 events. In the decay Eq. (3) the final state tb invariant mass distribution has

[3] For the benchmark point considered here, the effect of the SUSY background (i.e. events other than the $\tilde{q}_{\mathrm{R}}$ pair production which pass the event selection) on the position of the edge is small. This has also been shown to be true for other benchmark points [10]. However, the identification of the edge as a measurement of the $\tilde{q}_{\mathrm{R}}$ mass may not hold for all the SUSY parameter space.

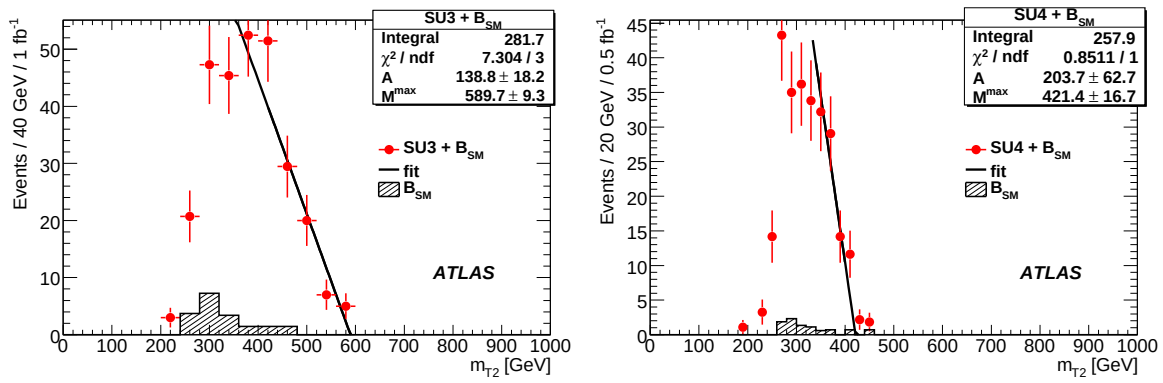

Figure 9: Fit of the sum of the reconstructed m_{T2} distributions in the selected SUSY and the remaining Standard Model background events with 1 fb^{-1} for SU3 and 0.5 fb^{-1} for SU4.

the upper kinematic endpoint:

$$M^{\max}(tb) = \left[m_t^2 + \frac{m_{\tilde{t}_1}^2 - m_{\tilde{\chi}_1^\pm}^2}{2m_{\tilde{t}_1}^2} \left((m_{\tilde{g}}^2 - m_{\tilde{t}_1}^2 - m_t^2) + \sqrt{(m_{\tilde{g}}^2 - (m_{\tilde{t}_1} - m_t)^2)(m_{\tilde{g}}^2 - (m_{\tilde{t}_1} + m_t)^2)} \right) \right]^{1/2}. \quad (16)$$

With $m_{\tilde{g}} = 413$ GeV, $m_{\tilde{\chi}_1^\pm} = 113$ GeVand a top mass of 175 GeV, Eq. (16) gives

$$M^{\max}(tb) \sim 300 \text{ GeV}. \quad (17)$$

The other significant decays at this benchmark point which lead to the same final state are:

$$\tilde{g} \rightarrow \tilde{b}_1 b \rightarrow \tilde{\chi}_1^\pm tb, \quad (18)$$
$$\tilde{g} \rightarrow \tilde{b}_1 b \rightarrow \tilde{t}_1 W b \rightarrow \tilde{\chi}_1^\pm bbW, \quad (19)$$
$$\tilde{g} \rightarrow \tilde{b}_2 b \rightarrow \tilde{\chi}_1^\pm tb, \quad (20)$$
$$\tilde{g} \rightarrow \tilde{b}_2 b \rightarrow \tilde{t}_1 W b \rightarrow \tilde{\chi}_1^\pm bbW. \quad (21)$$

The final states from the decays Eq. (19) and Eq. (21) are equivalent to the final state from the decay Eq. (3) if the bW invariant mass is close to the top mass. Associated gluino production with left or right squark followed by these decays occurs in 4% (Eq. (18)), 9% (Eq. (19)), 0.1% (Eq. (20)) and 0.9% (Eq. (21)) of all SU4 events. Due to the small mass difference between $\tilde{g}$ and the $\tilde{b}_1$ or $\tilde{b}_2$, the final states Eq. (18) and Eq. (19) can be suppressed by imposing a minimum cut on the p_T of the b jet, while the final states Eq. (20) and Eq. (21) are suppressed because b jets originating from the gluino decay $\tilde{g} \rightarrow \tilde{b}_2 b$ are on the average below the detection threshold.

In order to extract light stop signal from the $\tilde{g}\tilde{q}$ events where gluino decays to stop and top, the final state tb invariant mass distribution in Eq. (3) is reconstructed for top quark decays into hadronic final states only:

$$t \rightarrow Wb \rightarrow qqb \quad (22)$$

making no assumptions about the $\tilde{\chi}_1^\pm$ decay modes which dominantly produce two additional light-quark jets. The hardest jet in the event is assumed to be the light-quark jet originating from the decay of the left or right squark produced in association with the gluino.

We select jets with $p_T > 20$ GeVand $|\eta| < 2.5$. In this range the b-tagging efficiency is about 60% [1]. The event selection requires the following:

- At least 5 jets in the event with $p_{\mathrm{T}} > 30$ GeV, where
  - The hardest jet is a light-quark jet with $p_{\mathrm{T}} > 100$ GeV,
  - 2 and only 2 jets are tagged as b jets and they have $p_{\mathrm{T}} > 50$ GeV and
  - At least 2 of the light-quark jets have $p_{\mathrm{T}} > 30$ GeV
- $E_{\mathrm{T}}^{\mathrm{miss}} > 150$ GeV, $M_{\mathrm{eff}} > 400$ GeV, $E_{\mathrm{T}}^{\mathrm{miss}}/M_{\mathrm{eff}} > 0.2$
- $S_T > 0.1$.

Of the Standard Model backgrounds simulated, only events from our $t\bar{t}$ and QCD samples satisfy these selection criteria. No $W+$jets or $Z+$jets events pass the cuts.

The dominant detector-performance systematic uncertainties come from the jet and $E_{\mathrm{T}}^{\mathrm{miss}}$ energy scale and resolution. Assuming that the uncertainties for 200 pb^{-1} are the same as for 100 pb^{-1}, i.e. 10% uncertainties on the jet and $E_{\mathrm{T}}^{\mathrm{miss}}$ energy scale and resolution [20], and including 5% uncertainty on the b-tagging efficiency, the resulting systematic uncertainty in the number of selected events would be $\sim 40\%$ for SU4 and $\sim 50\%$ for $t\bar{t}$.

The top-bottom invariant mass is reconstructed for events satisfying the selection criteria for the light stop search:

- Excluding the hardest jet, all light-quark jets with $p_{\mathrm{T}}^{\mathrm{jet}} > 30$ GeV are combined into dijet pairs.
- All such pairs with invariant mass within the window $|m_{jj} - m_W| < 15$ GeV are combined with each of the two b jets and the bjj combination with invariant mass closest to the top mass is selected.
- The four-vectors of this dijet pair are rescaled such that $m_{jj} = m_W$ and m_{bjj} is recalculated and accepted as top candidate if $|m_{bjj} - m_{top}| < 30$ GeV.
- The same bjj combination is combined with the other b jet and m_{tb} calculated, with the requirement that the angle between top and bottom be $\Delta R(t,b) < 2$.

The W sideband method [21–23] is used to estimate SUSY combinatorial background originating from supersymmetric processes in which jet pairs accidentally have an invariant mass within our W-mass window, and so fake W bosons. The sidebands used are the regions of dijet invariant mass 30 GeV below and 30 GeV above our W-mass window. The fake W boson contribution to the m_{tb} distribution is evaluated as the average contribution of the jet pairs from the W sidebands after they have been scaled linearly to the W mass zone and the procedure of m_{tb} reconstruction has been repeated.

The numbers of signal and the remaining Standard Model background events, together with the total event yield at 200 pb^{-1}, are listed in Table 6. The m_{tb} distribution reconstructed in signal events without the subtraction of the SUSY combinatorial background and the SUSY combinatorial background itself are plotted in Figure 10. The contribution of fake W bosons in SU4 is higher than the number of events remaining after subtraction.

The m_{tb} distributions before and after the subtraction of the SUSY combinatorial background are shown in Figure 10. The background-subtracted distirbution is fitted in order to extract the endpoint. The resulting m_{tb} distribution is fitted with a triangular function smeared with a Gaussian:

$$f(M) = A\int_{-1}^{1} e^{-\frac{(M-M^{\max}\sqrt{\frac{1+x}{2}})^2}{2\sigma^2}}dx + (a+bM),$$

where the kinematic endpoint, $M^{\max}$, and the smearing, σ, are two of the five fit parameters. The smearing, σ, models the experimental resolution of the reconstructed m_{tb}. The position of the upper kinematic

Table 6: The number of signal and remaining Standard Model background events and the total event yield at 200 pb^{-1}. The last row gives the signal-to-background ratio. The errors quoted are from detector sources of systematic uncertainty.

L = 200 pb^{-1}	Initial selection	$\lvert m_{bjj} - m_t \rvert < 30$ GeV		$\Delta R(t,b) < 2$	
		without W sub.	with W sub.	without W sub.	with W sub.
SU4	963	537	224	267	120
$t\bar{t}$	99	28	13	9	4
QCD	6	3	2	3	2
Total	1068 ± 426	568 ± 225	239 ± 95	279 ± 109	126 ± 50
SU4 / ($t\bar{t}$ + QCD)	9.2 ± 4.1	17.3 ± 7.3	14.9 ± 6.3	22.3 ± 9.1	20.0 ± 8.3

endpoint obtained from the 5-parameter fit (Figure 10) is $M^{\max} = 297 \pm 9$ GeV with $\sigma = 28 \pm 7$ GeV corresponding to $\sim 10\%$ of the $M^{\max}$ value. The position of the upper kinematic endpoint obtained from the 4 parameters fit is $M^{\max} = 298 \pm 6(\text{stat})^{+16}_{-41}(\text{sys})$ GeV with σ set to 10% of $M^{\max}$. The expected value of m_{tb} given by Eq. (17) is 300 GeV.

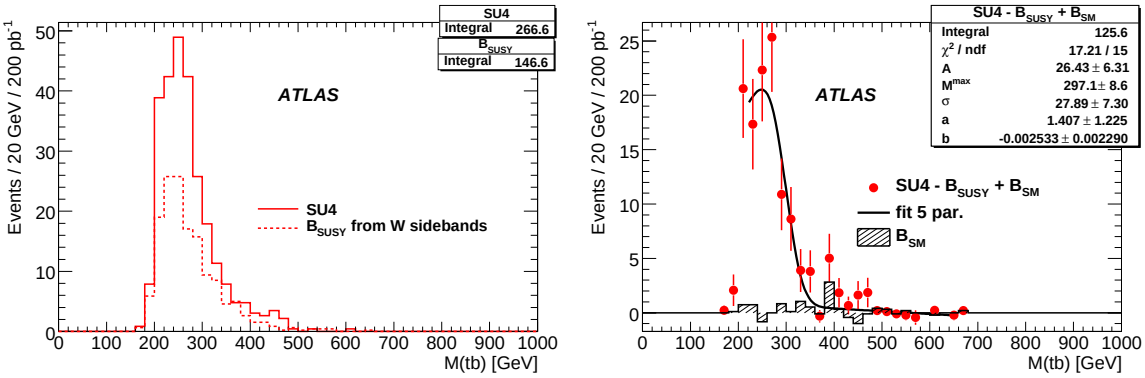

Figure 10: Left: Reconstructed m_{tb} distributions in signal and SUSY combinatorial background events. Right: The 5 parameters fit of the sum of the reconstructed m_{tb} distributions in signal and the remaining Standard Model events after the subtraction of the SUSY combinatorial background; all at 200 pb^{-1}.

8 Higgs signatures in SUSY events

In the context of supersymmetric models, Higgs bosons at the LHC can be produced in proton collisions either through direct interaction of Standard Model particles, such as gluon-gluon fusion, or through the decay of a supersymmetric particle produced in the initial interaction.

We will consider the possibility of observing the lightest CP-even h boson via the second mechanism. In this case, a missing transverse energy signature, typical of R-parity conserving SUSY scenarios, can be reconstructed in association with the Higgs boson and exploited to reduce the background, making it possible to study the dominant decay channel $h \to b\bar{b}$, which is otherwise hidden by the enormous QCD continuum.

Within mSUGRA the most promising source of Higgs production is the decay of a second-lightest neutralino. Indeed, $\tilde{\chi}_2^0 \to \tilde{\chi}_1^0 h$, if open, dominates the $\tilde{\chi}_2^0 \to \tilde{\chi}_1^0 Z$ mode, because the two lightest neutralinos are basically gauginos, so that the higgsino-gaugino-Higgs vertex is enhanced with respect to the higgsino-higgsino-gauge one. However, if the sleptons are lighter than the $\tilde{\chi}_2^0$, the decay channels $\tilde{\ell}^{\pm}\ell^{\mp}$ and $\tilde{\nu}_\ell \bar{\nu}_\ell$ open up, dominating the $\tilde{\chi}_2^0$ width. As a consequence, we expect that mSUGRA points interesting for Higgs searches will not show a clear di-lepton signature. The benchmark point chosen for this analysis is SU9, at which $BR(\tilde{\chi}_2^0 \to \tilde{\chi}_1^0 h) \sim 87\%$.

Exploiting the capabilities of the ATLAS detector in missing transverse energy measurement and b tagging, the passage of weakly interacting particles may be revealed and a $b\bar{b}$ pair with invariant mass peaking around the Higgs mass can be reconstructed.

Standard Model events with similar signatures which are backgrounds for this analysis, include events with neutrino production causing a genuine $E_{\mathrm{T}}^{\mathrm{miss}}$ signal and QCD events with fake $E_{\mathrm{T}}^{\mathrm{miss}}$ generated by instrumental effects. SUSY events can themselves constitute a background, as they contain many b-jet candidates, both true and mistagged. These can be divided into two categories: SUSY cascades without and with production of a Higgs decaying to $b\bar{b}$. In the latter case potential signal events may be incorrectly reconstructed as the selected $b\bar{b}$ pair is not the one coming from the Higgs decay. We will refer to the former type simply as "SUSY background" and to the latter as "combinatorial background".

The following selection cuts are applied:

1. $E_{\mathrm{T}}^{\mathrm{miss}} > 300$ GeV;
2. two light-flavoured jets with $p_{\mathrm{T}} > 100$ GeV;
3. two b jets with $p_{\mathrm{T}} > 50$ GeV;
4. no leptons with $p_{\mathrm{T}} > 10$ GeV.

The first two cuts are typical of SUSY analyses, while the pupose of the last cut is to suppress backgrounds from $t\bar{t}$ and W production.

When three or more b jets with transverse momentum greater than 50 GeV are found in a single event, the second and third leading-p_{T} b-jets are chosen as the candidate Higgs decay pair. This is because an important source of b jets is the decay of a bottom squark to $\tilde{\chi}_2^0$ and b and since $m_{\tilde{b}} - m_{\tilde{\chi}_2^0} \sim 500\,\mathrm{GeV} > m_h$ the sbottom daughters get more allowed phase space than the Higgs daughters and thus, in general, higher p_{T}.

In Figure 11 (left) the invariant mass of the selected b jet pairs is shown assuming 10 fb^{-1} of collected luminosity. The shaded histogram corresponds to the sum of the Standard Model backgrounds, the dashed and dotted lines are the SUSY and combinatorial backgrounds respectively. These last two, together with the $t\bar{t}$ production, are the most important backgrounds. The black curve is the result of a least squares fit to a Gaussian function, representing the Higgs resonance, superimposed on a second degree polynomial background. The estimated number of signal and background events is obtained by counting the b pairs with invariant mass inside a ± 25 GeV range around the fitted peak centre. The signal significance, computed in the Gaussian approximation as the number of signal events over the square root of the background, is about 14.

Table 7 summarises the expected event rates after the application of the selection cuts and after the additional mass window request.

SUSY mass spectrum information is reconstructed in the SU9 model by studying the decay:

$$\tilde{q}_{\mathrm{L}} \to \tilde{\chi}_2^0 q \to \tilde{\chi}_1^0 h q. \tag{23}$$

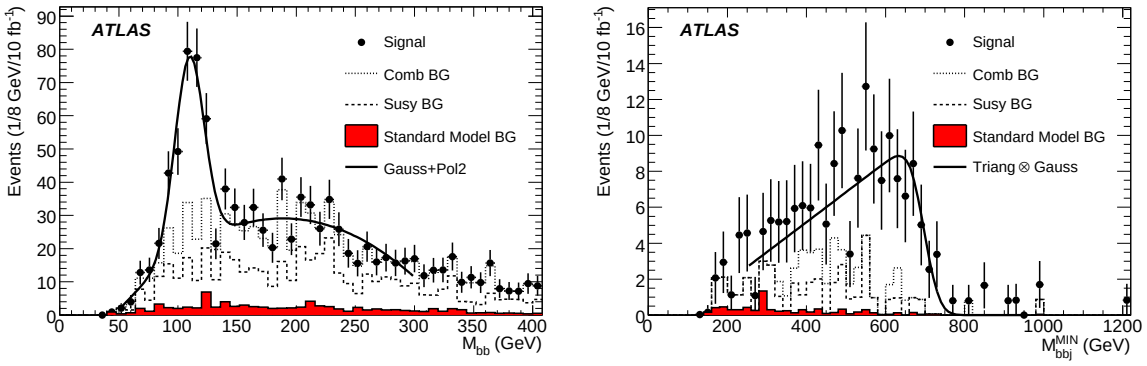

Figure 11: Invariant mass of the selected b-jet pairs (left) and invariant mass of the system consisting of the Higgs plus the jet minimising m_{hq} (right) for 10 fb^{-1} of integrated luminosity.

Table 7: Summary of the number of expected SUSY and Standard Model events after the application of the different selection cuts, for 10 fb^{-1} of integrated luminosity.

SU9	Signal	Comb BG	Susy BG
No cuts		11050	21950
Cut *1, 2, 3*	356	946	908
Cut *4*	230	449	433
$\pm$25 GeV mass window	179	76	76

Standard Model	$t\bar{t}$	Z	W	$b\bar{b}$
Cut *1, 2, 3*	133	12	22	43
Cut *4*	53	8	10	21
$\pm$25 GeV mass window	11	2	4	4

As a consequence of two-body kinematics, the invariant mass of the Higgs-quark system shows both a minimum and a maximum value, related to different combinations of the masses of the SUSY particles involved.

The events passing the previous selection cuts, including the mass window cut, are also required to have at least one b jet with $p_{\mathrm{T}} > 100$ GeV. Furthermore, a veto is imposed on additional b-tagged jets with $p_{\mathrm{T}} > 50$ GeV. This will result in fewer signal events, but also in a reduced background contamination yielding a clear distribution shape, albeit with lower signal significance. As in Section 4 the quark from the $\tilde{q}_{\mathrm{L}}$ is expected to produce one of the two highest-p_{T} jets and the two distributions m_{hq}^{min} and m_{hq}^{max} are reconstructed using the jet that maximises and minimises the m_{hq} value, respectively. Since the background events will tend to concentrate toward low mass values, the m_{hq}^{min} (Figure 11, right) is used to determine the mass upper limit $m_{hq,\mathrm{edge}}$. The $m_{hq,\mathrm{threshold}}$ value can determined from the m_{hq}^{min} distribution.

The mass edge value is obtained by fitting a triangular shape convolved with a Gaussian:

$$m_{hq,\mathrm{edge}} = 695 \pm 15\ (\mathrm{stat}) \pm 3\ (\mathrm{syst}) \pm 35\ (\mathrm{JES}),$$

to be compared to the true value of 732 GeV. The statistical uncertainty is the error on the fitted parameter,

while the systematic comes from the parameter dependence on the fitting boundaries. An additional 5% systematic error is expected from the jet energy scale (JES) uncertainty.

The mass threshold evaluation is more challenging, since background events tend to populate the low mass region. For an integrated luminosity of 10 fb^{-1}, it was not possible to fit to the mass distribution. However, high-statistics studies performed with a fast simulation of the ATLAS detector show that a mass threshold value could be extracted from 300 fb^{-1} of collected data, expected after 3 years of LHC running at design luminosity.

9 Mass and parameters measurement

This section is devoted to the extraction of SUSY mass spectra and parameters from the measurements described in the previous sections of this note. As an example, the mSUGRA benchmark points SU3 (with a luminosity of 1 fb^{-1}) and SU4 (with 0.5 fb^{-1}) are chosen to give a flavour of what might be expected in the initial phase of the experiment in case of a rather optimistic SUSY scenario. The small luminosity at this stage results in a limited number of available measurements and rather large uncertainties. In such a situation only models with few parameters can be fitted. In Section 9.1 the masses of the decay chain Eq. (1) are derived from the measurement of the kinematic endpoints described in Section 3 and 4. In Sections 9.2 to 9.4 the parameters of the mSUGRA model are derived instead.

9.1 Measurement of masses from SUSY decays

We use the information from the experimentally measured endpoints to extract the masses of the SUSY particles. As described earlier in this paper, in many cases analytic expressions have been deduced for the endpoints expressed in terms of the masses. Examples are shown in Eq. (4) and Eq. (5). If sufficient endpoints are known, then the masses can be deduced. Here we use a numerical χ^2 minimization based on the MINUIT package to extract the SUSY particle masses from a combination of endpoints. We define the χ^2 as

$$\chi^2 = \sum_{k=1}^{n} \frac{(m_k^{\max} - t_k^{\max}(m_{\tilde{\chi}_1^0}, m_{\tilde{\chi}_2^0}, m_{\tilde{\ell}_R}, m_{\tilde{q}_L}))^2}{\sigma_k^2}. \quad (24)$$

For each of the n endpoint measurements, k, the quantities $m_k^{\max}$ and σ_k denote the fit value and its uncertainty respectively. The t_k^{max} are the theoretical endpoint expressions [6, 10], which contain as parameters the masses of the two lightest neutralinos, the scalar quark $\tilde{q}_L$, and (for the two-body decay chain only) the scalar lepton $\tilde{\ell}_R$. As a starting point for the fit the generated masses are used. The masses are constrained to be positive in the fit and the mass hierarchies from the model input are enforced.

With the statistics expected for an integrated luminosity of 1 fb^{-1} (0.5 fb^{-1}) for SU3 (SU4) we observe instabilities in the fit. Depending on the fluctuation and precision of the endpoint measurements the fit does not converge. Some of the measured endpoints have shown possible deviations from the generated values of up to several standard deviations. Systematic effects to explain such discrepancies are identified in earlier sections of this article. Significant deviations distort the results and also negatively affect the fit convergence, especially in the presence of degenerate kinematic endpoint equations. We also note large correlations (typically larger than 95%) among the fitted parameters. This is expected, since the endpoints are most sensitive to mass differences. The correlations can also lead to difficulties with convergence and result in larger uncertainties for the fitted masses.

To show a potential result with early data, we quote here the results from converging fits for both the SU3 and SU4 points. We use the endpoints from the lepton+jets edges summarized in Table 4 and the dilepton edge fit from Section 3 ($99.7 \pm 1.4 \pm 0.3$ GeV for SU3 and $52.7 \pm 2.4 \pm 0.3$ GeV for SU4). For the SU3 fit, all dilepton+jets edges are used. In the SU4-fit, we discard the $m_{\ell q(\mathrm{low})}$ measurement as it has been shown not to be very reliable and does not provide additional constraints in three-body

Table 8: Resulting SUSY particle masses and mass differences within SU3 and SU4 from the χ^2 minimization fit using the dilepton and lepton+jets edges. Shown are the measured masses m_{meas} and mass differences Δm_{meas} followed first by the parabolic errors as returned by MIGRAD and then by the jet energy scale errors. When the measured parameter is anticorrelated with the jet energy scale variation, this is indicated by a $\mp$ sign. The input Monte Carlo masses m_{MC} and mass differences Δm_{MC} are also shown. The integrated luminosity assumed is 1 fb^{-1} for SU3 and 0.5 fb^{-1} for SU4.

Observable	SU3 m_{meas} [GeV]	SU3 m_{MC} [GeV]	SU4 m_{meas} [GeV]	SU4 m_{MC} [GeV]
$m_{\tilde{\chi}_1^0}$	$88 \pm 60 \mp 2$	118	$62 \pm 126 \mp 0.4$	60
$m_{\tilde{\chi}_2^0}$	$189 \pm 60 \mp 2$	219	$115 \pm 126 \mp 0.4$	114
$m_{\tilde{q}}$	$614 \pm 91 \pm 11$	634	$406 \pm 180 \pm 9$	416
$m_{\tilde{\ell}}$	$122 \pm 61 \mp 2$	155		
Observable	SU3 Δm_{meas} [GeV]	SU3 Δm_{MC} [GeV]	SU4 Δm_{meas} [GeV]	SU4 Δm_{MC} [GeV]
$m_{\tilde{\chi}_2^0} - m_{\tilde{\chi}_1^0}$	$100.6 \pm 1.9 \mp 0.0$	100.7	$52.7 \pm 2.4 \mp 0.0$	53.6
$m_{\tilde{q}} - m_{\tilde{\chi}_1^0}$	$526 \pm 34 \pm 13$	516.0	$344 \pm 53 \pm 9$	356
$m_{\tilde{\ell}} - m_{\tilde{\chi}_1^0}$	$34.2 \pm 3.8 \mp 0.1$	37.6		

decay scenarios such as SU4. The $m_{\ell q(\text{high})}$ endpoint can be measured more reliably and its kinematic expression only differs from the one of $m_{\ell q(\text{low})}$ by a constant factor. The di-tau edges are not used here.

The masses resulting from the χ^2 fit are shown in Table 8 (upper part). The parabolic errors are the first errors shown in the table and the jet energy scale errors are the second. Asymmetric errors show a large uncertainty on the positive side. The jet energy scale errors are determined by varying all the endpoints along with their fully correlated jet energy scale uncertainties and refitting the masses. The difference in the central values of the fit is taken as the jet energy scale uncertainty for Table 8. One can see that the jet energy scale errors are small compared to the error on the masses, but might be relevant to the mass difference measurements.

We note that a fit with SU3 kinematic assumptions applied to the SU4 endpoints also returns consistent masses. The decision about the mass hierarchy would thus have to be based on additional information from collider data. A possible source is the shape of the dilepton edge as discussed in Section 3.

Besides the masses we can also extract differences of SUSY particle masses. These are more directly related to the endpoints and we expect to be able to determine them more reliably than the masses of individual sparticles. For mass differences, a χ^2 similar to Eq. Eq. (24) is used, where the parameters are written in terms of mass differences to the neutralino $\tilde{\chi}_1^0$. We obtain the results shown in Table 8 (bottom part).

We conclude that a first look at sparticle masses is possible with early data, although with large uncertainties. Appropriate model assumptions and additional information will probably have to be used to constrain the fits.

9.2 Observables and fit assumptions

To demonstrate the feasibility of parameter determination with initial data, we show the constraints one would obtain for our benchmark points if one assumed an mSUGRA framework.

The SUSY parameter-fitting package Fittino version 1.4.1 [24] is used, interfaced to a beta version of SPheno3 [25] to perform the theoretical calculations for a given set of parameters.

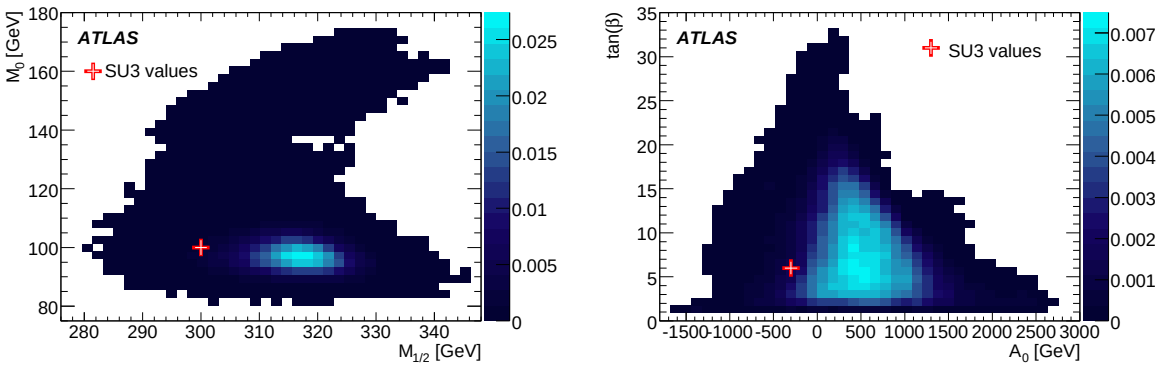

Figure 12: Two-dimensional Markov chain likelihood maps for mSUGRA parameters M_0 and $M_{1/2}$ (left) as well as $\tan\beta$ and A_0 (right) for sign $\mu = +1$, for benchmark point SU3, with integrated luminosity of 1 fb^{-1}. The crosses indicate the actual values of the parameters for that benchmark point.

The fit is given the measurements presented in sections 3, 4 and 6. The lepton and the jet energy scale uncertainties are each considered to be 100% correlated between measurements. Uncertainties on the theoretical predictions are not taken into account. For illustration purposes an additional parameter determination is performed where – following a prescription used in [26] – 1% (0.5%) uncertainty on the theoretical calculation of the pole masses of coloured (un-coloured) sparticles is assumed. No correlations between the theoretical uncertainties on the pole masses are considered.

9.3 Markov chain analysis

To obtain a first glimpse of the possible parameter space a Markov chain analysis is performed. With this technique it is possible to efficiently sample from a large-dimensional parameter spaces. This allows us to check whether there are several topologically disconnected parameter regions which are favoured by the given measurements.

Figure 12 shows two-dimensional likelihood maps for M_0 and $M_{1/2}$ (left) as well as $\tan\beta$ and A_0 (right) for sign $\mu = +1$ obtained for the given set of measurements. The plots demonstrate that for a given sign μ preferred parameters are found around the true parameter points independent of the starting point. No further preferred regions occur. For M_0 and $M_{1/2}$ a clearly preferred region is found around the SU3 values of 100 GeV and 300 GeV, respectively. As expected, given the measurements used, the determination of $\tan\beta$ and A_0 is more difficult. Nevertheless, here too the region around the nominal SU3 values is the preferred one.

9.4 Parameter determination

In order to determine the derived central values of the parameters and their uncertainties, for each assumption of the sign of μ a set of 500 toy fits are performed. For each fit the observables are smeared using the full correlation matrix. Simulated annealing followed by a Minuit fit started with the best parameter estimates from simulated annealing is subsequently run using the smeared observables. The four-dimensional distribution of parameters obtained from the toy fits is used to derive the parameter uncertainties and their correlations. Figure 13 shows the one-dimensional projections of parameter distributions for M_0, $M_{1/2}$, $\tan\beta$ and A_0. The mean and RMS values of the results of the fit are reported in Table 9. As already indicated by the Markov chain analysis M_0 and $M_{1/2}$ can be derived reliably with

uncertainties $\pm$ 9.3 GeV and $\pm$ 6.9 GeV (RMS of the toy fit results), respectively whereas for $\tan\beta$ and A_0 only the order of magnitude can be derived from these measurements. The χ^2 distribution of the toy

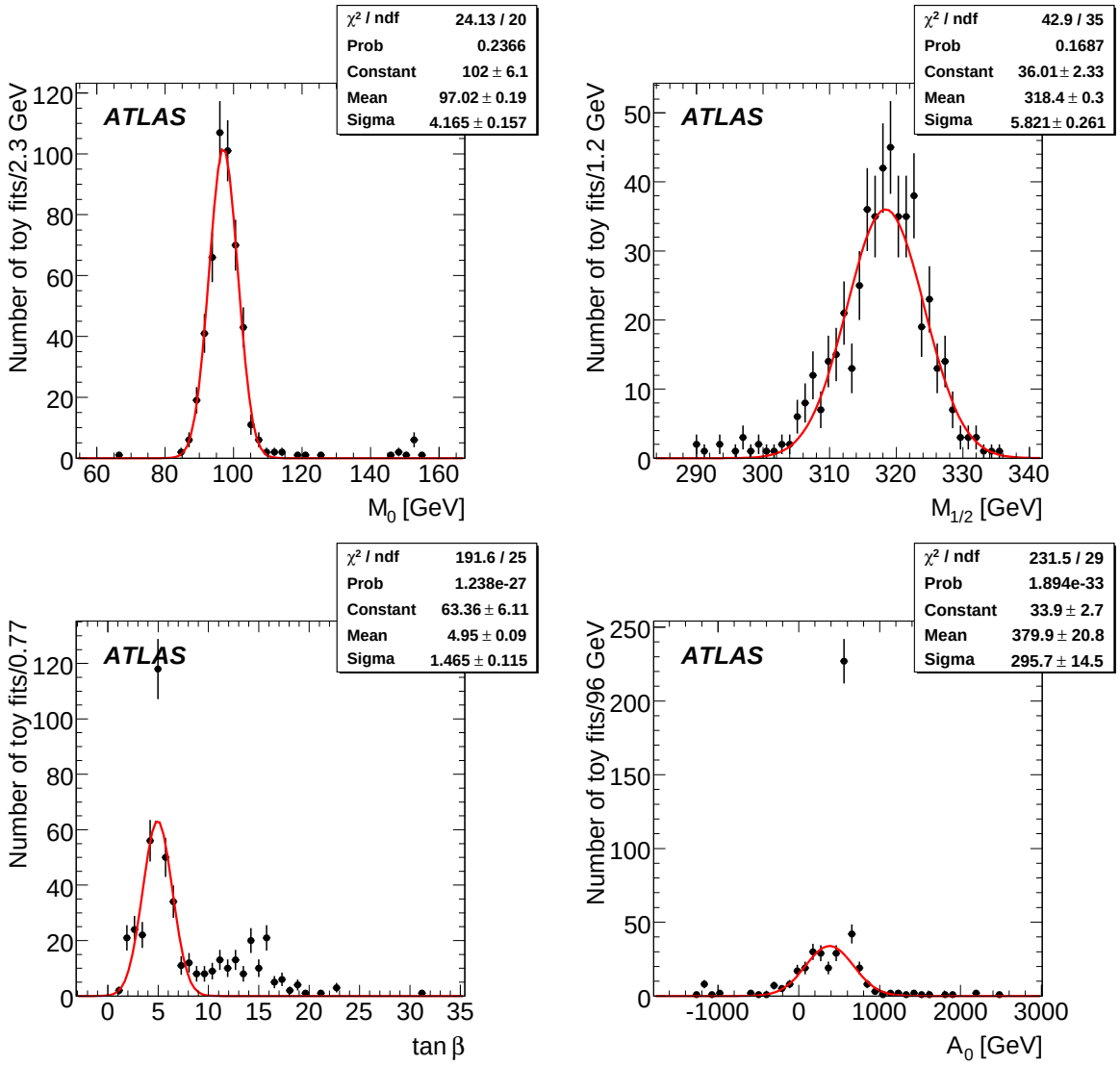

Figure 13: Distributions of the mSUGRA parameters obtained with the fits to pseudo-experiment results.

fits can be used to evaluate the toy fit performance. The observed mean $\chi^2 = 12.6 \pm 0.2$ for sign μ = +1 is compatible with the expected value of $N_{dof} = 11$. The solutions for the wrong assumption sign $\mu = -1$, also reported in Table 9, cannot however be ruled out as the observed mean $\chi^2 = 15.4 \pm 0.3$ is also acceptable.

10 Conclusions

If the supersymmetric partners of quarks and gluons exist at a moderate mass scale ($\lesssim$ 1 TeV) they will be abundantly produced in pp collisions at the LHC centre-of-mass energy of 14 TeV. In this scenario, a few fb^{-1} of ATLAS data will allow the discovery of the new particles [1], once the commissioning of

Table 9: Results of a fit of the mSUGRA parameters to the observables listed in Sections 3, 4 and 6 for the SU3 point. The mean and RMS of the distribution of the results from the toy fits is reported. The two possible assumptions for the digital parameter $\mathrm{sign}(\mu) = +1$ $\mathrm{sign}(\mu) = \pm 1$ have been used, resulting in different preferred regions for the other parameters. The effect of different assumptions on theoretical uncertainties is also shown.

Parameter	SU3 value	fitted value	exp. unc.
		$\mathrm{sign}(\mu) = +1$	
$\tan\beta$	6	7.4	4.6
M_0	100 GeV	98.5 GeV	$\pm$9.3 GeV
$M_{1/2}$	300 GeV	317.7 GeV	$\pm$6.9 GeV
A_0	$-$300 GeV	445 GeV	$\pm$408 GeV
		$\mathrm{sign}(\mu) = -1$	
$\tan\beta$		13.9	$\pm$2.8
M_0		104 GeV	$\pm$18 GeV
$M_{1/2}$		309.6 GeV	$\pm$5.9 GeV
A_0		489 GeV	$\pm$189 GeV

the detector has been completed and the Standard Model backgrounds have been well understood.

The next step after discovery will be to select specific supersymmetric decay chains to measure the properties of the new particles. Here we have focused on those measurements that will be possible using 1 fb^{-1} of integrated luminosity. Specific benchmarks in parameter space have been used to demonstrate the precision that can be expected from these measurements, but the same (or similar) techniques can be applied to much of the SUSY parameter space accessible with early LHC data.

For the benchmark points considered, the most promising decay chain involves the leptonic decay of the next-to-lightest neutralino ($\tilde{\chi}_2^0 \to \tilde{\chi}_1^0 \ell^+ \ell^-$). The invariant mass of the two leptons shows a clear kinematic maximum (Section 3) which could already be measured with a precision of a few per cent with the limited data set considered. The combination of one or both leptons with the hardest jets in the event would allow observation of several other kinematic minima and maxima (Section 4).

For high values of $\tan\beta$ the decays into taus will be far more abundant than those involving electrons or muons; the excellent performance expected for the identification and measurement of hadronic τ decays in ATLAS will also allow observation of the dilepton edge in the $\tau^+\tau^-$ invariant mass distribution (Section 5).

The leptonic decays will not be the only channel for early measurements with supersymmetric decays. The $\tilde{q}_R \to q\tilde{\chi}_1^0$ decay can be used to determine the $\tilde{q}_R$ mass (Section 6). The combination of hadronically decaying top quarks and b-jets in supersymmetric events is also a promising possibility for low-scale Supersymmetry with decay chains involving scalar top and bottom quarks, as shown by the reconstruction of the edge of the tb invariant mass discussed in Section 7.

If the $\tilde{\chi}_2^0 \to \tilde{\chi}_1^0 h$ decay is open, it will provide a substantial source of Higgs bosons. Since the Standard Model backgrounds can be suppressed by the usual SUSY cuts, it will then become possible to observe the $h \to b\bar{b}$ decay with moderate (5 fb^{-1}) integrated luminosity (Section 8).

The different channels will provide complementary information about the SUSY mass phenomenology. The various measurements will have to be combined to reconstruct the SUSY mass spectrum and attempt to understand the SUSY-breaking mechanism. In Section 9 it is discussed how a selected set

of early studies can be combined to obtain the first measurements of supersymmetric masses and of the parameters of the mSUGRA model. With 1 fb^{-1} the reconstruction of part of the supersymmetric mass spectrum will only be possible for favourable SUSY scenarios and with some assumptions about the decay chains involved. Larger integrated luminosity will help to overcome these limitations, as more measurements become possible and the precision of each increases.

References

[1] ATLAS Collaboration, *Prospects for Supersymmetry Discovery Based on Inclusive Searches*, this volume.

[2] ATLAS Collaboration, *Supersymmetry Searches*, this volume.

[3] ATLAS Collaboration, *Supersymmetry Signatures with High-p_T Photons or Long-Lived Heavy Particles*, this volume.

[4] M. N. Nojiri, Y. Yamada, Phys. Rev. D **60** (1999) 015006.

[5] U. De Sanctis, T. Lari, S. Montesano, C. Troncon, Eur. Phys. J. C **52** (2007) 743.

[6] B. C. Allanach, C. G. Lester, M. A. Parker and B. R. Webber, JHEP **0009** (2000) 004.

[7] C. G. Lester, M. A. Parker and M. J. White, JHEP **0710** (2007) 0051.

[8] ATLAS Collaboration, *Reconstruction and Identification of Electrons*, this volume.

[9] ATLAS Collaboration, *Muon Reconstruction and Identification: Studies with Simulated Monte Carlo Samples*, this volume.

[10] B. K. Gjelsten, D. J. Miller, P. Osland, JHEP **0412** (2004) 003.

[11] D. J. Miller and P. Osland and A. R. Raklev, JHEP **0603** (2006) 034.

[12] C.G. Lester, Phys. Lett. **B655** (2007) 39–44.

[13] ATLAS Collaboration, *Reconstruction and Identification of Hadronic τ Decays*, this volume.

[14] D. J. Mangeol, U. Goerlach, Search for $\tilde{\chi}_2^0$ decays to $\tilde{\tau}\tau$ and SUSY mass spectrum measurement using di-τ final states, 2006, CMS NOTE 2006/096.

[15] Richter-Was, Elzbieta and Froidevaux, Daniel and Poggioli, Luc, *ATLFAST 2.0 a fast simulation package for ATLAS* Atlas Note ATL-PHYS-98-131.

[16] S. Y. Choi, K. Hagiwara, Y. G. Kim, K. Mawatari and P. M. Zerwas, Phys. Lett. B **648** (2007).

[17] A.J. Barr, C.G. Lester, P. Stephens, J.Phys.G **29** (2003) 2343.

[18] C.G. Lester, D. Summers, Phys.Lett.B **463** (1999) 99.

[19] J. Krstic, M. Milosavljevic and D. Popovic, *Studies of a low mass SUSY model at ATLAS with full simulation*, ATL-PHYS-PUB-2006-028.

[20] ATLAS Collaboration, *Data-Driven Determinations of W, Z and Top Backgrounds to Supersymmetry*, this volume.

[21] J. Hisano, K. Kawagoe and M.M. Nojiri, Phys. Rev. D **68** (2003) 035007.

[22] J. Hisano, K. Kawagoe and M.M. Nojiri, *A Detailed Study of the Gluino Decay into the Third Generation Squarks at the CERN LHC*, ATL-PHYS-2003-29.

[23] ATLAS Collaboration, *ATLAS detector and physics performance. Technical design report* Vol. 2, CERN-LHCC-99-15 (1999).

[24] P. Bechtle, K. Desch, and P. Wienemann, Comput. Phys. Commun. **174** (2006) 47–70.

[25] W. Porod, Comput. Phys. Commun. **153** (2003) 275–315.

[26] R. Lafaye, T. Plehn, M. Rauch and D. Zerwas, Eur. Phys. J. **C54** (2008) 617–644.

Paper 3: On the Possibility of the Search for Top–Antitop Resonances at the LHC

ISSN 1547-4771, Physics of Particles and Nuclei Letters, 2008, Vol. 5, No. 6, pp. 515–519. © Pleiades Publishing, Ltd., 2008.
Original Russian Text © E.V. Khramov, A.N. Tonoyan, V.A. Bednyakov, N.A. Rusakovich, 2008, published in Pis'ma v Zhurnal Fizika Elementarnykh Chastits i Atomnogo Yadra, 2008, No. 6 (148), pp. 865–873.

PHYSICS OF ELEMENTARY PARTICLES AND ATOMIC NUCLEI. EXPERIMENT

On the Possibility of the Search for Top–Antitop Resonances at LHC

E. V. Khramov[a], A. N. Tonoyan[b], V. A. Bednyakov[a], and N. A. Rusakovich[a]

[a] *Joint Institute for Nuclear Research, Dubna, Russia*

[b] *University of Bergen, Bergen, Norway*

Received January, 16, 2008

Abstract—The possibility of discovering top–antitop resonances with masses of 700, 1000, 1500, 2000, and 3000 GeV/c^2 at proton–proton collision energy of 14 TeV in the center of a mass system is considered. The minimum cross sections for the resonance production necessary for their detection in a lepton + jets channel of $t\bar{t}$ pair decay with a 5σ confidence level is estimated. The analysis is performed both with and without taking into account the possibility of hadronic jets reconstruction from b quarks (b-tagging).

PACS numbers: 12.60.Cn; 14.65.Ha

DOI: 10.1134/S1547477108060058

INTRODUCTION

The top quark is the heaviest of all known elementary particles. Since all other quarks have bound states (mesons), it is quite natural to expect that the top quark has a bound state which has not been discovered. There are several theoretical models predicting the existence of sufficiently heavy resonances decaying into the $t\bar{t}$ pair. For example, in the framework of the Standard Model (SM), it is the Higgs boson H with a large mass, which can decay into the top–antitop pair.

However, the probability of SM Higgs boson decay H to the $t\bar{t}$ pair is relatively low. For example, for the Higgs boson with a mass of 500 GeV/c^2 and a width of ~60 GeV/c^2, the branching Br($H \longrightarrow t\bar{t}$) is ~0.17 [1–3]. Nonetheless, the probability of heavy resonance decaying to the top–antitop quark pair is increased in theoretical models beyond the Standard Model, such as the Technicolor model [1] and some other models with a strong violation of electroweak symmetry [4, 5]. Moreover, if SM is extended by additional gauge symmetries or is embedded in the large gauge group, as a rule, there are new heavy electrically neutral gauge bosons (the so called Z' bosons). These neutral bosons are mixed with the SM Z^0 boson and contribute to all processes which take place via weak neutral currents. The fact that these contributions have not yet been discovered imposes the constraints on the mass of the Z' boson and the parameters of $Z' - Z^0$ mixing. Usually, experimentally resolvable masses for Z' bosons are rather large. The recent results of the CDF collaboration showed with a confidence level of 95% that the Z' boson mass should be larger than 850 GeV/c^2 [6, 7].

The maximum energy that can be achieved in the center of a mass system in the near future is 14 TeV at the Large Hadron Collider (LHC) at CERN. On the one hand, these high energies reveal the capability of the direct production of heavy resonances with invariant masses much larger than 850 GeV/c^2, but, on the other hand, the cross section of "direct" production of top–antitop quark pair (σ ~ 833 pb), which is the background event, is increased considerably in this case [1]. Here, the estimation of the minimum cross section necessary for detecting $t\bar{t}$ resonance (denoted by Z' for certainty) of different mass at the confidence level 5σ with account of the background from direct $t\bar{t}$ pair production is presented. Only the lepton + jets (electrons or muons) channel of the $t\bar{t}$ pair decay is considered (see Section 1).

1. RESEARCH IN LONG-TERM PERSPECTIVE (WITH b-TAGGING)

Z' resonances with masses of $M_{Z'}^{\text{gen}}$ = 700, 1000, 1500, 2000, and 3000 GeV/c^2 and widths of 2.3% of the mass decaying into the top–antitop pair were studied. The resonance production was calculated using the event generator PYTHIA [8] without taking into account the possible interference with the Z^0 or γ* bosons. The background process of the direct $t\bar{t}$ pair production ($pp \longrightarrow t\bar{t}$) was generated using the generator MC@NLO [9]. The proton structure function was described by the function CTEQ6 [10].

Since the value of the Cabbibo–Kobayashi–Maskawa (CKM) matrix element $|V_{tb}| \sim 1$, almost 100% of the top quark decays occur in the mode $W + b$ quark.

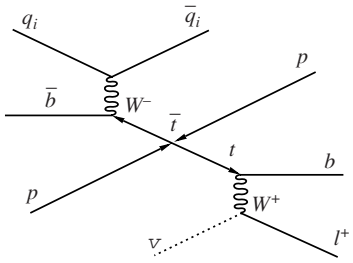

Fig. 1. "Lepton + jets" decay channel of top–antitop pair. Only electron and muon are accepted as leptons.

The width of this top quark decay channel has the form [11]

$$\Gamma(t \longrightarrow Wb) = |V_{tb}|^2 \frac{G_F m_t^3}{8\pi\sqrt{2}}\left(1 - \frac{M_W^2}{m_t^2}\right)^2 \times\left(1 + 2\frac{M_W^2}{m_t^2}\right)\left[1 - \frac{2\alpha_s}{3\pi}\left(\frac{2\pi^2}{3} - \frac{5}{2}\right)\right], \quad (1)$$

where M_W is the W boson mass, G_F is the Fermi constant, m_t is the top quark mass, α_s is the strong interaction coupling. Thus, the space–time signature of the decay of the top–antitop pair produced in pp ($p\bar{p}$) collisions is significantly determined by the decays of two W bosons which in turn can decay both in the lepton channel ($W \longrightarrow l\nu$), which makes up approximately 33% of all decays with account of the contribution of tau-lepton pair, and the hadronic channel ($W \longrightarrow qq'$) responsible for approximately 67% of all $t\bar{t}$ pair decays. The top–antitop pair decay mode, in which one of the W bosons is decayed in the lepton channel and the other one in the hadronic channel, $t\bar{t} \longrightarrow b\bar{b}W^+W^- \longrightarrow b\bar{b}(l^+\nu)(jj)$, is called the "lepton + jets" mode (see Fig. 1). It makes up approximately 43.5% of all top–antitop pair decays. The decay products in this mode are the $b\bar{b}$ quark pair, one charged lepton, and the pair of light quarks (i.e., quarks with the mass smaller than the b quark mass). About 46.2% of all top–antitop pairs are decayed in the "multijet" channel, $t\bar{t} \longrightarrow b\bar{b}W^+W^- \longrightarrow b\bar{b}(jj)(jj)$, when both W bosons yield the quark–antiquark pair. The remaining 10.3% of decays fall in the dilepton channel when both W bosons are decayed in the lepton channel. As a result, there are two charged leptons and the $b\bar{b}$ quark pair, $t\bar{t} \longrightarrow b\bar{b}W^+W^- \longrightarrow b\bar{b}(l^+\nu)(l^-\bar{\nu})$ [12].

Only the lepton + jets channel of the top–antitop quark pair decay was used in analysis; for this channel, the event was separated both using the "old" criteria used in the previous work [13] and the "new," less severe, criteria of event selection. The "old" criteria are (1) the event should contain one isolated lepton with $p_T > 20$ GeV/c in the pseudorapidity range $|\eta| < 2.5$; (2) the missing transverse energy in the event should satisfy the condition $E_T^{\text{miss}} > 20$ GeV; (3) there should be four or more hadronic jets with $E_T \geq 40$ GeV in the pseudorapidity interval $|\eta| < 2.5$ in the event (two of these jets should be b jets).

The "new" criteria are (1) in pseudorapidity range $|\eta| < 2.5$ of the event there should be one isolated electron with $p_T > 25$ GeV/c or an isolated muon with $p_T > 20$ GeV/c; (2) the missing transverse energy in the event should satisfy the condition $E_T^{\text{miss}} > 20$ GeV; (3) there should be four or more hadronic jets with $E_T \geq 30$ GeV in the pseudorapidity interval $|\eta| < 2.5$ (two of these jets should be b jets).

Due to these selection criteria, the main background process for the studied $t\bar{t}$ resonance becomes the SM $t\bar{t}$ pair. The other sources of the physical background, where $pp \longrightarrow W$ + jets dominate, become negligible.

As was already noted, the search for the Z' resonance decaying to the $t\bar{t}$ pair was performed based on lepton + jets events. The objective of the analysis was reconstruction of the peak in the invariant mass spectrum of the $t\bar{t}$ pair corresponding to the sought Z' resonance.

Upon reconstructing the invariant mass of $t\bar{t}$ pair, the invariant masses of W boson and the t quark decayed in the hadronic channel ($t \longrightarrow Wb \longrightarrow q\bar{q}b$) were reconstructed, followed by the invariant masses of t quark decayed in the lepton channel ($t \longrightarrow Wb \longrightarrow l\nu_l b$). From two or more hadronic jets which were not reconstructed as b jets, the combination of two jets whose invariant mass was the closest to the generated value of the W boson mass ($M_W^{\text{PDG}} = 80.4$ GeV/c^2) was chosen. It is necessary to choose the combination of the hadronic W boson and one of the two b jets to reconstruct the hadronic top quark. Three methods for selecting this combination were considered: the combination providing the largest transverse momentum of the reconstructed top quark, the combination with the invariant mass closest to the generated t quark mass ($M_{\text{top}}^{\text{gen}} = 175$ GeV/c^2), and the combination with the smallest value of $\Delta R = \sqrt{(\Delta\eta)^2 + (\Delta\phi)^2}$. Figure 2a shows the invariant mass of the hadronic t quark reconstructed using three methods after applying the "old" and "new" event selection criteria for different Z' boson masses (the value of the $t\bar{t}$ resonance mass 350 GeV/c^2 was used to denote the reconstructed t quark masses in background events). The efficiency of reconstructing the hadronic top quark can be increased by introducing

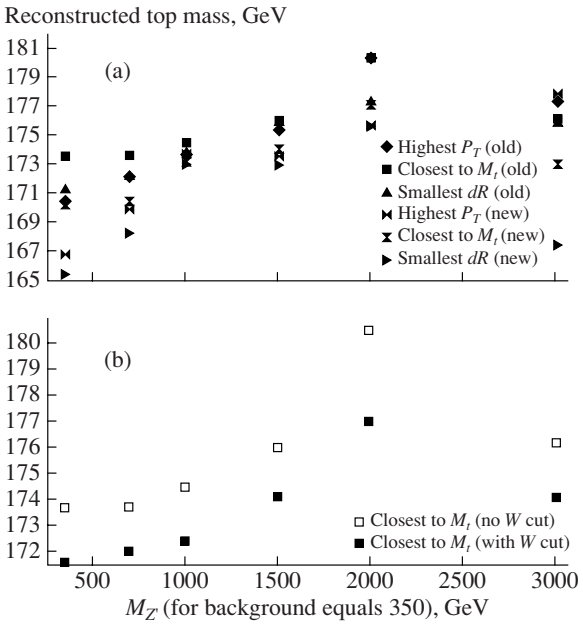

Fig. 2. (a) Hadronic top quark reconstructed using three methods after the application of "old" and "new" event selection criteria depending on the $t\bar{t}$ resonance mass (the value of Z' mass equal to 350 GeV/c^2 corresponds to the results obtained for the background, direct $t\bar{t}$ pair production; (b) reconstructed invariant mass of hadronic top quark after application of "old" event selection criteria (dark squares) with and (light squares) without the additional condition on the mass of hadronic W boson ($|M_{jj} - 80.4| < 30$ GeV/c^2).

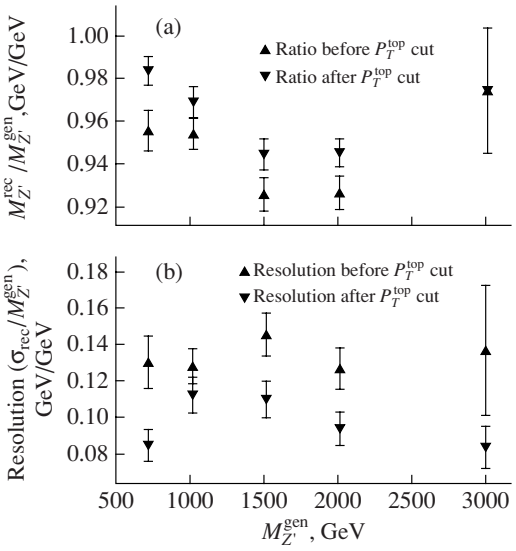

Fig. 3. (a) Ratio of reconstructed invariant mass of $t\bar{t}$ resonance and generated value depending on $M_{Z'}^{gen}$; (b) resolution of reconstructed $t\bar{t}$ resonance as a function of $M_{Z'}^{gen}$.

the additional condition on the mass of the hadronic W boson, $|M_{jj} - 80.4| < 30$ GeV/c^2 (see Fig. 2b).

Since, on average, the values of the reconstructed mass of the hadronic top quark after applying the "old" selection criteria without the requirement $|M_{jj} - 80.4| <$ 30 GeV/c^2 are closer to $M_{top}^{gen} = 175$ GeV/c^2, this reconstruction method was chosen for further analysis.

The next step is reconstructing the lepton t quark; however, because there is only information on the missing transverse energy in the event, the following assumption is made for reconstruction: all missing energy is the consequence of the non-detected neutrino in the W boson decay ($W \longrightarrow l\nu_l$), i.e., $E_T^{miss} \equiv P_T^{\nu}$. Thus, by solving the quadratic equation $M_W = 80.4 = \sqrt{(E_l + E_{\nu_l})^2 - (\mathbf{p}_l + \mathbf{p}_{\nu_l})}$ with respect to $p_{\nu_l}^z$, we either obtain no solution, then the event is rejected or we obtain two solutions, and then the combination of the lepton W boson and the second b jet with the closest value of the invariant mass to the generated value is chosen.

Since the transverse momenta of top quarks from the decay of $t\bar{t}$ resonance are higher than the transverse momenta of top quarks in direct $t\bar{t}$ pair production, the additional criterion on the transverse momentum of the hadronic t quark [13] ($p_T^{had} > 200$, 250, 300, 350, and 450 GeV/c for the resonances with the masses 700, 1000, 1500, 2000, and 3000 GeV/c^2, respectively) can be used for background suppression. The ratio of the reconstructed invariant mass of $t\bar{t}$ resonance and the generated value as a function of the generated values is shown in Fig. 3a. In Fig. 3b, the resolution of the reconstructed $t\bar{t}$ resonance as a function of its mass is shown. It is seen clearly that the application of the criterion on the transverse momentum of the hadronic top quark makes the reconstructed value of the invariant mass of the Z' boson closer to the generated value and improves its resolution.

The calculation of the minimum cross section necessary for detecting $t\bar{t}$ resonance in the lepton + jets decay channel was performed using the formula

$$\sigma \times \mathrm{Br} = 5\frac{\sqrt{\sigma_{bkg}\epsilon_{bkg}}}{\epsilon_{sig}\sqrt{L}}, \qquad (2)$$

where σ_{bkg} is the cross section of the direct $t\bar{t}$ pair production, L is the assumed integral luminosity of the accelerator, and ϵ_{bkg} and ϵ_{sig} are the efficiencies of event selection criteria and additional condition on the trans-

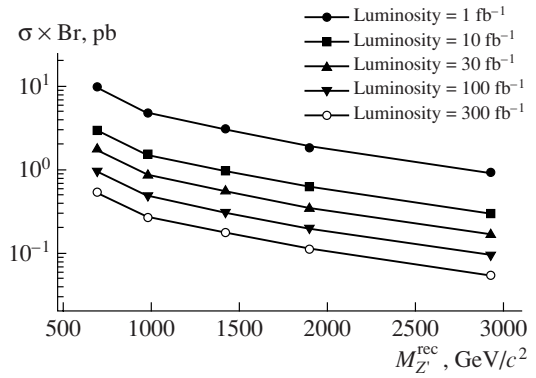

Fig. 4. Minimum cross section of Z' resonance production necessary for confidence level 5σ in lepton + jets channel as a function of $t\dot{t}$ resonance mass for different assumed integral luminosity of the accelerator.

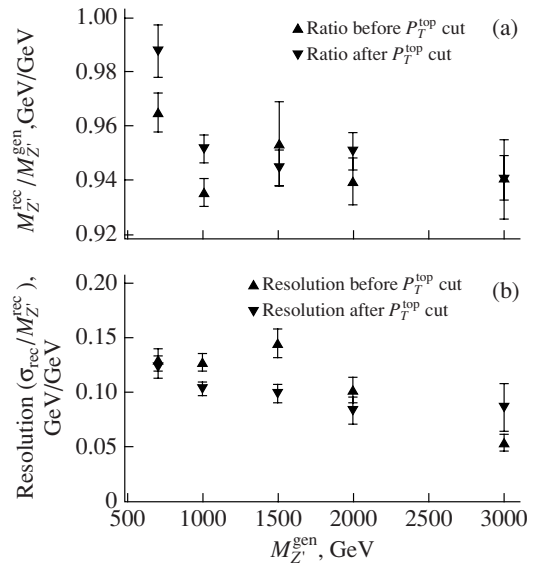

Fig. 5. (a) Ratio of reconstructed invariant mass of $t\dot{t}$ resonance and generated value depending on generated values without b-tagging; (b) resolution of reconstructed $t\dot{t}$ resonance depending on generated value of its mass without b-tagging.

verse momentum of the hadronic top quark within $M^{\text{rec}}_{Z'} \pm 2\sigma^{\text{rec}}_{Z'}$.

Figure 4 shows minimum cross sections (2), which are necessary for reaching the confidence level 5σ for different values of the assumed integral luminosity of the accelerator depending on the Z' boson mass. For example, it is seen that, for an integral LHC luminosity of 300 fb^{-1}, the Z' resonance with a mass of 2 TeV/c^2 could be detected if its production cross section exceeds 0.1 pb.

2. RESEARCH IN SHORT-TERM PERSPECTIVE (WITHOUT B-TAGGING)

As a rule, at the early stage of operation of an experimental setup, it is practically impossible to determine whether the hadronic jet was initiated by b quark or not; however, in this case it is possible to reconstruct hadronic jets. Naturally, the selection criteria of the lepton + jets event change:

(1) in the event, there should be one isolated lepton with $p_T > 20$ GeV/c in the pseudorapidity interval $|\eta| < 2.5$;

(2) the missing transverse energy in the event should satisfy the condition $E_T^{\text{miss}} > 20$ GeV;

(3) there should be four hadronic jets in the event with a maximum transverse energy and $E_T \geq 40$ GeV in the pseudorapidity interval $|\eta| < 2.5$.

The lepton W boson in this case is reconstructed similar to Section 1. After that, in order to reconstruct the lepton t quark and hadronic W boson and t quark it is necessary to choose the combination of four hadronic jets (12 possible combinations) and two values of $p^z_{\nu_l}$. The combination assumed to be correct was the one yielding the minimum value of the quantity $|\chi^2/\text{ndf} - 1|$, where ndf = 12 and χ^2 was calculated using the following expression:

$$\chi^2 = \frac{(m_{l\nu j_a} - M^{\text{gen}}_{\text{top}})^2}{(\Gamma^{\text{lept}}_{\text{top}})^2} + \frac{(m_{j_b j_c j_d} - M^{\text{gen}}_{\text{top}})^2}{(\Gamma^{\text{had}}_{\text{top}})^2} + \frac{(m_{j_b j_c} - M^{\text{gen}}_{W})^2}{(\Gamma^{\text{had}}_{W})^2}. \quad (3)$$

Further, after reconstructing the invariant mass of Z' boson, the additional condition on the transverse momentum of the hadronic top quark was imposed. The obtained ratios of the reconstructed invariant mass of the resonance and the generated value dependent on the generated Z' mass are shown in Fig. 5a. Figure 5b shows the dependence of the resolution of the reconstructed $t\dot{t}$ resonance on its mass. After the additional condition on the transverse momentum of the hadronic top quark was imposed, the invariant mass of the resonance and the resolution were, on average, reconstructed better than without this additional condition.

The minimum cross section of $t\dot{t}$ resonance production calculated using expression (2) as a function of the

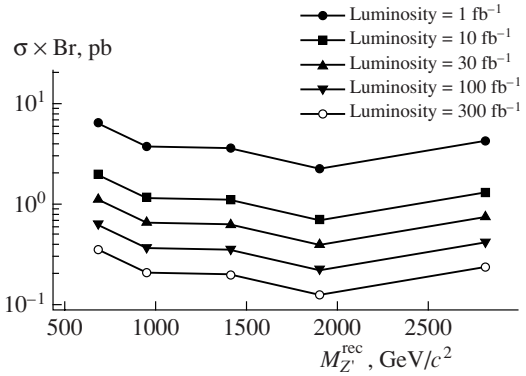

Fig. 6. Minimum cross section of Z' resonance production necessary for confidence level 5σ in lepton + jets channel as a function of $t\bar{t}$ resonance mass for different assumed integral luminosity of the accelerator without b-tagging.

resonance mass for different values of the assumed integral luminosity of the accelerator is shown in Fig. 6.

CONCLUSIONS

In this work, the possibility of detecting the heavy $t\bar{t}$ resonance at LHC was estimated. The electrically neutral gauge Z' boson with masses 700, 1000, 1500, 2000, and 3000 GeV/c^2 and a width of 2.3% its mass was chosen as the example. The lepton + jets channel of the $t\bar{t}$ pair decay was chosen for the search and reconstruction of the invariant mass of the resonance; in this case, the main background process was the direct production of top–antitop pair, the other sources of background processes make insignificant contributions. Moreover, the new additional criterion on the transverse momentum of the "hadronic" t quark was applied; this criterion made it possible to improve the reconstruction accuracy for the resonance invariant mass. The minimum cross section of $t\bar{t}$ resonance production, which makes its detection possible in the lepton + jets channel with a confidence level of 5σ for different values of integral luminosity both with and without b-tagging, was estimated. It is seen (e.g., from Fig. 6) that at LHC integral luminosity 10 fb^{-1}, Z' resonance with a mass of 2 TeV/c^2 could be detected if the production cross section exceeds 0.7 pb/c^2.

REFERENCES

1. ATLAS Collab., ATLAS Technical Design Report 15, CERN/LHCC 99-015, Vols. I, II (1999).
2. E. Accomando et al., Phys. Rev. **299**, 1–78 (1998); A. Djouadi, "The Anatomy of Electro-Weak Symmetry Breaking. I. The Higgs Boson in the Standard Model," hep-ph/0503172.
3. S. Gonzales, "MSSM Higgs Decay to Top Quarks," ATL-PHYS-2000–006; S. Gonzales, "Comparison btween Full and Fast Simulation of the ATLAS Detector for the Channel $H/A \longrightarrow t\bar{t}$," ATL-HYS-2003-019.
4. C. T. Hill and Parke, Phys. Rev. D: Part. Fields **49**, 4454 (1994).
5. R. Casalbuoni et al., Z. Phys. C **69**, 519 (1996).
6. Schwanenberger (CDF and DX0 Collab.), PoS HEP2005, 349 (2006); hep-ex/0602048.
7. CDF Collab., CDF/ANAL/EXOTIC/PUBLIC8421 (2006).
8. T. Sjostrand et al., "PYTHIA 6.3 Physics and Manual," hep-ph/0308153 (2003).
9. S. Frixione and B. R. Webber, "The MC@NLO 2.3 Event Generator," hep-ph/0402116 (2004).
10. J. Pumplin et al., "New Generation of Parton Distributions with Uncertainties from Global QCD Analysis," JHEP **0207**, 012 (2002).
11. M. Jezabek and J. H. Kuhn, "QCD Corrections to Semileptonic Decays of Heavy Quarks," Nucl. Phys. B **314**, 1 (1989).
12. A. B. Balantekin, "Review of Particle Physics (PDG)," Nucl. Part. Phys. **33**, 1 (2006).
13. E. Khramov et al., "Search for $t\bar{t}$ Resonances with the ATLAS Detector," ATL-PHYS-INT-2007-010.

Paper 4: Commissioning of the ATLAS reconstruction software with first data

17th International Conference on Computing in High Energy and Nuclear Physics (CHEP09) IOP Publishing
Journal of Physics: Conference Series **219** (2010) 032059 doi:10.1088/1742-6596/219/3/032059

Commissioning of the ATLAS reconstruction software with first data

J.T. Boyd[1], M.J. Costa[2], A. Tonoyan[3] on behalf of the ATLAS Collaboration

[1] CERN, CH-1211 Geneva 23, Switzerland
[2] Instituto de Física Corpuscular UVEG-CSIC, Aptdo 22085, E-46071 Valencia, Spain
[3] Department of Physics and Technology, University of Bergen, Allégaten 55, N-5007 Bergen, Norway

E-mail: Jamie.Boyd@cern.ch, Maria.Jose.Costa@cern.ch, Arshak.Tonoyan@cern.ch

Abstract. Looking towards first LHC collisions, the ATLAS detector is being commissioned using all types of physics data available: cosmic rays and events produced during a few days of LHC single beam operations. In addition to putting in place the trigger and data acquisition chains, commissioning of the full software chain is a main goal. This is interesting not only to ensure that the reconstruction, monitoring and simulation chains are ready to deal with LHC physics data, but also to understand the detector performance in view of achieving the physics requirements. The status of the integration of the complete software chain will be presented as well as the data analysis results.

1. Introduction

ATLAS (A Toroidal Lhc ApparatuS) [1] is one of four main experiments at the Large Hadron Collider (LHC). It is a multipurpose detector and is designed to provide excellent physics performance in the busy environment of LHC, where bunches of protons with energy of 7 TeV collide with each other. ATLAS consists of three main sub-systems: the Inner Detector (ID), the Calorimeters and the Muon Spectrometer (MS). The ID is placed in 2 T solenoidal magnetic field and the MS is operating inside an air-core toroid magnet system with a peak field in the coil windings of 4 T. Fig. 1 shows a schematic view of the ATLAS detector and its sub-systems. The ID is a tracking detector which is responsible for momentum and vertex measurements of charged particles and electron identification. It consists of high-resolution semiconductor pixel and strip detectors in the inner part of the tracking volume (Pixels and SCT), and straw-tube tracking detectors (TRT) in the outer part with the capability to generate and detect transition radiation to improve the electron identification. The Calorimeters consist of electromagnetic and hadronic parts. The electromagnetic calorimeter uses liquid argon (LAr) as the active medium to detect photons and electrons with excellent performance in terms of energy and position resolution. The hadronic calorimetry is provided by a scintillator-tile calorimeter (TileCal) in the central part and by liquid argon calorimeters in the endcaps. The outermost sub-detector is the MS, consisting of precision tracking chambers, monitored drift tubes (MDT) and cathode strip chambers (CSC), as well as trigger chambers with excellent timing resolution made from resistive plate (RPC) and thin gap (TGC) chambers. The CSCs and TGCs are only in the endcaps.

17th International Conference on Computing in High Energy and Nuclear Physics (CHEP09) IOP Publishing
Journal of Physics: Conference Series **219** (2010) 032059 doi:10.1088/1742-6596/219/3/032059

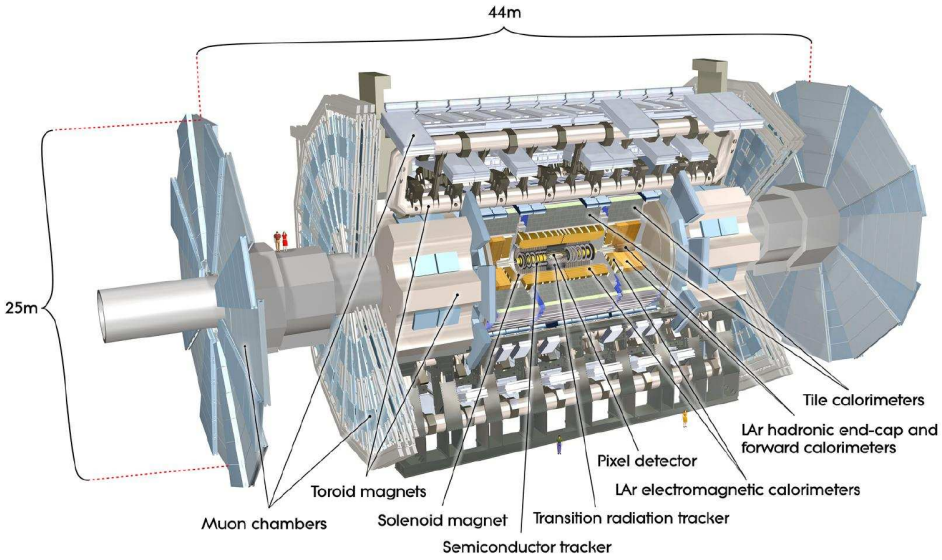

Figure 1. Schematic view of ATLAS detector.

The ATLAS commissioning with cosmic rays began more than four years ago, first with individual sub-detectors and then with larger slices of the entire detector. As an integral part of this commissioning process we have also commissioned the reconstruction software. The main motivations were to gain experience of the detector operation (from trigger and data acquisition up to analysis in the grid Tier-2 centers) and to obtain first track based alignment and calibration constants and a list of bad channels. These are necessary for understanding the detector performance to achieve the physics requirements. Combined cosmic runs to integrate new systems were organized in the so-called Milestone weeks, when cosmic rays were taken with different detector and magnet configurations as systems were ready. Since July 2008, while preparing for the first LHC beam on September 10th, ATLAS entered in semi-continuous data taking mode. During the three days, when one of the two LHC beams were circulating, ATLAS recorded LHC beam data which were also used for commissioning purposes. The beam consisted of one bunch with $2{\cdot}10^9$ protons at 450 GeV. After the LHC incident on September 19th, a long combined cosmic run took place in order to collect enough statistics for detailed detector performance studies.

2. Software operation chain

The ATLAS reconstruction software framework is Athena [2]. It is used for a variety of purposes, including high-level triggering, simulation, reconstruction, monitoring and analysis. The data flow in the ATLAS experiment [3] is sketched in Fig. 2: the data from the detector are filtered in a three-stage Trigger system [4] before they are sent to the Tier-0 for initial processing by the offline reconstruction software. A small amount of data called "express stream" is sent to the Tier-0 at CERN to be processed in quasi real time, running the complete reconstruction and monitoring chain. Data quality is monitored online at the trigger level as well as offline during reconstruction. Monitoring histograms are checked both by shifters using the Online Histogram Presenter [5] and automatically via the Data Quality Monitoring Framework [6]. Dedicated data streams are written out at the trigger level to allow for detector alignment and calibration. The

17th International Conference on Computing in High Energy and Nuclear Physics (CHEP09) IOP Publishing
Journal of Physics: Conference Series **219** (2010) 032059 doi:10.1088/1742-6596/219/3/032059

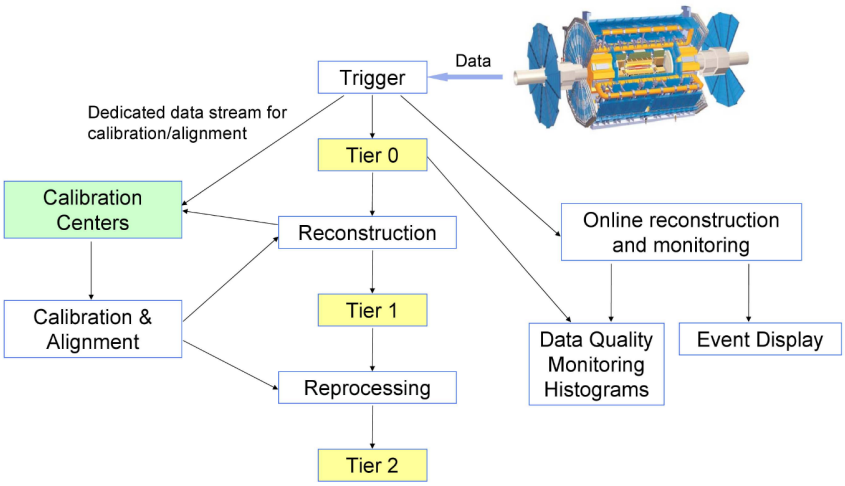

Figure 2. Flowchart of the ATLAS data.

calibration centers, which include some Tier-2 Grid centers as well as the CAF (CERN Analysis Facility), perform a first pass calibration and alignment within 24 hours after the data have been taken. The obtained constants are then used for the bulk processing of the data, once they have been validated by a second re-processing of the express stream. For cosmic reconstruction we do not use the 24 hour calibration loop that will be used for collisions. Up to now, all streams have been treated in the same way from point of view of reconstruction at the Tier-0, i.e. all events have only been processed once using the latest available alignment and calibration constants. At the end of the reconstruction chain the data are distributed to the Tier-1 and Tier-2 centers which are used for analysis and production of simulated data. The Tier-1 centers are also responsible for data reprocessing, i.e. re-running reconstruction with improved calibration and alignment constants and with improved reconstruction algorithms. A large scale reprocessing of about 300 million events has already taken place successfully at the Tier-1 centers in December 2008. Several improvements have been made in reconstruction software which was used for reprocessing campaign. Some of them are improvements in physics object reconstruction algorithms, use of a new tracking algorithm and modifications in calorimeter data reconstruction software which can deal with horizontal tracks from single beam runs. In addition to software improvements, new calibration and alignment constants, and noisy and dead channels maps were also provided. Another reprocessing campaign has taken place in April 2009.

Given the obvious differences between LHC collision data and the data recorded by ATLAS so far from cosmic rays and LHC single beam operations, LHC collisions are, of course, needed to make the final test of the operation chain described above. However, the majority of this chain has already been exercised with real data.

3. Results from data analysis

3.1. Cosmic rays

A large amount of cosmic ray data has already been collected by ATLAS with different detector and magnet configurations. The most useful data for analysis were collected in the autumn 2008 run period when all subdetectors except the CSCs were included in combined runs. During this period, data were collected with different magnet configurations to allow for some specific studies such as the determination of alignment constants. Fig. 3 shows the accumulated statistics in

17th International Conference on Computing in High Energy and Nuclear Physics (CHEP09) IOP Publishing
Journal of Physics: Conference Series **219** (2010) 032059 doi:10.1088/1742-6596/219/3/032059

the global cosmic run for the different streams (left) and how that translates into number of reconstructed tracks in the Pixel detector, the system with the smallest geometrical cross section for cosmic rays (right). Over 200 million events have been recorded in 45 days of combined runs. These large statistics allows us to perform detailed detector studies although it is still not enough to reach the precision required in the alignment of the tracking devices. Some examples of these studies will be given below for each sub-system: the ID, the Calorimeters and the MS.

To support data analysis and detector commissioning it is useful to have simulated data for a variety of commissioning scenarios. A Monte Carlo generator was used for simulating muons from cosmic rays, based on measurements of the differential vertical muon cross section and analytical calculations extrapolated to low muon energy [7]. Cosmic muons are generated with a production vertex within a 600m×600m square centered above the ATLAS detector at the surface of the earth. In order to reduce simulation time, only the muons that, at the generator level, point into a sphere around the ATLAS detector are then propagated through the rock and only the ones that produce simulated hits in the detector are kept.

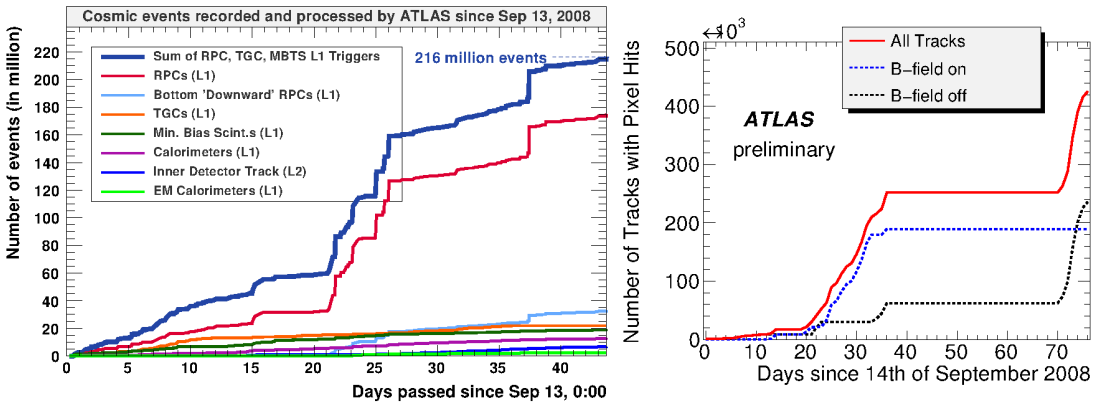

Figure 3. Number of events in collected different trigger streams during combined runs in autumn 2008 (left). Number of cosmic muon tracks seen by Pixel detector since September 2008 (right).

One of the main analyses concerning the ID is calculations of alignment constants for its subdetectors. Alignment constants for all three sub-systems (Pixels, SCT and TRT) have been provided with the level of granularity appropriate for the given statistics. The residuals distributions before and after the alignment procedure as well as from Monte Carlo simulated events are shown in Fig. 4 for the TRT and SCT and in Fig. 5 for the Pixel detector. Calibration constants for the Pixels and TRT R-t relations (radius of the track's position in a single straw to the drift time), as well as a list of bad channels have also been provided to allow for detector and tracking studies.

Cosmic ray data have also allowed detailed studies in the calorimeters, for example, validating the timing, energy calibrations and uniformity of the energy response. An example of the latter is seen in Fig. 6 (left), which shows the normalized reconstructed energy in LAr as a function of pseudo-rapidity together with the depth of the cells in the second sampling of the electromagnetic calorimeter. Three curves are shown: two different cluster algorithms applied to real data and the true cluster from the cosmic simulation. The data curves clearly track the cell depth as one would expect for a minimum ionizing particle and the uniformity of the response agrees with simulation at the level of 2%.

Results from the analysis evaluating the synchronization of the TileCal readout channels are summarized on Fig. 6 (right), which shows the time difference between measured and expected

17th International Conference on Computing in High Energy and Nuclear Physics (CHEP09) IOP Publishing
Journal of Physics: Conference Series **219** (2010) 032059 doi:10.1088/1742-6596/219/3/032059

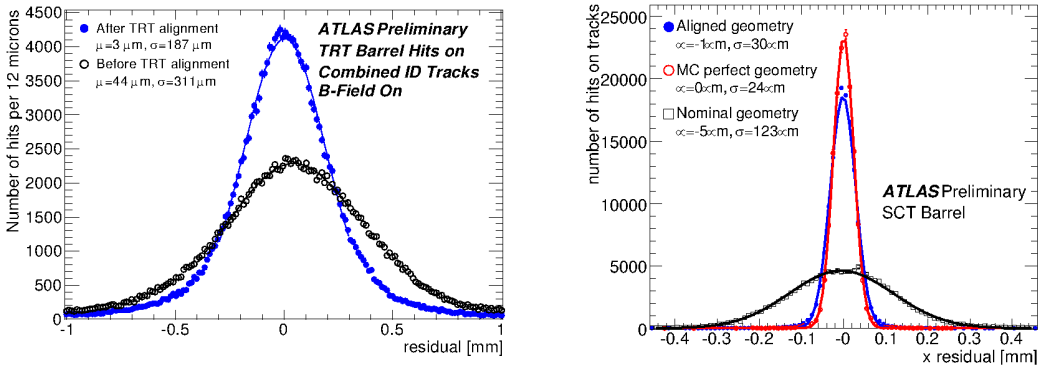

Figure 4. Residual distribution in the TRT (left) and SCT (right) barrel for the nominal geometry and the preliminary aligned geometry.

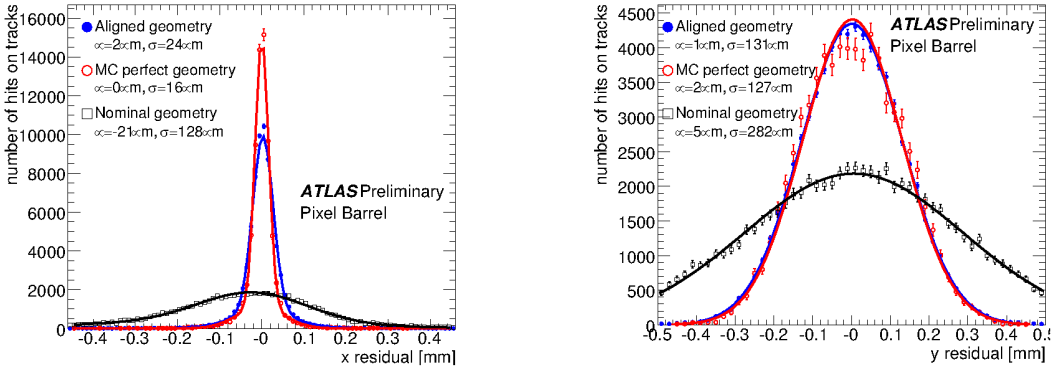

Figure 5. Residual distributions along x (left) and y (right) axes in Pixel barrel for the nominal geometry and the preliminary aligned geometry.

time of flight. The shown results are for Long Barrel partition A of TileCal. One of the modules on the top side of TileCal was used as reference. The analysis proves that the intra-partition calibration of TileCal channels during 2008 commissioning was of the order of 2 ns.

Progress in the understanding of the MS performance has been achieved in terms of both tracking and triggering, providing first alignment and calibration corrections as well as lists of problematic channels. An example of the alignment status is shown in Fig. 7 (left) where the improvement of the residual distributions in one of the muon chambers thanks to the optical and track based alignment is clearly visible.

After checking the performance of the individual systems, the overall performance of the ATLAS reconstruction algorithms can be studied with cosmic rays. For example, the performance of combined tracking algorithms using measurements from both the ID and MS or muon identification algorithms based on the calorimeters or the muon system information can be verified. Fig. 7 (right) shows the difference in the azimuthal angle ϕ_0 (top) and momentum (bottom) obtained for tracks reconstructed in the ID and MS for both real and simulated data. For the momentum measurement in the muon system, tracks from the bottom part were used, and therefore due to the energy loss in the calorimeters the values obtained are lower than for the ID. In spite of the fact that no alignment corrections were applied, the data/Monte Carlo agreement is fairly good. One example of a reconstructed track is shown in Fig. 8.

17th International Conference on Computing in High Energy and Nuclear Physics (CHEP09) IOP Publishing
Journal of Physics: Conference Series **219** (2010) 032059 doi:10.1088/1742-6596/219/3/032059

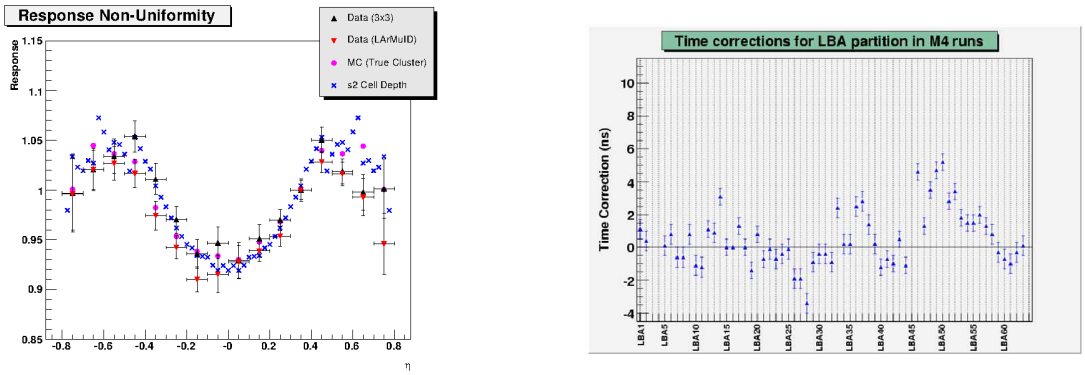

Figure 6. Normalized energy response in the electromagnetic calorimeter as a function of pseudo-rapidity η for real and simulated data as well as second sampling cell depth η dependence (left). The time difference between measured and expected time of flight for the Tile calorimeter barrel modules (right).

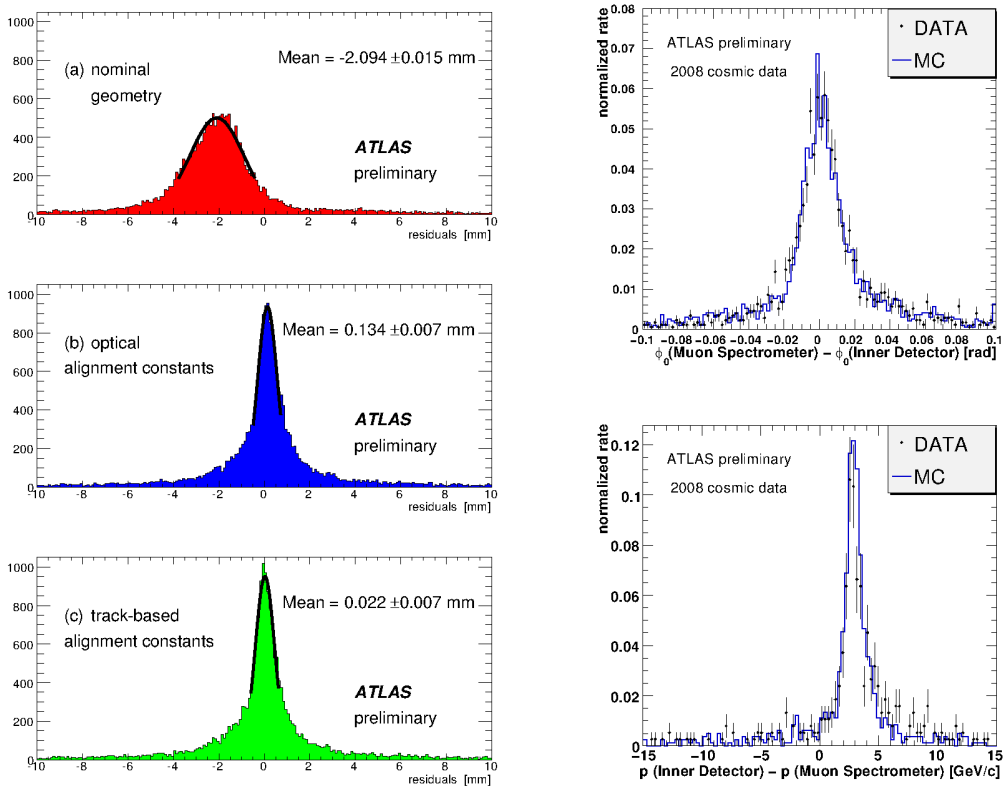

Figure 7. Measured sagitta for tracks passing in a middle muon chamber before alignment (top left) and after applying the alignment corrections obtained by the optical system (middle left) and those obtained using tracks (bottom left). Difference in azimuthal angle (top right) and momentum (bottom right) measured in the ID and MS.

17th International Conference on Computing in High Energy and Nuclear Physics (CHEP09) IOP Publishing
Journal of Physics: Conference Series **219** (2010) 032059 doi:10.1088/1742-6596/219/3/032059

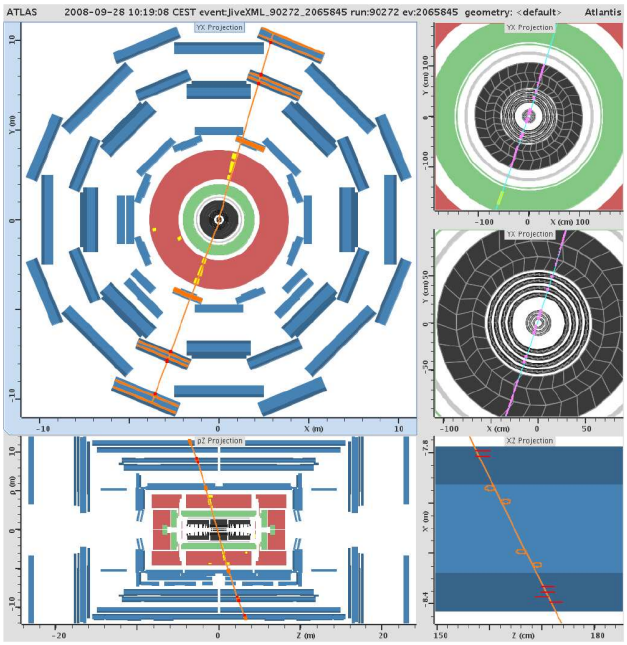

Figure 8. Event display of a cosmic ray event with hits in all barrel detectors at XY plane (top) and XZ plane (bottom).

3.2. LHC single beam

As already mentioned, on September 10, 2008, the first LHC beam started to circulate through the ATLAS detector. At first, for safety reasons, the collimators positioned 140 meters away from the center of the ATLAS detector were closed and therefore for each beam injection a spray of particles was expected to go through the detector, producing the so-called splash events. Once the collimators were opened and beam was circulating through ATLAS, it was expected to observe events coming from interactions of beam halo with collimators and pipe walls as well as events from beam interactions with residual gas in the pipe.

Thanks to the previous commissioning period with cosmic rays, the ATLAS detector was ready to take data and reconstruct it successfully at the start-up of the LHC. For safety reasons, the Pixel detector was turned off and the SCT, the muon chambers and the forward calorimeter were working at reduced high voltage. The first level trigger and the data acquisition were fully operational. The High Level Trigger (HLT) was available. However, since the plan was to store all events, it was decided to only use the HLT for streaming the data based on the first level trigger results.

One of the first splash events, with the detector timing not yet well tuned for the beam pickup trigger, is shown in Fig. 9. Dozens of these events were recorded with more than 1000 TeV of reconstructed energy in the calorimeters, hundreds of thousands of hits in the MS, etc. They are perhaps the highest energy events ATLAS will ever record. Since these events produce a signal in almost all channels of the detector, they are very useful to find dead channels and also to time in all channels with high precision with only a few events.

Once the collimators were opened and a single beam of protons was circulating through the ATLAS detector, before RF capture was achieved, quite a few particles were detected crossing the detector horizontally at the same time, corresponding to beam halo muons. Fig. 10 (left) shows one of these events, where horizontal tracks can be seen. These horizontal tracks were used in the hadronic calorimeter to validate the energy intercalibration of the Tile calorimeter

17th International Conference on Computing in High Energy and Nuclear Physics (CHEP09) IOP Publishing
Journal of Physics: Conference Series **219** (2010) 032059 doi:10.1088/1742-6596/219/3/032059

cylinders, by computing the energy deposit per path length along the beam axis. As can be seen in Fig. 10 (right), the most probable value of muon energy loss per path length over all cells within a given partition was checked to be uniform within 4% precision level which was already obtained from calibration with radioactive gamma sources.

Once RF capture was achieved, the beam was much cleaner and therefore very few beam halo muons were seen in ATLAS. Unfortunately, due to the LHC transformer failure on the 12th of September, ATLAS could not record a large amount of data in these conditions. Concerning beam-gas interactions, none of these events have been observed in the ATLAS recorded data, probably because of the excellent vacuum in the pipe. Some observed events may have been due to protons hitting the beam pipe. But, given that the the ID was not fully operational during this period, the identification of this kind of events is difficult.

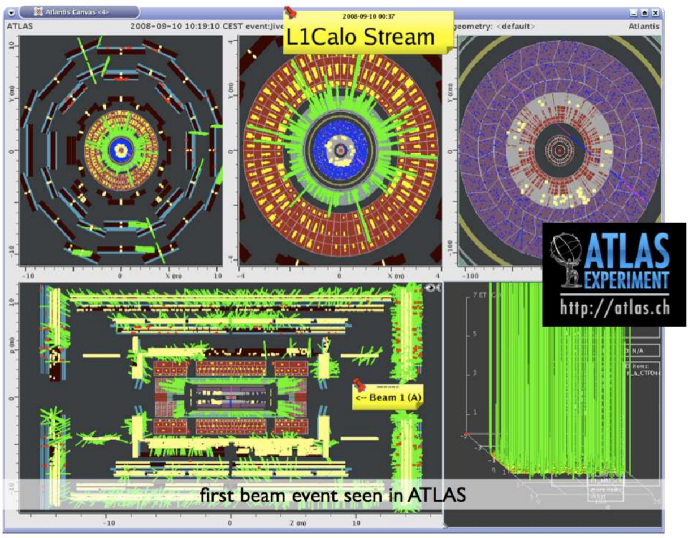

Figure 9. One of the first LHC event seen by the ATLAS detector (event 40050, run 87764) produced by the interaction of the beam with the closed tertiary collimators: XY projection (top), XZ projection (bottom)

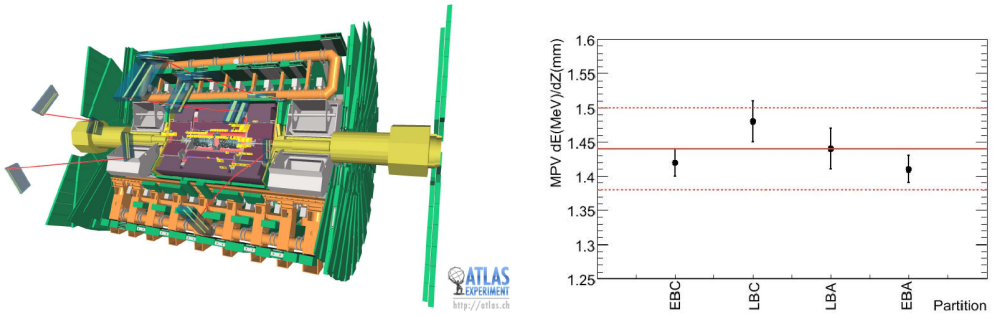

Figure 10. Event display of beam halo muons reconstructed in the ATLAS (left). Energy deposit per path length in different partitions of TileCal barrel (right). The red lines represent the average value from the 4 barrels and its 4% uncertainty.

17th International Conference on Computing in High Energy and Nuclear Physics (CHEP09) IOP Publishing
Journal of Physics: Conference Series **219** (2010) 032059 doi:10.1088/1742-6596/219/3/032059

4. Conclusions

The commissioning of the ATLAS detector with physics data started more than four years ago with cosmic rays. The ATLAS reconstruction software, closely following the commissioning of the ATLAS detector, is being commissioned with all available physics data. The full offline reconstruction chain is in place providing reconstruction for the high level trigger, monitoring, event displays, calibration and alignment studies, and offline analysis. At the same time we commission the ATLAS computing and grid environment. The analysis of both cosmic ray and LHC single beam data has improved our understanding of the detector, reconstruction, monitoring and simulation software and has enabled us to obtain the first calibration and alignment corrections. We are prepared for and looking forward to first LHC collisions in 2009.

References

[1] The ATLAS Collaboration, Aad G *et al.*, The ATLAS Experiment at the CERN Large Hadron Collider, JINST 3 (2008) S08003.
[2] The ATLAS Collaboration, Duckeck G *et al.*, ATLAS Computing Technical Design Report, CERN-LHCC-2005-022
[3] The ATLAS Collaboration, Adams D *et al.*, The ATLAS Computing Model, proceedings of CHEP2004, CERN-LHCC-2004-037-G-085
[4] ATLAS HLT/DAQ/DCS Group, ATLAS High-Level Trigger, Data Acquisition and Controls Technical Design Report, CERN-LHCC-2003-022, ATLASTDR-016 (2003).
[5] Dotti A *et al.*, OHP: An Online Histogram Presenter for the ATLAS experiment, ATL-DAQ-CONF-2006-006
[6] Corso-Radu A, Kolos S, Hadavand H, Kehoe R, Hauschild M, Data Quality Monitoring Framework for the ATLAS Experiment at the LHC, ATL-DAQ-CONF-2008-006
[7] Dar A, *Phys. Rev. Lett* **51** (1983) 227